# Durham E-Theses

## *Electronic conduction in silicon-rich thin films*

Buchanan, D.A

**How to cite:**

Buchanan, D.A (1986) *Electronic conduction in silicon-rich thin films*, Durham theses, Durham University. Available at Durham E-Theses Online: http://etheses.dur.ac.uk/7101/

**Use policy**

# ELECTRONIC CONDUCTION

## IN SILICON-RICH

## THIN FILMS

by

D.A. Buchanan, B.Sc, M.Sc.

A thesis submitted for the

Degree of Doctor of Philosophy

in the University of Durham

August 1986

-1. DEC 1986

# DECLARATION

I hereby declare that the work reported in this thesis has not previously been submitted for any degree and is not currently submitted in candidature for any other degree.

Signed     *LBuchanan*

Candidate

The work reported in this thesis was carried out by the candidate.

Signed     *LBuchanan*

Candidate

# ABSTRACT

Silicon-rich silicon nitride (SRN) films were grown by low pressure chemical vapour deposition (LPCVD) with excess silicon concentrations varying from 8.8% to 12.8% by varying the reactant gas phase ratio from $R_n = 4.0$ to $R_n = 0.25$. Dichlorsilane and ammonia were the reactant gases and nitrogen was used as the carrier gas. All films were found to be predominantly $\alpha$-$Si_3N_4$ with free silicon crystallites being found in the films with the greatest silicon content. The conduction mechanism at high temperatures and electric fields is due to Poole-Frenkel emission of trapped electrons (holes) from relatively deep defect levels to the conduction (valence) band tails. From a steady-state analysis the effective trap depth, $\phi_t$ was found to be approximately 1.1 eV and it decreased slightly with increasing silicon content of the films. Low values of calculated dielectric constant were found and attributed to the build up of space charge near the injecting contact. For thin films ($< 1000$ Å) steady state analysis cannot be considered accurate unless the effects of trapped space charge are taken into account.

For positive (negative) applied bias voltages, the flat band shift is in a positive (negative) direction implying a net increase in negative (positive) charge within the SRN film. A logarithmic time dependence is found for the transient flat band shift while for long periods of time (i.e. $t > 1s$) the current transient was inversely proportional to time. A charge trapping model is presented which predicts a logarithmic increase in the flat band shift with time. The model is based on the assumption that charge carriers, holes for negative bias and electrons for positive bias, tunnel from the silicon valence and conduction bands into the deep defect levels in the SRN film. Very good agreement was found between the data and the model for low electric fields. At high electric fields, the situation becomes complicated by Poole-Frenkel 're-emission' from the traps which leads to a 'saturation of the flat band shift with time. At high electric fields, the current transient also becomes dominated by Poole-Frenkel emission of trapped carriers. It was also found from the current transients, that the calculated dynamic dielectric constant decreases with increasing time reflecting the increase in trapped charge. From the Schottky curves for times of one second. $\varepsilon_d$ was found to vary from 5.09 to 5.26 for excess silicon content 8.8% to 12.3%. For these SRN films the density of trapping centres near the SRN-silicon interface was found to be of the order of $3 \times 10^{19} cm^{-3}$.

Silicon-rich silicon oxide (SRO) films were grown in a atmospheric pressure CVD reactor using nitrous oxide and silane as the reactants and nitrogen as the main carrier gas. The conduction in silicon-rich oxide (SRO) was investigated using standard I-V techniques. Three models of conduction were investigated. These were a symmetrical Schottky barrier model similar to that used for polycrystalline silicon. a model based on a type of Fowler-Nordheim tunnelling between silicon crystallites in the SRO film and a model based on Poole-Frenkel emission from the silicon crystallites into the conduction band or band tails of the film. It was extremely difficult to assess the true nature of the conduction in the silicon-rich oxide (SRO) films. However, the evidence seems to point towards the Poole-Frenkel mechanism as being responsible for conduction.

CONTENTS

# Chapter 1

## Introduction

Insulating films are of crucial interest to the microelectronics industry today. The most commonly used insulators are silicon dioxide and silicon nitride. Silicon dioxide is used primarily for its dielectric properties as in MOS transistors and capacitors. Silicon nitride, on the other hand, is used for surface passivation or as a charge storage medium as in MNOS structures. With the possible exception of MIS tunnel diodes, neither material is suitable for taking an 'active' rather than a 'passive' role in microelectronics because of their highly insulating nature.

Recent advances in fabrication technology allowing the study of non-crystalline materials, although used predominantly for semiconductors, have made it possible to adjust the conductivity of insulating films by the addition of suitable dopants. Generally speaking, to enable insulators such as silicon dioxide to pass a substantial current with a reasonable applied voltage, tunnelling thicknesses (i.e. < 50 Å) are needed. The difficulty in growing such thin layers, that are still of uniform thickness over large areas, is substantial. For this reason some researchers have turned to studying semi-insulating materials that can be grown with much greater thicknesses and subsequently greater uniformity and reliability while maintaining a sufficient conductivity for device applications

In some devices it is desirable to have a dielectric film that is able to pass substantial currents with low applied bias voltages. The MISS device is such a structure where the 'I' is a semi-insulating film. In the past, these devices have been made with thin tunnel oxides. However, these are difficult to grow consistently. If thicker films were to be used, much higher conductivities would be also required of the insulating films. Silicon rich films such as silicon-rich silicon dioxide and silicon-rich silicon nitride, are two examples of dielectric films that may be used for this application.

Both silicon dioxide and silicon nitride can be made more conducting by increasing the silicon content from the stoichiometric value. Films of both materials can be grown using any standard chemical vapour deposition (CVD) process, be it atmospheric, low pressure or even plasma enhanced. The composition and structure of the resultant material is dependent upon deposition temperature, carrier gas pressure, type and flow rate, plasma power, etc., but it is predominantly dependent upon the volume concentration of the reactant gases. With careful control of the deposition and post-deposition processes, the conductivity of these materials can be varied, and in some cases over many orders of magnitude.

The processes responsible for the electronic conduction of such materials are the main topic of this thesis. The main aim was to discover the mechanisms responsible for conduction as the silicon content of films of these materials was varied. The majority of the work is concerned with silicon-rich silicon nitride (SRN) with silicon-rich silicon oxide (SRO) taking a

2

secondary role.

The basic structure used for the study of the SRN and SRO thin films was the metal-insulator-semiconductor (MIS) device with silicon as the semiconducting substrate. As these materials are extensions of their insulating predecessors, a short review of the properties of thick MIS devices is given in Chapter 2. The MIS device, apart from being of interest for the application of these films, is a valuable structure for research in conduction processes as the capacitance characteristics enable conclusions to be drawn on charge storage in the films. This has enabled additional information to be obtained for the SRN films, which have often been studied in the past using metal electrodes only. MIS structures give much valuable extra information on thin film properties as shown in Chapter 7 of this thesis.

Chapter 3 contains a discussion of the main forms of electronic conduction found in insulating and dielectric materials. Both bulk and injection limited mechanisms are included. In Chapter 4, the material growth and device fabricationtechniquesare presented. Included in this chapter is a description of the basic experimental measurement techniques used in this work.

It was not only fundamental to discover how the conduction mechanisms in these materials change with increasing silicon content. It was equally important to discover why. Therefore results of some structural measurements. i.e. reflection high energy electron diffraction (RHEED). Rutherford backscattering (RBS) and Auger electron spectroscopy (AES), were included to

3

look for correlation between material composition, structure, or crystallinity and the electronic properties. These techniques and the experimental results and discussion of the SRN thin films, are included in Chapter 5.

Chapters 6 and 7 contain the experimental electrical results and their discussion of the SRN devices. Chapter 6 discusses the DC or steady state conduction properties, while Chapter 7 presents the transient capacitance and conduction. A simple model is presented in Chapter 7 that explains the charge storage and transient charging in the SRN films. The characterization, both structural and electronic, of the silicon-rich silicon dioxide (SRO) thin films is given in Chapter 8. Included are Auger, RBS and RHEED analysis as well as a discussion of the conduction mechanism based on current-voltage measurements. Chapter 9 summarises the conclusions of this study and gives suggestions for further work.

# Chapter 2

## Thick MIS devices

### 2.1  Introduction

A thick insulator MIS device may be defined as one in which the leakage current by tunnelling or emission of carriers is negligible.  This is generally true for insulators of thickness greater than 50 Å.  Since the first MIS structure was proposed as a voltage controlled capacitor in 1959 [1,2], they have proved to be very useful for the study of semiconductor interfaces and surfaces.  The reliability and stability of all semiconductor devices relies on an understanding of surface physics and the production of reproducible, high quality interfaces.  The study of surface physics and semiconductor devices has therefore been centred around MIS devices.

The following sections give a brief overview of thick MIS device physics.  In section 2.2 the 'ideal' MIS device is presented while the following sections are devoted to the most common non-idealities and their effect on the 'ideal' MIS operating characteristics.  These non-idealities include non-zero work function differences, surface and bulk charges (fixed and mobile), temperature effects and illumination effects.

### 2.2  The 'Ideal' Metal-Insulator-Semiconductor (MIS) Diode

The structure of an ideal MIS device is shown schematically in Fig. 2.1 where d is the thickness of the insulating layer and V is the bias voltage applied to the metal with respect to the

5
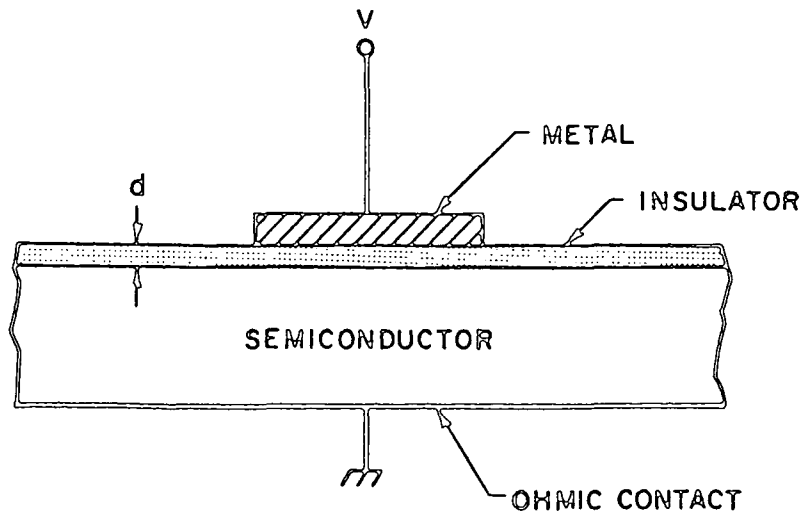
Figure 2.1    Metal-insulator-semiconductor (MIS) diode.
              (from Ref. 3)
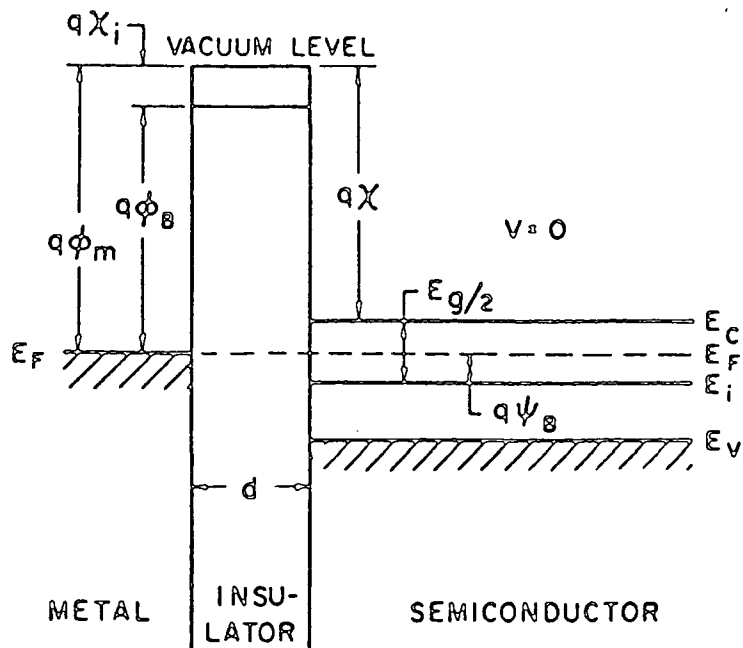


Figure 2.2    Energy band diagram of an ideal MIS (n-type)
              diode at zero bias. (from Ref. 3)

semiconductor. Figure 2.2 shows the energy band diagram of the same structure. An ideal MIS diode is defined by the following :

i) With no applied bias, there is no band bending (see Fig. 2.2). This condition is known as 'flat-band'. The energy difference between the metal and the semiconductor is zero. The work function difference is given by

$$\phi_{ms} = \phi_m - \phi_s$$

$$= \phi_m - \left[ \chi - \frac{E_g}{2q} - \psi_B \right] \tag{2.1}$$

$$= 0 \quad \text{(in the 'ideal case)}$$

where $\chi$ is the semiconductor electron affinity, $E_g$ is the energy band gap and $\psi_B$ is the potential difference between the Fermi level ($E_f$) and intrinsic Fermi level ($E_i$) in the semiconductor bulk.

ii) The only charge that exists in the system is either at the metal-insulator interface or in the semiconductor. The total charge in the metal is equal and opposite to the total charge in the semiconductor, such that charge neutrality is maintained at all bias voltages.

iii) The insulator is of infinite resistance. There is no DC carrier transport through the insulating films. Thus the ideal MIS structure is a true voltage or, more accurately, a field controlled device.

With an applied bias the band structure is changed to accommodate the change in potential of the system. The bias of

6

an MIS device is usually defined as the potential of the metal with respect to the semiconductor. The 'forward' bias condition is when the metal is positive (negative) for an n-type (p-type) semiconductor. A similar situation exists for the 'reverse' bias condition with the polarities reversed. The energy band diagrams of an MIS device under three bias conditions are shown in Fig. 2.3. For the sake of simplicity an n-type semiconductor will be used as the example throughout this section though the extension to a p-type material is trivial.

Consider the energy band diagram of an 'ideal' MIS device (Fig. 2.3a) with a positive voltage on the metal. Under forward bias the bands bend down. From Fermi-Dirac statistics the density of electrons in the conduction band, if $(E_c-E_f)$ ›› kT, is exponentially proportional to the separation of the Fermi level and the conduction band.

$$n_n = N_c \exp\left[-\frac{(E_c - E_f)}{kT}\right] \qquad (2.2)$$

where $N_c$ is the effective density of states in the conduction band. With increasing forward bias, the conduction band bends towards the Fermi level reducing $(E_c - E_f)$ at the surface. A negative charge density concentrates at the surface due to the increase of the majority carrier density. This negative charge at the surface of the semiconductor is of course balanced by an equal and opposite positive charge in the metal. This condition is known as accumulation so as to reflect the accumulation of majority carriers at the surface.

With a negative voltage applied to the metal, the bands are
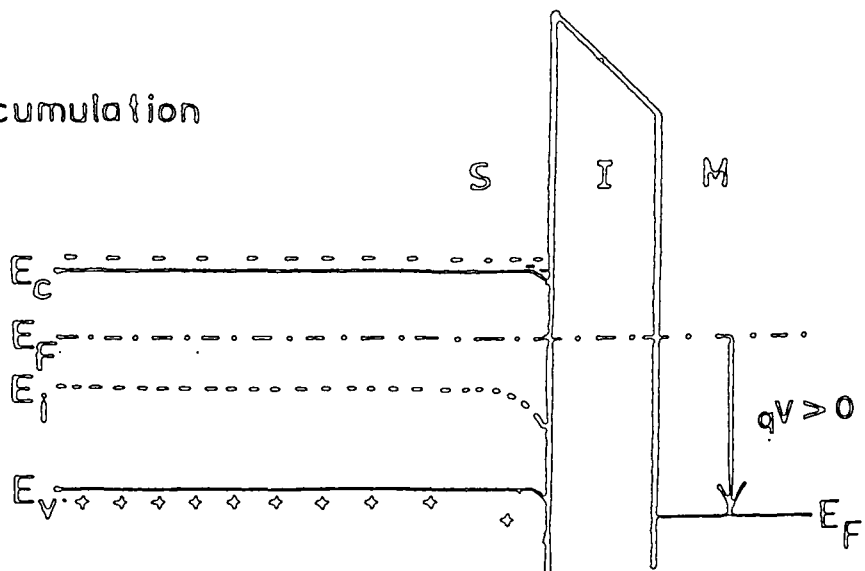
Figure 2.3    Energy band diagram for an MIS structure showing
              (a)  accumulation,   (b)  depletion   and (c)
              inversion.

bent upwards as shown in Fig. 2.3b. At the surface the separation between the conduction band edge and the Fermi level is increased. Therefore the density of majority carriers at the surface is reduced from the zero bias value. Majority carriers are swept from the surface leaving behind the fixed positive charge of the ionized donor atoms. The surface is now said to be depleted of majority carriers.

As the negative voltage is increased, the surface becomes more depleted of majority carriers and minority carriers start to accumulate. At the point where the Fermi level ($E_f$) crosses the intrinsic level ($E_i$) at the interface, the surface of the semiconductor is said to be inverted. The number of minority carriers at the surface now exceeds the number of majority carriers in the bulk. Thus the surface of the semiconductor has been inverted from an n-type material to a p-type material.

In an ideal MIS system, the bias condition is described by the position of the intrinsic Fermi level at the surface with respect to its position in the bulk of the semiconductor. Figure 2.4 shows the surface potential ( $\psi_s$ ) in inversion. The following regions of surface potential can be defined.

| | |
|---|---|
| $\psi_s > 0$ | accumulation - bands bend down |
| $\psi_s = 0$ | 'flat band' condition |
| $\psi_B < \psi_s < 0$ | depletion - bands bend up |
| $\psi_s = \psi_B$ | midgap |
| $\psi_s > \psi_B$ | inversion |

The surface concentrations of both the minority and
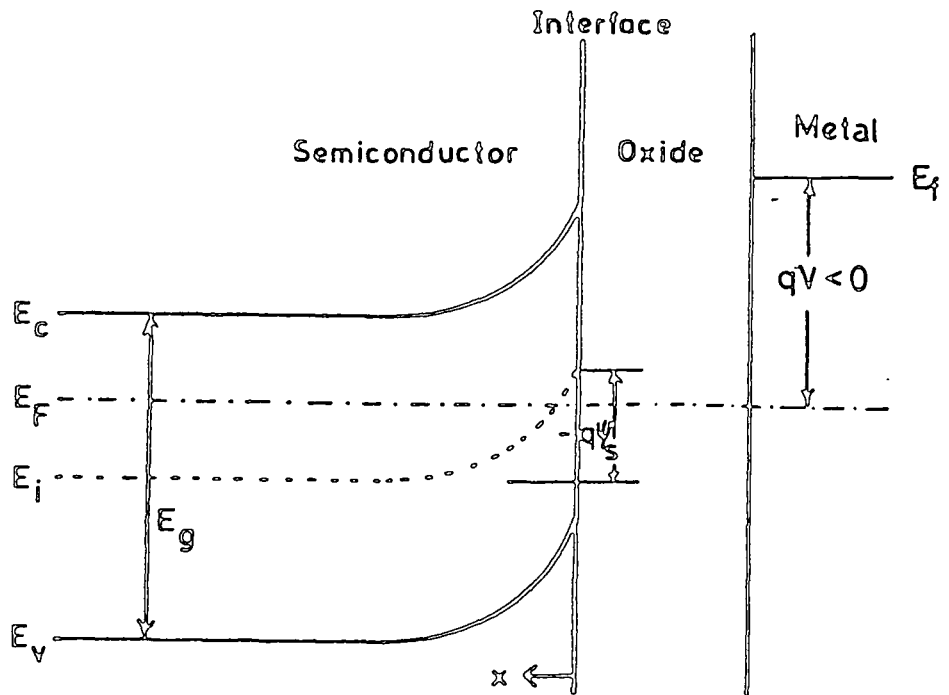
Figure 2.4    Energy band diagram of an MIS diode in inversion
              showing surface potential



(a) BAND DIAGRAM

(b) CHARGE DISTRIBUTION (IDEAL MIS)

(c) ELECTRIC FIELD

(d) POTENTIAL DISTRIBUTION
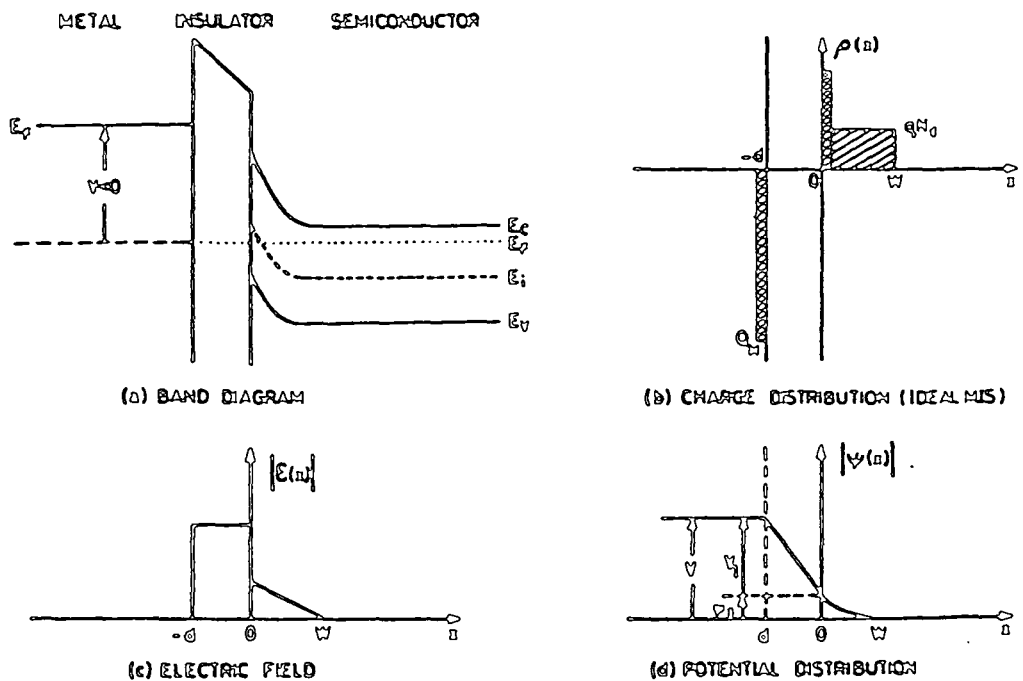
Figure 2.5    (a) band diagram of MIS diode (inversion)
              (b) charge distribution
              (c) electric field
              (d) potential distribution

majority carriers can be found as a function of the surface potential. For an n-type semiconductor, these are given by

$$n_s = n_{no} \exp\left[\frac{q\psi(x)}{kT}\right] \qquad P_s = P_{no} \exp\left[-\frac{q\psi(x)}{kT}\right] \qquad (2.3)$$

where $n_s$ ($p_s$) and $n_{no}$ ($p_{no}$) are the majority (minority) carrier concentrations at the surface and in the bulk respectively. The potential distribution can be found by successive integrations of Poisson's equation as a function of distance from the surface (x).

$$\frac{\partial^2\psi}{\partial x^2} = -\frac{\rho(x)}{\varepsilon_s \varepsilon_o} \qquad (2.4)$$

where $\rho(x)$ is the charge density and $\varepsilon_o$ and $\varepsilon_s$ are the free space permittivity and dielectric constant of the semiconductor. Using Gauss' law and Poisson's equation, the charge density distribution in the semiconductor can be found and related to the bias voltage. Figure 2.5 shows the variation of the charge density, electric field and potential as a function of distance for an n-type semiconductor in inversion.

For a given bias, there is an equal and opposite charge on either side of the insulating layer. Any double layer of charge that varies with voltage has the property of capacitance. The capacitance of the device is directly related to the change of charge density which in turn is related to the surface potential

9

$\psi_s$ when the bias voltage changes. The capacitance is therefore a function of the bias voltage and capacitance-voltage (C-V) plots give a good representation of the charge state of the device. A normalised C-V curve for an n-type MIS device is shown in Fig. 2.6 while the device structure is shown schematically in the inset. In all such curves the capacitance is expressed per unit area throughout this thesis.

The MIS system can be represented by two capacitors in series : one representing the geometrical capacitance of the insulator, the other representing the capacitance due to the induced charge in the semiconductor which is bias dependent. The total capacitance is given by the parallel combination of the two.

$$C_T = \frac{C_{sc} \, C_i}{C_{sc} + C_i} \qquad (2.5)$$

where $C_i$ and $C_{sc}$ are the insulator and the semiconductor space charge capacitances respectively. As the bias voltage changes, the value of $C_T$ changes reflecting the variation in $C_{sc}$. The variation of $C_{sc}$ is, of course, due to the change in the surface charge as the bias changes.

The regions of operation of an MIS diode can be related to the total capacitance. In accumulation there is a high density of charge at the interface due to the accumulation of majority carriers. As a result, a high differential capacitance is associated with the space charge at the surface. However $C_{sc}$ is large relative to the geometrical capacitance, the total capacitance approaches a maximum value of $C_i$.
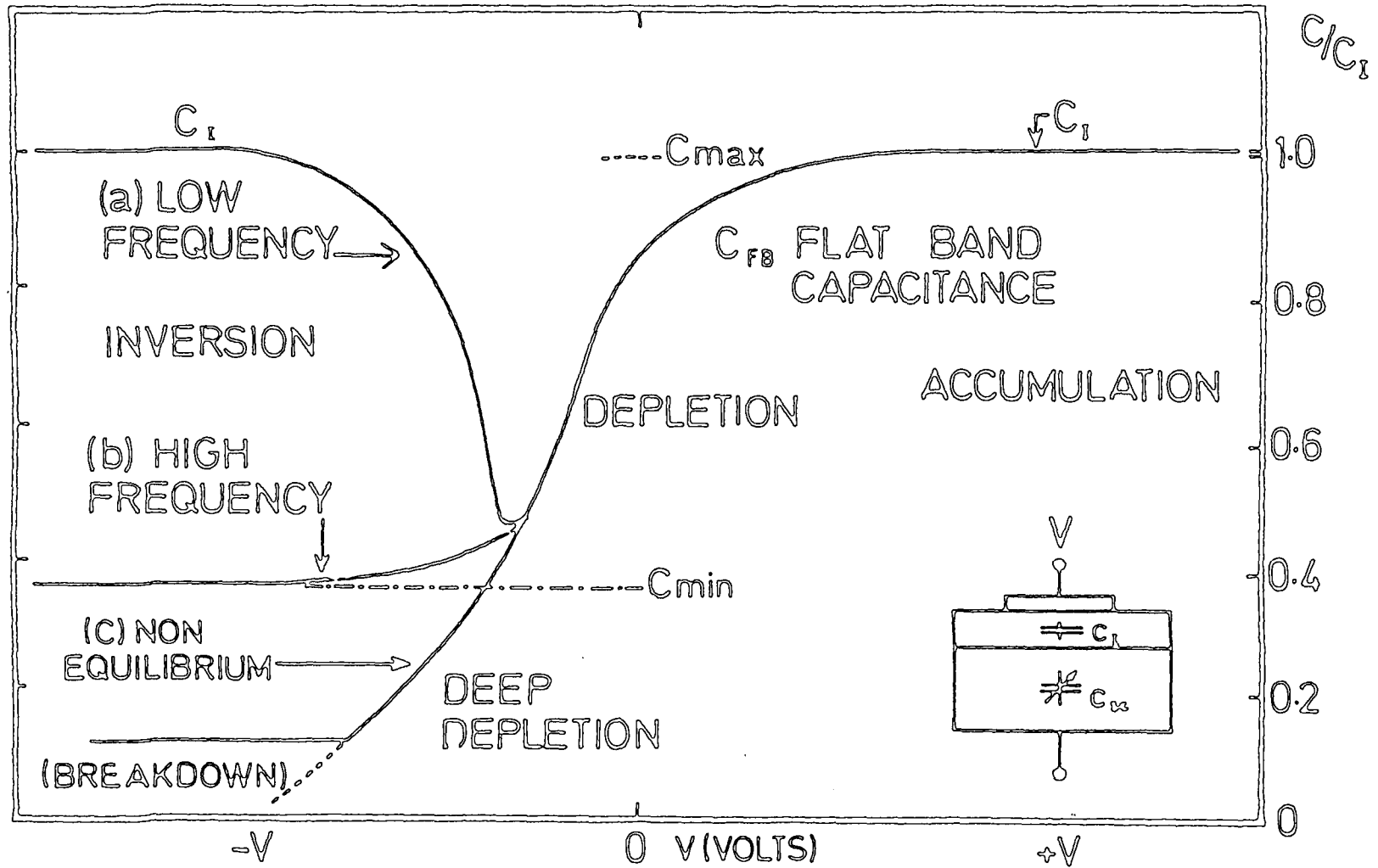
Figure 2.6    Normalized ideal MIS Capacitance-voltage curve
(n-type semiconductor).

For a small negative bias a depletion region is formed  and acts  like  a  dielectric  in series with the insulator.  As the negative bias is increased, the width of the  surface  depletion region  increases  with  a  corresponding  decrease  in  $C_{sc}$. Subsequently the total capacitance also decreases.

With  a  continued  increase  in  negative  bias, the total capacitance  approaches  a  minimum  if  the  frequency  of  the differential  capacitance  signal  is  sufficiently low.  At this point  an  inversion  layer  of  minority  carriers  forms  at  the interface.

The formation of the inversion layer is dependent upon bulk generation  of  minority carriers and their subsequent transport to the surface.  Its formation also depends upon the removal  of the  majority  carriers  from  the  surface and their subsequent recombination in the bulk.  It is usually found that the  former process is the limiting factor.

The increase in total (low frequency) capacitance  through the minimum with increasing negative bias (see Fig. 2.6) depends on the ability of the minority carriers to  respond  to  the  ac signal.   This  phenomenon  is  only  realised  at  very  low frequencies  where  the  recombination-generation  rate  of  the minority  carriers  can  follow  the  small  ac  signal.  At low frequencies (usually ‹ 100 Hz), the increasing total capacitance reflects  the  increase  in  inversion  charge.  However at high frequencies, even though the inversion layer is still  produced, the  inversion  charge  is  not  able  to  keep in step with the measurement signal.  Thus it makes no contribution to the  total measured  capacitance.   For  both high and low frequencies, the

formation of the inversion layer effectively screens the depletion region from further voltage increases. Subsequently the depletion capacitance is maintained at a minimum as is the total capacitance if the frequency is such that the inversion charge does not respond.

In the discussion thus far it has been assumed that the bias voltage is either constant or extremely slowly changing relative to the small ac signal. If the rate of change of the bias voltage is faster than the response time of the minority carriers, an inversion region does not form. The width of the depletion region then increases, the depletion capacitance decreases, and the total capacitance decreases. This phenomenon is known as deep depletion and it describes the condition where the depletion region extends beyond its normal maximum width. Since the inversion layer does not have time to form, the depletion region is not screened and it continues to grow with increasing bias, so that $C_{sc}$ decreases as does $C_T$. To produce such fast rising bias voltages short pulses are usually used. If a voltage pulse is fast enough and its magnitude high enough, impact ionization occurs which eventually leads to a catastrophic breakdown of the semiconductor or insulator.

From the ideal (C-V) curves there are certain parameters which are of some importance. The 'flat band capacitance' is defined as the total capacitance of the device when $\psi_s = 0$ and is given by [3]

$$C_{FB} = \frac{\epsilon_i \epsilon_o}{d + \frac{1}{\sqrt{2}}\left(\frac{\epsilon_i}{\epsilon_s}\right)L_D} \qquad (2.6)$$

where $\varepsilon_i$ and d are the dielectric constant and thickness of the insulator and $L_D$ is the Debye length which represents the effective depth of penetration of the surface electric field into the semiconductor. The Debye length is given by

$$L_D = \left( \frac{2 \, kT \, \varepsilon_s \, \varepsilon_o}{n_{no} \, q^2} \right)^{\frac{1}{2}} \qquad (2.7)$$

where $n_{no}$ is the equilibrium density of the majority carriers (electrons) in the semiconductor bulk. The maximum total capacitance is the geometric capacitance of the insulating layer and is given by

$$C_{max} = \frac{\varepsilon_i \, \varepsilon_o}{d} \qquad (2.8)$$

The minimum capacitance (for the high frequency case) is the series combination of $C_i$ and the $C_{sc}$ for a maximum depletion width ($W_{d_{max}}$). The total minimum capacitance is given by

$$C_{min} = \frac{\varepsilon_i \, \varepsilon_o}{d + \left( \dfrac{\varepsilon_i}{\varepsilon_s} \right) W_{d_{max}}} \qquad (2.9)$$

where the maximum depletion width ($W_{d_{max}}$) is given by

$$W_{d_{max}} = \left[ \frac{4 \, \varepsilon_o \, \varepsilon_s \, kT}{q^2 \, N_d^+} \, \ln \left( \frac{N_d^+}{n_i} \right) \right]^{\frac{1}{2}} \qquad (2.10)$$

13

and where $N_d^+$ is the ionized donor density and $n_i$ is the intrinsic carrier concentration.


## 2.3 Non Idealities in MIS Devices

Practical MIS devices differ from the ideal case in many ways. The following sections outline the major causes of these deviations and how they modify device characteristics.


### 2.3.1 Work Function Difference

For an ideal MIS device the work function difference ($\phi_{ms}$) is zero, and therefore with no applied bias the potential between the metal and semiconductor is zero and there is no band bending (i.e. flat band). However if $\phi_{ms} \neq 0$, flat band does not occur when the bias is zero but rather at a voltage shifted by an amount equal to $\phi_{ms}$. The voltage shift (for an n-type semiconductor) was given by (2.1). The magnitude of $\phi_{ms}$ determines whether the surface is accumulated, depleted or in extreme cases inverted at zero bias.


### 2.3.2 Interface States

It is well known and understood that if a crystal structure comes to an abrupt end (as there is at a surface or an interface between two materials) the bonding arrangement at the surface or interface is not completely satisfied. These imperfections (impurities or defects) result in localised energy states that exist within the energy gap of the semiconductor. Such localised electronic energy states are usually termed either surface states and/or interface states.

14

It is quite common to find the terms surface and interface states used in an incorrect interchangeable manner which only leads to ambiguity and uncertainty. It is from this that the use of the term surface state will be restricted to devices that have a 'real' bare surface. A surface that has been passivated by an oxide may contain interface states. For the sake of clarity the term interface state will be used hence to describe those states that occur between the semiconductor and the insulator in an MIS system. It is difficult, if not impossible, to distinguish generally between the origins of these states.

Interface states are usually characterized in terms of their density (per unit area, per unit energy), their position in the gap relative to one of the band edges of the semiconductor and their capture cross section. It should be noted that the density of interface states is given per unit area and not per unit volume, as they would be for bulk states, for the simple reason that they occur in a two dimensional plane. Interface states may trap electrons and/or holes but their occupancy depends upon their position in the gap relative to the position of the Fermi level at the interface.

Interface states are usually described as being donor-like or acceptor-like. A donor-like state is neutrally charged when filled and positively charged when empty. An acceptor-like state is neutral when empty and negative when filled.

The probability of occupancy of any state is determined from Fermi-Dirac statistics and is given by [4]

$$f(E_t) = \frac{1}{1 + g \exp\left(\dfrac{E_t - E_f}{kT}\right)} \qquad (2.11)$$

15

for donors and

$$f(E_f) = \frac{1}{1 + g \exp\left(\dfrac{E_f - E_t}{kT}\right)}$$

(2.12)

for acceptors where $E_f$ is the Fermi level at the interface, $E_t$ is the energy associated with the trap level and $g$ is the ground state degeneracy factor which accounts for effect of spin on the occupancy of the state. Common values for the degeneracy factor are $g \sim 1/2$ for donors and $g \sim 2$ for acceptors.

When a bias voltage is applied to the MIS structure, the Fermi level remains constant (providing thermal equilibrium is maintained). However the resulting band bending shifts the entire band structure with respect to the Fermi level at the semiconductor surface. This results in a change in the separation $E_f - E_t$ (for donors) and hence in the occupancy of the interface states. The change in occupancy and subsequently the change in the charge state of the device alters its electrical characteristics.

Each additional allowed state at the interface adds one electronic charge to the total system. This charge contributes additionally to the total capacitance. The occupancy of the states and hence the total charge, depends on the value of $\psi_s$ and therefore on the applied bias. The peak charge due to interface states contributing to the capacitance occurs when $E_f$ crosses $E_t$.

Consider the application of a small ac signal to an MIS structure containing a certain density of interface states.

Assume that all interface states below the Fermi level are filled and those above are empty since the device is considered to be in thermal equilibrium (see Figure 2.7). With the device biased into accumulation the bands are pulled down towards the Fermi level by the positive half cycle of the small ac applied bias. As $E_f$ (at the surface) crosses $E_t$, the interface states occupancy changes. In this case the traps capture electrons because $E_t < E_f$ while previously $E_t > E_f$. On the second half cycle of the signal, the conduction band moves away from the Fermi level and some of the states emit their trapped electrons. This process of capture and emission takes place in an average time $\tau$ which is related to the capture and emission rates of the states. It should be noted that the relative times for capture and emission are not necessarily the same although they are usually of the same order of magnitude. As the frequency of the ac signal increases, the amount of charge exchanged by the interface traps decreases. It is from this process of capture and emission that an MIS structure shows ac conductance as well as a perturbation of the shape of an 'ideal' C-V curve. The conductance is usually characterized as a peak on a conductance-voltage (G-V) curve at the bias voltage where $E_f$ crosses $E_t$.

It must be remembered that these interface states can trap charge and as such affect the charge state of the device. With charge trapped at the surface, the electric field and hence $\psi_s$ is modified. To produce a change in $\psi_s$ by a given amount, a different applied voltage is needed from the 'ideal' situation. The existence of the interface state charge has the effect of

$E_C$

$E_F$

$E_i$

$E_V$

FILLED

$qV > 0$

$E_F$

(a)

EMPTY

$E_C$

$E_F$

$E_i$

$E_V$

$E_F$

$qV < 0$

FILLED

(b)
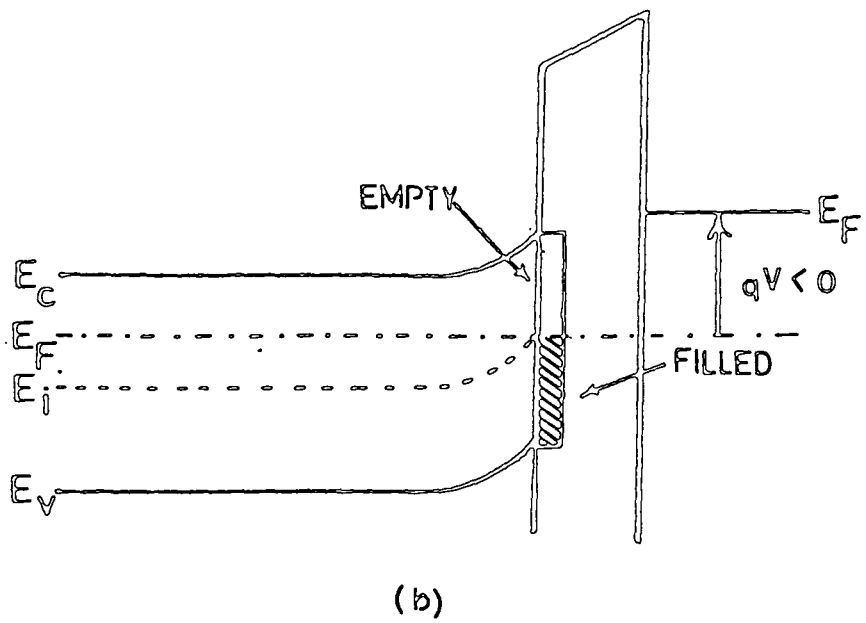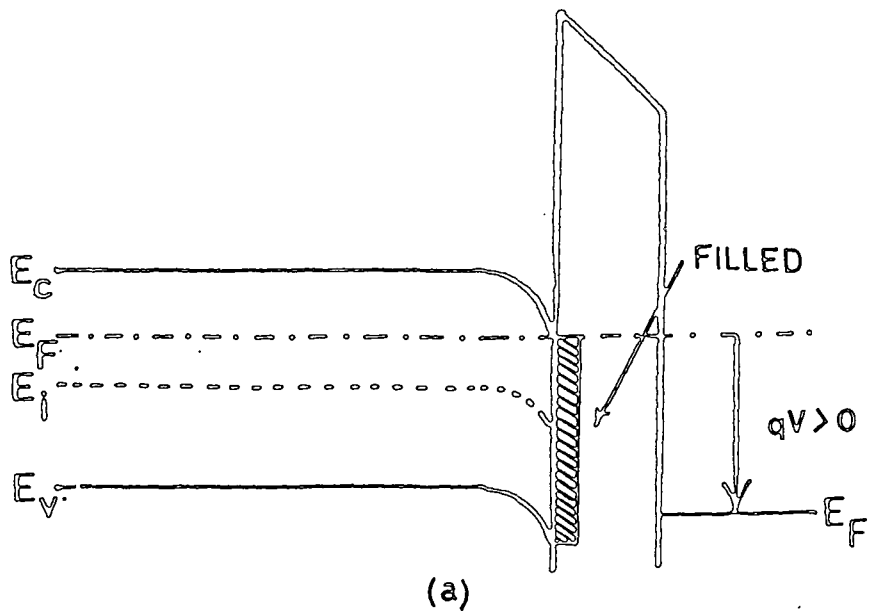
Figure 2.7    Energy  band  diagram  showing  change  in  occupancy
of  interface  states  with  (a)  positive   bias   and
(b) negative bias.

stretching out a C-V curve at low frequencies as shown in Fig. 2.8.

### 2.3.3 Surface and Insulator Space Charge

The existence of any additional charge near or at the interface modifies the surface potential ($\psi_s$) from that for the ideal device. It is also possible for charge to exist in the bulk of the insulator which again modifies $\psi_s$. Although it is very difficult to make a rigid distinction between bulk and interface states, those that exist within tunnelling distance ($< 100$ Å) of the semiconductor surface are usually considered as interface states since they are said to 'communicate' with the semiconductor.

The density and type of charge that may exist (whether from interface traps, bulk traps or fixed charge) is usually a result of the fabrication process. Especially crucial is the deposition of the insulating layer onto the semiconductor surface.

Figure 2.9 shows how a fixed charge density shifts a C-V curve laterally along the voltage axis. Consider a certain density of fixed positive charge near or at the interface and a negative bias on the metal as is shown in Fig. 2.10. Remembering that the device as a whole must maintain charge neutrality, the positive charge acts partly to compensate the charge at the metal/insulator interface. The remainder of the compensating charge is from ionized donors in the semiconductor so that fewer ionized donors are needed than for the ideal case. As a result, the depletion width is smaller at any given bias

18

C (vertical axis)

Interface state smear-out

low frequency

high frequency

(n-type semiconductor)

−V      0      +V
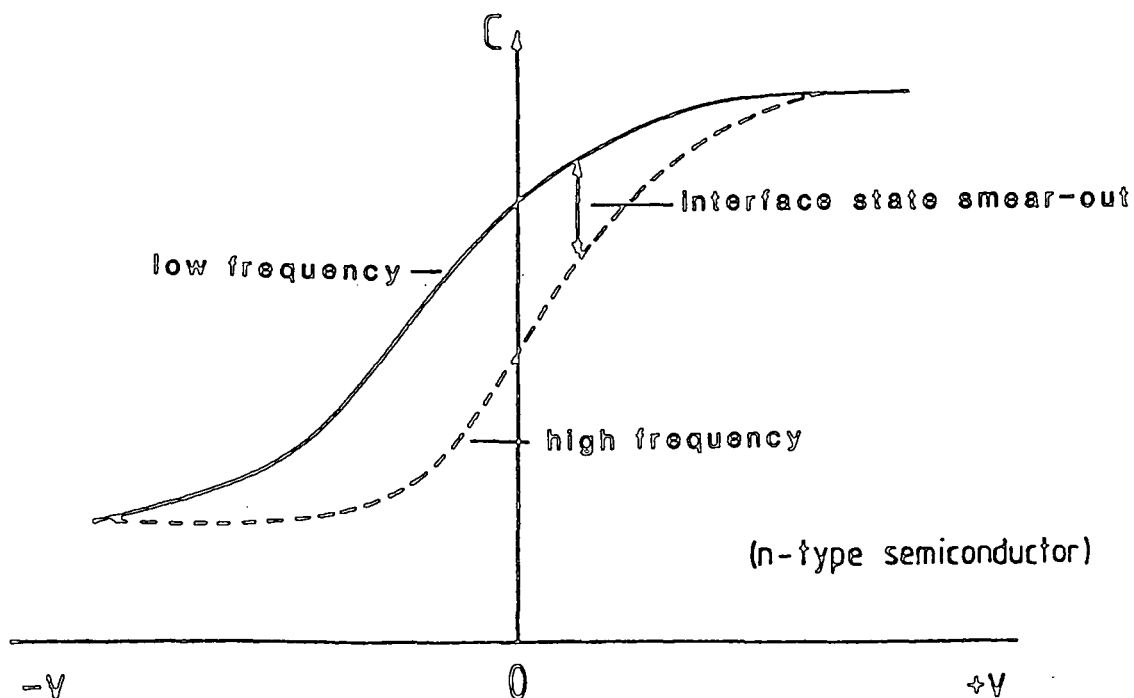
**Figure 2.8**   Frequency   dependence   of   C-V   curves   due   to interface effects.



$C_i$

$V_{FB}$
$(+Q_f)$

IDEAL
C-V CURVE

$C_i$

$V_{FB}$
$(-Q_f)$

IDEAL C-V CURVE

−  0  +      V

−  0  +      V

(a)



$V_{FB}$
$(+Q_f)$

$C_i$

IDEAL C-V CURVE

IDEAL
C-V CURVE

$C_i$

$V_{FB}$
$(-Q_f)$

−  0  +      V

−  0  +      V

(b)
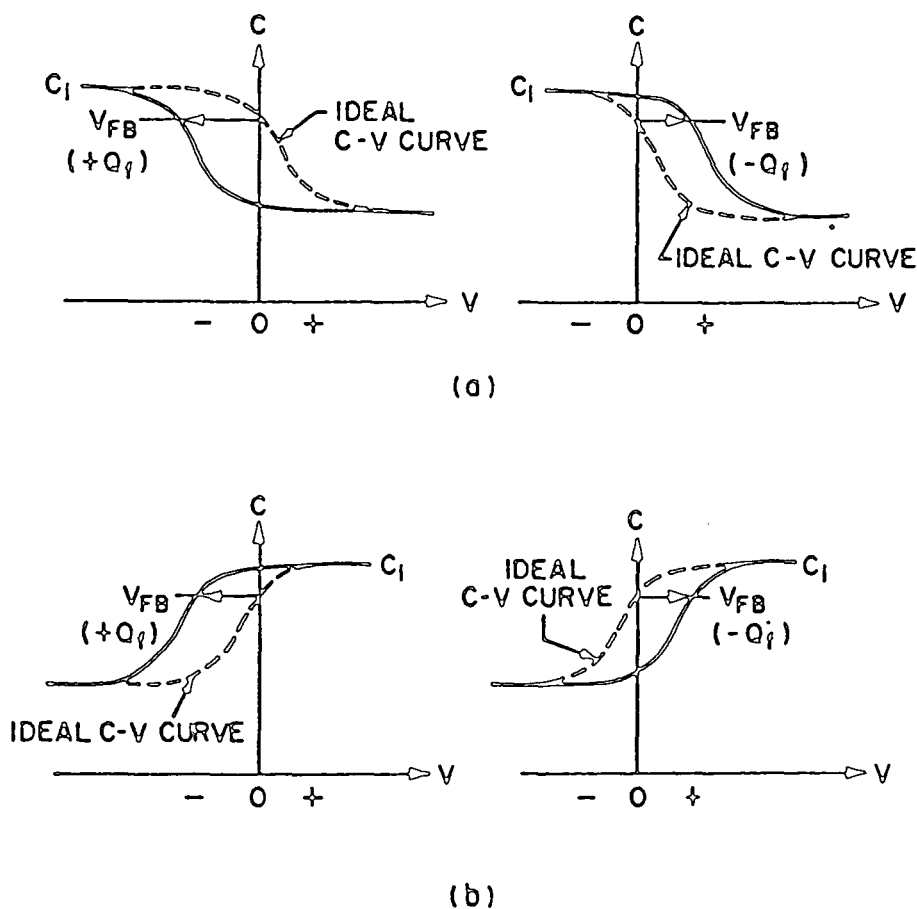
**Figure 2.9**   C-V curve shift along the voltage   axis   due   to positive and negative fixed insulator charge for (a) a p-type   semiconductor   and   (b)   a   n-type semiconductor.

METAL    SiO$_2$                     Si

FIXED OXIDE CHARGE ($Q_f$)
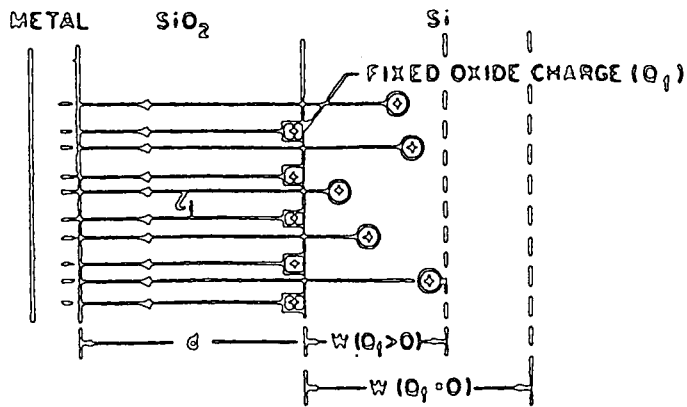
Figure 2.10    Effect of fixed charge on an MIS diode.



$+$ve ions    (a)

$-$ve ions    (b)
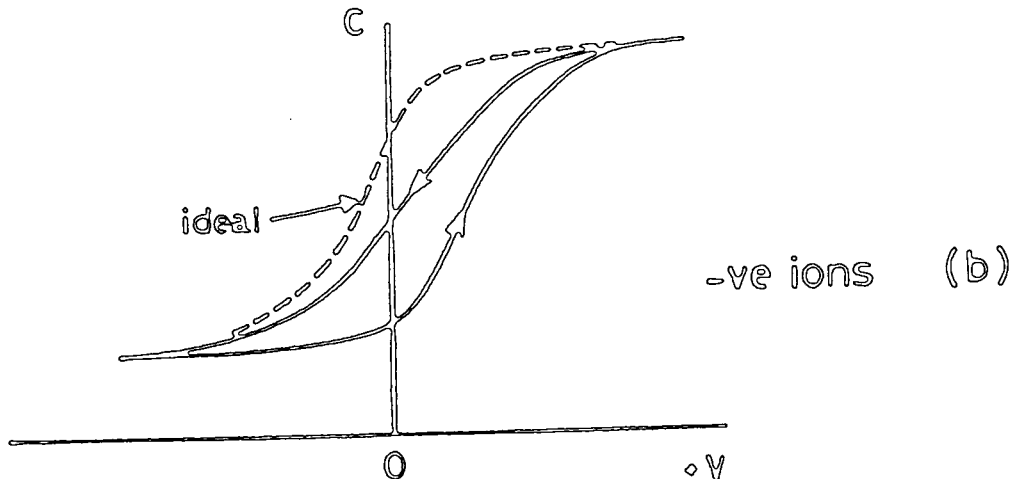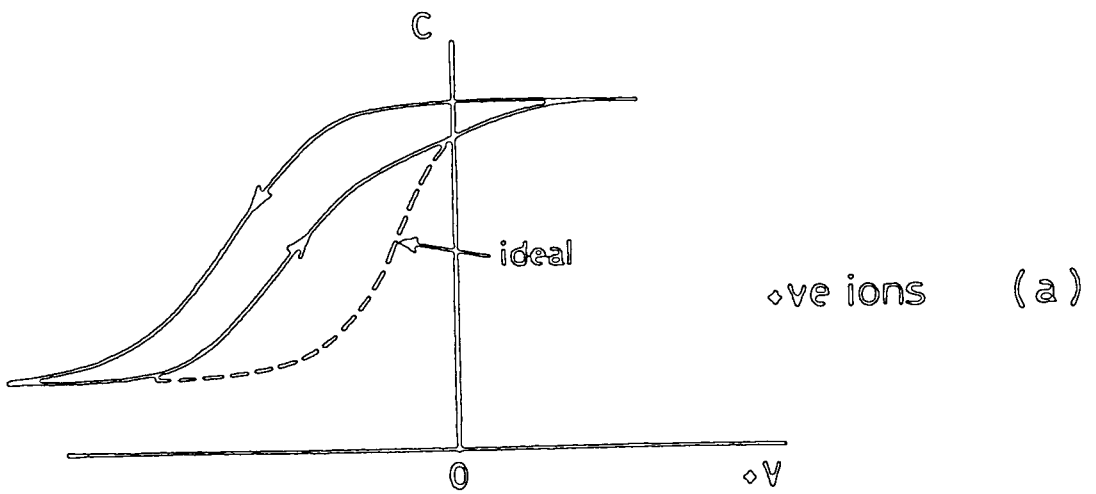
Figure 2.11    Hysteresis effects in an n-type MIS device due to (a) positive ion movement and (b) negative ion movement.

and the capacitance is higher for all bias voltages throughout the depletion range of the C-V characteristic. For a negative fixed charge the C-V shift is in the opposite direction. The magnitude of the voltage shift is given by

$$\Delta V = - \frac{Q_{fc}}{C_i} \qquad (2.13)$$

Often the largest charge contribution existing in real insulators is that of mobile ions which may drift under an applied electric field. If we consider an n-type semiconductor and positive mobile charges, under forward bias the ions are repelled from the metal and towards the interface, while under negative bias they are attracted to the metal and away from the interface. If the drift of the ions is fast and the ramp rate of the bias voltage is slow, the ions move with the bias. Mobile ions therefore have a tendency to distort the shape of the C-V curves. However, due to their charge (positive in this case), the C-V curve is also shifted towards a more negative voltage. As the ramp rate is increased the ions tend not to respond and hysteresis of the curves results. For positive charges, with a negative going voltage ramp, the C-V curve is shifted to a more negative voltage. For the return ramp, the curve falls between the previous and the ideal curve as is shown in Fig. 2.11. It should be noted that the direction of hysteresis (i.e. anti-clockwise) is the same for both positive and negative charges. The actual voltage shift, however is in opposite directions for the two polarities; positive voltage

shift for negative charge and negative voltage shift for positive charge.

Other causes of hysteresis in C-V curves includes polarization of, or charge injection into an insulating layer. In the former, one polarity of electric field aligns the dipoles in the corresponding direction and a similar and opposite field is needed to realign the dipoles in the opposite direction.

Charge injection into the insulator can be from the metal, the semiconductor or both but usually the effect of the semiconductor injection dominates due to its proximity to the semiconductor surface. Some of the injected charge remains at the surface and some is trapped in the insulator bulk. The trapped charge shifts the C-V curves in a similar manner as that mentioned previously. However the direction of hysteresis produced by the charge injection is dependent upon the injecting contact. Since the semiconductor usually dominates, the effect of injection is usually seen as clockwise hysteresis.

## 2.3.4 Effect of Temperature

An increase in temperature moves the Fermi level closer to the conduction band but produces no band bending in the ideal case (i.e. $\phi_{ms}$ = 0) at zero bias. If however, there are interface states, a change in temperature affects the occupancy of the states at any given bias by virtue of the change in position of the Fermi level. Therefore a system with interface states shows a shift in the C-V curve with temperature.

Considering only the ideal case, the main effect of an increase in temperature is seen in the inversion region of a C-V

curve. The generation and recombination rates are strong functions of temperature and as the temperature increases so do both rates. As the generation rate increases, the density of minority carriers at the surface therefore increases so that the inversion charge is increased. A typical C-V curve is shown in Fig. 2.12 for a range of temperatures. It shows that the inversion response at elevated temperatures is similar to the low frequency response at room temperature. As the temperature is increased, the generation rate is increased and the inversion charge is more able to follow the ac signal.

## 2.3.5  Effect of Illumination

The effect of illumination on an MIS device is quite similar to the effect of temperature and again it is seen most strikingly in the inversion region. In contrast to the temperature situation, illumination does not provide thermal equilibrium as the radiation only penetrates into a very shallow region of the semiconductor. The effect of illumination is twofold. Firstly, because of the extra carriers that are produced, the effective minority carrier generation rate increases causing a 'low frequency' inversion C-V curve. Secondly, the generation of electron hole pairs at the surface causes a decrease in $\psi_s$ for given applied bias. For this reason the depletion width is reduced and the total capacitance is increased. Both these phenomena enhance the formation and subsequent response of the inversion layer.

The production of electron - hole pairs due to the illumination at the surface also enhances the ac conductivity of
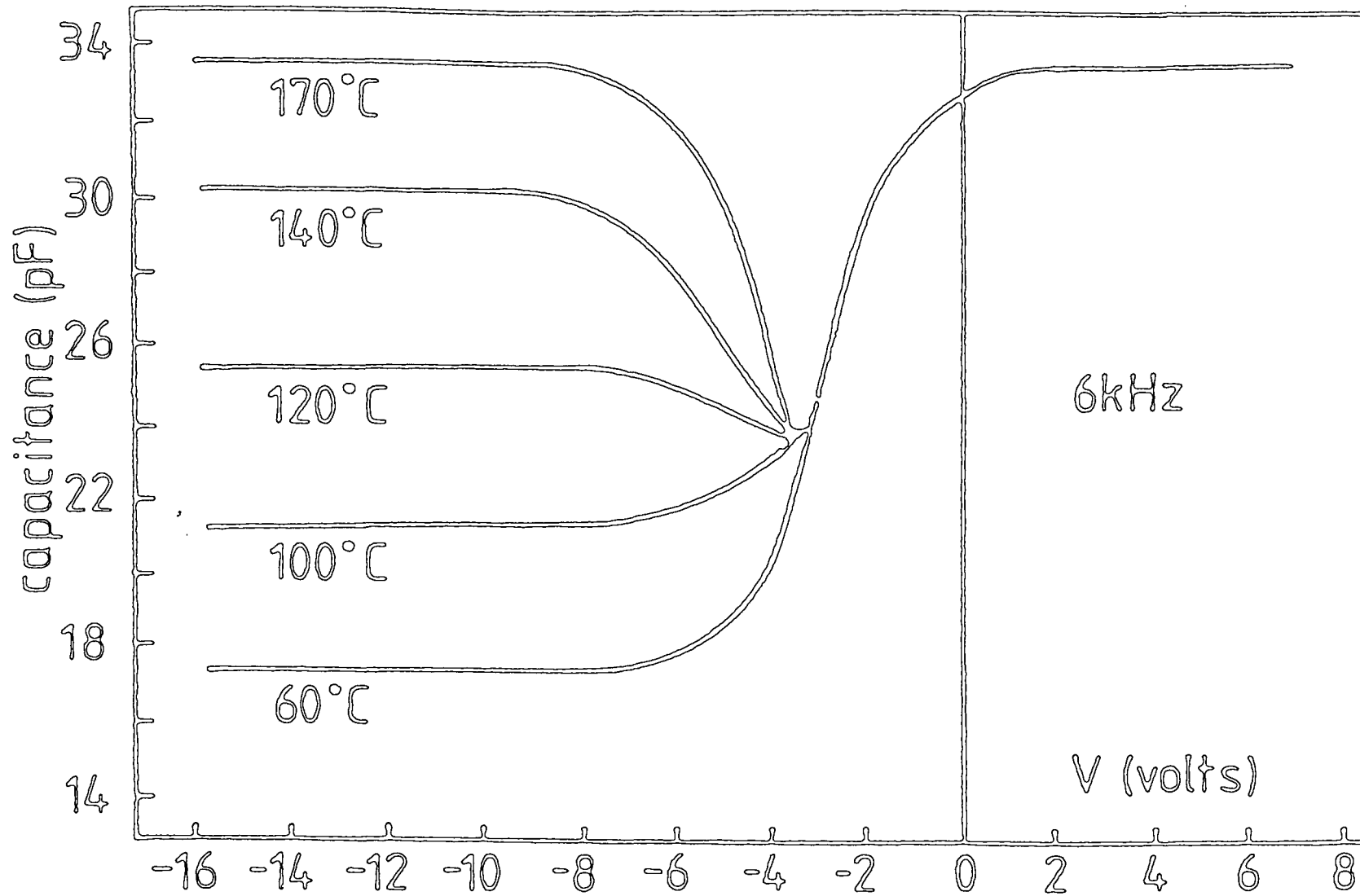
**Figure 2.12** The effect of a temperature on a high frequency MIS C-V curve.

the device for a given density of surface states. Poon and Card [5] showed that the magnitude of the peak of the G-V curve increases with increasing levels of illumination.

The effects of illumination will not be considered further because they are not of primary interest to this thesis.

## References for Chapter 2

[1] J.L. Moll,Wescon Conv. Rev., p32 (1959)

[2] W.G. Pfann and C.G. Garret, Proc. IRE, <u>47</u>, 2011 (1959)

[3] see for example - S.M. Sze, <u>Physics of Semiconductor Devices</u> 2nd Ed., Wiley-Interscience, Chapter 7 (1981).

[4] E.H. Nicollian and J.R. Brews, <u>MOS (Metal Oxide Semiconductor) Physics and Technology</u>, John Wiley and Sons, New York, pp. 35-39, 178-185 (1982)

[5] T.C. Poon and H.C. Card, J. Appl. Phys., <u>51</u>, 5880 (1980).

# Chapter 3
## Electronic Conduction in Dielectric Thin Films


In the ideal MIS system the insulating layer is regarded as a perfect insulator implying that the DC conduction is zero at all bias voltages. Real insulating materials are however neither perfect nor ideal and they always show some form of DC conduction if the electric field and/or the temperature is high enough.

There are many different mechanisms for leakage currents. Bulk limited and contact limited conduction processes are the two main categories. A bulk limited process is one in which the current limiting process occurs within the bulk of the insulating layer. A contact-limited process is one in which the current is effectively limited by a potential barrier at the interface. Bulk - limited conduction processes include such mechanisms as ohmic, space-charge limited currents and the Poole-Frenkel effect. Schottky and thermionic emission, and most tunnelling mechanisms are examples of contact limited processes.

In general an insulating layer has many competing processes occurring simultaneously. All conduction processes are affected in different ways by changes in temperature and electric field. In some cases by varying the temperature, electric field, and thickness in the correct manner, different mechanisms can be separated.

The following sections give a brief outline and review of

the major forms of electronic conduction that are found in common dielectric materials.

### 3.1 Introduction to Electronic Conduction

All materials are electrically conductive to a greater or lesser extent. With low electric field strength, the conduction mechanism in dielectrics is usually ohmic. However, a field dependence arises frequently with increasing electric field strength, eventually leading to some form of permanent breakdown. The movement of charge, either ions or electrons, is what gives rise to all conduction processes.

In a general form, the low field conductivity may be described by [1]

$$\sigma = \sum_i n_i \, q_i \, \mu_i \qquad (3.1)$$

where $n_i$ is the density of the charge carriers of the ith species, $q_i$ is its charge and $\mu_i$ its mobility. Equation (3.1) may be used to describe any form of conduction. However within the scope of this thesis it is the electronic conduction that is of interest and as such no further discussion of ionic conduction is included.

The most simple understanding of electronic conduction in dielectric solids arises from modifications of the quantum-mechanical band theory of crystalline solids. All homogeneous materials show some form of structure (or a distinct lack of it) whether through long or short range order. Crystalline films demonstrate good long and short range order while amorphous films show some short range order but little or

no long range order. Crystalline and amorphous films represent the extremes of the long range order scale, but there is a wide range of polycrystalline and microcrystalline films which show intermediate structures.

It is generally agreed [cf. Ref.2], that the band structure of thin films depends upon the nearest neighbour distance in the lattice matrix. For crystalline and amorphous materials of the same elemental composition, it is not surprising that there exists a substantial similarity between their band structures, although there are also many differences. The sharp band edges that exist in crystalline materials tend to become diffuse in amorphous films leading to a series of localised states in the band gap called band tails. Figure 3.1 shows a comparison of the conduction band structures of crystalline and amorphous films.

In crystalline films, conduction is usually due to the movement of thermally activated 'free' carriers in the conduction band. However, conduction in amorphous films tends to shift towards 'hopping' or tunnelling of carriers through localized deep trapping states [3,4]. In a perfect crystal conduction is described by the motion of electrons (holes) in the conduction (valence) band. In non-crystalline materials, however, the effects of the deep trapping levels on the conduction mechanism are found to dominate. It is therefore not always the best procedure, when considering the conduction mechanisms in non-crystalline films, to think in terms of conduction and valence bands. From band theory the motion of charge carriers in such bands is due to an electric field

CRYSTALLINE

AMORPHOUS

↑ENERGY

↑ENERGY

CONDUCTION
BAND

CONDUCTION
BAND

QUASI-LOCALIZED
LEVELS

DONOR LEVELS

DEEP
TRAPS

TRAPPING LEVELS

DENSITY OF STATES

DENSITY OF STATES
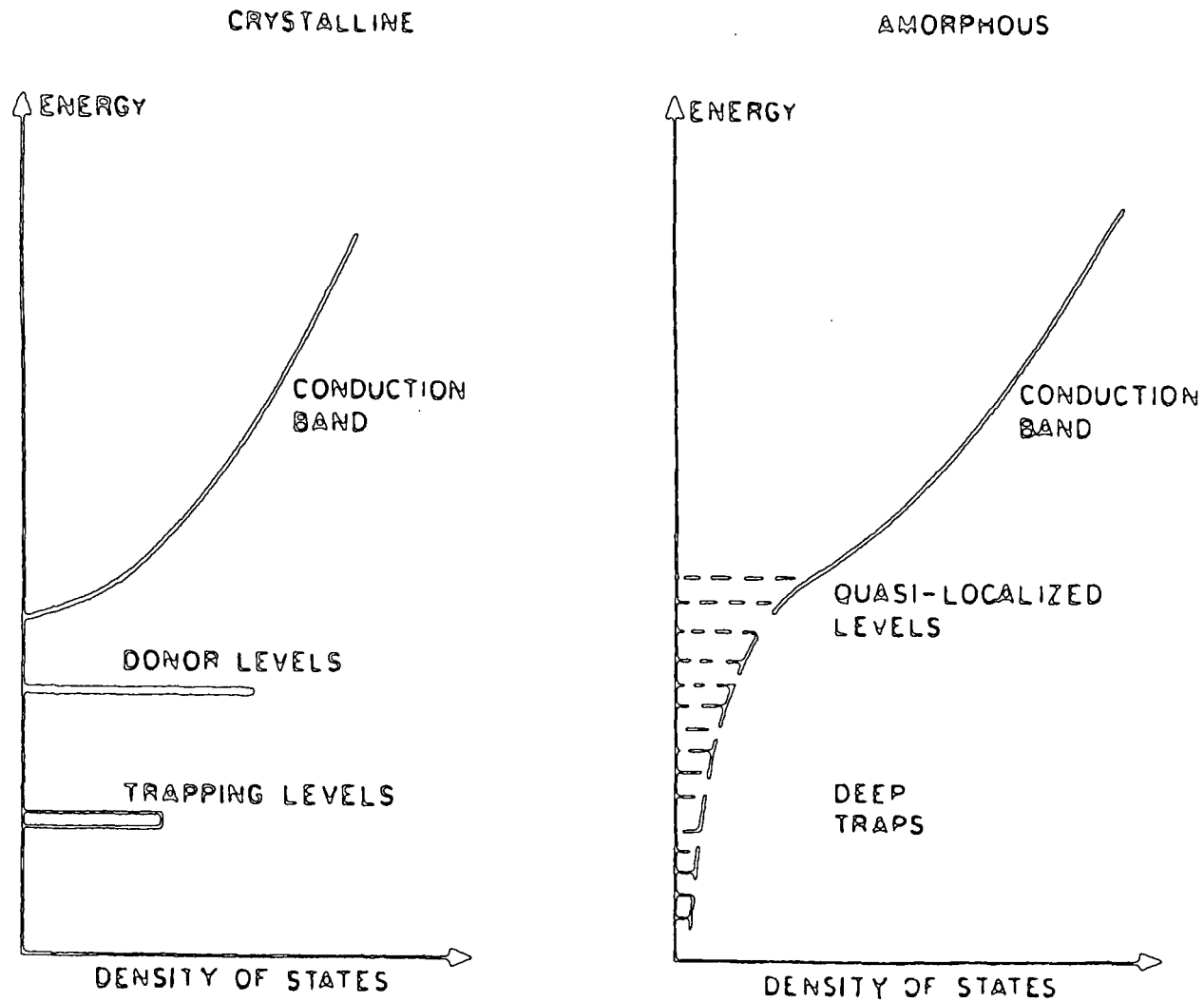
<u>Figure 3.1</u>     Schematic   comparison    of   the   electronic
conduction band structures   of   crystalline   and
amorphous dielectrics.

accelerating electrons between scattering events. It may be more appropriate to think in terms of the electric field causing an electronic transition or charge transfer between a set of more or less discrete levels. Thus the conduction is more a series of discrete 'hoppings' from state to state than the continuous motion of electrons (holes) in a conduction (valence) band.

Steady state ohmic conduction may be described by

$$J = \sigma F \qquad (3.2)$$

where J is the current density, $\sigma$ is the (constant) conductivity and F is the electric field strength. This simple relationship is usually derived from the current-voltage (I-V) measurements where

$$J = \frac{I}{A} \qquad and \qquad F = \frac{V}{d} \qquad (3.3)$$

and A is the cross sectional area, I is the current, V is the applied voltage and d is the thickness of the dielectric film. It is implicit within equations (3.3) that the current is assumed to be constant over the entire cross section. If pinholes or filimentary conduction exist, this will not be the case. Secondly, there is no accounting for any build up of space charge within the dielectrics since it is assumed here that the field strength is uniform throughout the material.

In addition to the theoretical difficulties, there are many practical problems that may be encountered with the characterization of conduction mechanisms in dielectrics. Long duration current transients are quite common making steady state

(I-V) measurements extremely difficult to obtain. These long transients may be related to the dielectric relaxation time [1] or to charge injection and subsequent trapping near an electrode. Space charge resulting from trapped charge perturbs the local electric field and affects further injection from the contact. Increased trapping into very deep levels often gives rise to very long time constants. The final steady state current will therefore depend upon the rates of trapping and detrapping, injected current levels, the local electric field, plus a host of other phenomena. Thus the problem becomes very complex.

In general many conduction processes may and usually do coexist simultaneously. Very often, however, for a given temperature and electric field, one mechanism will dominate. It is the discovery of this dominant mechanism that is of importance. In the following sections, the most commonly found forms of conduction in dielectric films are reviewed.

3.2 Quantum Mechanical Tunnelling and Field Emission

The first calculations of current flow by quantum mechanical tunnelling or field emission from a metal into a vacuum were reported by Fowler and Nordheim [5] in 1928. Since then, their theory has been extended to include a variety of physical situations and phenomena. The original calculations have been extended to include larger ranges of electric field strength and temperature [7], the effects of image forces, the effective mass for emission into dielectrics [8] and a variety of shapes of the interfacial barrier. Reviews of this subject

have been produced by Duke [6], Simmons[7], Good and Muller [8] and Lamb [9] and as such the presentation of some final results should be sufficient.

Fowler and Nordheim [5] showed that field emission and thermionic emission, both injected limited phenomena, are distinct mechanisms which dominate over different ranges of temperature and applied electric field. For low temperatures and high electric field strengths, field emission dominates over thermionic emission while at high temperatures and moderate or low electric fields, the reverse is true. At intermediate temperatures both mechanisms may be present and domination of one over the other depends on the particular physical circumstances. This intermediate process may manifest itself as what might seem a combination of field and thermionic emission in the form of thermally assisted tunnelling. These injection limited mechanisms are shown schematically in Fig. 3.2. Specific applications of tunnelling phenomena are presented in the following subsections. Thermionic emission, although an injection limited phenomenon is a distinct mechanism in its own right and as such is treated later in section 3.3

### 3.2.1 Tunnelling Through Thin Insulating Layers

The tunnelling of electrons through thin insulating films between metals, (unlike emission into a vacuum), was first considered by Frenkel [10] in 1930. Sommerfeld and Bethe [11], Holm [12], and Simmons [13-15] have all made significant extensions and modifications to Frenkel's original work. However the most frequently quoted treatment is that of Stratton

29
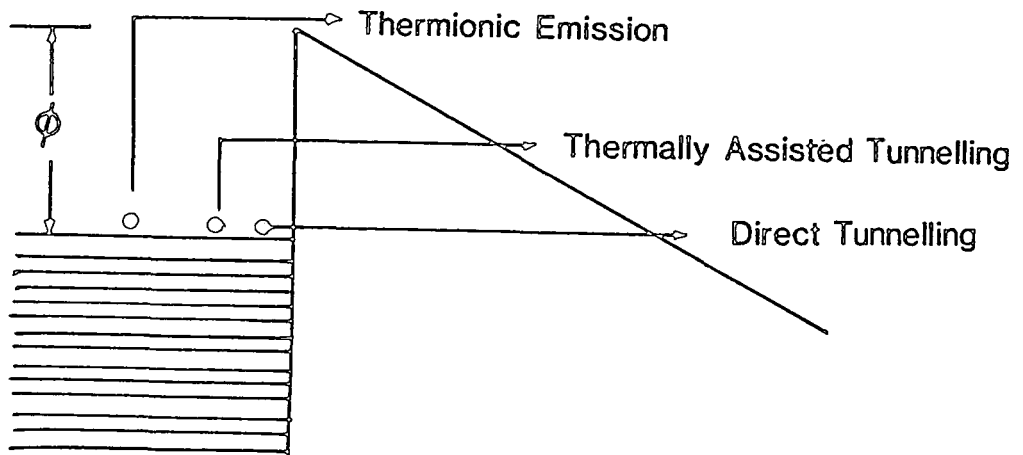
Figure 3.2    Schematic diagram showing thermionic emission,
              thermally assisted and direct tunnelling
              conduction mechanisms.
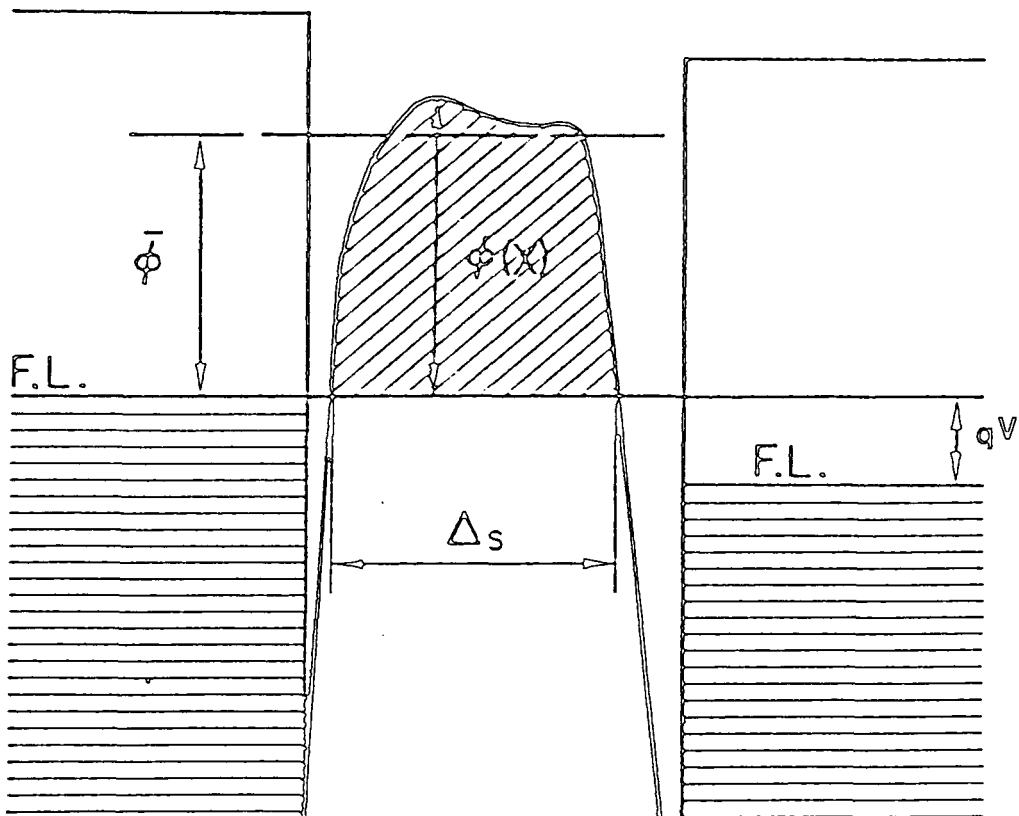


Figure 3.3    Energy band diagram of a metal-insulator-metal
              (MIM) structure with an arbitrary interfacial
              potential barrier.

[16]. For very high electric fields, it was found that the current density was essentially the same as that given by the Fowler-Nordheim [5] equation for emission from metals into a vacuum.

It has been shown [6-9] that for a general insulator between two metals, as shown in Fig. 3.3, the tunnel current density is given by

$$J = \frac{q}{h^3} 4\pi m^* \int_0^\infty [f_1(E) - f_2(E)] dE \int_0^{E_{max}} P(E_x) \, dE_x \qquad (3.4)$$

where h is Planck's constant, $m^*$ is the effective mass of the electrons in the metals, $f_1$ and $f_2$ are the Fermi-Dirac probability distribution functions in the metals on either side of the insulator and $P(E_x)$ is the tunnelling probability in the x direction. It is implicitly assumed here that there are parabolic energy-momentum relationship in all three areas. Using a rectangular shaped potential barrier and the free electron mass, Frenkel [10] showed the tunnelling probability of electrons through the insulating film to be of the form

$$P(E_x) = \exp \left\{ -2 \int_{x_1}^{x_2} \frac{2(m_o)^{\frac{1}{2}}}{\hbar} \cdot [\phi(x) - E_x] \, dx \right\} \qquad (3.5)$$

where $m_o$ is the free electron mass, $x_1$ and $x_2$ are the classical turning points, $E_x$ is the electron energy in the x direction and $\phi(x)$ is the barrier potential energy. For different potential

barrier shapes (i.e. rectangular, triangular, trapezoidal) the tunnelling probabilities will of course be different.

Energy diagrams for two similar metals sandwiching an insulating film under different bias conditions are shown in Fig. 3.4. It is quite clear that each bias range has a distinct barrier shape and likewise a current characteristic of its own.

For a constant voltage, and an arbitrarily shaped barrier, Simmons [13-15] showed that the general equation connecting the tunnelling current at some finite temperature, $J(V,T)$, to the tunnelling current at 0 K, $J(V,0)$ given by

$$\frac{J(V,T)}{J(V,0)} = \frac{\pi A k T / 2 \bar{\phi}^{-\frac{1}{2}}}{\sin(\pi A k T / 2 \bar{\phi}^{-\frac{1}{2}})} \qquad (3.6)$$

where

$$J(V,0) = \left[\frac{q}{2\pi h (\Delta s)^2}\right] \left\{ \exp(-A\bar{\phi}^{-\frac{1}{2}}) - (\bar{\phi}+qV) \exp\left[-A(\bar{\phi}+qV)^{\frac{1}{2}}\right] \right\}$$

$$A = \frac{4\pi\Delta s (2m^*)^{\frac{1}{2}}}{h}$$

where k is Boltzmann's constant, T is the absolute temperature, $\Delta s$ is the width of the potential barrier at the Fermi level of the metal (as in Fig. 3.3) and $\bar{\phi}$ is the mean barrier height. This expression for the thermally assisted $J$-$V$ characteristics of tunnel conduction is essentially the same as that derived by Stratton [16]. Simmons [14] has also derived expressions for

31
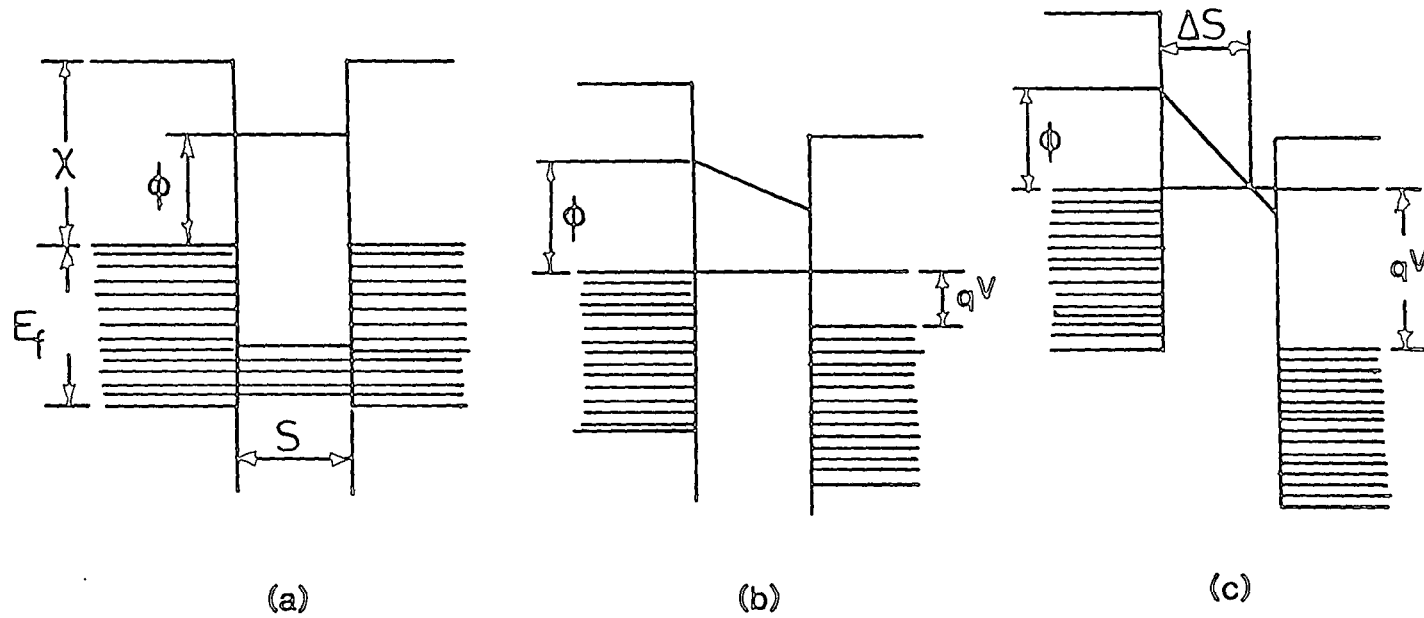
Figure 3.4    Rectangular potential barrier for a metal-insulator-metal (MIM) structure under different bias conditions. a) V=0; b) V‹ φ/ q; c) V› φ/q.

tunnelling current-voltage characteristics when asymmetric contacts are used. Under such conditions the tunnel currents for positive and negative polarities are distinctly different.

For direct tunnelling through an insulating film, the applied voltage only affects the relative positions of the Fermi levels in the metals, and therefore the tunnelling probability, assuming the field does not perturb the effective barrier appreciably. This is shown clearly in Figs. 3.4a and 3.4b and equation 3.6. In Fig. 3.4c however, the electric field is shown to substantially alter the effective barrier height. In this case, the carriers are tunnelling into the insulator rather than through it. The tunnelling probability is now not only a function of the postions of the Fermi levels but also of the electric field within the insulating material. As a consequence of the field dependent barrier, the current-field characteristics for tunnelling into an insulating material are subtly different from that given by equation 3.6.

### 3.2.2  Tunnelling Into Dielectric Films

Consider electrons tunnelling into the conduction band of an insulator instead of right through it. Normally the barrier height between the common metals and insulators is quite large (on the order of a few eV). The tunnelling distances must also be relatively short for any appreciable tunnelling probability. With these two pre-conditions, it would appear extremely difficult for tunnelling to occur unless : i) the electric field is high enough to bend the insulator conduction band so as to allow tunnelling through the triangular top of the barrier;  ii)

space charge is present either in the form of trapped or mobile charge, and is large enough to lower the effective barrier height at the injecting contact; or iii) there exists a large distribution of trapping or recombination centres near the Fermi level of the injecting contact that could promote tunnelling through interface states. The simplest model for field emission into a dielectric assumes that there is a triangular potential barrier and that the electron distribution in the metal does not differ greatly from that at the absolute zero of temperature. The emitted current is given by [1]

$$J = \frac{q^3 F^2}{8\pi h \phi} \exp\left[-\frac{4(2m^*)\phi^{3/2}}{3\hbar qF}\right] \qquad (3.7)$$

where $m^*$ is the effective mass of the electrons in the metal. Figure 3.5 illustrates a triangular barrier at a metal-insulator junction with the image force taken into account (dotted line). The reduction in the barrier height due to the image forces is given by

$$\Delta\phi = \left(\frac{q^3 F}{\varepsilon}\right)^{\frac{1}{2}} = \frac{1}{2}\left(\frac{q^3 F}{\pi\varepsilon_o\varepsilon_d}\right)^{\frac{1}{2}} \qquad (3.8)$$

where $\varepsilon_o$ is the free space permittivity and $\varepsilon_d$ is the high frequency dielectric constant of the insulator. Burgess, Kroemer and Houston [17] showed that the zero temperature current is given by

$$J(0) = \frac{q^3 F^2}{8\pi h \phi}\frac{m}{m^*}\frac{1}{t^2(\Delta\phi/\phi)}\exp\left[\frac{-4(2m^*)\phi^{3/2}}{3\hbar qF}\,v(\Delta\phi/\phi)\right] \qquad (3.9)$$
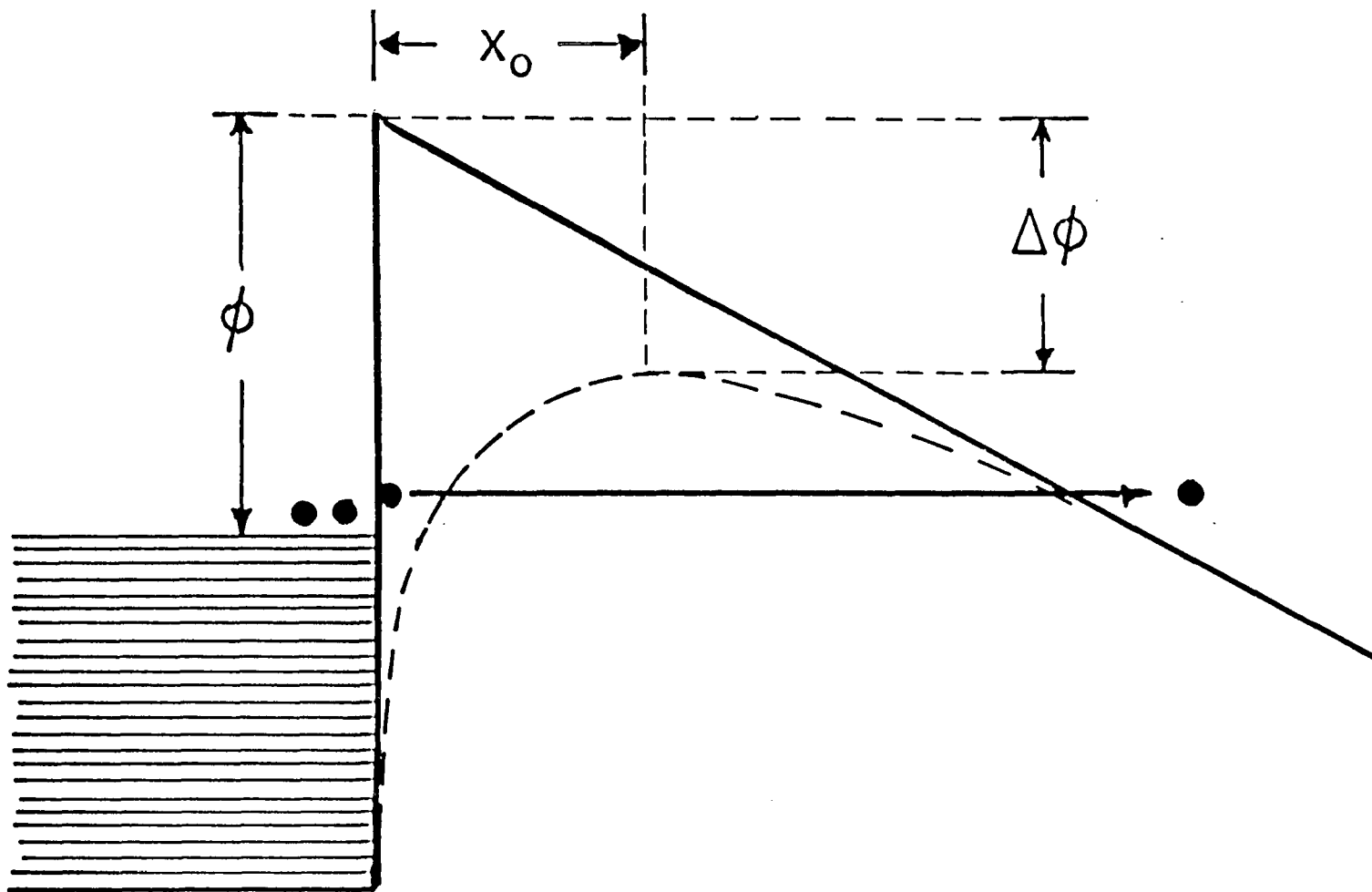
Figure 3.5    Energy band diagram of a metal-insulator junction showing a triangular barrier and the image force lowering of the potential barrier.

where $t^2(\Delta\phi / \phi)$ and $v(\Delta\phi / \phi)$ are sets of functions containing elliptical integrals and are tabulated in [1,17] At finite temperatures the current density is found to be

$$\frac{J(T)}{J(0)} = \frac{\pi kT/d}{\sin(\pi kT/d)} \qquad (3.10)$$

where

$$d = \frac{\hbar qF}{2(2m^*\phi)^{\frac{1}{2}}} \frac{1}{t(\Delta\phi/\phi)}$$

Equation 3.10 is very similar in form to those expressions derived by Stratton [16] and Simmons [13-15] for the temperature dependence of currents tunnelling through insulating films.

### 3.2.3 Thermally Assisted Tunnelling (TAT)

Direct tunnelling involves the transfer of electrons between the Fermi levels of the electrodes. If, in the injecting electrode, the electron energy is raised above the Fermi level, an electron may tunnel into the insulator conduction band with a raised electron energy when a field is applied across the insulator as shown in Fig. 3.6. This mechanism is called thermally assisted tunnelling (TAT) and has been analyzed by Roberts and Polanco [18]. The equations that describe the current flow cannot be solved analytically but an empirical relationship, that fits their [18] numerically computed results has been shown to be
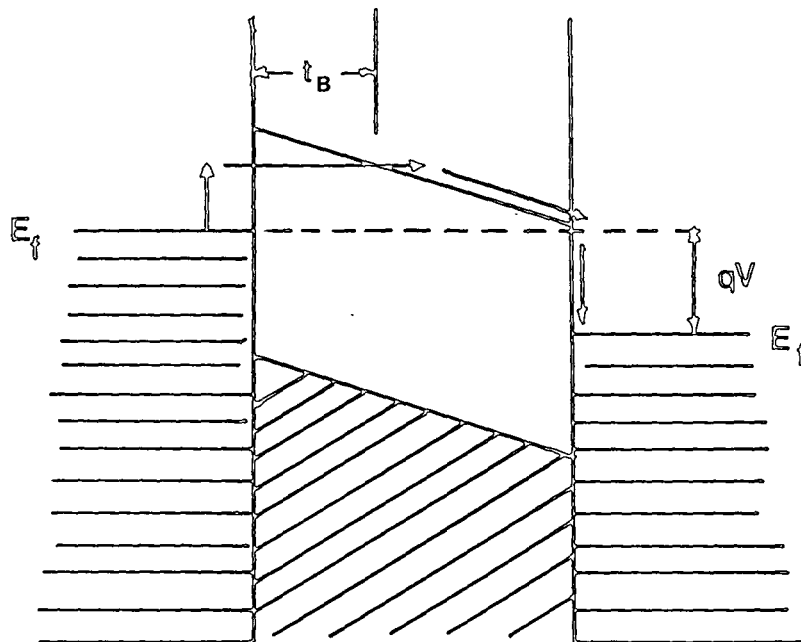
Figure 3.6    Energy band structure of a metal-insulator metal
(MIM)    device    showing    thermally    assisted
tunnelling.
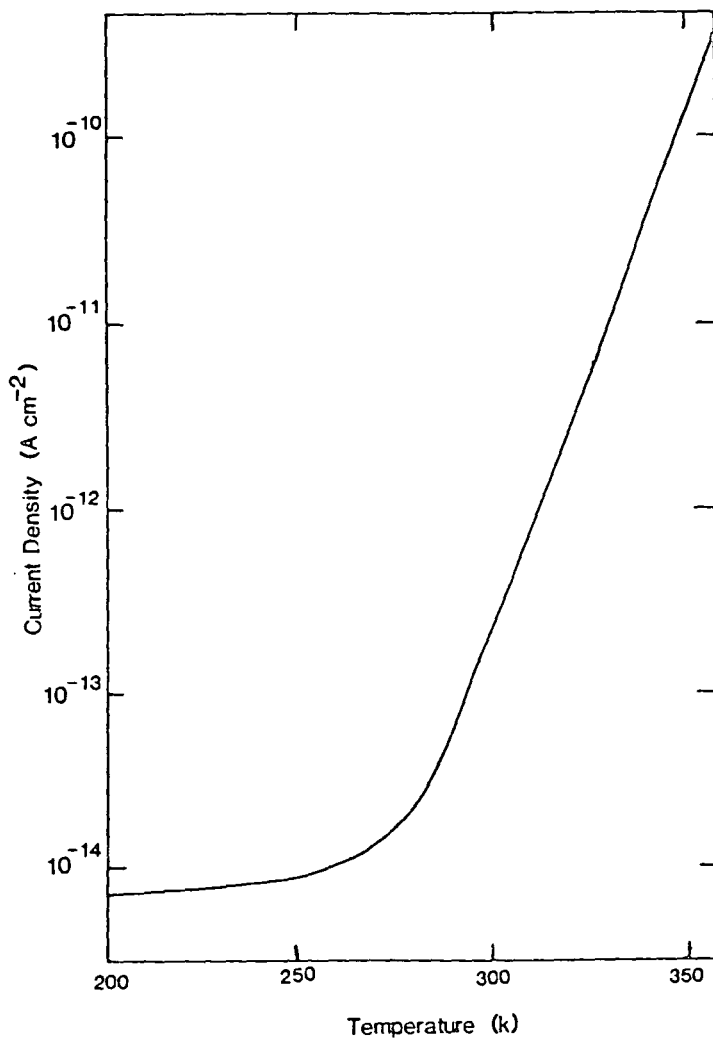


Figure 3.7    Temperature    variation    of    thermally    assisted
tunnel current.

$$J_{TAT} = a \, \exp\left(\frac{-\phi}{kT}\right) \exp\left[\left(\frac{b}{kT} + c\right) \frac{V^{\frac{1}{2}}}{t_B^{\frac{1}{2}}}\right] \qquad (3.11)$$

where a, b, and c are constants given as $a = 6.8 \times 10^7$ A cm$^{-2}$, $b = 1.65 \times 10^{-24}$ J m$^{\frac{1}{2}}$ V$^{-\frac{1}{2}}$, and $c = 1.2 \times 10^{-4}$ m$^{\frac{1}{2}}$ V$^{-\frac{1}{2}}$. V is the potential drop across the insulator and $t_B$ is the tunnelling thickness as shown if Fig. 3.6. Figure 3.7 shows the relative importance of TAT to direct tunnelling. The strong increase in the slope of the J - T curve (from Roberts and Polanco [18]) implies that at low temperatures direct tunnelling dominates but with increasing temperatures TAT will show its contribution. It should be noted that the exponential rise in the TAT current with temperature is very similar to that for Schottky emission (i.e. emission over the barrier) and the two are often indistinguishable.

## 3.3  Thermionic and Schottky Emission

If an insulator is too thick to allow any form of quantum-mechanical tunnelling to occur, the conduction may be due principally to electrons that are thermally excited over an interfacial potential barrier. From section 3.2, the general expression for current flowing into an insulator from a metal contact was given by

$$J = \frac{4\pi q m^*}{h^3} \int_0^\infty \left[f_1(E) - f_2(E)\right] dE \int_0^{E_{max}} P(E_x) \, dE_x \qquad (3.12)$$

35

where $f_1(E)$ and $f_2(E)$ are the Fermi-Dirac probability distribution functions on either side of the interface and $P(E_x)$ is the tunnelling probability. The current over the barrier may be calculated by setting the lower limit of the energy integral to the interfacial barrier height, $\phi_o$ and the tunnelling probability to unity above this. Thus equation (3.12) becomes [1,7,9]

$$J = \frac{4 \; qm^*}{h^3} \int_{\phi_o}^{\infty} \left[ f_1(E) - f_2(E) \right] \; dE \qquad (3.13)$$

For $V \gg kT/q$, $f_2(E) \approx 0$ and after integration equation 3.13 becomes

$$J = A^* T^2 \exp \left( \frac{-\phi_o}{kT} \right) \qquad (3.14)$$

where $A^*$ is called the Richardson constant and is given by

$$A^* = \frac{4\pi m^* k^2}{h^3}$$

Equation 3.14 defines the current that flows due to thermally excited electrons surmounting the interfacial barrier into the insulator. This mechanism is called thermionic emission. For most materials, the thermionic emission model must be adapted to account for the image forces that arise due to the polarization of the interface region. The effective barrier height, $\phi_{eff}$, now becomes a function of the applied electric field. The effect of the image potential is shown in

36

Fig. 3.5 as a dotted line where the solid line is the potential due to the applied field. The effective barrier height becomes

$$\phi_{eff} = \phi - \Delta\phi \tag{3.15}$$

where

$$\Delta\phi = \frac{1}{2} \left( \frac{q^3 F}{\pi \varepsilon_o \varepsilon d} \right)^{\frac{1}{2}}$$

With this reduction in the effective interfacial barrier height, the current density is now given by

$$J = A^* T^2 \exp\left( \frac{-\phi_o}{kT} \right) \exp\left( \frac{\beta_s F^{\frac{1}{2}}}{kT} \right) \tag{3.16}$$

where the Schottky constant $(\beta_s)$ is

$$\beta_s = \frac{1}{2} \left( \frac{q^3}{\pi \varepsilon_o \varepsilon d} \right)^{\frac{1}{2}}$$

This current equation is known as the Richardson-Schottky equation [19] and defines the current flowing from a metal into a dielectric by 'Schottky emission'. Schottky emission being simply thermionic emission with the image force barrier lowering taken into account.

## 3.4 The Poole-Frenkel Effect

In most amorphous materials a distinct non-linear current-voltage (I-V) characteristic is usually found with the application of very strong electric fields (F > $10^5$ V/cm). The

37

Poole-Frenkel effect [20] is commonly used to explain such high field characteristics. This mechanism is somewhat similar to the Schottky effect, the Poole-Frenkel effect being its bulk analogue.

In the case of the Schottky effect, the lowering of the potential barrier at the cathode is due to the interaction between image forces and the applied electric field. For Poole-Frenkel conduction, the interaction is between a coulombic potential associated with an ionized trap and the applied field. Both effects produce a lowering of the potential barrier that allows the movement of charge carriers. It has been found however [21], at least theoretically, that either conduction mechanism and its associated physical effect may dominate in the same material under certain conditions and that these mechanisms are simply limiting cases of a more general mechanism.

### 3.4.1 Elementary Poole-Frenkel Theory

Figure 3.8a shows the coulombic potential that is associated with a single ionized (empty) donor-like trap where $\phi_t$ is the trap depth measured from the trap level to the bottom of the insulator conduction band. A fixed coulombic potential of the ionized donor is given by

$$qV(x) = \frac{-q^2}{\varepsilon \, x} \qquad (3.17)$$

At high field strengths, the band edges of the insulator are tilted as shown in Fig. 3.8b. The total potential is now given by
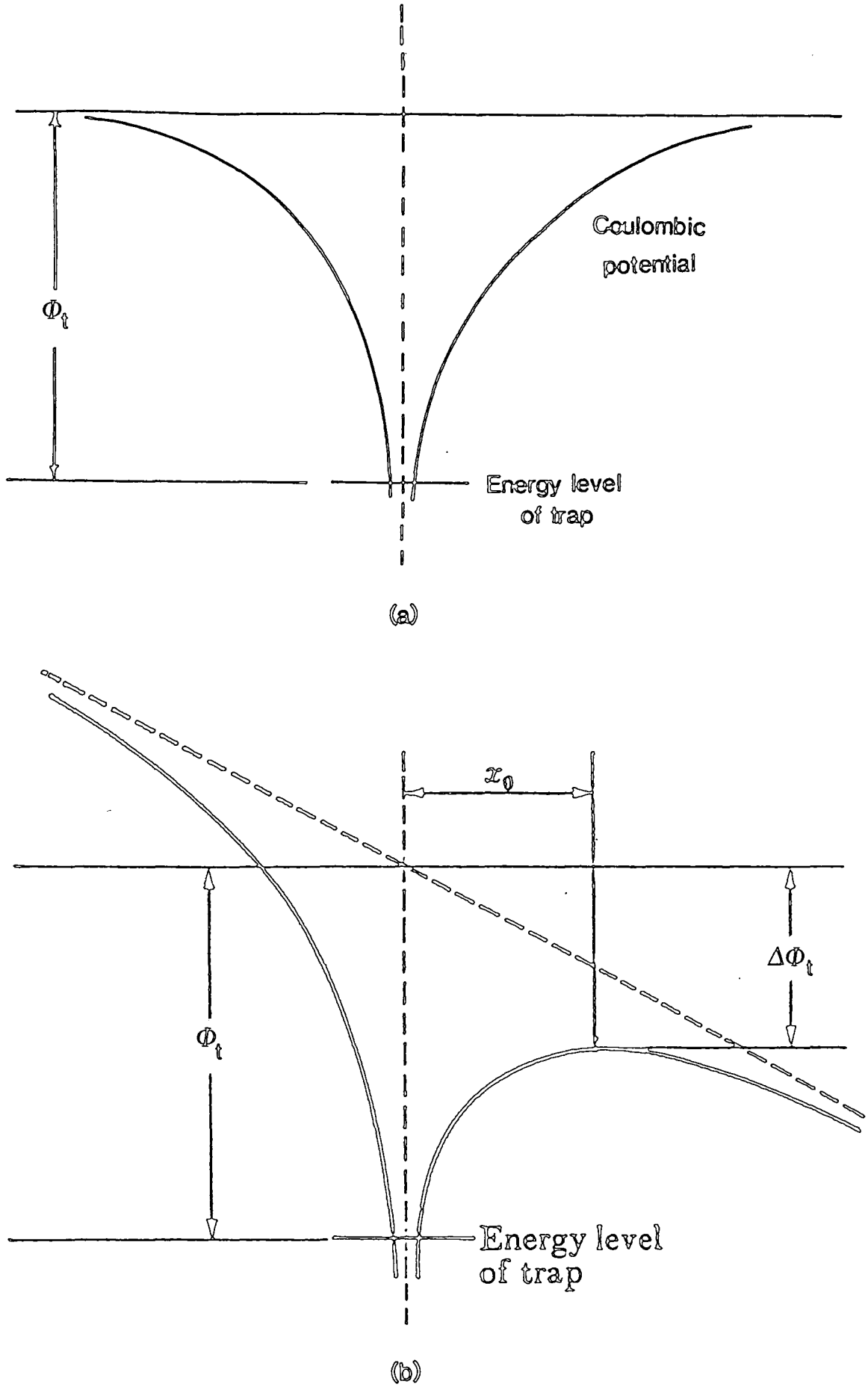
Figure 3.8     One dimensional potential-energy diagram illustrating (a) a coulombic potential from a charged trapping centre with no applied field. (b) the reduction in the effective barrier due to an applied field. the Poole-Frenkel affect.

$$qV(x) = -qFx - \frac{q^2}{\epsilon\,x} \qquad\qquad (3.18)$$

It is implicitly assumed here that the field is constant throughout the material and there is no significant build up of space charge (i.e. the space charge is not large enough in magnitude to perturb the local electric field). The barrier lowering $\Delta\phi_t$, is given by

$$\Delta\phi_t = 2\left(\frac{q^3 F}{\epsilon}\right)^{\frac{1}{2}} \qquad\qquad (3.19)$$

It should be noted that the Poole-Frenkel lowering of the barrier is twice that of the Schottky effect (see equation 3.16). The factor of two arises from the difference in the form of the potential barriers associated with a fixed ionized donor and an image charge. By changing to SI units where $\epsilon = 4\pi\epsilon_o\epsilon_d$ , equation 3.19 becomes

$$\Delta\phi_t = \beta_{PF}\ F^{\frac{1}{2}}$$

where $\qquad\qquad\qquad\qquad\qquad\qquad\qquad\qquad$ (3.20)

$$\beta_{PF} = \left(\frac{q^3}{\pi\,\epsilon_o\,\epsilon_d}\right)^{\frac{1}{2}}$$

### 3.4.2 Limitations of the Elementary Poole-Frenkel Theory

It is necessary, at this point, to consider the range of electric fields and temperatures acting upon the trap centre. Even at low field strengths and moderate temperatures, it is possible for thermionic emission to take place. Under these conditions, a carrier could be thermally excited over the potential barrier around the trap centre. This process, however, is very unlikely to occur at low temperatures. If the field strength is high enough to produce a significant reduction of the barrier width, tunnelling through the barrier could occur. These processes are equivalent to Richardson-Schottky emission and Fowler-Nordheim tunnelling at an interface. Emission or tunnelling can occur either from states that are localized or from states that are characterised by a broad band distribution. It will be assumed, however, for the sake of simplicity, that the emission occurs from well defined localized states. It has been found in silicon monoxide, for example, that a certain degree of localization is present [22] so that this assumption may be valid in other amorphous materials.

We will assume initially, that the conduction is due entirely to the excitation of carriers over the potential barrier as modified by the electric field. It was originally assumed by Frenkel [20] that in the absence of an electric field, the number of free electrons in the conduction band is proportional to

$$\exp\left(\frac{-\phi_t}{2kT}\right) \qquad (3.21)$$

Implicit in this assumption is the belief that the Fermi level in the insulator lies halfway between the trap level and the bottom of the conduction band. This gives rise to the factor two in the denominator of the exponential. This assumption may or may not be true, as it depends upon the degree of compensation that exists due to acceptor-like traps or impurities. For an n-type material, with no compensation (i.e. no acceptor sites), Frenkel's original argument is correct.

Taking, for the moment, Frenkel's argument as fact, with an applied field, the number of electrons in the conduction band will be proportional to

$$\exp\left[-\frac{(\phi_t - \Delta\phi_t)}{2kT}\right]$$

(3.22)

giving a conductivity

$$\sigma(F) = \sigma(0)\,\exp\left[\frac{\Delta\phi_t}{2kT}\right]$$

$$= \sigma(0)\,\exp\left[\frac{1}{kT}\left(\frac{q^3 F}{\epsilon}\right)^{\frac{1}{2}}\right]$$

where $\sigma(0)$ is the zero field conductivity.

The temperature dependence of the Poole-Frenkel conductivity may be contrasted with that of the Richardson-Schottky current (see eqn. 3.16). It has frequently been assumed that the temperature dependent exponents differ by a factor of two. However, this is obviously not true if one follows through Frenkel's original arguments. This point has

41

been raised by many authors [23-26]. The temperature dependent exponential factor, for the Poole-Frenkel case, is completely dependent on the choice (somewhat arbitrarily it seems at times) of the position of the Fermi level, thus reflecting the degree of compensation in the material. If compensation is present, the deep lying acceptor levels have the effect of lowering the Fermi level thus altering the statistics of the free carrier density in the conduction band.

It should be noted that Frenkel's original model itself (i.e. a single coulombic trap in a dielectric continuum having a single dielectric constant) is also open to some question. Materials displaying Poole-Frenkel emission are often amorphous and as such are most likely to contain a distribution of trapping energies and of dielectric constants, however small these may be. The values for the trap depth and dielectric constant derived from experiments are averages over their respective distributions. Therefore Frenkel's model gives only an order of magnitude calculation of the field dependence and that may be all he originally intended. A number of reviews of conduction in dielectrics have been produced [1,3,27,28] and Jonscher [29] argued that the usual explanations of the Poole-Frenkel effect are substantially correct as long as the results are not taken too literally. In 1971 Jonscher and Ansari [30] showed that to differentiate between the Poole-Frenkel and Richardson-Schottky mechanisms, the temperature dependence of the currents should not be used due to the possible closeness of the exponential factors. The proper distinction is to decide whether the conduction is bulk limited

or contact limited as required for the Poole-Frenkel and Richardson-Schottky mechanisms respectively.

Many authors [22-26,30,31] have gathered experimental data on different materials trying to show the validity of certain theoretical conduction mechanisms. Sze [31], for example analysed the results of his I-V characteristics of silicon nitride films based on a highly compensated material. He concluded that the mechanism in question was Poole-Frenkel and found values of the dielectric constant and trap depth of 5.5 and 1.5 eV respectively. Others have tried to formulate their results by the use of empirical or phenomenological models resulting in wide variations of film parameters within their own preset limitations. Hartman et al [32] found that, depending on the degree of compensation that was added to their model, the dielectric constant of their material (silicon monoxide) could be varied from 3.0 to 12.0. This factor of four difference arises from the original assumptions of the position of the Fermi level. It seems unreasonable to expect that a model that predicts such wide variation could be considered seriously.

Others workers have tried to formulate more reasonable theoretical models incorporating many different facets of Poole-Frenkel conduction. Jonscher [29] and Hartke [33] developed a model that attempted to overcome the restrictions of a one dimensional model. Instead of just considering emission from the trap in the direction of the applied electric field, they also considered the probability of emission in the reverse direction. They found not surprisingly that for any non zero electric field the barrier in the reverse direction would be

very high and that the probability of emission in that direction very small. Ieda et al [34] extended this model and assumed that the release rate in the reverse direction was field dependent. They also defined a 'free' electron as one with energy, $\delta$, within kT of the conduction band edge. Using the experimental data of Hartman et al [32] they obtained a reasonably good fit to their model. It should be noted however, that this model again used the statistics of Frenkel's original model and is therefore appropriate only to an uncompensated material.

### 3.4.3 Hill's Conduction Model

By far the most comprehensive and thorough review of Poole-Frenkel conduction was written by Hill [35] in 1971. He started from the 'beginning' and developed one and three dimensional models for single and multiple centre conduction for both amorphous and crystalline materials. Hill also applied his theoretical models to the experimental results of others [22,32,36] and showed that it was possible to interpret all measurements as being simple variations of one basic model.

In this major analysis [35], Hill firstly considers the case of single centre conduction (such that the coulombic potentials from adjacent centres do not overlap) for low temperatures and high electric field strengths. Such limitations imply that emission from the trap level to the insulator conduction band edge should predominate. Using the analysis of quantum-mechanical field emission from isolated imperfections in dielectrics, presented by Franz [37], the

application of a one dimensional model and Simmons' [13] expansion of the emission probability function, Hill [35] showed the current density to be of the form

$$J = \frac{N_i v_i q}{B^2} \exp\left(-A\phi_t^{-\frac{1}{2}}\right) \frac{\pi BkT}{\sin(\pi BkT)} \left[2 - \exp(-B\phi_t)\right]$$

(3.23)

where all the parameters are defined as follows :

$$A\phi_t^{-\frac{1}{2}} = \frac{\sqrt{2}(2m^*)}{\hbar qF} \phi_t^{3/2}\lambda\left[1 - \frac{\gamma F}{2\lambda} \ln\left(\frac{1+\lambda}{1-\lambda}\right)\right]^{\frac{1}{2}}$$

$$B = \frac{2(m^*\phi_t)^{\frac{1}{2}}}{\hbar qF} \left[1 - \frac{\gamma F}{2\lambda} \ln\left(\frac{1+\lambda}{1-\lambda}\right)\right]^{-\frac{1}{2}}$$

$$\gamma = \frac{B^2}{\phi_t^2}$$

$$\lambda = (1 - F)^{\frac{1}{2}} = \left[1 - \left(\frac{\Delta\phi_t}{\phi_t}\right)\right]^{\frac{1}{2}}$$

and the remaining symbols have their usual meanings. The quantity $N_i v_i$ is treated as an assignable parameter and reflects the difficulties of calculating an appropriate supply function for the emission of the electrons from the trap centres.

45

For higher temperatures and fields low enough such that the probability of thermally assisted tunnelling (TAT) through the barrier is small, the dominating mechanism should be purely thermionic emission, modulated to a small degree by the reduction in the barrier potential by the applied electric field. In his original calculation, Frenkel [20] makes the theoretical 'jump' from equilibrium to steady state by describing the ratio of steady state conductivity $\sigma(F)$ to its value in the limit towards equilibrium, $\sigma(0)$. Hill [35] however, attempts an absolute calculation. He assumes that for the crystalline material the velocity of the carriers is independent of energy and is

$$v_x = \mu_1 F \tag{3.24}$$

while for an amorphous material

$$v_x = \mu_2 F^{\frac{1}{2}} \tag{3.25}$$

It should be noted here that, while $\mu_1$ is a mobility in the crystalline material, $\mu_2$ is not a mobility in the ordinary sense and it has no definite physical meaning. Even though others [29,33,34] had already taken the reverse emission into account, Hill modified their results by assuming that the increase in the barrier height in the reverse direction was equal to the decrease in the forward direction (i.e. by an amount $\beta_{PF} F^{\frac{1}{2}}$ where $\beta_{PF} = (q^3/\pi \varepsilon_o \varepsilon_d)^{\frac{1}{2}}$ is the Poole-Frenkel constant). Hill argued that this gives zero current for zero electric field and it is, at least to that extent, a reasonable model. From these assumptions Hill developed the current density for the

46

following :

For a crystalline material with one dimensional emission

$$J = \frac{2qN_i\mu_1}{\beta^2} \ (kT)^4 \ \exp\left(\frac{-\phi_t}{kT}\right) \ \alpha^2\sinh\alpha \qquad (3.26)$$

Crystalline material - three dimensional emission

$$J = \frac{2qN_i\mu_1}{\beta^2} \ (kT)^4 \ \exp\left(\frac{-\phi_t}{kT}\right)\left[\alpha\cosh\alpha \ - \ \sinh\alpha\right] \qquad (3.27)$$

Amorphous material - one dimensional emission

$$J = \frac{2qN_i\mu_2}{\beta} \ (kT)^3 \ \exp\left(\frac{-\phi_t}{kT}\right) \ \alpha\sinh\alpha \qquad (3.28)$$

Amorphous material - three dimensional emission

$$J = \frac{2qN_i\mu_2}{\beta} \ (kT)^3 \ \exp\left(\frac{-\phi_t}{kT}\right)\left[\frac{\alpha\cosh\alpha \ - \ \sinh\alpha}{\alpha}\right] \qquad (3.29)$$

where

$$\alpha = \frac{\beta_{PF}F^{\frac{1}{2}}}{kT}$$

Finally, for the case of multiple centres, where the emission is not into the conduction band of the insulator, but rather into an adjacent centre, Hill found for the one dimensional case, that

$$J = qN_i s(kT)^2 \nu \ \exp\left(\frac{-\phi_t'}{kT}\right) \ \sinh\alpha' \qquad (3.30)$$

47

where

$$\alpha' = \frac{qFs}{kT}$$

and s is the distance between centres, $\nu$ is the attempt to escape frequency and $\phi'$ is the effective barrier height between the centres. A diagram of the energy band structure for multiple centre emission is shown in Fig. 3.9.

For the purpose of analysing experimental results using Hill's model(s) it can be shown that in general

$$J' = f(\alpha, \sinh\alpha) \qquad (3.31)$$

where

$$J' = JT^{-n} \exp\left(\frac{\phi}{kT}\right)$$

and n = 3 or 4 depending on the crystallinity of the material.

## 3.4.4  Interpretations of Experimental Results

For most analysis, Arrhenius plots (J vs 1/T) and Schottky plots (J vs $F^{\frac{1}{2}}$) are used to determine the parameters of the Poole-Frenkel conduction. Since such plots can lead to large uncertainties, Hill's procedure of plotting J' vs $F^{\frac{1}{2}}$/T may produce better results. However, he showed that his model could be used to analyse the data of other authors [22,32,36] and that the resulting parameters fit in well with those originally found by the Arrhenius and Schottky plot analysis. From this it would
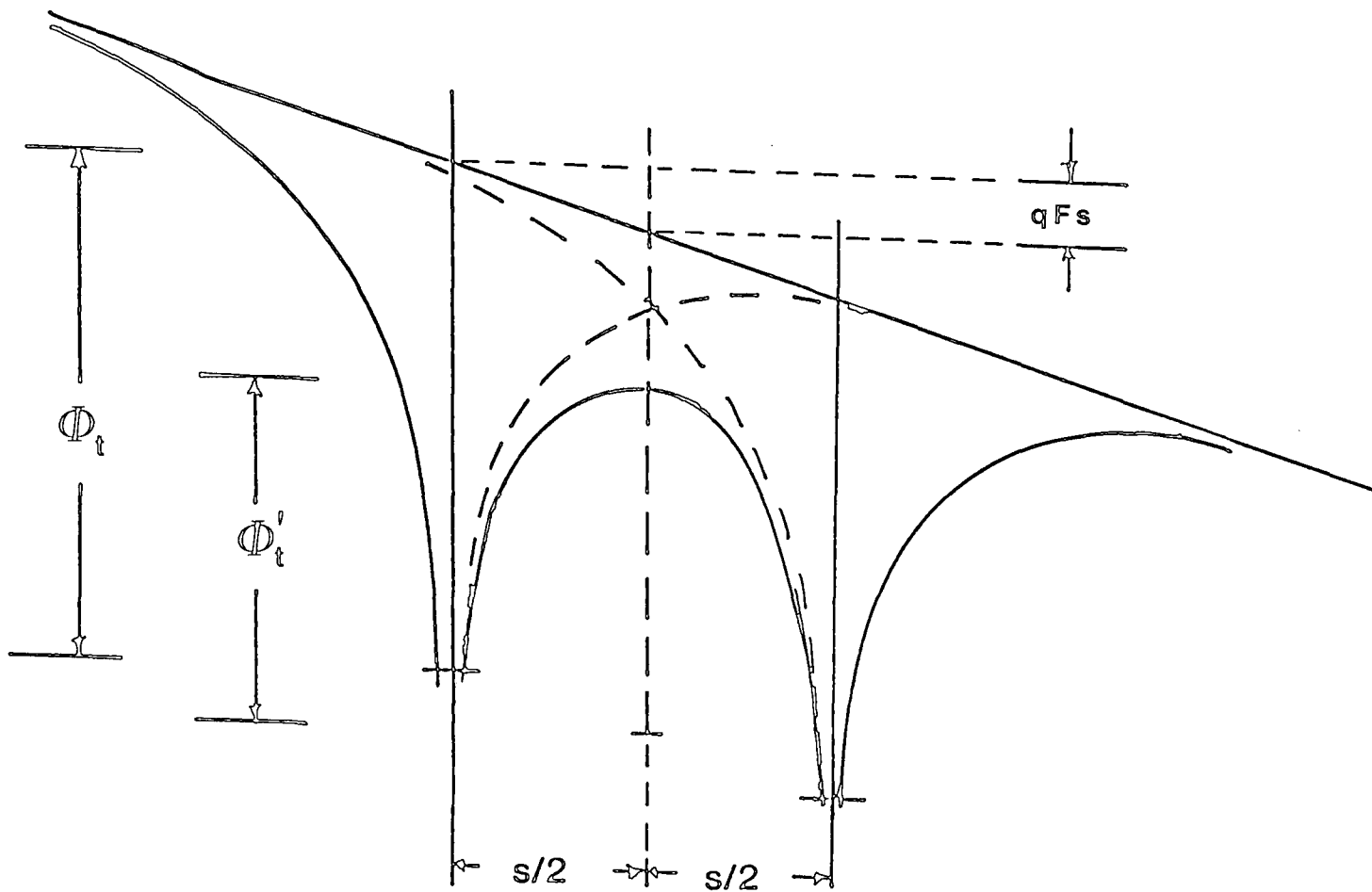
Figure 3.9    The potential energy diagram of multiple trapping centres where there is overlap of the coulombic potentials of closely spaced centres under the influence of an applied field.

seem that Hill has gone into a great amount of detail in discovering the origins of the conduction mechanisms, while the approximate analysis of the others seems to be adequate.

Still yet another error in the interpretations presented so far is that it is implicitly assumed that the amount of space charge due to either ionized donors/acceptors and/or from free carriers has no effect on the electric field throughout the material. For any bulk controlled mechanism, there is a build up of space charge at or near the injecting contact. This space charge builds up to adjust the local electric field at the contact until the injected current is equal to the bulk limited current. For very thick films the space charge will have little or no effect on the average electric field in the insulator. Assuming that the charge centroid of the space charge is about 100 $\overset{o}{A}$ from the injecting contact [38,39], any dielectric with a thickness of less than a few thousand angstroms will be affected by perturbation of the average electric field. Many authors [21,24,40-42] have put forward models to explain the effects of space charge on the conduction mechanism for very thin films. In fact Pulfry et al [21] showed that the Richardson-Schottky and Poole-Frenkel mechanisms are only the limits of a wide range of characteristics dependent upon the film and trap parameters.

Even though many authors have put forward improvements to the original model of Frenkel [20] it is still very difficult to determine with a great deal of certainty the actual mechanism(s) and their associated parameters. It would seem that the results and the subsequent explanations of the conduction processes are dependent upon the type of plot chosen to exhibit the results.

Therefore one must obviously exercise a certain amount of caution before making too many strict interpretations.

References for Chapter 3

[1]  J.J. O'Dwyer, Theory of Electronic Conduction and Breakdown in Solid Dielectrics Clarendon Press, Oxford (1973).

[2]  N.F. Mott and E.A. Davis, Electronic Processes in Non-Crystalline Materials, Clarendon Press, Oxford (1979).

[3]  A.K. Jonscher, J. Electrochem. Soc., 116, 217C (1969).

[4]  A.K. Jonscher, J. Vac. Sci.and Tech., 8, 135 (1970).

[5]  R.H. Fowler and L. Nordheim. , Proc. Roy. Soc., A 119, 173 (1928).

[6]  C.B. Duke, Tunnelling in Solids, Academic Press, New York (1969).

[7]  J.G. Simmons, D.C. Conduction in Thin Films, Mills and Boon Ltd., London (1971).

[8]  R.H. Good and W. Muller, "Field Emission", Handbuch der Physik, 21, Springer Verlag (1956).

[9]  R. Lamb, Electronic Conduction Mechanisms in Thin Insulating Films, Meuthen and Co. Ltd., London (1967).

[10] J. Frenkel, Phys. Rev., 36, 1604 (1930).

[11] A. Sommerfeld and H. Bethe, Handbook of Physics, 24/2, (1933).

[12] R. Holm, J. Appl. Phys., 22, 569 (1951).

[13] J.G. Simmons, J. Appl. Phys., 34, 1793 (1963).

[14] J.G. Simmons, J. Appl. Phys., 34, 2581 (1963).

[15] J.G. Simmons, J. Appl. Phys.. 35, 2472 (1964).

[16] J. Stratton, J. Phys. Chem. Solids, 23, 1177 (1962).

[17] R.E. Burgess, H. Kroemer and J.M. Houston, Phys. Rev., 90, 515 (1953).

[18] G.F. Roberts and J.J. Polanco, Phys. Status Solidi, 1, 409 (1970).

[19] W. Schottky. Physik Z., 15, 877 (1914).

[20] J. Frenkel, Phys. Rev., 54, 647 (1938).

[21] P.L. Pulfrey, A.H.M. Shousha and L. Young, J. Appl. Phys., 41, 2838 (1970).

[22] A. Servini and A.K. Jonscher,Thin Solid Films, 3, 341 (1969).

[23] H. Seki, Phys. Rev. B, 2, 4877 (1970).

[24] J.G. Simmons, Phys. Rev., 155, 657 (1967).

[25] P.Mark and T.E. Hartman,J. Appl. Phys., 39, 2163 (1968).

[26] J.R. Yeargan and H.L. Taylor,J. Appl. Phys., 39, 5600 (1968).

[27] J.C. Anderson, J. Vac. Sci. and Tech., 9, 1 (1972).

[28] R.M. Hill, Thin Solid Films, 1, 39 (1967).

[29] A.K. Jonscher, Thin Solid Films, 1, 213 (1967).

[30] A.K. Jonscher and A.A. Ansari, Phil. Mag., 23, 205 (1971).

[31] S.M. Sze, J. Appl. Phys., 38, 2951 (1967).

[32] T.E. Hartman, J.C. Blair and R. Bauer, J. Appl. Phys., 37, 2468 (1966).

[33] J.L. Hartke, J. Appl. Phys., 39, 4871 (1968).

[34] M. Ieda, G. Sawa and S.Kato, J. Appl. Phys., 42, 3737 (1971).

[35] R.M. Hill, Phil. Mag., 23, 59 (1971).

[36] N. Klein and Z. Lisak, Proc. IEEE, 54, 979 (1966).

[37] W. Franz, Handbuch der Physik, 17, Springer-Verlag (1956).

[38] B.H. Yun. Appl. Phys. Lett., 25, 340 (1974).

[39] P.C. Arnett and B.H. Yun, Appl. Phys. Lett., 26, 94 (1975).

[40] P.C. Arnett, J. Appl. Phys., 46, 5236 (1975).

[41] R.I. Frank and J.G. Simmons. J. Appl. Phys., 38, 832 (1967).

[42] R.H. Walden, J. Appl. Phys., 43, 1178 (1972).

# Chapter 4

## Experimental Details

### 4.1 Sample Fabrication

All samples fabricated for this work consisted of a metal-insulator-semiconductor (MIS) structure. These 'devices' may be considered to be capacitors, junctions or diodes depending on the particular measurement or use. For the purpose of this thesis they will simply be referred to as 'devices'.

### 4.1.1 Chemical Vapour Deposition - An Introduction

Chemical vapour deposition (CVD) is the term applied to the process in which a film is deposited by a chemical reaction or pyrolytic decomposition in the gas phase near the substrate surface. Epitaxial growth of semiconductors is a typical example of CVD. Various systems have been developed for CVD at low temperatures, low pressures and with plasma enhancement. Typical applications for CVD in microelectronics include the depositions of silicon dioxide ($SiO_2$), silicon nitride ($Si_3N_4$) and polycrystalline silicon.

Silicon dioxide is the most widely used insulating film in microelectronics. Thermal oxidation of silicon produces high quality films of $SiO_2$ but it is only applicable to silicon substrates. Quite often it is necessary to deposit $SiO_2$ onto existing oxide layers, metals, nitrides and semiconductors other than silicon. A thick oxide layer may be deposited by the oxidation of silane ($SiH_4$) or by one of the chlorosilanes ($SiCl_2$, $SiHCl_3$, $SiH_2Cl_2$) with either nitrous oxide ($N_2O$) or

carbon dioxide ($CO_2$) at temperatures between 800 and 1000 $^\circ$C. These are high quality oxides but are usually inferior to thermally grown oxides.

Silicon nitride is used as a passivating layer or as an insulator in some integrated circuit processes. A typical $Si_3N_4$ CVD system uses the reaction of silane ($SiH_4$) and ammonia ($NH_3$) at a temperature between 600 and 800 $^\circ$C in a nitrogen carrier gas.

Low temperature CVD can be performed in a system that provides for continuous deposition. The substrates are passed through a nitrogen curtain as they are heated to the deposition temperature. They are then transported into the reaction chamber and finally through another nitrogen curtain before leaving the system.

Atmospheric pressure CVD usually takes place in a cold wall reactor. The cold wall reduces the amount of wall deposit and subsequently the degradation of the films due to falling particles. The substrates are placed horizontally on a susceptor that may be heated by resistive elements, RF or by tungsten-halogen lamps.

Low pressure CVD systems have been developed that operate in the pressure range 0.1 to 1.0 torr. These systems are usually hot wall reaction chambers with vertically mounted substrates. This type of reactor is similar to a thermal oxidation furnace. It has been found that with low pressure CVD systems throughput is greater, the need for carrier gas is reduced, and the uniformity is improved compared with their atmospheric counterparts [1].

Plasma enhanced CVD has been demonstrated for the growth of $Si_3N_4$ and $SiO_2$ [2,3]. In a glow discharge plasma the "electron temperature" in the plasma is typically 10 to 100 times that of the average gas molecule temperature. The gases are therefore maintained at a relatively low temperature while the electron energy is sufficient to break molecular bonds leading to a chemically active species. As an example, a plasma enhanced deposition of $SiH_4$ and $NH_3$ in an $N_2$ carrier at 240 $^{o}C$ and 0.2 torr is similar to that of an 800 $^{o}C$ deposition in a conventional atmospheric pressure reactor [1].

4.1.2  Chemical Vapour Deposition of Silicon-Rich $Si_3N_4$ Films

A large part of this work was concerned with conduction in silicon-rich $Si_3N_4$ (SRN) films prepared as described below. Some comparative work was done with silicon-rich $SiO_2$ (SRO) films the preparation of which is described in Chapter 8.

The system used to grow the silicon-rich nitride (SRN) was a low pressure chemical vapour deposition (LPCVD) reactor in the Department of Electronics at the University of Southampton. A schematic diagram of such a system is shown in Fig. 4.1. All of the films studied here were grown at temperatures between 740 and 750 $^{o}C$ and at a pressure of approximately 0.3 torr. Nitrogen was used as the carrier gas while the reactants were dichlorosilane ($SiH_2Cl_2$) and ammonia ($NH_3$). The flow of the carrier was maintained at five litres/minute and the reactant flow rates were varied between 20 and 80 sccm depending on the desired film composition.

The composition of the films was controlled by varying the

55

PRESSURE
SENSOR

WAFER
LOAD/UNLOAD
END CAP

EXHAUST
TO
PUMP

3·ZONE RESISTANCE HEATER

GAS
INLET
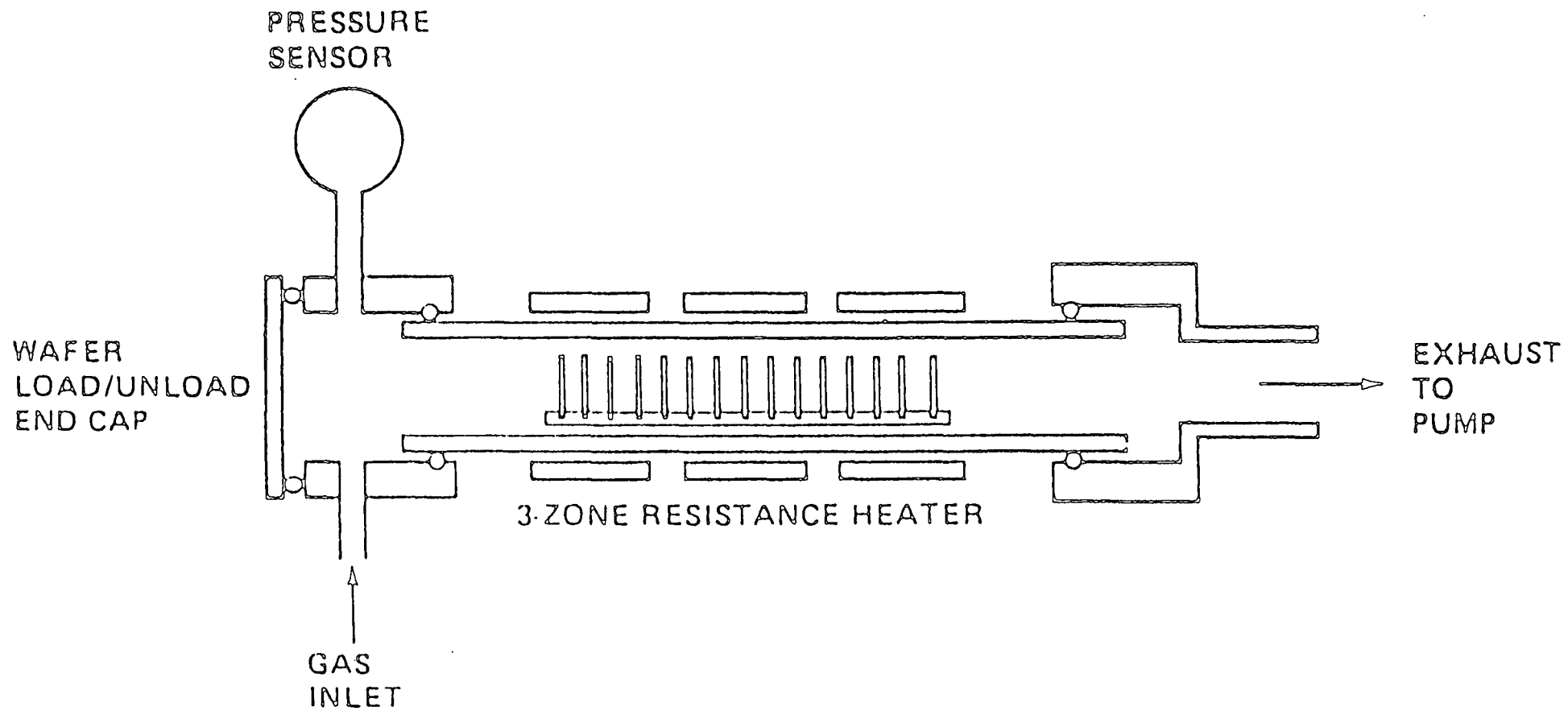
Figure 4.1    Low  pressure chemical vapour deposition (LPCVD)
reactor.

gas phase ratio of the reactant gases. The gas phase ratio, $R_n$, is given by

$$R_n = \frac{\text{flow rate of } [NH_3]}{\text{flow rate of } [SiH_2Cl_2]} \qquad (4.1)$$

Therefore an increase in the value of $R_n$ would give a decrease in the silicon content of the grown film.

For stoichiometric nitride layers used in industry as passivating or insulating layers, the gas phase ratio is typically $R_n \rangle 100$ [4,5] but this value is very dependent on the growth conditions and the choice of the reactants. However, it has been found that to produce any noticeable change in the conductivity of the films, a value of $R_n \langle 10$ is needed [5]. To obtain a large increase in the conductivity, the films were therefore grown in the range $0.25 \langle R_n \langle 4.0$ .

Table 4.1 gives a detailed outline of the films grown for the purpose of study here. All films were grown on n-type silicon with the exception of wafers 13 to 16 which were grown on n on p+ silicon. Aluminium top contacts of approximately one millimetre diameter were evaporated on to all films through a contact mask and either gold or aluminium was deposited to form back contacts. A typical flow chart of the process used is shown in Fig. 4.2. The example given is for the processing of wafers 9 through 11. It should be noted that wafers 9 and 11 and subsequently wafers 13 and 15 were annealed in nitrogen for one hour at 900 $^{o}$C. The thickness and refractive index of all films were measured using standard ellipsometry techniques.

Table 4.1 Silicon-rich silicon nitride films studied.

| Wafer No. | Gas Phase Ratio $R_n$ | Thickness ($\overset{o}{A}$) | Substrate | |
|---|---|---|---|---|
| | | | Resistivity ohm-cm | Type |
| 1 | 4.0 | 320 | 0.5 on 0.02 | n on n+ |
| 2 | 4.0 | 280 | 0.5 on 0.02 | n on n+ |
| 3 | 4.0 | 320 | 0.5 on 0.02 | n on n+ |
| 4 | 4.0 | 280 | 0.5 on 0.02 | n on n+ |
| 5 | 1.0 | 300 | 0.5 on 0.02 | n on n+ |
| 6 | 1.0 | 295 | 0.5 on 0.02 | n on n+ |
| 7 | 0.5 | 324 | 0.5 on 0.02 | n on n+ |
| 8 | 0.5 | 324 | 0.5 on 0.02 | n on n+ |
| 9* | 0.25 | 206 | 0.5 on 0.02 | n on n+ |
| 10 | 0.25 | 206 | 0.5 on 0.02 | n on n+ |
| 11* | 0.5 | 218 | 0.5 on 0.02 | n on n+ |
| 12 | 0.5 | 218 | 0.5 on 0.02 | n on n+ |
| 13* | 0.25 | 206 | 0.5 on 0.02 | n on p+ |
| 14 | 0.25 | 206 | 0.5 on 0.02 | n on p+ |
| 15* | 0.5 | 218 | 0.5 on 0.02 | n on p+ |
| 16 | 0.5 | 218 | 0.5 on 0.02 | n on p+ |
| D1 | 0.5 | 197 | 0.02 | n+ |
| D2 | 0.5 | 423 | 0.02 | n+ |
| D3 | 0.5 | 781 | 0.02 | n+ |
| D4 | 0.5 | 1537 | 0.02 | n+ |

* annealed for 1 hour at 900 $^{o}$C in nitrogen.

**Figure 4.2    Flow chart of silicon-rich nitride processing.**

```
┌─────────────────────────────────────────────────────────────────────┐
│      4 x 2 inch diameter n on n+ (0.5 ohm-cm on 0.02 ohm-cm)         │
│                   slices numbered 9,10,11,12                          │
└─────────────────────────────────────────────────────────────────────┘
                                │
              ┌─────────────────────────────────────────┐
              │               9,10,11,12                 │
              │        30 sec.  dip in buffered HF        │
              │     3 x 1 min rinse in deionized water    │
              │              3 min spin dry               │
              └─────────────────────────────────────────┘
              │                                           │
  ┌───────────────────────┐               ┌───────────────────────┐
  │        9,10            │               │        11,12           │
  │      deposit SRN       │               │      deposit SRN       │
  │     $R_n$ = 0.25       │               │     $R_n$ = 0.5        │
  │   Target = 200 Å       │               │   Target = 200 Å       │
  └───────────────────────┘               └───────────────────────┘
              │                                           │
              └─────────────┐           ┌─────────────────┘
                    ┌─────────────────────────┐
                    │       9,10,11,12         │
                    │    plasma etch SRN off   │
                    │       sample backs       │
                    └─────────────────────────┘
              ┌─────────────┘           └─────────────────┐
  ┌───────────────────────┐               ┌───────────────────────┐
  │        9,11            │               │        10,12           │
  │ anneal in $N_2$ at 900 °C │           │        - - - - -        │
  │      for one hour      │               │        - - - - -        │
  └───────────────────────┘               └───────────────────────┘
              │                                           │
              └─────────────┐           ┌─────────────────┘
                    ┌─────────────────────────┐
                    │       9,10,11,12         │
                    │ 1 mm diameter Al top contacts │
                    │     Au back contacts     │
                    └─────────────────────────┘
```
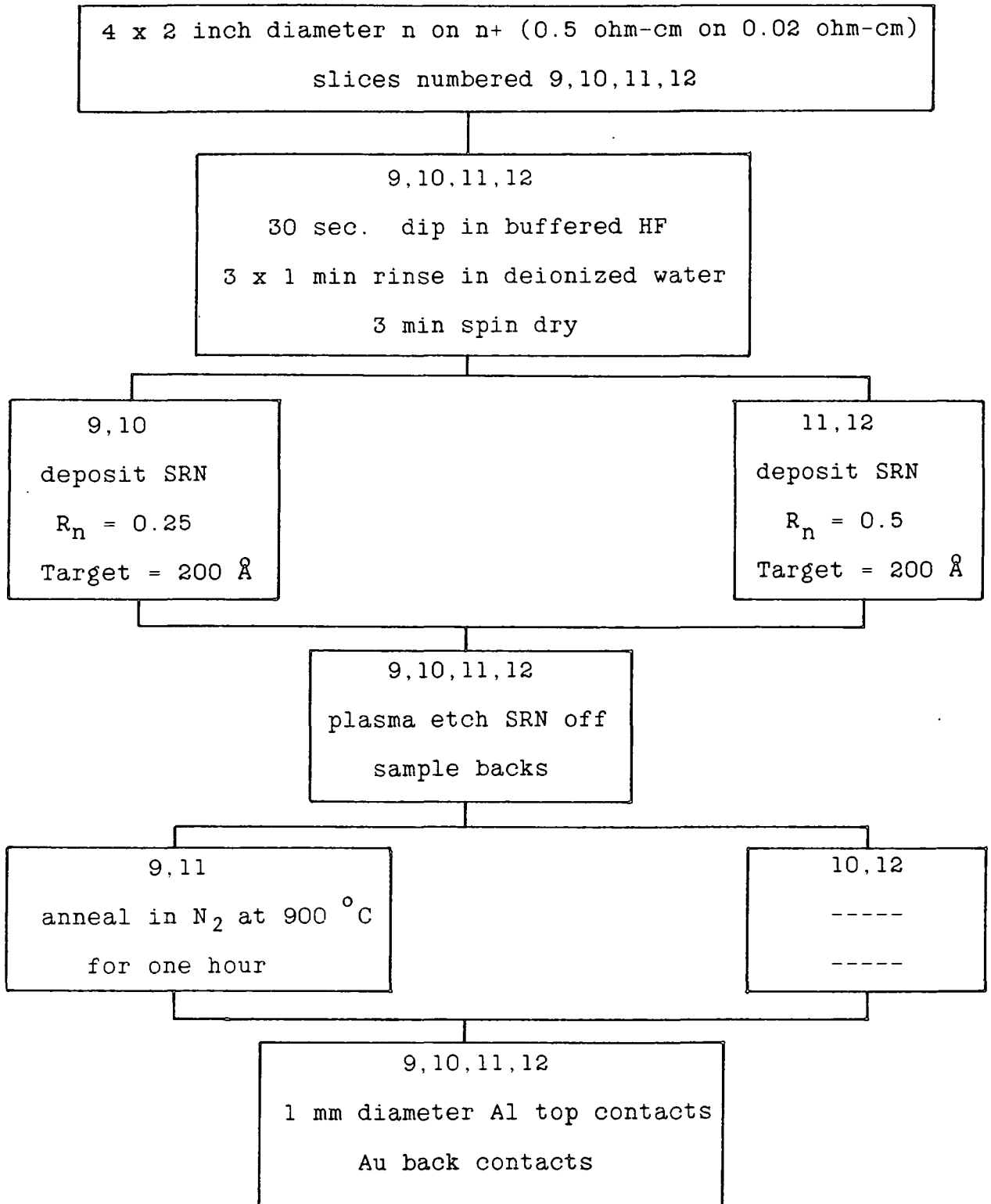
## 4.2 Device Characterization

Figure 4.3 shows a schematic diagram of the geometry of the devices used. Each wafer processed contained between 100 and 400 individual devices thus enabling a large number to be measured for checks on reproducibility. Reproducibility over a single two inch wafer was found to be good and within the limitations posed by the thickness variation of the films (typically 1-2%). It was found that the most reliable and convenient method of testing reproducibility was to monitor the current-voltage (I-V) characteristics. In practice, the current was measured for a number of devices at a few predetermined voltage levels. The data were then used to choose typical devices. This technique was found to be more sensitive than, for example, measuring the device capacitance as the current through the MIS structure is highly susceptible to defects or irregularities in the silicon-rich nitride (SRN) film.

All room temperature measurements were performed in an enclosed sample chamber. A photograph of the sample chamber is shown in Fig. 4.4 . Electrical contact was made either using a gold ball (0.5 mm in diameter) or a fine point tungsten probe. The position of the probe was controlled by a micromanipulator. The back contact was made either by vacuum to the sample mount or by silver paste to an aluminium or brass chuck.

For measurements at elevated or reduced temperatures, the samples were scribed and mounted on copper blocks (1.0 x 0.5 cms). The blocks were then mounted in a standard liquid nitrogen cryostat. The details of the measurement techniques are given in the following sections.
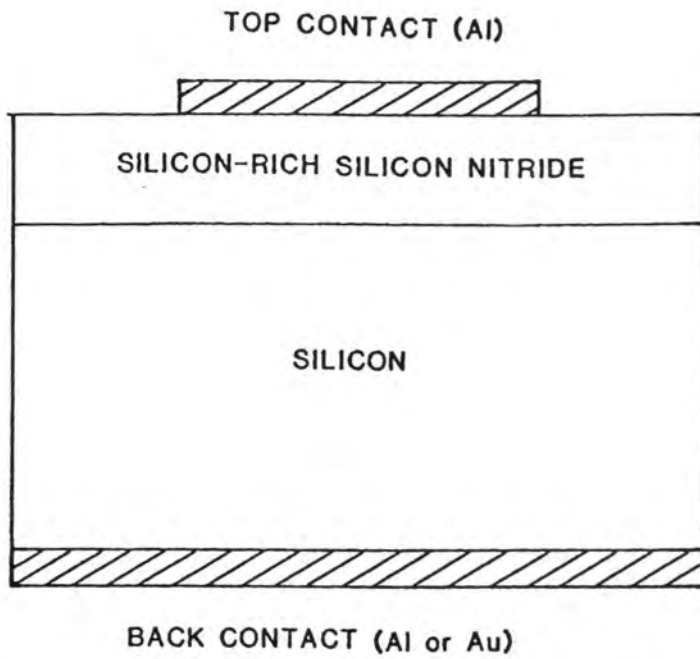
Figure 4.3    Metal-insulator-semiconductor (MIS) structure.



Figure 4.4    Photograph of sample chamber and sample wafer.

## 4.2.1 Electrical Measurements

All electrical measurements were automated using a Cifer 1886 microcomputer and an IEEE bus system. The peripheral measuring equipment (i.e. ammeters, voltmeters, temperature sensors etc.) were all IEEE compatible and controlled through the Cifer microcomputer.

## 4.2.1.1 Current-Voltage (I-V) Measurements

Figure 4.5 shows a schematic diagram of the measurement system used to collect the current-voltage (I-V) data at room temperature. Long current transients (up to several hours) were observed after a change in the applied voltage. The transients were therefore monitored by the Cifer computer and the current was recorded only when it remained constant to within 1% over a period of five minutes. It was assumed that by this technique the measured currents were close to their steady-state values.

For the collection of I-V data for varying temperatures an Oxford Instruments cryostat (DN704) and temperature controller (3120) were used in conjunction with the previously mentioned (I-V) system. A detailed diagram of the cryostat and probe assembly is shown in Fig. 4.6. The temperature of the sample under test was controlled by the temperature controller through the IEEE link to the Cifer computer. For all measurements the sample was loaded into the cryostat and after evacuation of the sample chamber the system temperature was lowered to 77 K. By monitoring and adjusting the power output from the temperature controller to the cryostat heater, the temperature of the sample was ramped at a constant rate (approximately 2-3 K/min.) from
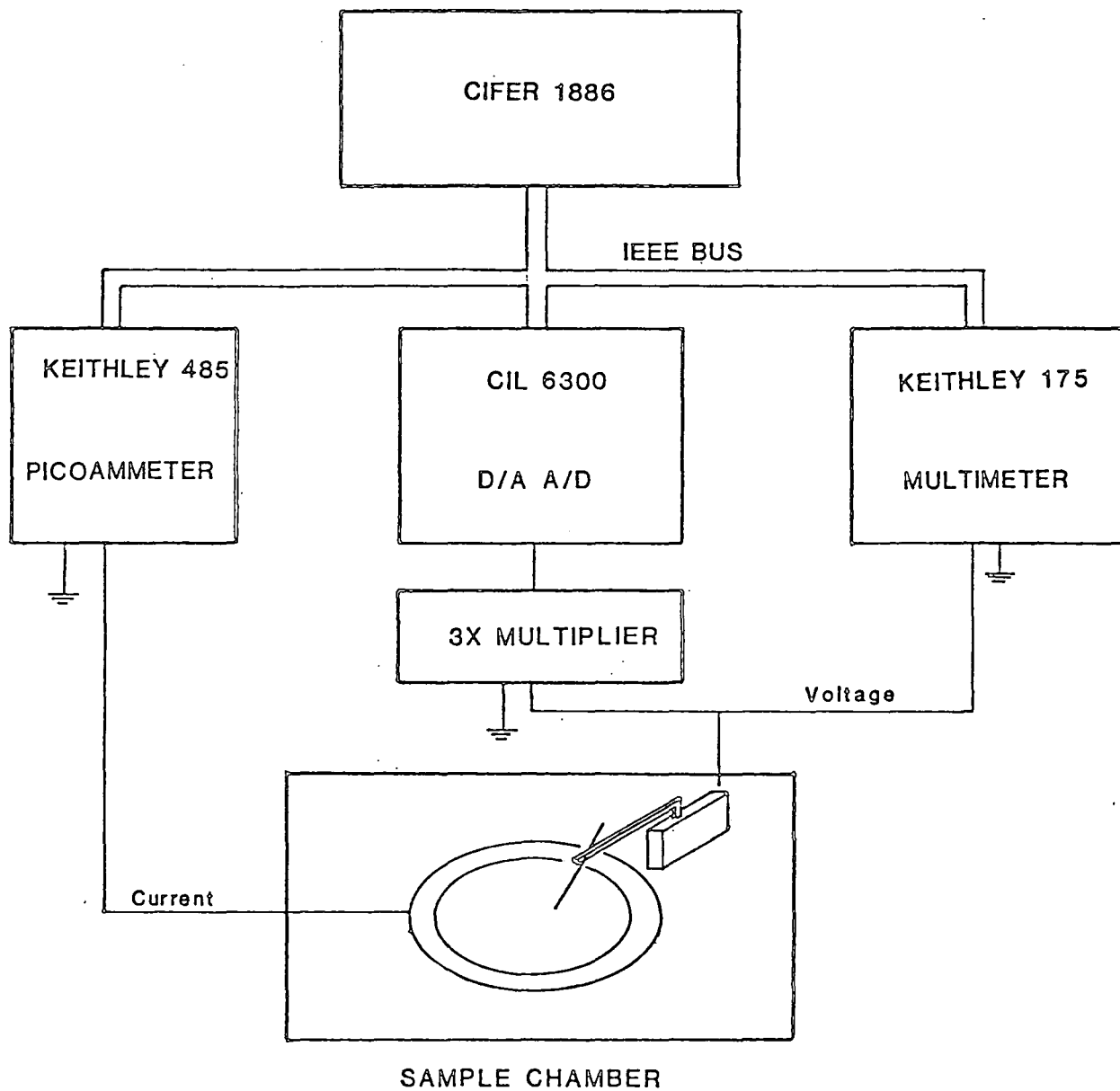
Figure 4.5    Current-voltage (I-V) measurement system.

IEEE BUS

TEMPERATURE CONTROLLER

Heater ──── Temperature

SAMPLE PROBE

ACCESS PORT

To multimeter

To Picoammeter

CRYOSTAT PROBE

LIQUID NITROGEN

RESEVOIR

TEMPERATURE

SAMPLE CHAMBER

HEATER          SENSOR

Back contact

SAMPLE

Top contact

CRYOSTAT
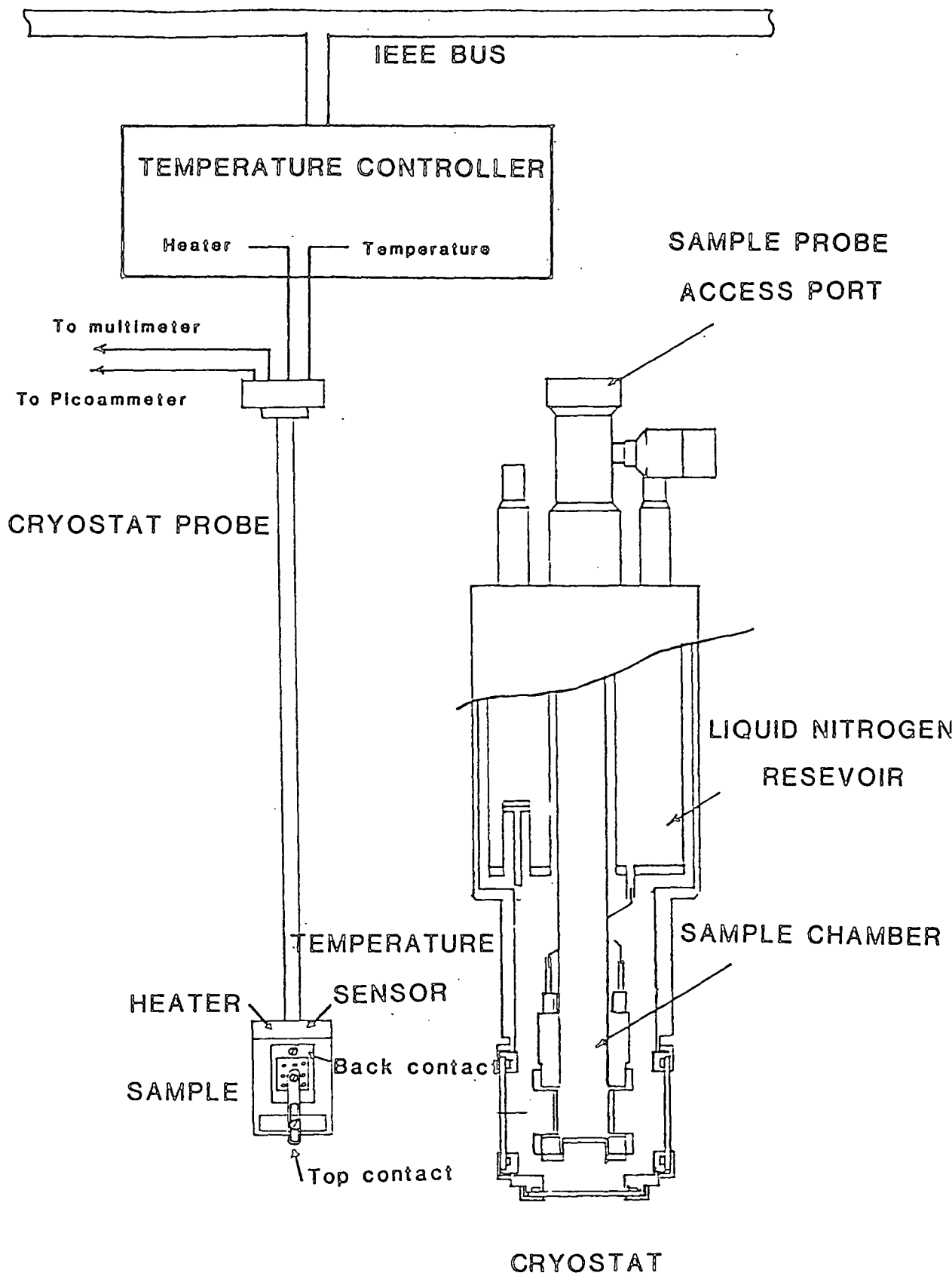
Figure 4.6    Detailed  schematic of the cryostat and cryostat
              probe  for  current-voltage-temperature  (I-V-T)
              measurements.

77 K to either 350 or 450 K. The voltage was maintained at a constant value while the current and temperature were recorded as the temperature increased.

## 4.2.1.2  Capacitance-Voltage (C-V) Measurements

To measure the capacitance-voltage (C-V) characteristics of the MIS devices a Boonton 72DB capacitance meter was used. Figure 4.7 shows a schematic diagram of the ramped C-V measurement system. The voltage on the MIS device was ramped at rates varying between 1mV/s to 7 V/s. The device voltage and the capacitance (from the analog output of the Boonton) were plotted using a Gould Series 60000 X-Y recorder. Point by point (quasi steady-state) measurements were also performed using the Cifer computer and the Boonton capacitance meter as shown in Fig. 4.8. The device voltage was set and after a predetermined period of time (usually $> 10^3$ secs), the device capacitance was recorded. The voltage on the device was then incremented to the next point. In this way point by point measurements over long time periods were performed.

## 4.2.1.3  Transient Flat Band Voltage Measurements

Due to the transient nature of the currents in the SRN films, it was found that monitoring the flat band voltage shift as a function of time could give an insight into the trapping and detrapping mechanisms of the films. Figure 4.8 shows a schematic diagram of the system that was used for these measurements. This transient flat band measurement technique has been reported elsewhere [6-8] but it is described here for

RAMP GENERATOR

3X MULTIPLIER

Voltage In          Analog Out

BOONTON 72DB
CAPACITANCE METER

Lo          HI

SAMPLE CHAMBER

X-Y RECORDER
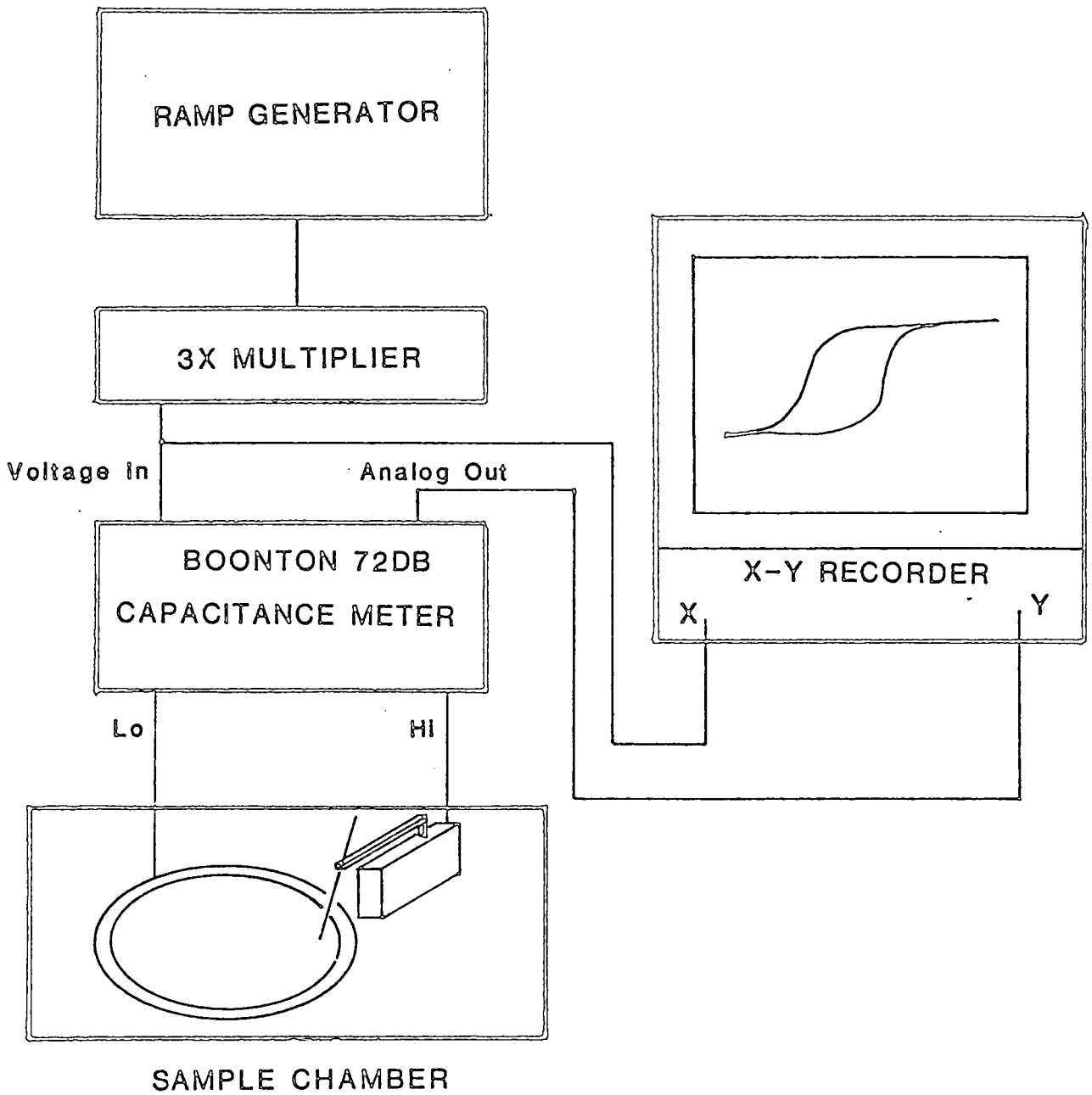
X          Y

Figure 4.7    Ramped    capacitance-voltage    (C-V)    measurement
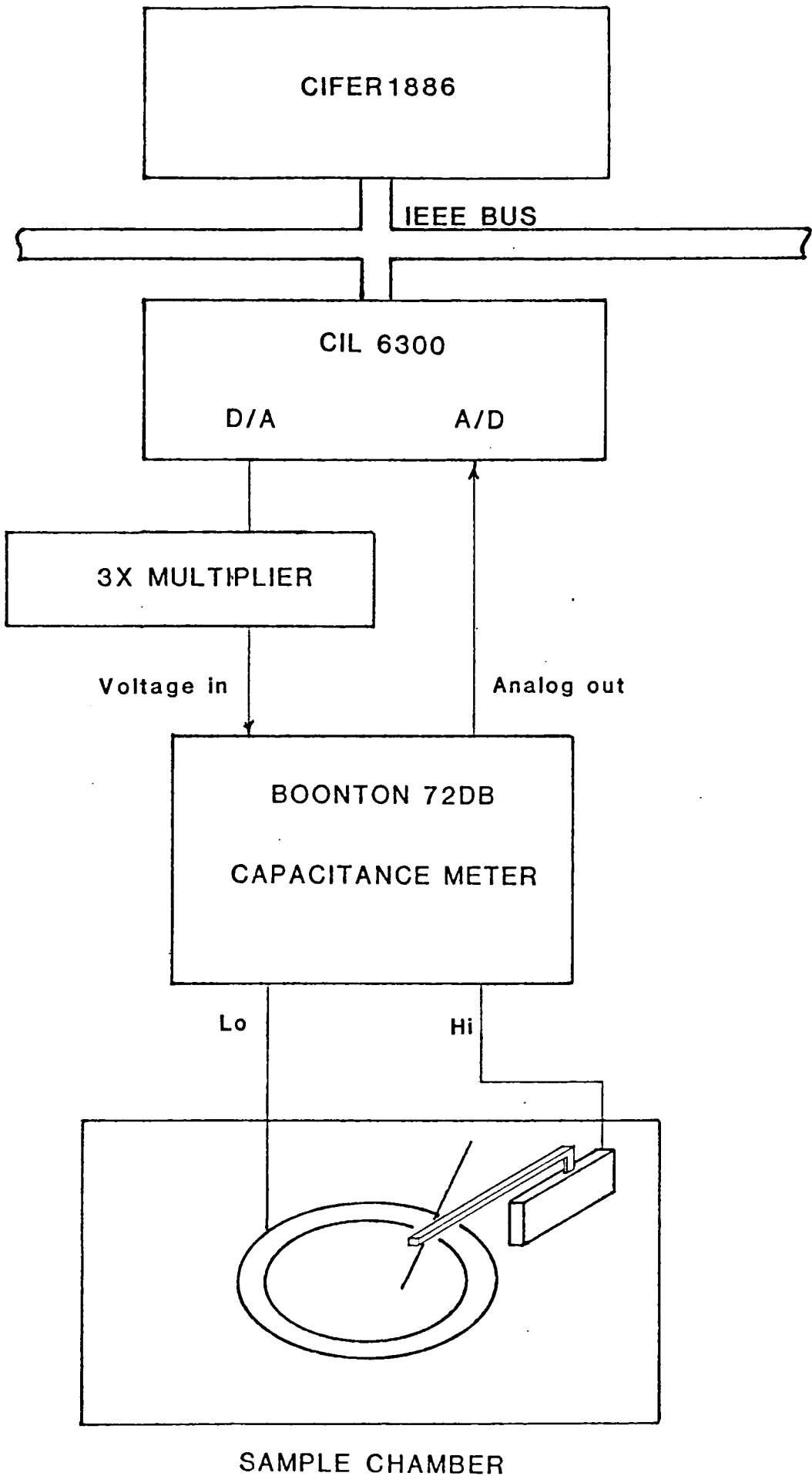              system.

Figure 4.8    Transient flatband voltage and point by point capacitance-voltage (C-V) measurement system.

the sake of completeness.

Firstly, the device voltage was ramped into accumulation. The accumulation capacitance was recorded via the analog output of the Boonton capacitance meter. A simple calculation was performed to obtain the 'ideal' flat band capacitance and its associated analog output voltage. The device voltage was then ramped to a predetermined holding voltage (typically -20 volts for films of thickness 200-300 $\overset{o}{A}$) for a sufficiently long period of time ( 2 min.). The purpose of the preset voltage was to allow the system to come to a known and repeatable initial steady-state. The voltage was then ramped towards the desired value at a rate of approximately 5 volts/second. The device capacitance was continuously monitored by the Cifer computer. At the point where the device capacitance was equal to the calculated 'ideal' flat band capacitance, the voltage on the device ($V_{FB_o}$) was recorded. The voltage ramp was continued towards the desired voltage and held there for a set length of time. After this time had expired, the voltage was ramped back towards the holding voltage. Again the capacitance was monitored by the computer and at the point where the capacitance was again equal to the 'ideal' flat band capacitance, the device voltage ($V_{FB}$) was recorded. This technique was repeated over a range of voltages (-15 to +15 V) and times (1 to $10^3$ s) to give a transient flat band shift characteristic as a function of time and voltage. Both positive and negative holding voltages and their associated ramping conditions were used to give a complete set of characteristics.

# References for Chapter 4

[1]   R.A. Colclasser,_Microelectronics : Processing and Device Design_,J.   Wiley and Sons, New York, 1980, Chapter 6.

[2]   E. Doering, INFOS '81, Erlangen, W.   Germany, North Holland, 1981, p208.

[3]   H. Huppertz and W.L. Engl, IEEE Trans.   on Electron.Dev., ED-26, 658 (1979).

[4]   S.M. Sze, J. Appl. Phys., 38, 2951 (1967).

[5]   D. Dong, E.A. Irene and D.R. Young, J. Electrochem. Soc., 125, 819 (1978).

[6]   R.H. Walden, J. Appl. Phys., 43, 1178, (1972).

[7]   P.C. Arnett and D.J. DiMaria, J. Appl. Phys., 47, 2092 (1976).

[8]   L.I. Popova, B.Z. Antov and P.K. Vitanov, Thin Solid Films, 36, 157 (1976).

# Chapter 5

## Structural Characterization of
## Silicon-Rich Silicon Nitride (SRN) Films

Samples of silicon-rich silicon nitride (SRN) films, depositied as described in Chapter 4, were examined using both reflection high energy electron diffraction (RHEED), and Rutherford backscattering spectrometry (RBS). This chapter describes these techniques and the results obtained.

## 5.1 Reflection High Energy Electron Diffraction (RHEED)

High energy electrons, 100 keV, can be employed to obtain electron diffraction from the surface of materials. This is a non-destructive technique and can be used to provide information on crystal orientation and perfection of surface films, the degree of preferred orientation of crystallites, and other crystal properties of thin films.

## 5.1.1 Theory

A mono-energetic beam of electrons is used to obtain diffraction from the atomic planes at the surface of a specimen in the RHEED technique. The wavelength of the electrons corresponding to an accelerating voltage (V) is given by [1]

$$\lambda = \left[ \frac{150}{V\,(1+10^{-6}V)} \right]^{\frac{1}{2}} \text{Å} \qquad (5.1)$$

Thus for an energy of 100 keV, the wavelength of the electrons

is about 0.04 Å.  The requirement for Bragg diffraction is that

$$\lambda = 2\ d_{hkl}\ \sin\theta \qquad\qquad (5.2)$$

where $d_{hkl}$ is the interplaner spacing and $\theta$ is the Bragg angle. Interplanar spacings can be on the order of 1 - 2 Å and as such the Bragg angle is very small, typically $<< 1^{\circ}$.  Consequently only planes that are inclined at less than a few degrees to the surface will diffract an electron beam that strikes it at a grazing incidence.

The conditions to produce an electron diffraction pattern are illustrated in Fig. 5.1.  When the incident beam strikes the crystal plane (hkl) at the Bragg angle $\theta$ , then it is diffracted to form a diffraction spot at P in the fluorescent screen or photographic plate which is at distance L from the sample.  From consideration of elementary geometry of Fig. 5.1, the distance $R_{hkl}$ from the diffraction spot P to the point O is given by

$$R_{hkl} = L\ \tan 2\theta \qquad\qquad (5.3)$$

For high energy electron diffraction, the value of $\theta$ is typically on the order of $1^{\circ}$ , so the following small angle approximations may be made :

$$R_{hkl} \approx 2\ L\ \theta \quad\quad \text{and} \quad\quad \sin\theta \approx \theta \qquad\qquad (5.4)$$

Thus, the Bragg relation of the equation 5.2 may be rewritten as

$$\lambda\ L = R_{hkl}\ d_{hkl} \qquad\qquad (5.5)$$

This is known as the camera equation and the camera length (L) is determined with reference to a standard specimen of known
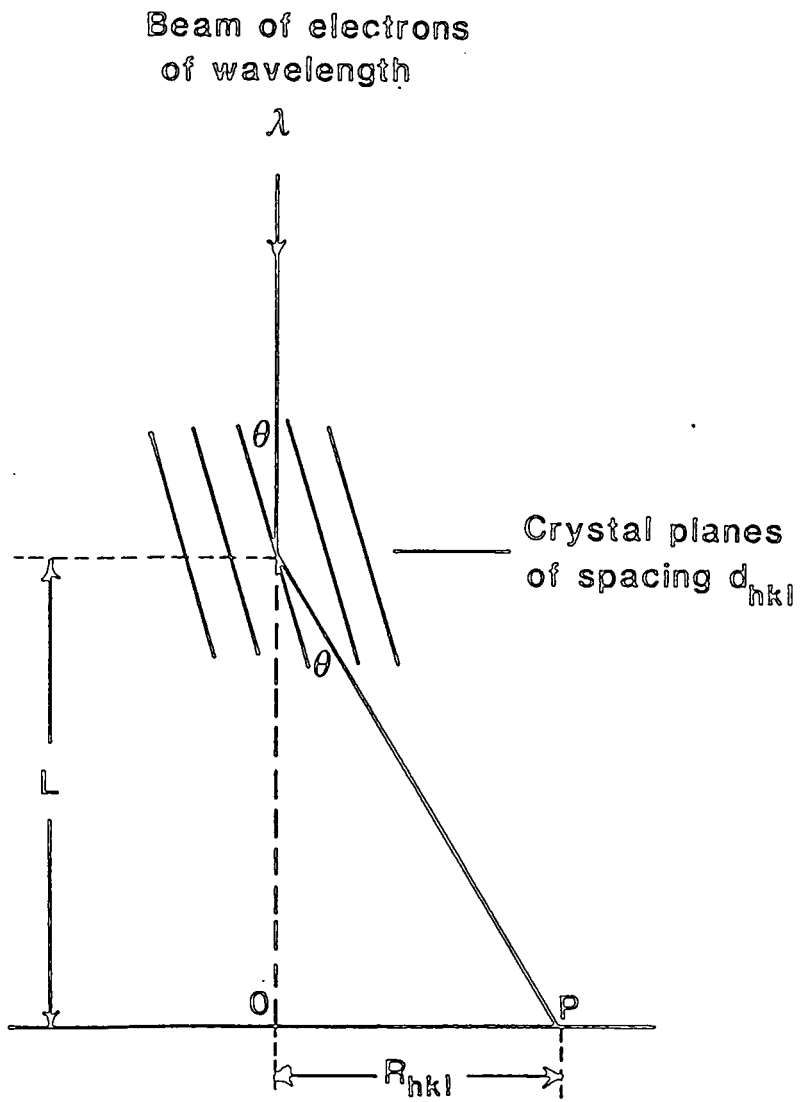
Figure 5.1    Schematic diagram of diffraction for the derivation of the camera equation.

crystal structure and lattice parameters. Once the camera constant ($\lambda$ L) has been calculated for a given pattern, the crystal structure and the lattice parameters of the sample may be determined.

In the analysis of RHEED patterns there are predominantly four distinct types of patterns that may emerge. These are diffuse, ring, arc and spot patterns. The latter two patterns are generally produced by crystalline materials of good long range order while the others correspond to materials lacking long range order.

Amorphous materials show little long range order and their diffraction patterns contain just a few very diffuse rings. Diffuse rings can also occur for materials that are predominantly crystalline but have very small grain sizes, usually of the order of about 3 to 100 unit cells in diameter. In this case a very diffuse pattern results from the broadening of the rings which is analogous to line broadening in x-ray diffraction.

If the grain size of the material is larger than that which gives rise to a broadening of the diffuse diffraction rings, the resulting diffraction pattern will consist of a number of continuous rings which become broken up and more spotty as the grain size increases. These rings arise from diffraction of a large number of randomly oriented crystallites.

The next level of crystalline order occurs when grains tend to have a preferred common orientation or fibre axis. Diffraction from such films can give rise to two quite different types of pattern depending on the orientation of the fibre axis

in relation to the direction of the electron beam. When the preferred orientation is approximately parallel to the beam, the resulting pattern still consists of rings but the relative intensities of these are abnormal and in certain cases the allowed reflections may be absent. When the preferred orientation is approximately normal to the beam, the diffraction pattern consists of a series of arcs of intensity instead of rings where the length of the arc is a measure of the misorientation of the grains.

Single crystals give rise to spot patterns which can provide information relating to two different aspects of the crystal structure. Firstly, the geometrical arrangement of spots permits the evaluation of the crystal structure and the determination of the lattice parameters. Secondly, a qualitative assessment of the surface may be inferred from other diffraction features of these patterns.

The materials used for the work contained in this thesis were either amorphous or in extreme cases, microcrystalline with relatively small grain sizes. Hence the predominant diffraction patterns are diffuse and solid ring structures. In the following section, a discussion of the nature of the structure of the SRN films is presented.


## 5.1.2 RHEED-Results and Discussion

Crystalline silicon nitride exists in two forms referred to as alpha and beta phases. Both are hexagonal in structure with a unit cell consisting of silicon nitrogen tetrahedra. The aim here is try and identify the structure of the silicon-rich

silicon nitride films and to study how this structure changes with increasing concentrations of silicon.

The samples that were used for the RHEED studies were the same as those used for the electrical characterization. Before the films were mounted in the transmission electron microscope (TEM) for the RHEED analysis, the aluminium top and bottom contacts were removed using a dilute solution of sodium hydroxide (NaOH).

Plates 5.2 and 5.3 illustrate the diffraction patterns of annealed and unannealed films respectively. These films contain the greatest amount of silicon (i.e. $R_n$ = 0.25) of the films grown for this work. The lattice spacings derived from these patterns are given in Table 5.1.

All the lines in Plates 5.2 and 5.3 can be attributed to either $\alpha$-$Si_3N_4$ or to silicon. In Table 5.1, the characteristic 'd' spacings for the $\alpha$-$Si_3N_4$ and silicon with the relative X-ray intensities [2] of each line are also presented. It should be noted that the intensities taken from X-ray analysis are comparable with RHEED patterns, but they should not be taken too literally.

From the data presented in Table 5.1, which is representative of all the RHEED data. certain peculiarities are noted. From the X-ray data [2]. the strongest lines for $\alpha$-$Si_3N_4$ occurs at a spacing of d = 2.55 Å. However, the measured line from the RHEED pattern is very weak. This phenomenon has been noted before [3,4] and has been attributed to the difference in the mechanisms involved in scattering electrons and X-rays in $\alpha$-$Si_3N_4$. The alignment of all the
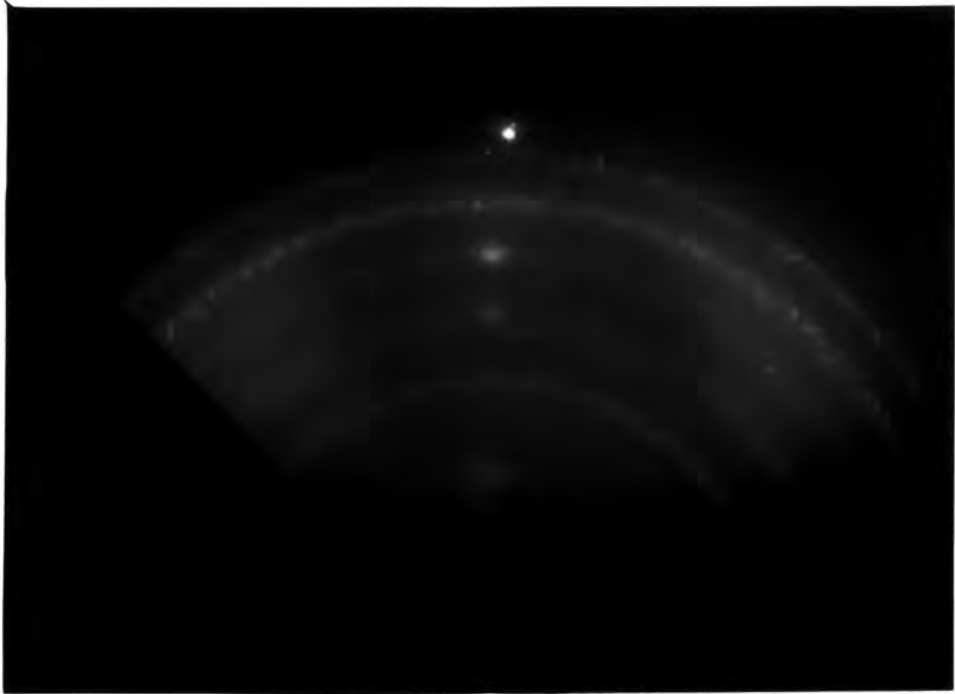
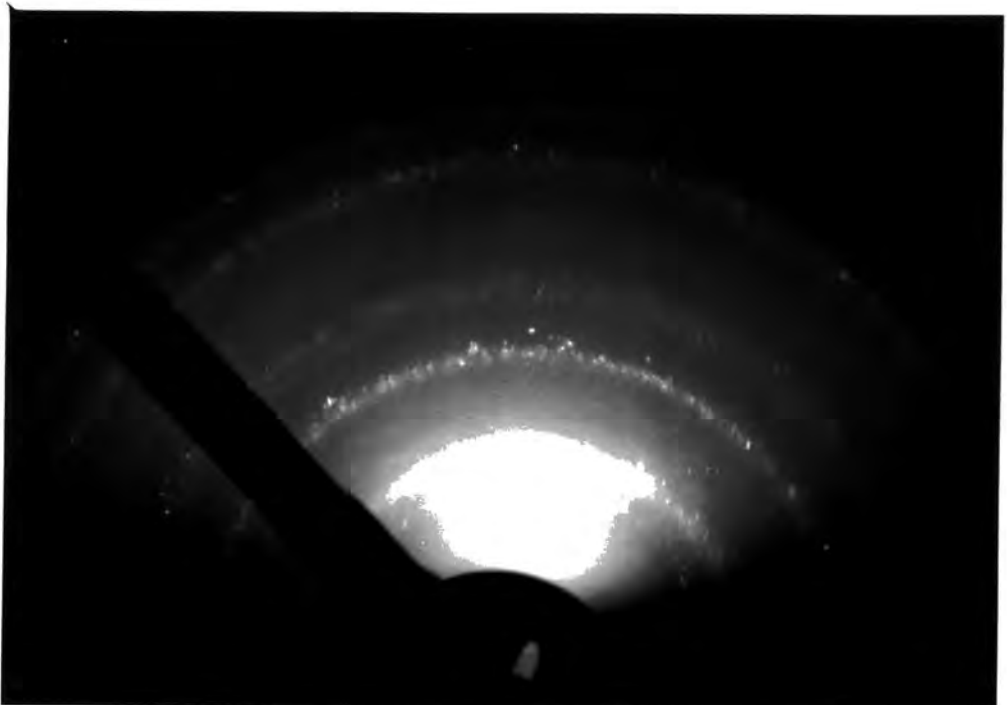Plate 5.2    RHEED pattern for an annealed $Si_3N_4$ film with $R_n$ = 0.25.



Plate 5.3    RHEED pattern for an unannealed $Si_3N_4$ film with $R_n$ = 0.25.

Table 5.1    Plane spacing, d, corresponding to the diffraction rings of Plates 5.2 and 5.3 for annealed and unannealed SRN films produced with $R_n = 0.25$. The spacings for $\alpha$ - $Si_3N_4$ and Si are obtained from ASTM X-ray data are given for comparison.

I = Relative intensity of electron diffraction ring in order very strong (vs) to very weak (vw). m = medium.

$I/I_o$ = Intensity of X-ray diffraction ring relative to the strongest (%).

| $R_n = 0.25$ | | | | X-ray Data [2] | | | |
|---|---|---|---|---|---|---|---|
| Annealed | | Unannealed | | $\alpha$-$Si_3N_4$ | | Silicon | |
| $d(\text{Å})$ | I | $d(\text{Å})$ | I | $d(\text{Å})$ | $I/I_o$ | $d(\text{Å})$ | $I/I_o$ |
| | | | | 3.37 | 30 | | |
| 3.22 | m | 3.25 | m | | | | |
| | | | | | | 3.14 | 100 |
| 2.83 | vs | 2.82 | s | 2.89 | 85 | | |
| | | | | 2.60 | 75 | | |
| 2.57 | vw | --- | | 2.55 | 100 | | |
| 2.02 | s | 2.01 | s | 2.08 | 55 | | |
| 1.86 | vw | --- | | | | 1.92 | 60 |
| | | | | 1.77 | 25 | | |
| 1.66 | m | 1.68 | m | | | | |
| | | | | | | 1.64 | 35 |
| 1.59 | m | 1.59 | m | 1.60 | 35 | | |
| 1.40 | vw | --- | | | | 1.36 | 8 |
| 1.24 | w | 1.24 | m | | | 1.25 | 13 |
| 1.12 | vw | 1.13 | m | | | 1.11 | 17 |

other major lines is good and gives no reason to doubt that the material is not $\alpha$-$Si_3N_4$ .

From Table 5.1 it can be seen that the the films contain a certain amount of free bonded silicon shown by the appearance of the silicon lines in the diffraction pattern. However, from the relative intensities of the lines attributed to $\alpha$-$Si_3N_4$ and silicon, one must assume that the free silicon makes up only a relatively small proportion of the film composition.

Plates 5.2 and 5.3 show that there is a characteristic structural change between the annealed and unannealed films, but the basic structure remains intact. The lines have become more continuous and constant in intensity in the annealed films. This implies that the average grain size has decreased, the smaller grains growing at the expense of the larger ones. It should also be noted that the diffraction pattern of the annealed films shows some very bright spots on a line normal to the film surface. These dots imply that during the annealing, there is a tendency for the grains to align with the substrate. However, these films would still be thought of as being amorphous or at best microcrystalline.

To compare the structures of films with varying composition. Plates 5.4 and 5.5 are shown for unannealed films with gas phase ratios of $R_n$ = 0.5 and $R_n$ = 4.0 respectively. The structure shown in Plate 5.4 is essentially identical to that shown previously (Plate 5.2). These films have gas phase ratios that are approximately the same (i.e. $R_n$ = 0.25 and $R_n$ = 0.5). However, the diffraction pattern for the film with the smallest silicon content, $R_n$ = 4.0 in Plate 5.5, is much
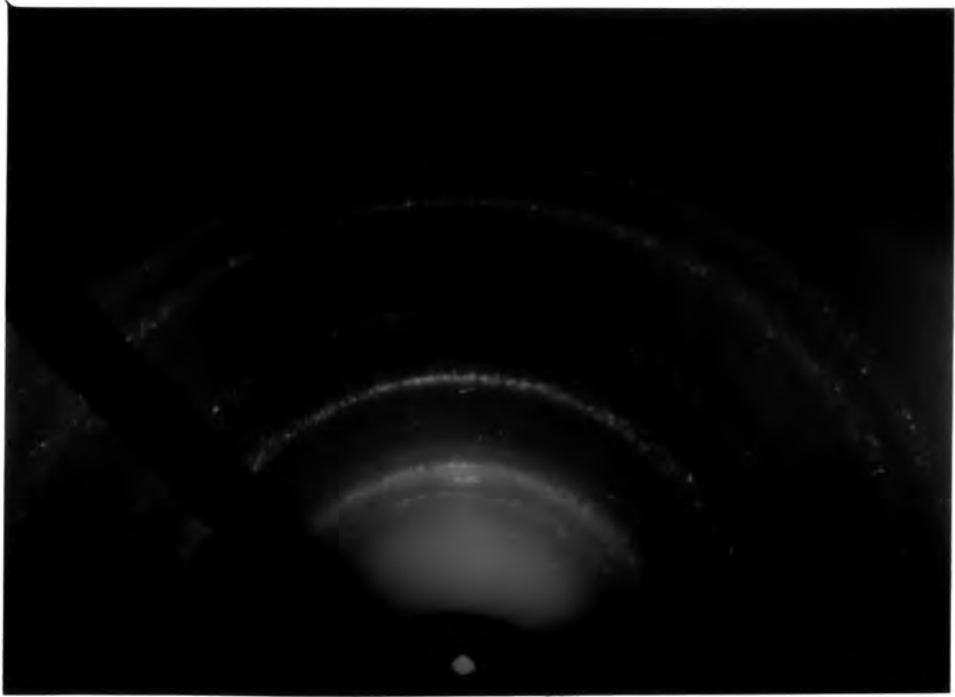
Plate 5.4    RHEED pattern for an unannealed $Si_3N_4$ film with $R_n = 0.5$.
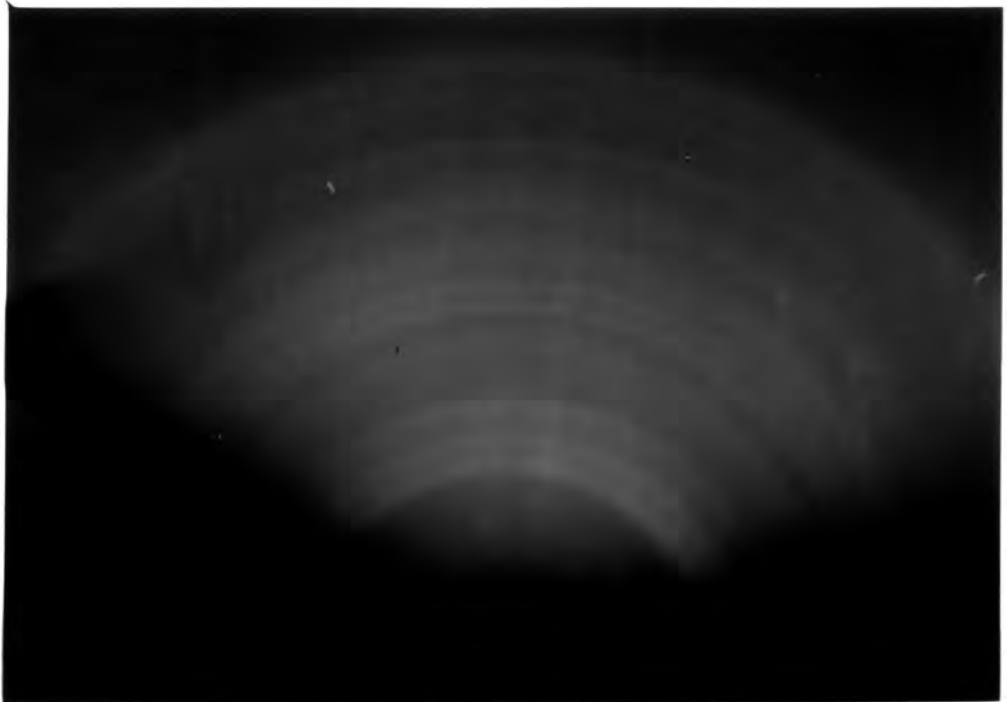


Plate 5.5    RHEED pattern for an unannealed $Si_3N_4$ film with $R_n = 0.4$.

different in that it contains the least amount of silicon. The diffraction pattern shows the film to have very little structure as is evident from the diffuse rings so characteristic of amorphous films. This also implies that the grain size is extremely small when compared to the films of higher silicon content.

In summary, these films are predominantly $\alpha$-Si$_3$N$_4$ . With increasing silicon content (i.e. decreasing R$_n$ ), the grain size increases and the films become less amorphous and more microcrystalline. After annealing, the basic structure remains intact, but the grains decrease in size. There is also some alignment of the films to the substrate after they have been annealed. There is evidence of a small amount of free bonded silicon in the these films although the relative amounts of silicon and $\alpha$- Si$_3$N$_4$ can not be determined by RHEED analysis.

In the following section, the elemental composition of these films is determined using another analytical technique called Rutherford Backscattering Spectrometry. This technique tells gives information on the composition of the films but not on their structure.


## 5.2 Rutherford Backscattering Spectrometry (RBS)

Backscattering analysis or spectrometry is a simple non-destructive technique that can be used to assess the elemental composition of a material. This method of compositional analysis is a surface sensitive technique that uses a monoenergetic stream of high energy alpha particles ($^4$He nuclei) which are directed at the target to be analysed. For

relatively thin materials, most of the beam passes straight through the material with only slight changes in energy or direction. Some of the particles do however undergo large changes in energy and direction due to close encounters of the incident particle and the nucleus of a single target atom. For a thick sample, only the particles that are scattered back at angles of more than 90 degrees from the incident direction are detected. The 'backscattered' signal is detected over a spectrum of energies; hence the name backscattering spectrometry.

## 5.2.1 Theory

Figure 5.6 gives a schematic outline of the major components of a backscattering system. Charged particles are generated in an ion source. Their energy is raised to several megaelectron volts by an accelerator, usually a van de Graaff generator or similar device. The high energy beam passes through a series of devices that collimate or focus the beam and filter it for a selected type of particle and energy. The beam then enters the scattering chamber and impinges on the sample to be analyzed. Some of the particles are backscattered and impinge on the detector that generates an electrical signal. The signal is amplified and processed usually with the aid of a computer. Apart from all the beam generation and data analysis equipment, the scattering chamber remains relatively simple. It contains only three major parts: the particle beam, the detector and the vacuum pump.

The two main features that can be analyzed in such a system
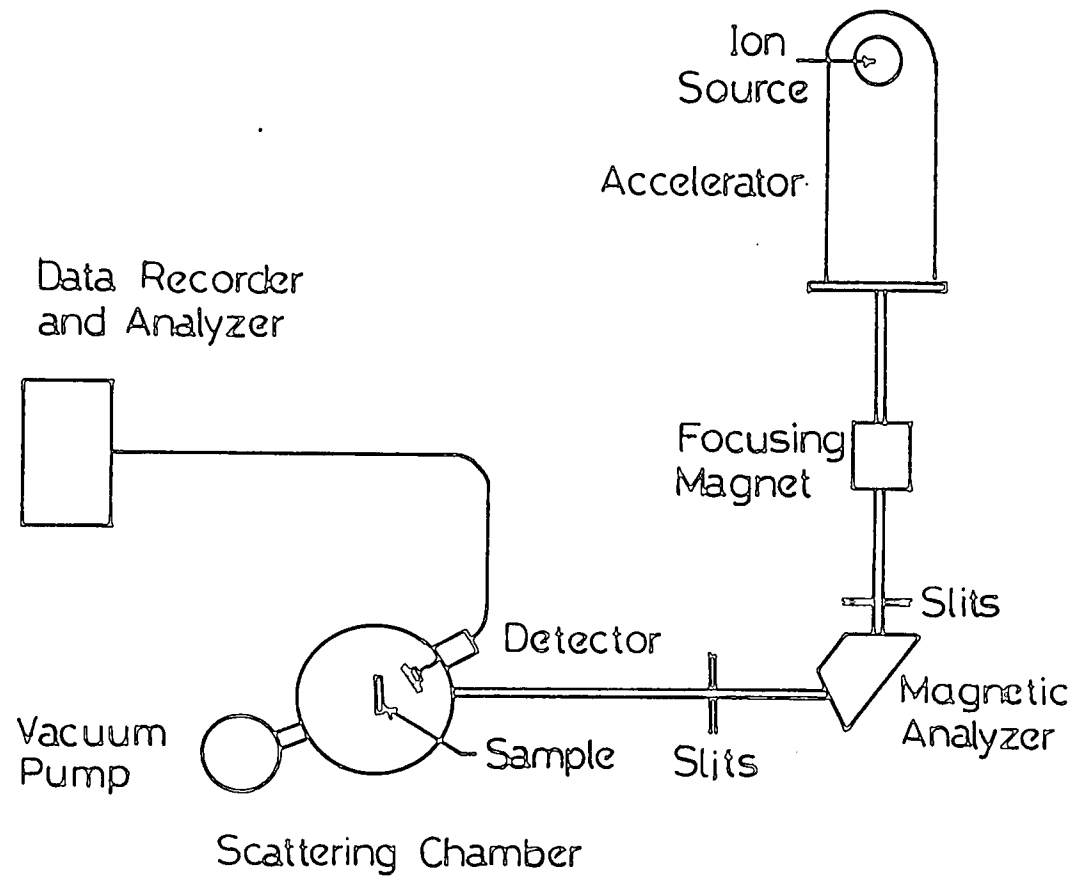
<u>Figure</u>  5.6    Schematic diagram of  a  typical  backscattering
                spectrometry system.

are elemental composition and film thickness. Figure 5.7 (a) and (b) show how the system can resolve both of these parameters. Consider a material that is made up of only two elements as shown in Fig. 5.7 (a). Assuming that the two elements in our material are of substantially different atomic masses, the energy of the scattered particle is dependent upon the element from which it was scattered. The larger sphere in Fig. 5.7 (a) represents an atom with a greater atomic mass than the smaller sphere, and as such the energy of the backscattered particle $E_1$ will be greater than $E_2$. The number of particles scattered with each energy is counted. From a suitably calibrated source the elemental composition of the material is determined. The problem however, is not quite so simple.

Consider now a material containing only one element with a certain thickness d, as is shown in Fig. 5.7 (b). The energy of the particles scattered from the front of the sample is not the same as those scattered from the back because of the loss of energy as the particles travel through a dense medium. Therefore, a particle that is scattered from the back face of the material has less energy than one scattered from the front. Scattering events that take place between the front and back surfaces are recorded at some intermediate energies. This is one way in which a concentration profile of a given element translates into a backscattering spectrum.

One of the largest advantages of backscattering spectrometry is that the spectrum can be analysed relatively easily. Consider a film of a uniform mixture of two elements which have atomic masses M and m, as shown in Fig. 5.8, such
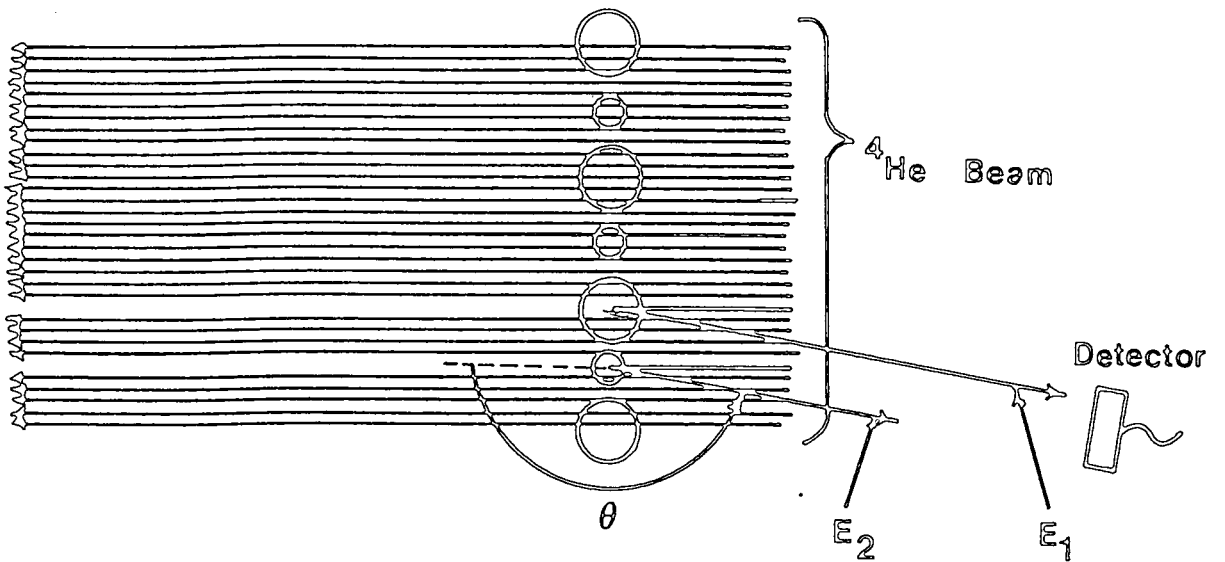
(a)
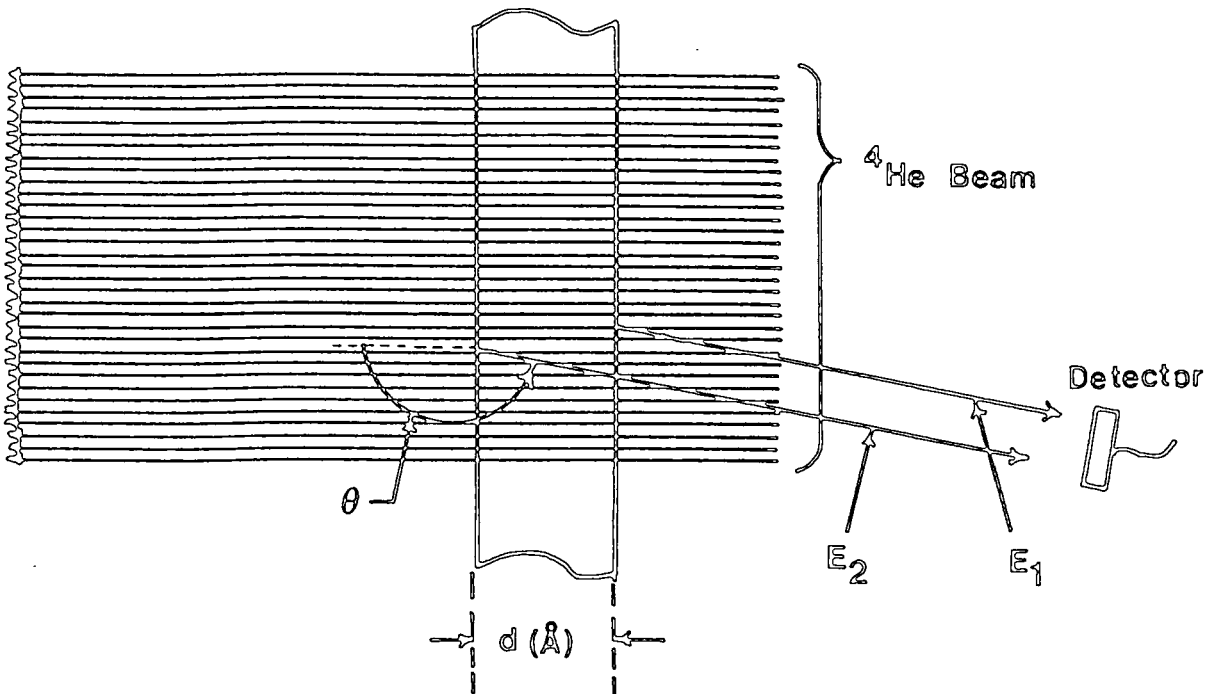


(b)

Figure 5.7   a) Schematic diagram showing collisions of
             α-particles with atoms of different atomic
             masses.
             b) Schematic diagram showing energy loss of
             scattered particles through a dense medium.

Thin
homogeneous
film
Surface
Substrate  Mm
Incident
beam
(a)

Atom
concentration
(b)
depth  O

m  M

Yield
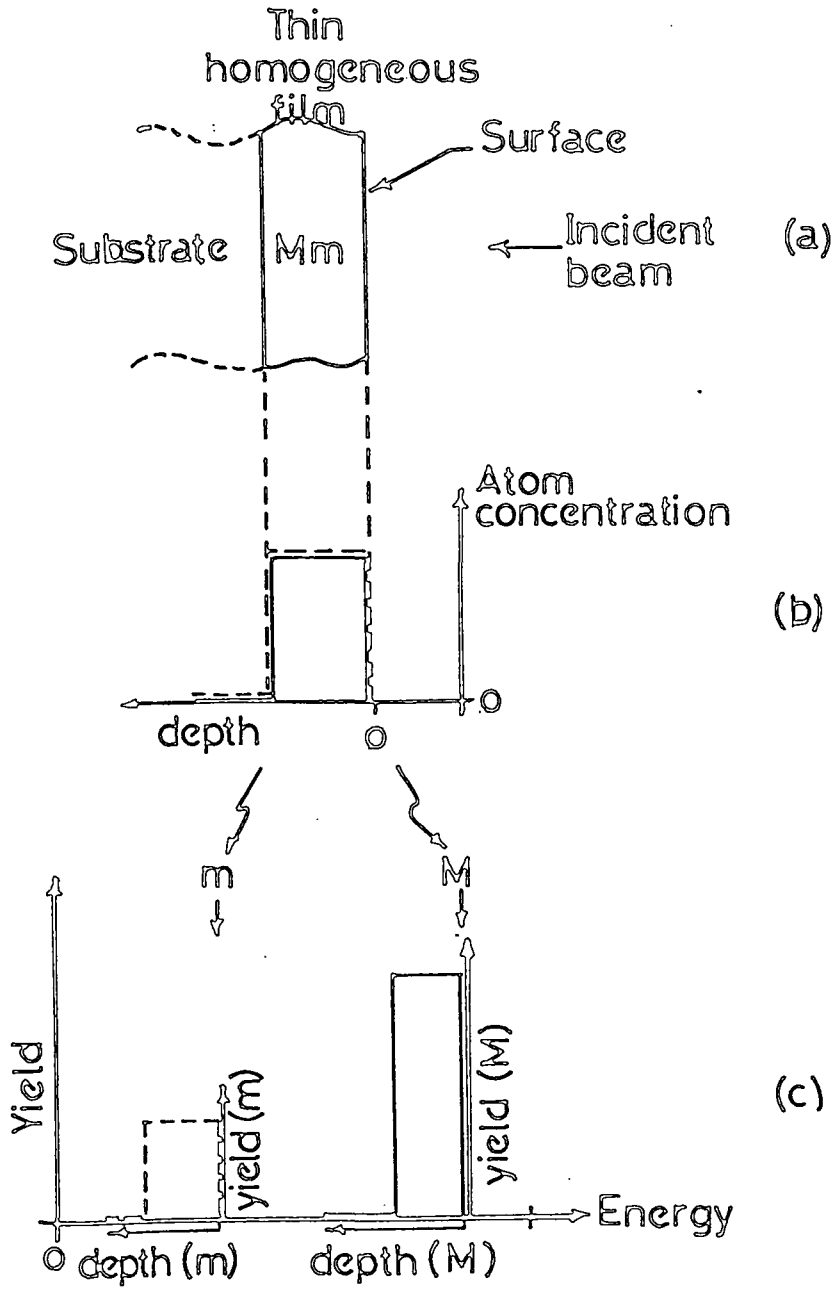yield (m)
yield (M)
(c)
O depth (m)  depth (M)  Energy

<u>Figure</u>  5.8  An  example showing a homogeneous thin film of a
binary compound with elements of heavy M  (solid
line) and light m (dotted line) atomic masses.

that   M › m.   We also assume the concentrations of these materials to be the same.   The resulting backscattered spectrum is shown in Fig. 5.8 (c).   The rectangle representing the element of heavier mass is located at an energy higher than that of the lower mass element.   In general, high masses go to high energies and low masses go to low energies on the energy axis (see Fig. 5.8c).

In general a system is calibrated in energy and depth for particular elements from known materials.   However, for a given element of given mass, it is more common to talk of the leading edge on the energy axis and the depth of the rectangle as the energy thickness.   The energy of the leading edge is only dependent upon the material and the energy and type of the incident particles.

There are other problems of interpretation for thin films on a substrate.   For instance, the backscattered signal from a silicon dioxide film contains two peaks: one from the silicon and one from the oxygen content in the film.   However, if this film is grown on a silicon substrate, the signal from the substrate will swamp that part of the silicon signal from the film.   The most common method of eliminating this problem is to effectively channel the α -particles that pass through the film along a particular axis of the crystal substrate.   By aligning the beam along certain orientations, the probability of a scattering event taking place in the substrate is much reduced. In this way, the elemental analysis of thin films on crystalline substrates can be performed.

## 5.2.2 RBS-Experimental Results and Discussion

For the films that were grown for this work, the only measure of the amount of silicon is the gas phase ratio, $R_n$. With the use of backscattering spectrometry, we can convert to the elemental composition of the films. It should be noted that the gas phase ratio is not a translatable parameter between different systems, but the elemental composition is. It is necessary, therefore, to have some absolute measure of the silicon concentration of these films.

The RBS measurements were performed in the Department of Electronic and Electrical Engineering at the University of Surrey. The author is indebted to Dr. C. Jeynes for these measurements and for the discussions of the results.

Figure 5.9 illustrates an example of the measured spectrum for one of the films used for this study. The x-axis in this figure is the energy axis for the spectrum where each channel corresponds to a calibrated energy. The y-axis is called the scattering yield and has units of counts per channel. As can be seen, there are two distinct peaks in the spectrum as expected. The peak at the lower end of the energy axis corresponds to the nitrogen yield and depth, while the higher energy peak corresponds to the silicon yield and depth. The actual calculation of the total amount of silicon and nitrogen in the films is performed by using a computer integration of the peaks shown in Fig. 5.9.

The results are given in Table 5.2. The actual silicon and nitrogen surface concentrations are given along with their relative percentage contributions. In the last column the
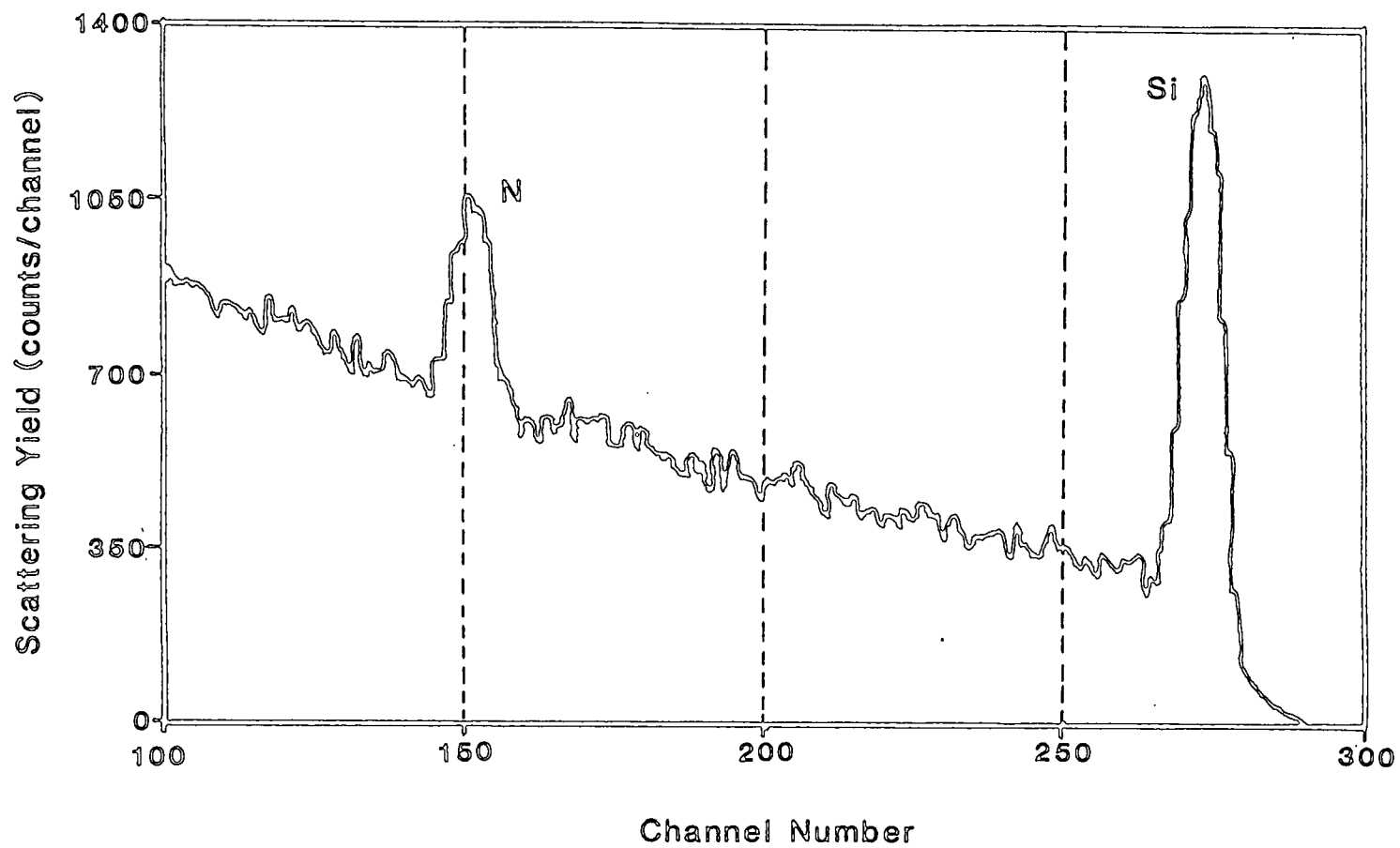
Figure 5.9 Backscattering spectrum from a thin $Si_3N_4$ film with $R_n = 4.0$.

**Table 5.2**   Summary of results from backscattering analysis of silicon-rich $Si_3N_4$ films and system calibration parameters.

| $R_n$ | Si $(cm^{-2})$ | N $(cm^{-2})$ | Si(%) | N(%) | excess Si(%) |
|---|---|---|---|---|---|
| 4.0 | $1.22 \times 10^{17}$ | $1.14 \times 10^{17}$ | 51.68 | 48.31 | 8.84 |
| 1.0 | $1.15 \times 10^{17}$ | $9.78 \times 10^{16}$ | 54.04 | 45.96 | 11.18 |
| 0.5 | $1.05 \times 10^{17}$ | $8.55 \times 10^{16}$ | 55.12 | 44.88 | 12.26 |
| 0.25 | $9.22 \times 10^{16}$ | $7.36 \times 10^{16}$ | 55.61 | 44.39 | 12.75 |

Calibration :   Si    1 count = $1.58 \times 10^{13}$ atoms $cm^{-2}$

N    1 count = $6.23 \times 10^{13}$ atoms $cm^{-2}$

Particle energy = 1.556 MeV

Channel energy = 3.195 keV/channel

Si edge at channel 278

N edge at channel 150

excess amount of silicon, relative to stoichiometric silicon nitride (42.86% silicon), is given. These results illustrate what has been inferred previously, that with decreasing gas phase ratio, the amount of excess silicon in the films increases. The relationship between the gas phase ratio and excess silicon is not linear and appears to be more logarithmic as is shown in Fig. 5.10. The intercept of the line has been extrapolated back for an excess silicon concentration of zero. The gas phase ratio at this point is about 500 and is higher than was expected. Due to the minimum error of +/- 0.5% in the measured value of the excess silicon (indicated by the error bars in Fig. 5.10) and the limited number of points on the curve, the value of $R_n$ to obtain a stoichiometric film is uncertain, although a value very much greater than 50 would be needed. This value is very dependent upon the particular type of reactor used for film growth. These results give a calibration for further growth of similar films for this particular CVD system.
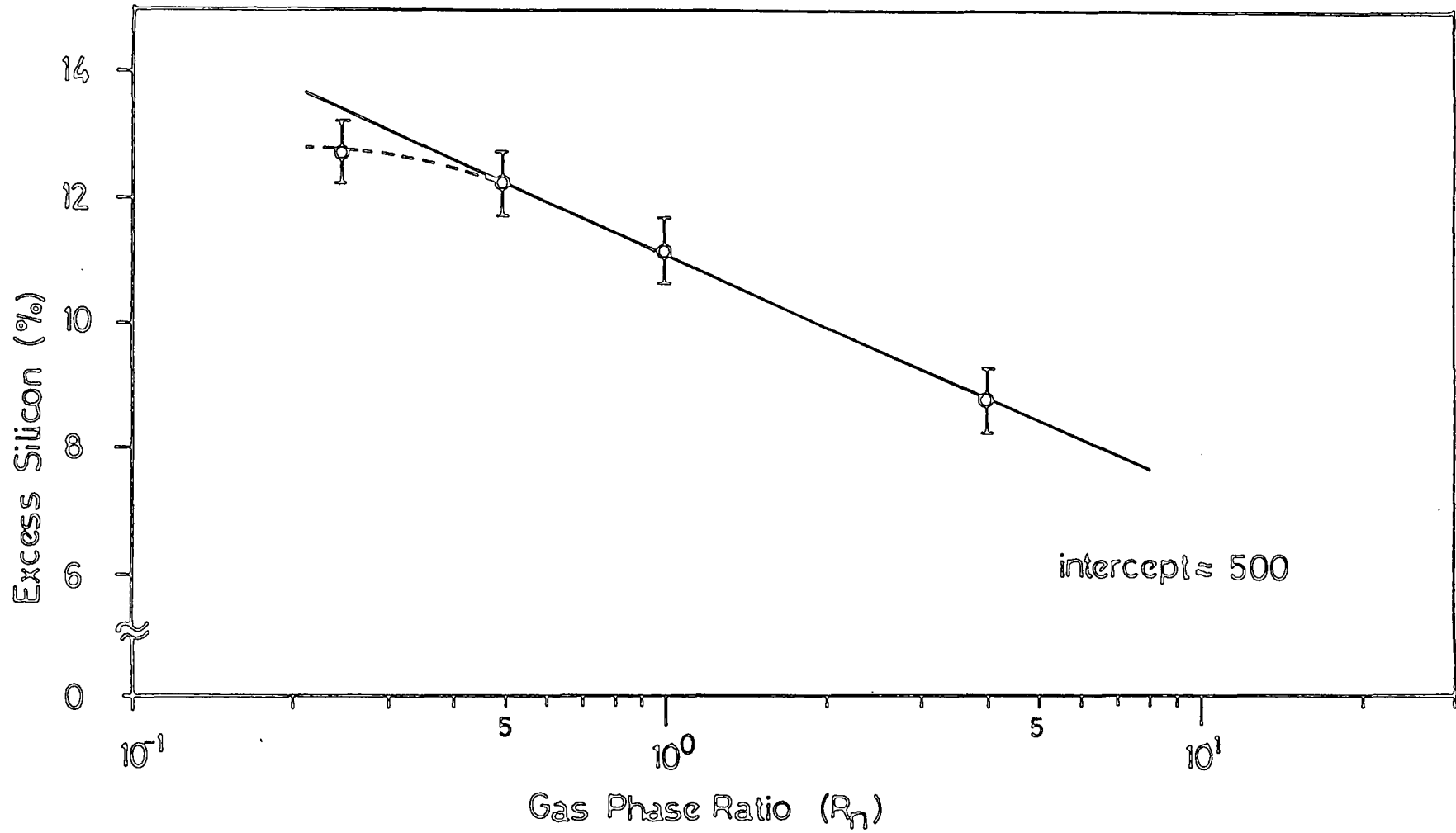
Figure 5.10 Measured excess silicon content (over stoichiometric silicon nitride) as a function of the gas phase ratio, $R_n$ .

# References for Chapter 5

[1]  G.J. Russell,   Prog. Crystal Growth & Charact.,   5,   291 (1982).

[2]  American Society for Testing Materials (ASTM) card index.

[3]  R. Puteh, Ph.D.  Thesis, University of Durham (1984).

[4]  G.J.Russell, private communication.

# Chapter 6
## Electronic Conduction in Silicon-Rich Si N Films
## Experimental Results and Discussion

This chapter is an account of attempts to discover the conduction mechanism(s) in silicon-rich silicon nitride thin films. The intention of this research was to show that the conductivity of these films could be controlled over a large range in a well defined manner with the simple adjustment of the ratio of the reactant gases during deposition. The properties of silicon nitride as a passivating or insulating material are well known in the microelectronics industry and it was for this reason that near stoichiometric silicon nitride was chosen as a starting material.

Many reports [see for example 2-15] on the conduction in stoichiometric $Si_3N_4$ films can be found in the literature, most suggesting Poole-Frenkel emission of trapped carriers is responsible at high electric fields. The literature on silicon-rich $Si_3N_4$ (SRN) films is however much less abundant [17-23]. Some of these authors [22,23] have concentrated on the bonding arrangement and structural assessment of their films rather than the electronic conduction mechanisms. Others [17-21] have presented conduction results for films grown by DC sputtering, glow discharge and plasma enhanced CVD techniques. As it has been found that different deposition techniques give rise to different types of conduction, the analysis of electronic conduction in SRN thin films is not complete.

## 6.1  Current-Voltage Characterization

The characteristics of typical devices were examined using steady-state current-voltage (I-V) and current-voltage-temperature (I-V-T) measurements. Time dependent measurements included current-time (I-t) and capacitance-voltage-time (C-V-t) techniques. The details of these techniques were presented in Chapter 4 and as such will not be repeated here. The steady-state results and discussion are presented in the following sections while transient results will be presented in Chapter 7.

All conduction processes may be described by a number of parameters (eg. resistance, trap depth, density of traps, capture cross-section, relaxation time, etc.). The elucidation of a conduction process from experimental measurement is, therefore not only the determination of the process itself but also the extraction of suitable physical parameters.

Stoichiometric silicon nitride is a well studied material with well known conduction properties. In its most simple form, the current-field relationship for the high field conduction process in silicon nitride is a result of the Poole-Frenkel effect and is given by [1]

$$J = C F \exp \left[ \frac{-1}{kT} \left( \phi_t - \beta_{PF} F^{\frac{1}{2}} \right) \right] \qquad (6.1)$$

where
$$\beta_{PF} = \left( \frac{q^3}{\pi \, \varepsilon_o \, \varepsilon_d} \right)^{\frac{1}{2}}$$

and F is the average electric field strength. $\phi_t$ is the trap depth, $\varepsilon_d$ is the high frequency or dynamic dielectric constant and C is a constant. The analysis presented in this

chapter uses this equation extensively and as such it is appropriate to mention some of its limitations.

It is assumed firstly, for the sake of simplicity, that the trap level is discrete. This may not be an accurate description for silicon nitride. It is quite feasible that conduction could occur as a result of trapped carrier emission from band tail states, which arise from the amorphous nature of these films, into the conduction band. It is equally feasible, however, that conduction could occur by virtue of emission of trapped carriers from deeper states, further away from the band edge. From experimental evidence, Sze [2] showed the trap depth for stoichiometric $Si_3N_4$ to be about 1.5 eV from the band edge. Such a large value suggests that conduction is due to emission of trapped carriers from relatively deep states into either the conduction band or band tail states. It is still feasible, however, that the measured trap depth could be an average of a range of trap energies. In this case conduction occurs through a narrow band of states or a number of closely packed discrete states.

It is also necessary to decide whether the conduction is due to the movement of electrons, holes or both. For stoichiometric nitrides. a great many authors [3-13] have reported different techniques for separating electron and hole currents through insulating films and for silicon nitride in particular. However. the picture still remains unclear. Reasonable arguments have been published supporting almost all permutations of electron. hole, or electron and hole conduction for both polarities. In the first instance, for this work, it

is assumed that a single carrier conduction exists and that the dominant species is electrons.

The last and probably the most significant limitation of this simple analysis is its exclusion of trapped space charge. It is generally accepted that conduction in stoichiometric silicon nitride is bulk limited. For any bulk limited conduction, space charge exists near the injecting contact to equalize the injected and bulk currents. This charge perturbs the local electric field at the contact. If the space charge extends through a significant proportion of the film thickness, the electric field within the insulator may no longer be considered constant.

Neglecting space charge the electric field, F, in equation 6.1. is the average electric field. given by

$$F = V_i / d_i \qquad (6.2)$$

where $V_i$ and $d_i$ are the voltage drop across and the thickness of the insulating layer respectively. Equation 6.2 does not take into account any effects of the silicon substrate or of the metal-semiconductor work function difference. For this MIS structure with aluminium as the metal and an n-type silicon substrate. the work function difference is very small and may be neglected. In forward bias (positive on the metal with respect to the substrate) the silicon is in accumulation and the surface potential is very small. In reverse bias however, a depletion region is formed at the silicon surface and the surface potential may become significant. The reverse bias case will be treated separately, but to begin the analysis it will be assumed that equations 6.1 and 6.2 are valid. The influence of space

78

charge on the characteristics will be discussed in more detail in the Chapter 7.

## 6.2 Experimental Results

Figures 6.1 (a) and 6.1 (b) show the current density as a function of the square root of the average electric field (Schottky plots) for a range of gas phase ratios for positive and negative polarities respectively. Each set of data represents an average of at least five different devices of the same film (i.e. from the same wafer). The currents plotted are the steady-state values obtained by the method described in Chapter 4. The characteristics shown here are from wafers 3, 5, and 7 for $R_n$ = 4.0, 1.0 and 0.5 respectively (see Table 4.1). All of these films are approximately 300 Å thick.

A number of features are immediately obvious from these characteristics. Firstly, the current for a given electric field increases with decreasing gas phase ratio (i.e. increasing silicon content) of the films. Secondly, at least for the positive polarity (Fig. 6.1a), the curves are 'linear' in the high field region. For the negative polarity (Fig. 6.1b), at high fields, F · 3.0 MV cm. the curves become non-linear.

All these films were grown on n-type silicon substrates with resistivities of 0.5 ohm-cm. The average electric field, for the data shown in Figs. 6.1 (a) and (b), was calculated assuming that the applied potential was dropped solely across the insulator. For positive bias, no depletion region is formed as the device is in accumulation and as such, only a very small
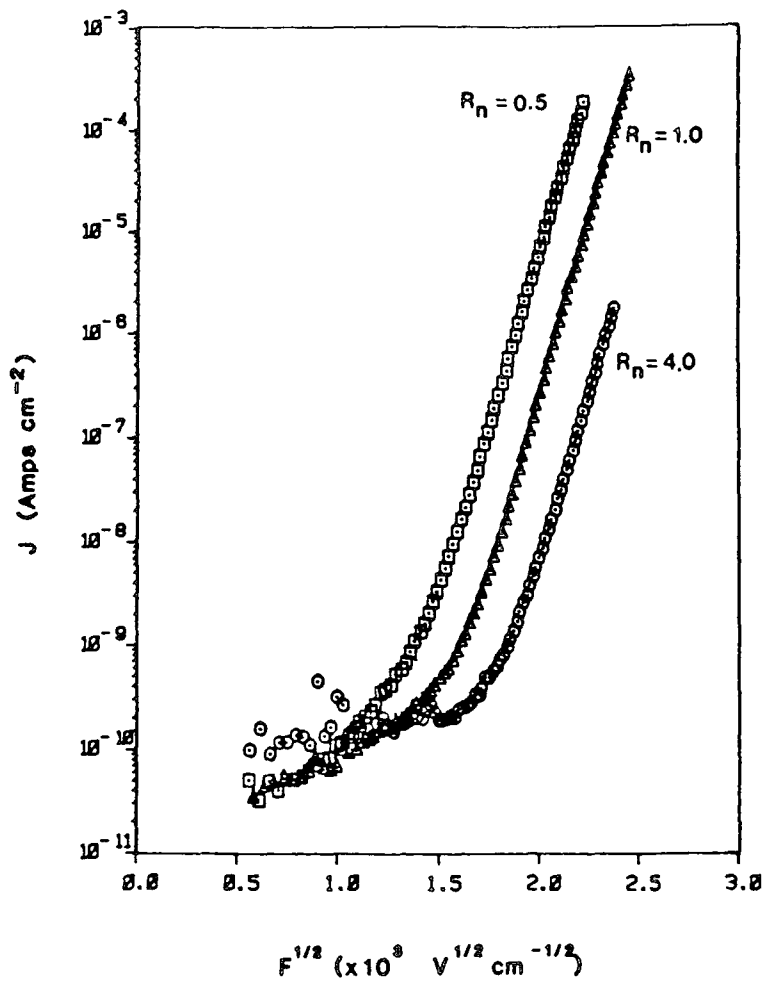
(a)
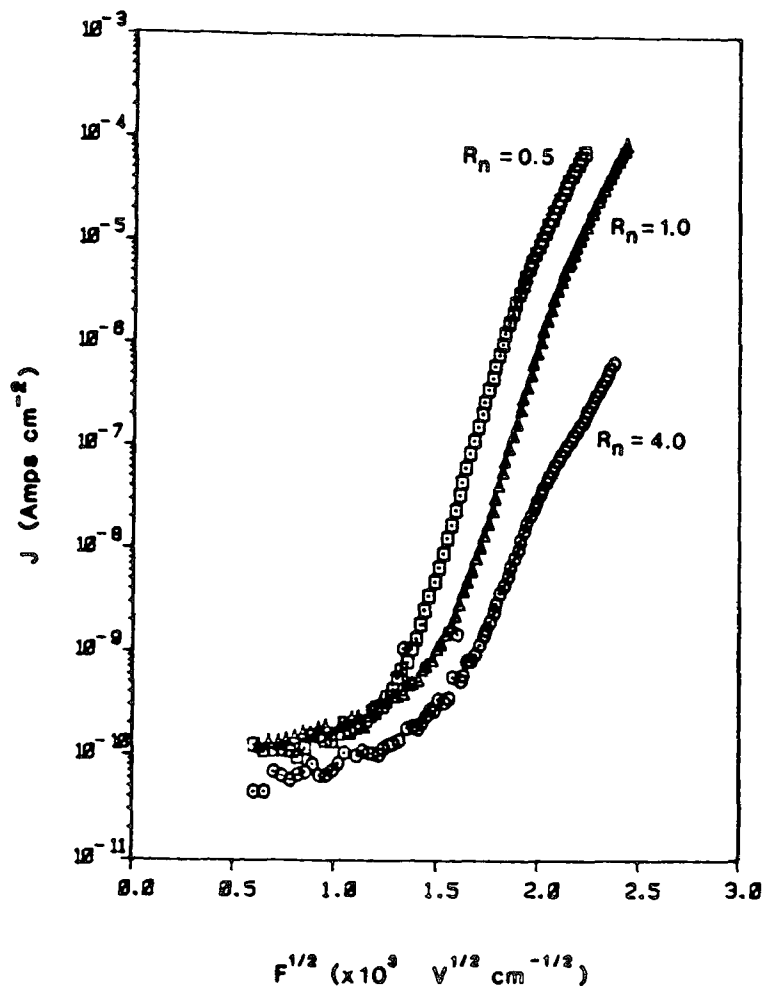


(b)

Figure 6.1    Current density field characteristics over a range of gas phase ratios, $R_n$, for a) positive polarity and b) negative polarity. $T = 300$ K.

proportion of the applied potential is dropped across the silicon. However, the characteristics shown in Fig. 6.1 (b) demonstrate that for high negative electric fields there a substantial proportion of the applied potential is dropped across the depletion region in the silicon.

Figure 6.2 shows an example of an Arrhenius plot, current density versus reciprocal temperature, (J vs 1/T), for a film of gas phase ratios $R_n$ = 1.0. The curves are for three values of electric field. Figures 6.2 (a) and 6.2 (b) are for positive and negative polarities respectively.

## 6.3 Parameter Extraction

The main film parameters of interest in this work are the trap depth, $\phi_t$ , the dynamic dielectric constant, $\varepsilon_d$ . and the pre-exponential constant, C (see equation 6.1). Assuming that equations 6.1 and 6.2 are valid, the extraction of the aforementioned parameters is straightforward.

By re-arranging equation 6.1, to give

$$\ln\left(\frac{J}{F}\right) = \ln(C) - \frac{\phi_t}{kT} + \frac{1}{kT}\left[\left(\frac{q^3}{\pi\varepsilon_o\varepsilon_d}\right)^{\frac{1}{2}} F^{\frac{1}{2}}\right] \qquad (6.3)$$

and by plotting $\ln(J/F)$ versus $F^{\frac{1}{2}}$ . the gradient is given by

$$gradient = \frac{1}{kT}\left(\frac{q^3}{\pi\varepsilon_o\varepsilon_d}\right)^{\frac{1}{2}} = \frac{\beta_{PF}}{kT} \qquad (6.4)$$

From the gradient, the dynamic dielectric constant is determined. In a different form, equation 6.1 becomes
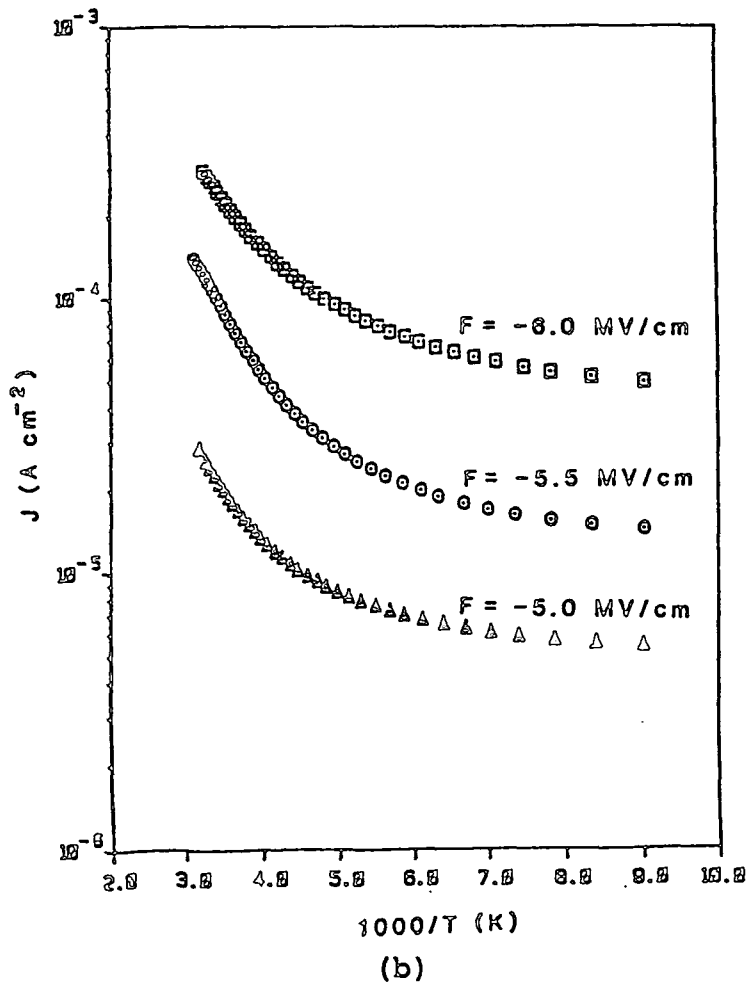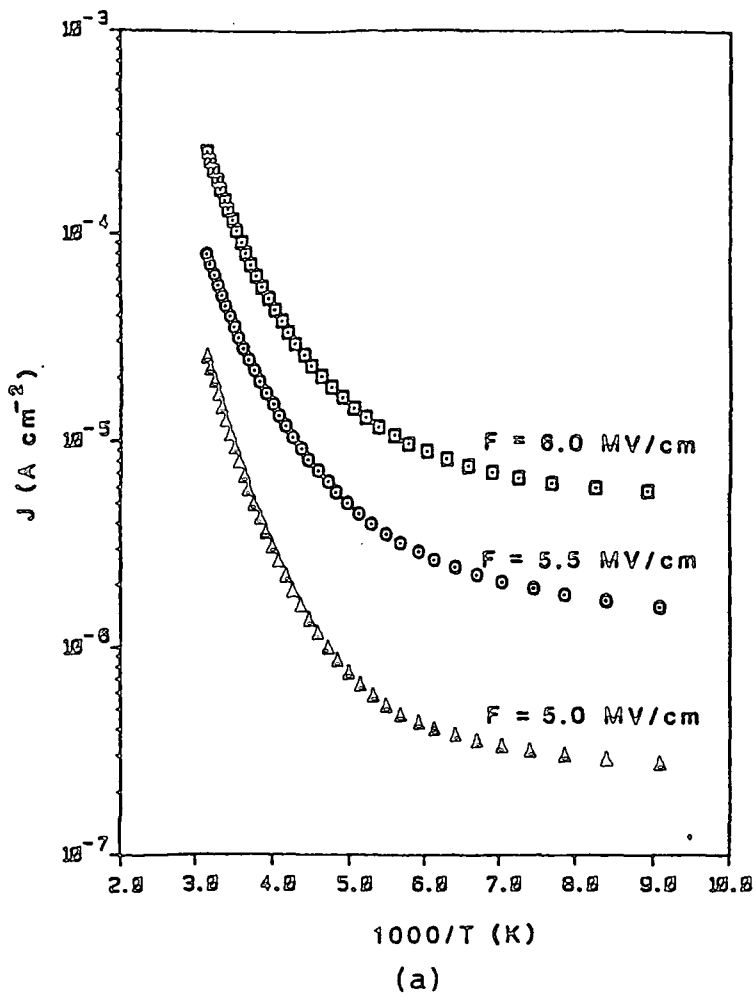
80

**Figure 6.2** Current density versus 1/T over a range of electric fields for a) positive polarity and b) negative polarity. $R_n = 1.0$.

$$\ln(J) = \frac{1}{kT} \left( -\phi_t + \beta_{PF} F^{\frac{1}{2}} \right) + \ln(CF) \qquad (6.5)$$

By plotting $\ln(J)$ versus $1/T$, an Arrhenius plot, the gradient is given by

$$\text{gradient} = \frac{1}{k} \left( -\phi_t + \beta_{PF} F^{\frac{1}{2}} \right) \qquad (6.6)$$

Given the dynamic dielectric constant, the trap depth can be determined from the gradient in equation 6.6. Once both the trap depth and dielectric constant are known, the pre-exponential constant, C, can be determined from equation 6.3.

In some work elsewhere [2-6] $\epsilon_d$ has been extracted from the slope of a Schottky plot, $\ln(J)$ vs $F^{\frac{1}{2}}$. This technique is based on the assumption that the exponential dependence of the current upon the field dominates over the pre-exponential factor. This, of course, introduces an element of error.

From an in-depth analysis of Poole-Frenkel conduction, Hill [16] (see section 3.4) showed the pre-exponential factor to be

$$q \, N_i \, \mu_1 \, (kT)^2 \, F \qquad (6.7)$$

for a crystalline material and

$$q \, N_i \, \mu_2 \, (kT)^2 \, F^{\frac{1}{2}} \qquad (6.8)$$

for an amorphous material. This analysis is based on a one dimensional model with only the emission in the direction of the field considered as contributing to the current. Clearly, if one were to assume the crystalline case to be the more accurate, a plot of $\ln(J/F)$ vs $F^{\frac{1}{2}}$ would determine the parameters needed. However, if the amorphous case is assumed, a plot of $\ln(J/F^{\frac{1}{2}})$ vs $F^{\frac{1}{2}}$ would be more appropriate. In the present analysis, all

Table 6.1    Parameters extracted from current-field and current-field-temperature data.

| $R_n$ | $\ln(J)$ vs $F^{\frac{1}{2}}$ | | $\ln(J/F^{\frac{1}{2}})$ vs $F^{\frac{1}{2}}$ | | | $\ln(J/F)$ vs $F^{\frac{1}{2}}$ | | |
|---|---|---|---|---|---|---|---|---|
| | $\varepsilon_d$ | $\phi_t$ (eV) | $\varepsilon_d$ | $\phi_t$ (eV) | C (A cm$^{-3/2}$ V$^{-\frac{1}{2}}$) | $\varepsilon_d$ | $\phi_t$ (eV) | C (A cm$^{-1}$ V$^{-1}$) |
| 4.0 | $3.43 \pm 0.02$ | 1.15 | $3.62 \pm 0.04$ | 1.13 | $3.3 \times 10^{-6}$ | $3.81 \pm 0.03$ | 1.11 | $1.6 \times 10^{-9}$ |
| 1.0 | $3.64 \pm 0.05$ | 1.15 | $3.75 \pm 0.08$ | 1.11 | $3.3 \times 10^{-5}$ | $4.26 \pm 0.08$ | 1.08 | $1.6 \times 10^{-8}$ |
| 0.5 | $3.71 \pm 0.07$ | 1.08 | $4.04 \pm 0.15$ | 1.04 | $7.5 \times 10^{-5}$ | $4.27 \pm 0.12$ | 1.01 | $3.2 \times 10^{-8}$ |

three methods of parameter extraction (i.e. $\ln(J)$ vs $F^{\frac{1}{2}}$, $\ln(J/F^{\frac{1}{2}})$ vs $F^{1/2}$ and $\ln(J/F)$ vs $F^{\frac{1}{2}}$) were used to show the uncertainty and experimental error in the values of the $\phi_t$, $\varepsilon_d$ and C.

The pre-exponential constant, C, is a strong function of temperature (i.e. $C \propto T^2$) and as such the intercept of the constant temperature plot (i.e. $J$ vs $F^{\frac{1}{2}}$) and not the Arrhenius plot, was used to determine its value.

Table 6.1 shows the values of the parameters extracted for the data presented previously. Each value shown represents not only an average of many devices from the same wafer, but also an average of all the wafers with that particular gas phase ratio. The errors quoted for $\varepsilon_d$ in each case represent the mean square error derived from a minimum sampling of five different devices. For $\phi_t$, however, the error values from the mean squares technique are less than 1%. It is believed that this is not a true measure of these errors because the trap depth is determined using the extracted values of $\varepsilon_d$. and as such one would normally expect the errors to become larger for $\phi_t$ than for $\varepsilon_d$. However, the factor $\beta_{PF}$. contains a square root and this tends to suppress the calculated errors. Therefore, we surmise that the actual errors in $\phi_t$ and likewise the errors in C are greater than 1% but probably less than 5%.

The parameters shown are calculated from the positive polarity curves, but the negative polarity parameters show approximately the same features once the effect of the silicon depletion region is taken into account. Due to the limited data on n+ substrates, it was decided to use the positive polarity

parameters to demonstrate the features of our films. A number of trends are immediately obvious from the data presented in Table 6.1.

### 6.3.1 Calculated Dielectric Constant

The dielectric constant increases with increasing silicon content (i.e. decreasing gas phase ratio). For stoichiometric nitrides, the optical dielectric constant is about 4 and the static dielectric constant is about 7 [2]. The measured dynamic dielectric constant of a stoichiometric nitride should therefore be somewhere between these values. Within the context of this work, a stoichiometric silicon nitride results from films grown where $R_n$ › 50. The static dielectric constant of crystalline silicon is about 12 and is the absolute upper limit for silicon rich films. For the least silicon-rich film ($R_n$ =4.0), $\varepsilon_d$ is less than 4.0, and is therefore. lower than expected. One possible explanation for the low measured values is that most of these films are relatively thin (i.e. a few 100 $\overset{\circ}{A}$) and any space charge from the injected carriers will have a pronounced effect on the electric field and subsequently the slope of the Schottky plot and therefore $\varepsilon_d$. If we consider electron injection from the silicon under positive bias. the electric field at the silicon-silicon-nitride interface is increased. Therefore at a given current. the actual average' electric field is somewhat higher than expected. Assuming the total trapped charge increases with increasing current, the curve of $\ln(J)$ vs $F^{\frac{1}{2}}$ therefore has a higher slope and a subsequently lower dynamic dielectric constant than an ideal device with no

trapped charge. A more rigorous discussion of the effects of space charge on the value of $\varepsilon_d$ is presented in the Chapter 7.

In addition to the space charge arising due to trapped charge, there may be space charge that arises from compensating acceptors. Equation 6.1 is derived from a very simplistic three dimensional model. The exponential factor, $\beta_{PF}$, is very dependent upon the degree of compensation (see section 3.4). It is therefore possible that $\varepsilon_d$ could be a factor of as much as four depending on the degree of compensation assumed so that the values of $\varepsilon_d$ presented here are quite acceptable.

It is obvious from Table 6.1, that the parameter extraction technique does have a pronounced effect on at least the value of $\varepsilon_d$. It is not possible to say with certainty which are the correct values but one can be certain that the pre-exponential factor cannot be ignored. The films used in this work are surely not crystalline and as such the values taken from the $\ln(J/F^{\frac{1}{2}})$ vs $F^{\frac{1}{2}}$ curves are taken to yield the most correct results. However, the effects of space charge could have a more pronounced effect on the value of $\varepsilon_d$ than the relatively small errors produced by these extraction techniques.

## 6.3.2 Calculated Trap Depth

Within experimental error, the extraction technique seems to have little effect on the calculated trap depth. There is however, a small decrease in the trap depth with increasing silicon content. Lowe et al [17] reported a similar trend for plasma deposited hydrogenated silicon-nitride films ($SiN_x:H$). Their results however, were for much higher $R_n$ values and the

change in trap depth was much greater than that noted here. The growth technique that Lowe et al used for their films is distinctly different from that used for the present films and as such the comparison between characteristics should be treated with care.

### 6.3.3  Calculated Parameter C

From the $\ln(J)$ vs $F^{\frac{1}{2}}$ plots, it is not possible to extract the value of the constant, C, directly. In Table 6.2, the value of C is translated into Hill's [16] 'disposable parameter', $N_i \mu_1$ and $N_i \mu_2$ for the one dimensional crystalline and amorphous cases respectively. The parameter $N_i$ is directly related to the density of defect states and has units of $cm^{-3} eV^{-2}$. The parameter $\mu_1$ is the 'effective' conduction band mobility for a crystalline material. On the other hand, $\mu_2$ is not a mobility and has units of $cm^{-3/2} cm^{-\frac{1}{2}} s^{-1}$, and as such the parameters $N_i \mu_1$ and $N_i \mu_2$ do not have the same units. The values for crystalline and amorphous materials are therefore not directly comparable.

Table 6.1 shows the value of C rises as $R_n$ falls If we assume that the values of $\mu_1$ and/or $\mu_2$ do not change significantly (i.e. by more than an order of magnitude) from a material of $R_n = 4.0$ to $R_n = 0.5$, the increase in C must be due to an increase in the density of defects. The change in $R_n$ reflects the increasing silicon content. We may surmise that the increase in conductivity with decreasing $R_n$ and increasing silicon content is due to a substantial increase in density of defect states.

## 6.3.4 Hill's Method of Analysis

Following further in Hill's footsteps, the data shown previously was plotted on a 'Hill plot'. The equation for such a plot was given in equation 3.28. The example shown in Fig. 6.3 is for data for both constant electric field and constant temperature (i.e. from Figs. 6.1 and 6.2). The solid curve represents a least squares fit to the data using $\phi_t$ =1.0 eV and $N_i\mu_2$ and $\varepsilon_d$ as variable parameters in Hill's one dimensional amorphous model (see section 3.4). It should be noted that the value of $\phi_t$ =1.0 eV was used throughout this analysis. The inset of Fig. 6.3 shows the variation of $\varepsilon_d$ (from the least squares fit) with increasing $\phi_t$ . The value of $N_i\mu_2$ did not change appreciably with similar changes in $\phi_t$ . Table 6.2 gives the values of $N_i\mu_1$ and $N_i\mu_2$ from this method and Table 6.3 gives a comparison between Hill's analysis and previous parameter extraction techniques.

This method of analysis gives higher and more reasonable values for the calculated dielectric constant. It also shows the same trends (i.e. increasing $\varepsilon_d$ and $N_i\mu_2$ with decreasing $R_n$ ) as the other methods. However, even though the values of $\varepsilon_d$ for $R_n$ =0.5 are probably accurate, for the higher $R_n$ values the dielectric constant is likely to be lower than that quoted in Table 6.3. For all values of $R_n$ , the 3-D model shows a closer agreement with the original analysis than the 1-D model, but one must remember that the degree of compensation is still unknown. All of the calculated parameters from the original analysis are interdependent and therefore dependent upon the degree of compensation chosen. As a final point, with the risk
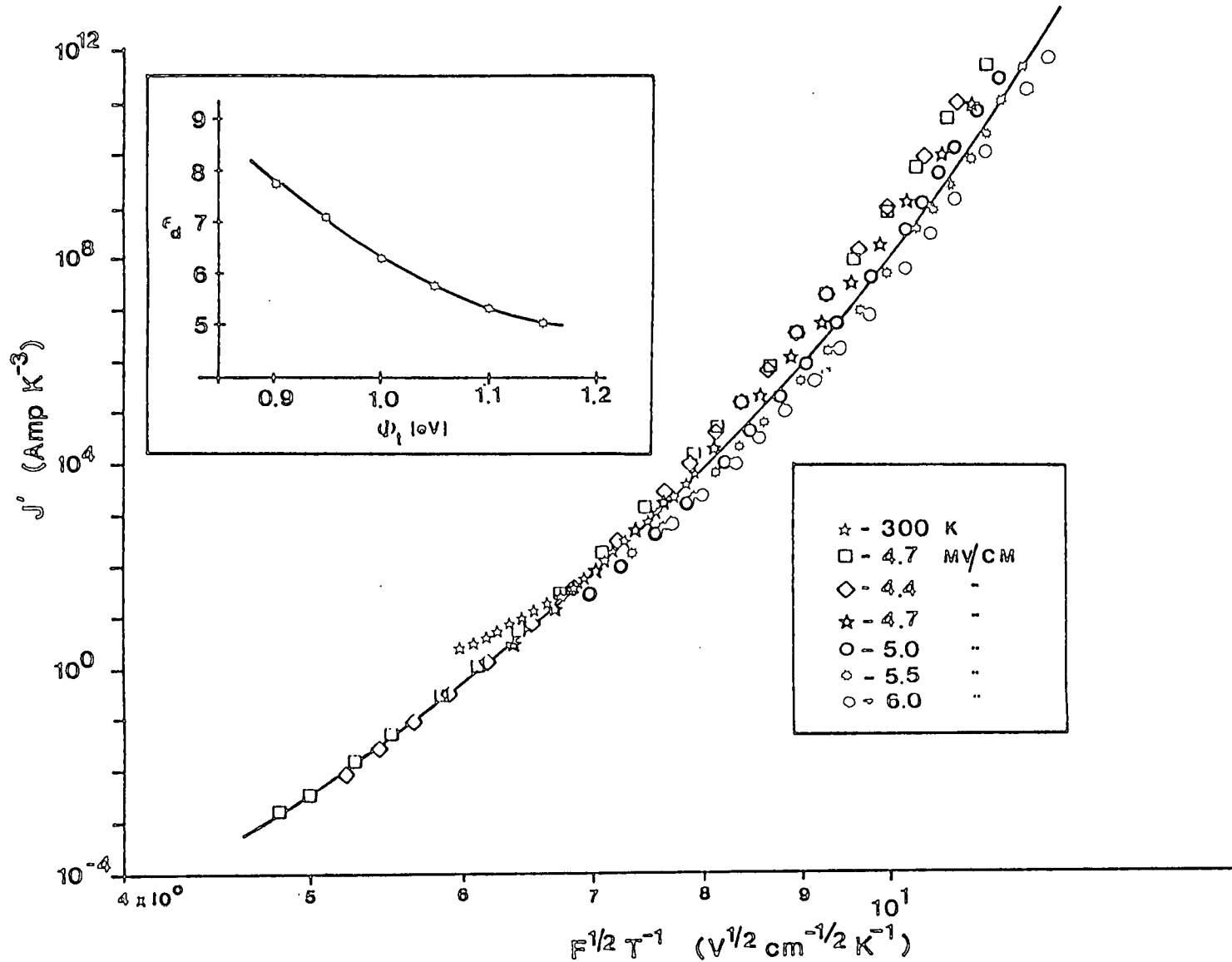
86

Figure 6.3    A one dimensional, reduced field Hill [16] plot. $J' = JT^{-3}\exp(\bar{q}\phi_t/kT)$ versus $F^{1/2}/T$.  Inset shows dependence of calculated dielectric constant upon trap depth.

Table 6.2     Hill's 'disposable' parameter calculated from current field and current field temperature data for amorphous and crystalline films.

| $R_n$ | Amorphous $N_i \mu_2$ | Crystalline $N_i \mu_1$ |
|---|---|---|
| 4.0 | $3.1 \times 10^{16}$ | $1.5 \times 10^{13}$ |
| 1.0 | $3.1 \times 10^{17}$ | $1.6 \times 10^{14}$ |
| 0.5 | $7.7 \times 10^{19}$ | $2.4 \times 10^{16}$ |

Table 6.3     Comparison of extracted data from Schottky and Arrhenius plot and Hill's [16] 1-D and 3-D amorphous models.

| $R_n$ | $J/F^{\frac{1}{2}}$ vs $F^{\frac{1}{2}}$ | | 1-D Model | | 3-D Model | |
|---|---|---|---|---|---|---|
| | $\varepsilon_d$ | $N_i \mu_2$ | $\varepsilon_d$ | $N_i \mu_2$ | $\varepsilon_d$ | $N_i \mu_2$ |
| 4.0 | 3.62 | $3.1 \times 10^{16}$ | 6.6 | $2 \times 10^{13}$ | 6.3 | $3 \times 10^{14}$ |
| 1.0 | 3.75 | $3.1 \times 10^{17}$ | 6.9 | $5 \times 10^{15}$ | 6.6 | $7 \times 10^{16}$ |
| 0.5 | 4.04 | $7.7 \times 10^{19}$ | 7.0 | $9 \times 10^{16}$ | 6.7 | $1 \times 10^{18}$ |

of repetition, none of Hill's models account for any trapped space charge and as such even these values may still be in error.

In summary of Tables 6.1, 6.2 and 6.3 with increasing silicon content, the trap depth decreases slightly ( i.e. shifts towards the band edge), and both the dynamic dielectric constant and the density of traps appears to increase. The different extraction techniques only affect the value of the calculated dynamic dielectric constant. Of the original extraction methods, the $\ln(J/F^{\frac{1}{2}})$ vs $F^{\frac{1}{2}}$ technique yields the most relevant results as the films have been shown to be amorphous or at most microcrystalline. However, the calculated dielectric constant is still somewhat lower than expected. Using Hill's [16] techniques for parameter extraction, higher and more reasonable values of $\varepsilon_d$ are obtained.

## 6.4 Polarity and Thickness Dependence

Normally, if the conduction of a material is bulk limited, it shows neither a polarity dependence nor a thickness dependence. However, it is possible to have a device containing a material that under differing circumstances may show the properties of either bulk or contact limited conduction.

Figures 6.4 (a) and (b) show Schottky plots for films with $R_n$ = 0.5 for both positive and negative polarities for film thicknesses d ~ 200 Å and d ~ 1550 Å respectively. These films were grown on n+ silicon substrates with resistivities of approximately 0.02 ohm-cm. Neither films show the high negative field, non-linear characteristic apparent in the previously

87
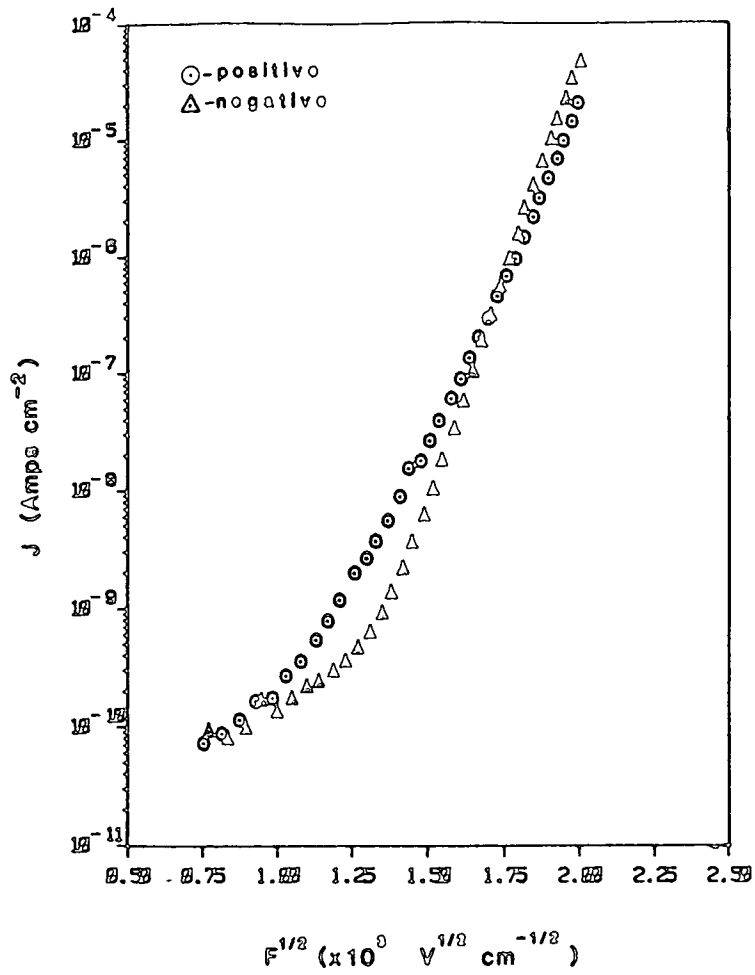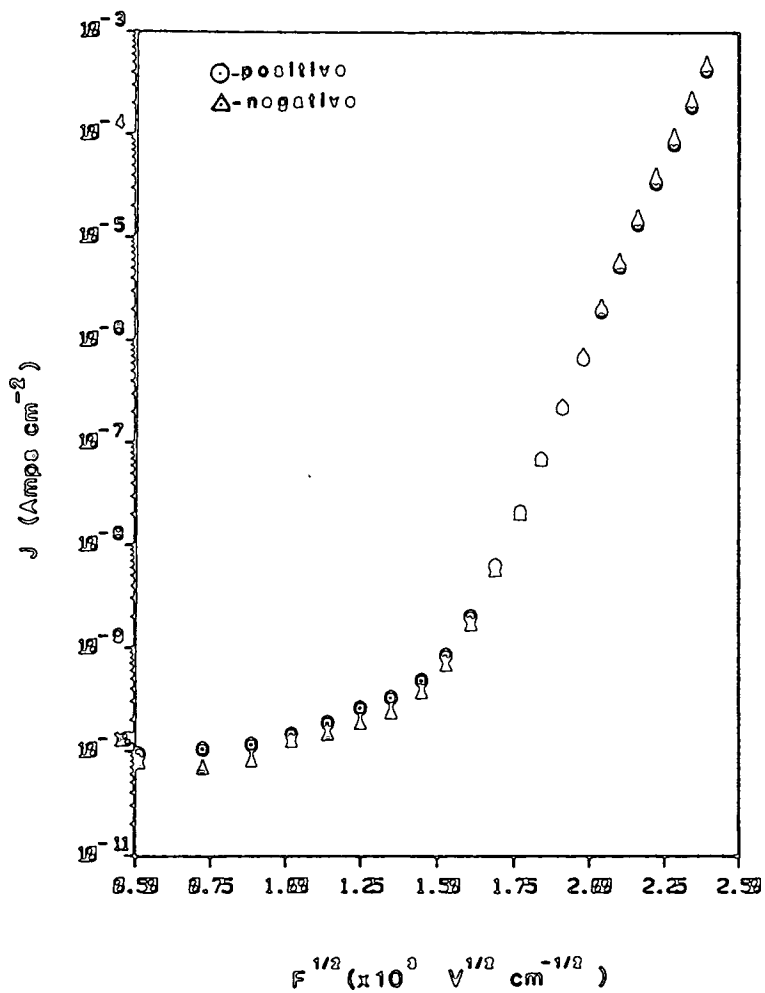
Figure 6.4 Positive and negative polarity current field
characteristic. Films thickness are a)
d ≈ 200 Å and b) d ≈ 1550 Å.

presented films. There is however, a distinct difference between the shape and slope of the positive and negative curves for the thinner of the two films.

Sullivan and Card [14] suggested that a polarity dependence in stoichiometric $Si_3N_4$ may be due to space charge arising from the nature of the injected carriers. If the dominant species responsible for conduction varies under different bias conditions (i.e. polarity), a change in the net space charge results. Subsequently the local perturbation of the electric field near the injecting contact or contacts is also dissimilar giving rise to a polarity dependent current-field characteristic.

It is interesting to note, however, that the polarity dependence disappears for thicker films. As the film thickness increases, assuming the space charge remains near the injecting contact, the relative proportion of the film directly affected by the space charge decreases. Yun [15] reported that the charge centroid, $\overline{X}$, for trapped charge from an injecting contact for stoichiometric silicon nitride, was on the order of 100 $\overset{\circ}{A}$, measured from the contact. If this estimate for $\overline{X}$ was true for our films also, the centroid for the thinner of the two (Fig. 6.4a), would be approximately halfway through the film. The effect of this charge on the average electric field would be substantial and near its maximum. For the thicker film (Fig. 6.4b), the same centroid would place the space charge near to the injecting contact and its effects would only be 'felt' over about 15% of the film thickness as opposed to nearly 100% for the thinner film. The effect on the average electric field

is therefore substantially reduced by increasing the film thickness.

Figure 6.5 (a) shows the positive polarity current density-electric field characteristic from wafers 12 and 10 with gas phase ratios of $R_n = 0.5$ and $R_n = 0.25$ respectively. These films are approximately 200 Å thick. These curves are also very linear in the high field regions. However, when the positive polarity characteristics of films of a constant gas phase ratio but marginally different thickness are compared as in Fig. 6.5 (b), a distinction between the slopes is noted. Assuming the films are compositionally alike, the variation in the slopes must be due to the effect of trapped space charge on the very thin films. Even a small change in the thickness produces a pronounced effect.

### 6.5 Electronic Conduction at Low Temperatures

The current in the low temperature regime is approximately temperature independent for all electric field strengths and gas phase ratios as shown in Fig. 6.2. It has been suggested [1.2] that this current is due to trapped electrons tunnelling directly into the conduction band. If this tunnelling was at all thermally assisted, the Arrhenius plot would not show a distinctly temperature independent region as shown in Fig. 6.2. A series of Fowler-Nordheim plots, (J vs 1/F) are given in Fig. 6.6 for films of three different $R_n$ values for both positive and negative polarities at a temperature of 85 K. The relatively straight curves suggest that the conduction in this region is due to field emission of trapped carriers into the conduction
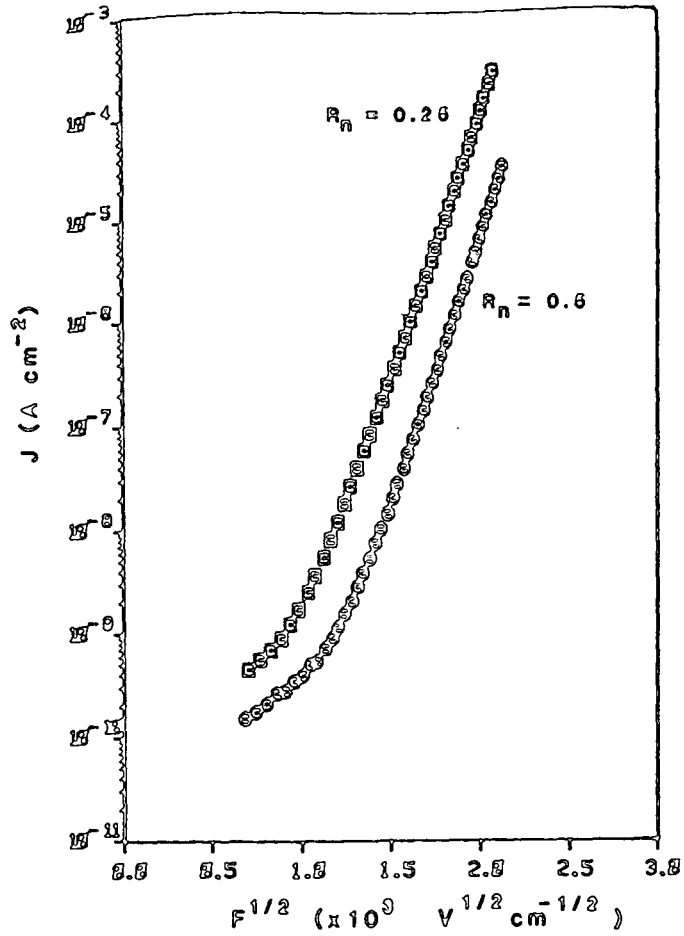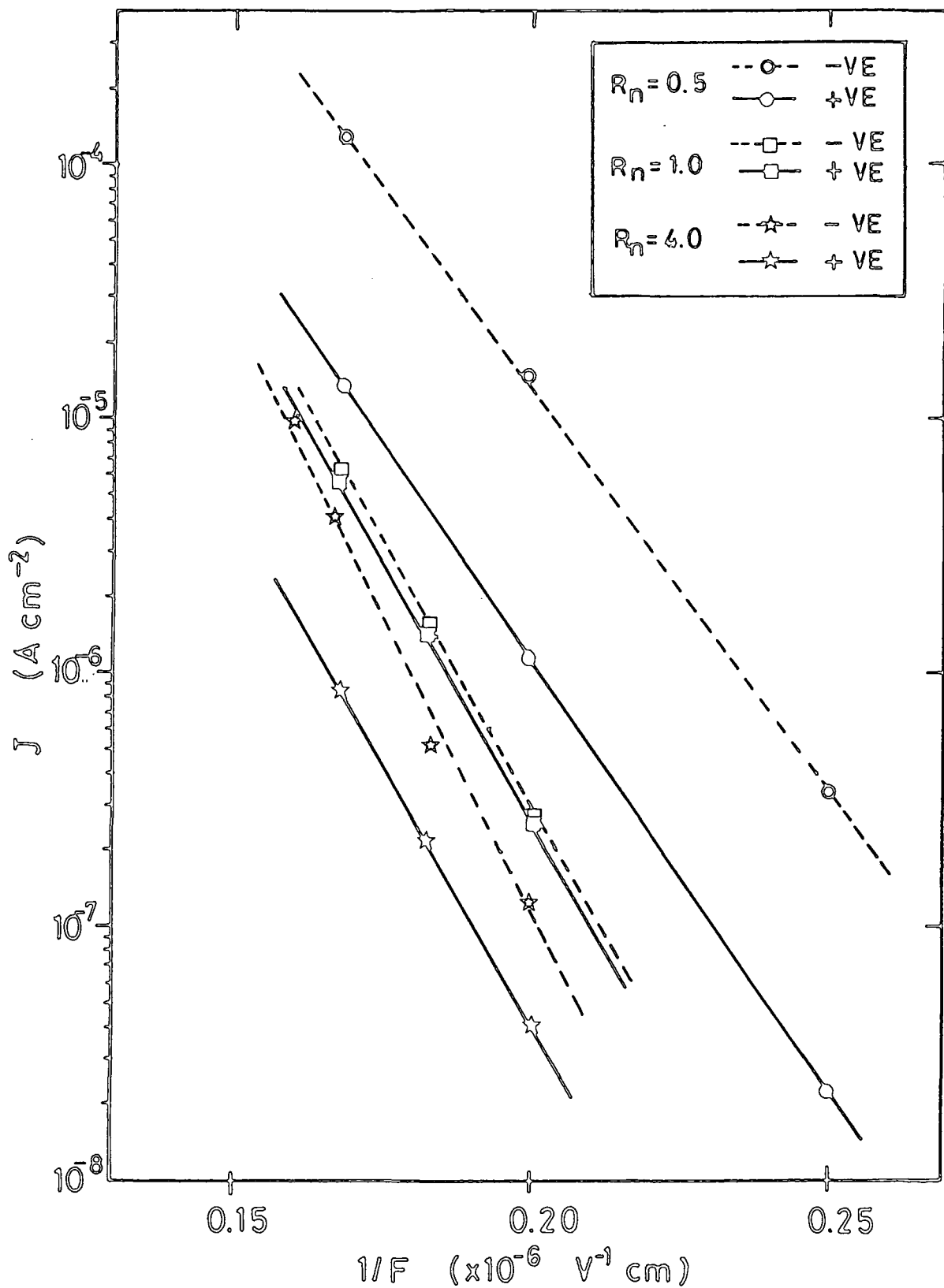
(a)
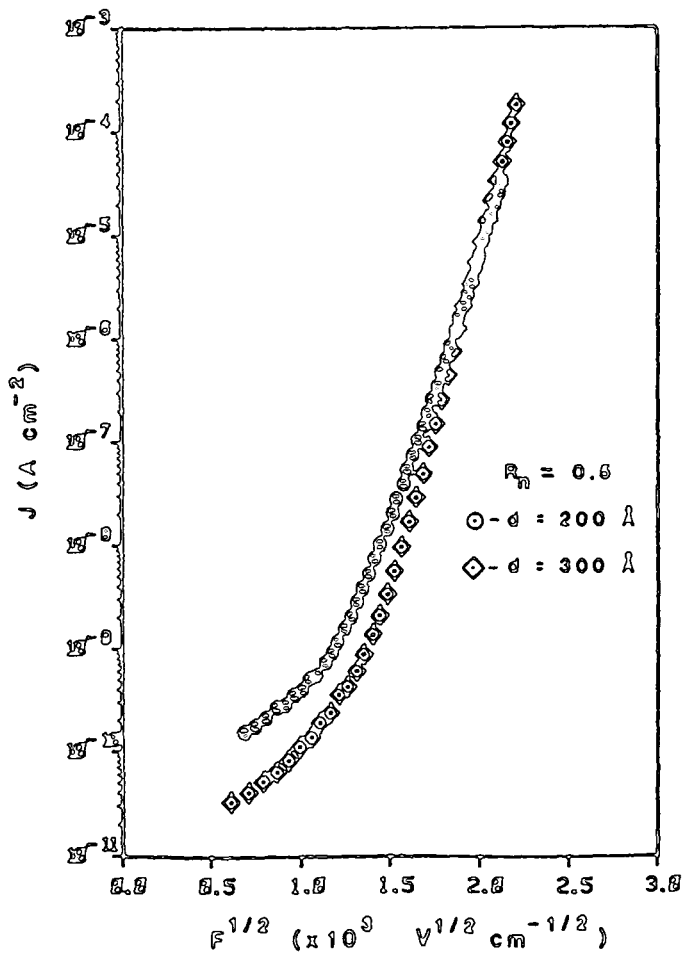


(b)

Figure 6.5   Positive current field characteristic for the thinnest films for two values of $R_n$. In a) both films are of a thickness d ≈ 200 Å and b) shows the thickness dependence for thinnest films.

**Figure 6.6** Current density versus 1/F (Fowler-Nordheim) for positive and negative polarities for films of three gas phase ratios. T = 85 K.

band or band tails. Equation 3.7 gave an expression for the current due to Fowler-Nordheim emission. The gradients of the curves in Fig. 6.6 are functions of the effective mass of the charge carriers and the effective barrier height. As neither of these is known for these films it is not possible to calculate the other. If however, a 1 eV barrier height is assumed, the effective mass is found to be of the order 0.011 +/- 0.001 for these films. The constant of proportionality (i.e. the pre-exponential term in equation 3.7) is inversely proportional to this effective barrier height which gives the lowest barrier height for the film with the greatest silicon content. This is consistent with the results obtained from the parameter extraction and implies a decreasing barrier height with increasing silicon content.

## 6.6 Annealing Effects

The growth conditions of the films from wafers 9 and 11 (see Table 4.1) were identical to those of wafers 10 and 12 respectively, except that the former two films were annealed in nitrogen for one hour at $1000^{\circ}C$. Figure 6.7 shows a Schottky plot of each of these films for a positive polarity electric field. It can be easily seen, within the realms of experimental error, that there is little or no difference between the characteristics. It was found from the RHEED analysis presented in Chapter 5, that the size of the silicon crystallites in the SRN film decreased with annealing. As the annealed and unannealed films show essentially the same characteristics, it is concluded that the electronic conduction in these films is
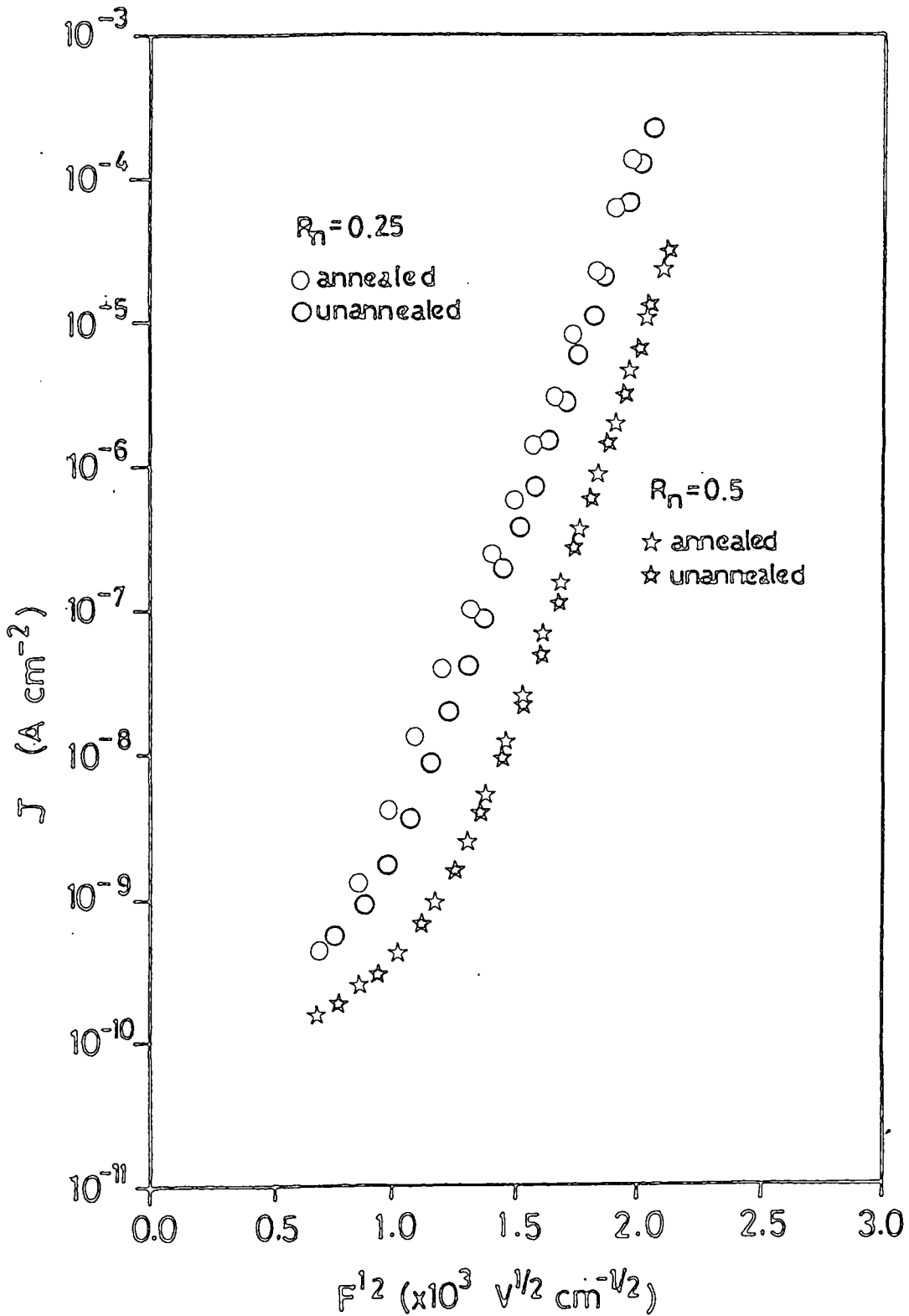
**Figure 6.7**    Positive polarity current density field characteristics for two values of $R_n$ for annealed and unannealed films.

not dependent upon the size of crystallites.

## 6.7  Other SRN Films

It has been reported [18,19] that large variations in current-field characteristics result when growing the same material using different techniques. Figure 6.8 compares the conductivity of the $Si_3N_4$ films used here with that reported elsewhere for different growth techniques. The films grown for the present work (solid line) and the films of Watanabe et al [19] (single double dashed line) were both grown using a low pressure CVD technique with $NH_3$ and $SiH_2Cl_2$ as the reactant gases. The films of Kobayashi [18] were grown using an atmospheric CVD process with $SiH_4$ and $NH_3$ as the reactant gases. The reactant temperature for all these films was about $750^{\circ}C$. It can be seen that there is a large difference in the conductivity of these films. Watanabe claims that his films were nitrogen rich, based on infrared absorption measurements. He also claimed that the nature of his films did not change appreciably with reactant temperature and gas phase ratio. $R_n$, which is somewhat difficult to believe. The slopes and magnitude of the Schottky plots of the films of Watanabe et al seem to fit well with the present work. For our films, we suggested that a value of at least $R_n \cdot 50$ would be needed for stoichiometric nitrides, yet using the same growth technique and an $R_n = 30$, Watanabe claims his films to be nitrogen rich. This suggests either that even films grown under the same conditions but using different apparatus have different conduction characteristics or that Watanabe's films are not as nitrogen
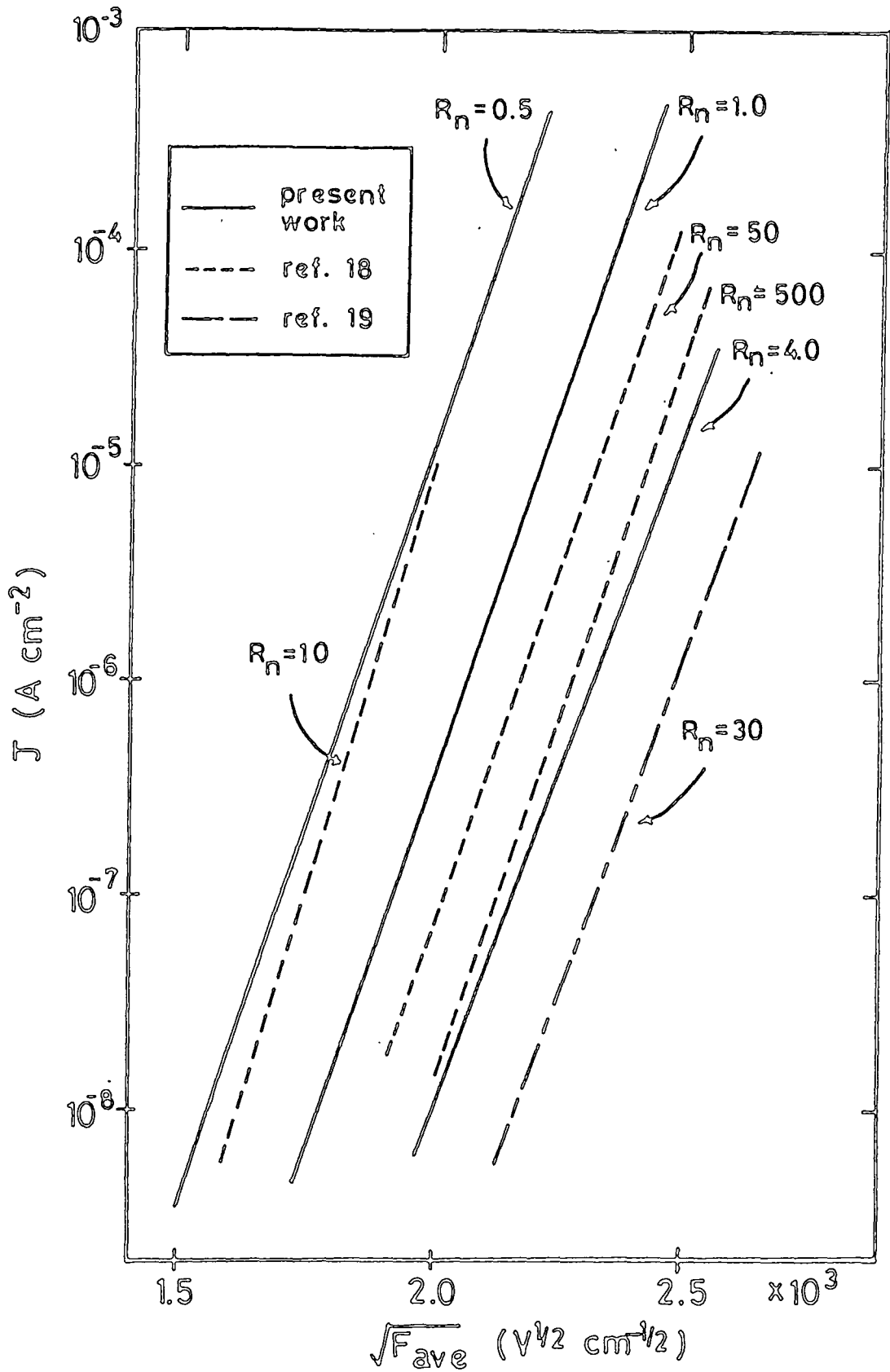
Figure 6.8    Schottky plots showing a comparison of different growth techniques. The present work (solid line) and that of Watanabe [19] (double dashed line) were grown using LPCVD with $NH_3$ and $SiCl_2H_2$ as reactants. The films of Kobayashi [18] (dashed line) were grown using atmospheric CVD with $SiH_4$ and $NH_3$ as reactants.

rich as claimed. The other work illustrated in Fig. 6.8 [18], shows a similar trend with decreasing gas ratio as found in the present work, although the absolute value of $R_n$ is very different. This results primarily from the use of different reactants and growth technique.

6.8  Summary

From steady-state I-V and I-V-T measurements it has been found that for our SRN films the effective trap depth is approximately 1.1 eV and it decreases slightly with increasing excess silicon. The calculated dielectric constant is lower than expected but it does increase with with increasing silicon content of the films as does the pre-exponential parameter C, which is related to the density of defects. It is assumed that with increasing silicon concentration the density of trapping states increases. From Hill's method of analysis, more reasonable values of $\varepsilon_d$ were extracted.

It was found that the high field, high temperature conduction appears to be due to Poole-Frenkel emission from relatively deep traps into the conduction band or band tails of the SRN film. At low temperatures, with high or moderate electric fields, the conduction appears to be due to Fowler-Nordheim tunnelling. Polarity and thickness dependencies have been attributed to the build up of space charge near the injecting contact. Both dependencies dissappear for films of thickness greater than 1500 $\overset{\circ}{A}$.

References for Chapter 6

[1] S.M. Sze, _Physics of Semiconductor Devices_, Second Edition, John Wiley and Sons, New York, 1981, p403.

[2] S.M. Sze, J. Appl. Phys., 38, 2951 (1967).

[3] S.M. Hu, D.R. Kerr and L.V. Gregor, Appl. Phys. Lett., 10, 97 (1967).

[4] D.J. DiMaria and P.C. Arnett, Appl. Phys. Lett., 26, 711 (1975).

[5] P.C. Arnett and D.J. Dimaria, Appl. Phys. Lett., 27, 34 (1975).

[6] Z.A. Weinberg and R.A. Pollack, Appl. Phys. Lett., 27, 254 (1975).

[7] B.H. Yun, Appl. Phys. Lett., 27, 256 (1975).

[8] Z.A. Weinberg, Appl. Phys. Lett., 29, 617 (1976).

[9] F.L. Hampton and J.R. Cricchi, Appl. Phys. Lett., 35, 802 (1979).

[10] E. Suzuki, H. Hiraishi, K Ishii and Y. Hayashi, Appl. Phys. Lett., 40, 681 (1982).

[11] L.D. Yau, F.T. Liou and S. Chen, IEEE Electron. Device Lett., EDL-4, 261 (1983).

[12] L.D. Yau, IEEE Electron. Device Lett., EDL-5, 318 (1984).

[13] F.T. Liou and S. Chen, IEEE Trans. on Electron. Devices, ED-31, 1736 (1984).

[14] L. Sullivan and H.C. Card, J. Phys. D : Appl. Phys., 7, 1531 (1974).

[15] B.H. Yun, Appl. Phys. Lett., 25, 340 (1974).

[16] R.M. Hill, Phil. Mag., 23, 59 (1971).

[17] A.J. Lowe, M.J. Powell and S.R. Elliot, J. Appl. Phys., 59, 1251 (1986).

[18] K. Kobayashi, Jpn. J. Appl. Phys., 11, 555 (1972).

[19] K. Watanabe and S. Wakayama, J. Appl. Phys., 53, 568 (1982).

[20] T. Noguchi, S. Usui, A. Sawada, Y. Kahoh and M. Kukuchi, Jpn. J. Appl. Phys., 21, L485 (1982).

[21] N. Ibaiki and H. Fritzsche, Phys. Rev. B, 30, 5791 (1984).

[22] R. Karcher, L. Ley and R.L› Johnson, Phys. Rev. B, 30, 1896 (1984).

[23] A. Chayahara, M. Ueda, T. Hamasaki and Y. Osaka, Jpn. J. Appl. Phys., 24, 19 (1985).

# Chapter 7
## Capacitive Characteristics of Silicon-Rich $Si_3N_4$ Films
### Experimental Results and Discussion

The theoretical aspects of the capacitance characteristics of thick MIS devices were discussed in Chapter 2. These theories apply to our devices but with certain differences that arise since the present films are neither thick nor ideal. Normally there must be some justification for the use of thick MIS theory for devices containing 'leaky' insulating materials, i.e. with a finite amount of DC conduction. If such an MIS structure shows a standard MIS capacitance curve, with well defined depletion and accumulation regions, usually the device follows these theories to at least a first order approximation. It will be shown that even though our devices are 'leaky', they do indeed fall within these criteria.

In section 7.1 ramped and point by point capacitance-voltage (C-V) experimental results are presented and discussed. Transient capacitance and current results and subsequent analysis are presented in section 7.2.

## 7.1 Ramped Capacitance-Voltage Results

Presented in Figs. 7.1 a), b), and c) are the standard C-V curves for MIS devices with films of gas phase ratio $R_n = 4.0$, $R_n = 1.0$ and $R_n = 0.5$ respectively. Contained within each plot there are four curves representing four different sweep or ramp rates separated by approximately an order of magnitude. These
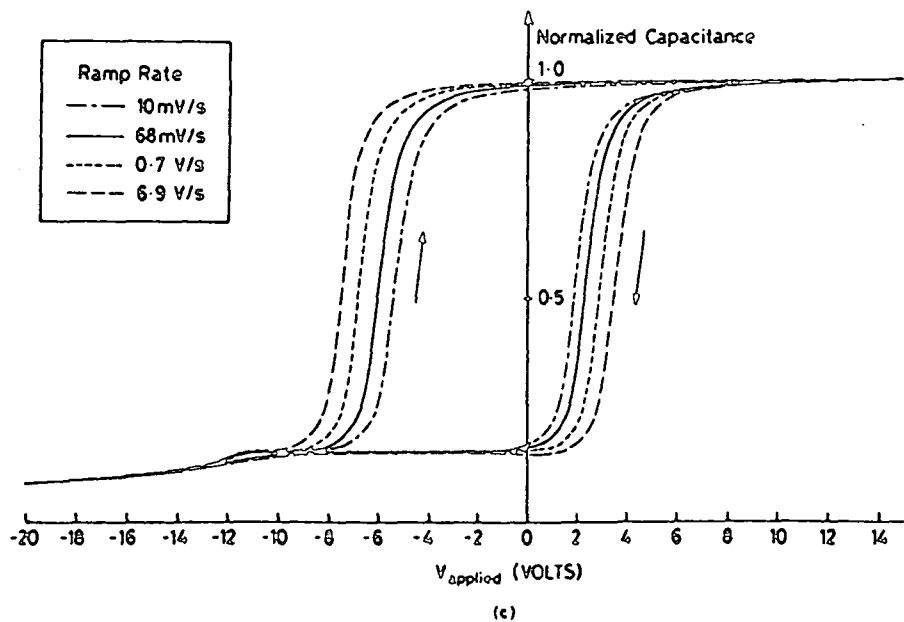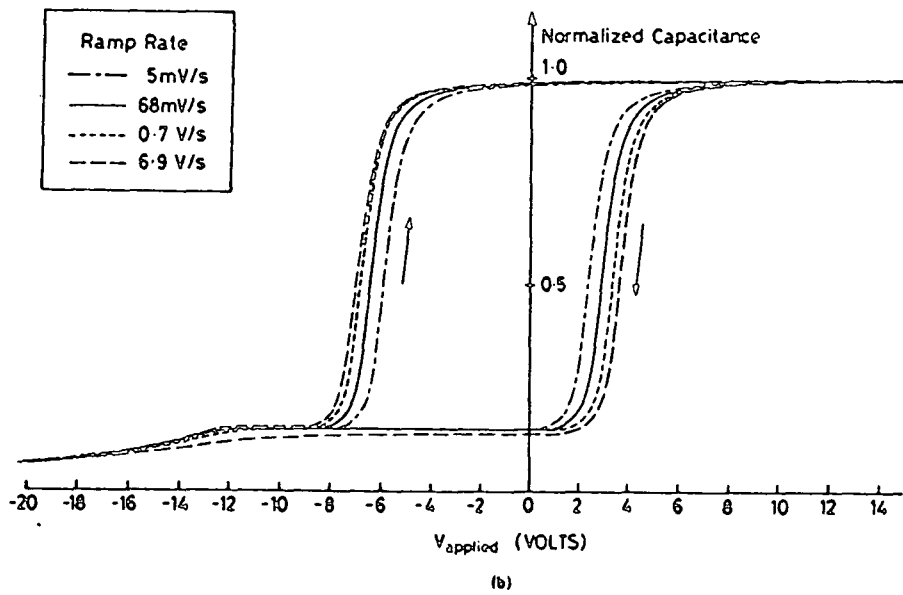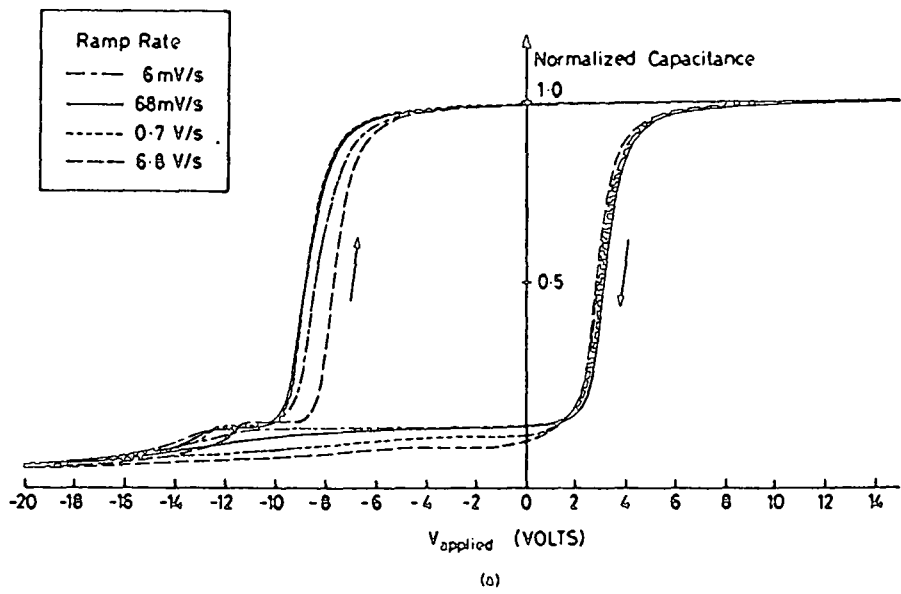
Figure 7.1    Capacitance-voltage curves as a function of ramp
rate for films with a) $R_n$ = 4.0, b) $R_n$ = 1.0 and
c) $R_n$ = 0.5.

curves illustrate the standard C-V curves that one would find for any MIS structure device. The depletion and accumulation regions of the curves are well defined although there are of course some differences from the 'ideal' case.

Firstly, there is a very large amount of hysteresis in all of the curves. The direction of the hysteresis is clockwise and this is characteristic of charge trapped either in interface states or bulk states in MIS devices.[1]. For all the curves presented, there is a distinct change in the amount of hysteresis for the differing sweep rates. The change in hysteresis or flat band shift arises because the rate of trapping (or detrapping) can not keep step with the sweep rate. In general, the magnitude of the flat band shift is proportional to the amount of trapped (or detrapped) charge. However, this is based on the assumption that the sweep rate is slow enough for the trapping mechanism to respond. From the curves illustrated in Fig. 7.1, it is shown that in general the flat band shift decreases with decreasing ramp rate. Normally, trapping and detrapping are much faster than the sweep rates in question and they therefore respond immediately to changes in the bias (i.e. they are said to 'communicate' directly with the substrate). This is not the case with these films. The very long current transients that have been mentioned earlier suggest that the trapping and/or detrapping mechanism is very slow.

In Fig. 7.1 (a), the C-V curves for the least conductive films are shown. For this film, the flat band shift increases with increasing ramp rate if the ramp rate is less than about

96

0.7 V/s. However, it can be seen that for the most rapid sweep rate (6.9 V/s), the flat band shift has decreased. It was found for all films, that the flat band shift did eventually start to decrease again with increasingly high ramp rates.

It is very important to remember that these films are leaky. The amount of trapped charge is not only dependent upon the time given to trap the charge but also on how fast this charge may be injected (i.e. the current). For very slow rates, the charge state of the device comes to a quasi-equilibrium with the ramp rate because sufficient time is given for trapping and/or detrapping. For the slow ramp rates, the flat band shift is generally at a minimum. As the ramp rate is increased, the trapping (and/or detrapping) starts to lose step with the ramp rate and the amount of hysteresis increases. Eventually a point is reached where the ramp rate is so high that the amount of trapped charge starts to decrease as there is less time at a given bias in which to trap the injected charge. As a result the hysteresis also decreases. For all the films studied here, very fast ramp rates (> 1000 V/s) and an oscilloscope were used to measure the 'higher' frequency response. In all cases, the flat band shift eventually decreased with increasing ramp rate although not going to zero even for extremely high ramp rates. This would seem to imply that there might be a combination of very fast and very slow states in these materials. The ramp rate at which the decrease in flat band shift was noted was greater for the most conductive of these films. At a given voltage (or field) the current (i.e. the supply of charge) is greater for

97

films with higher silicon content. This implies, of course, that the trapping (and/or detrapping) rates increase with increasing current. However, it may also mean that there is an increasingly higher density of traps with increasing silicon content of the films. These results could also be explained if the rate of trapping is proportional to the density of trapping states, which it often is.

If we compare the C-V curves of films of different silicon concentrations but of the same ramp rate, as shown in Fig. 7.2, we see that the positive edge of the hysteresis changes little while the negative changes markedly for increasing silicon content. As mentioned previously, this may be due to the increased current or to the increase in the density of trapping states. Whatever the cause, the trapping and/or detrapping rate is definitely increasing with increasing silicon content of the films.

It was stated earlier that if the C-V characteristics of these films have well defined accumulation and depletion regions, the thick MIS theories presented in Chapter 2 could be used at least as a first order approximation. There are however, certain anomalies that appear in the curves that have been presented thus far. Aside from the large hysteresis, the most striking feature is the anomalous 'ledge' that appears in the depletion region of all the curves shown in Fig. 7.1. Such 'ledges' or 'plateaus' have been seen previously in measurements made at low temperatures on MIS and MNOS devices incorporating silicon nitride and/or silicon dioxide thin films. The present results show similar effects at room
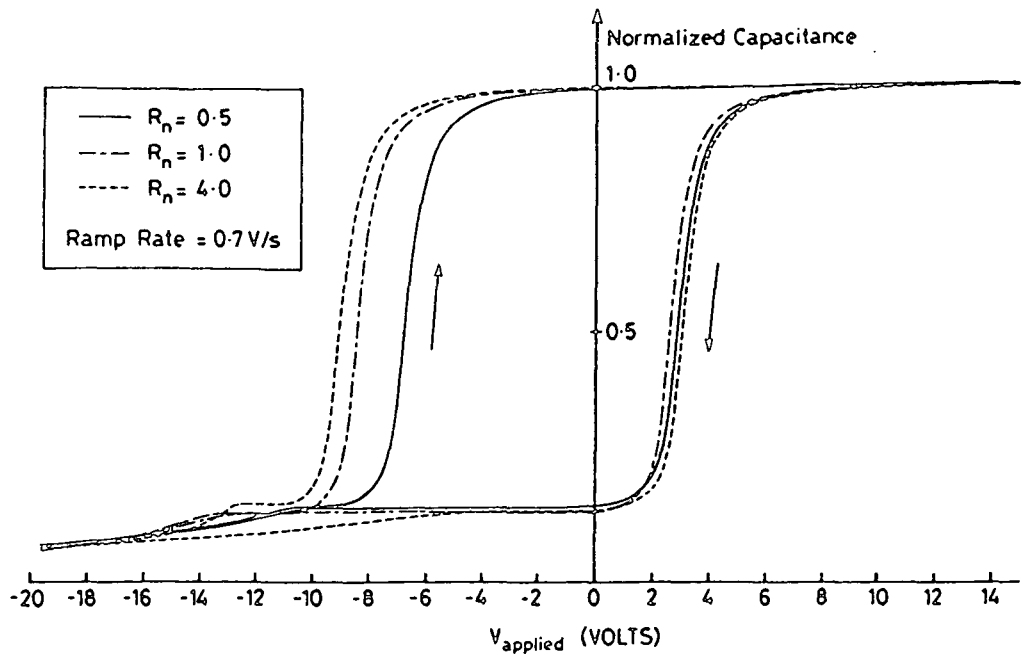
Figure 7.2    Capacitance-voltage curves as function of gas
              phase ratio, $R_n$, at a constant ramp of 0.7 V/s.


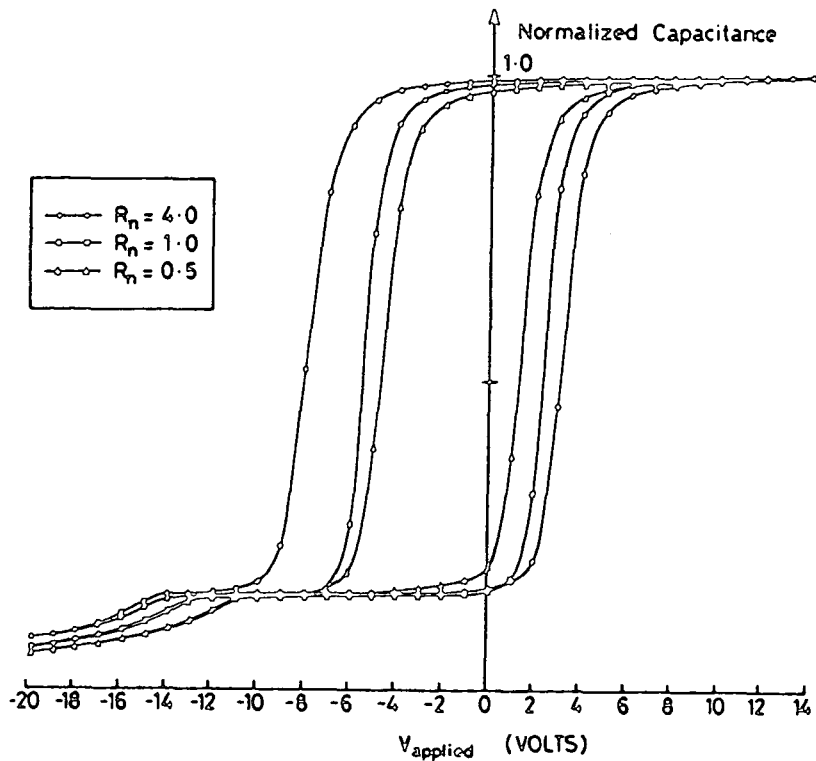
Figure 7.3    Static,    point-by-point    capacitance-voltage
              curves as a function of gas phase ratio, $R_n$.
              Holding time for each point was $10^3$ seconds.

temperature for our SRN films. The previously reported effects have been attributed to minority carriers when generated by light [2-4], supplied by a diffused layer [3-5] (i.e. a source or drain in an MOS transistor) or supplied by leakage current through the insulator [5]. The 'ledges' have been interpreted as due to the combined effects of interface traps and externally supplied minority carriers, and were used to estimate the density [2] and capture cross-section [3] of the interface traps.

Simmons and Wei [6,7] have developed theories of dynamic charging of interface traps based on both discrete and uniform trap distributions. They have also presented experimental evidence [8] of the effects of the ramp rate and temperature on the C-V characteristics of MIS capacitors. Consider firstly the effects of non-steady state emission and capture on the depletion part of the C-V curves of an MIS device. The traps that have the greatest effect on the state of the surface potential and thus on the capacitance are those sufficiently close to the interface to 'communicate' directly with the substrate. Under steady state conditions, meaning that the emission from and capture into the traps follows the voltage ramp, the rate of change of charge on the top (gate) contact is given by [7]

$$\left. \frac{dQ_s}{dt} \right|_{ss} = \left. \frac{dQ_t}{dt} \right|_{ss} - \left. \frac{dQ_D}{dt} \right|_{ss} \qquad (7.1)$$

where $dQ_t/dt$ (ss) is the 'steady state' current due to emission from the traps and $dQ_D/dt$ (ss) is the 'steady state' current

due to the change in the depletion charge. Under steady state conditions, the charge in the traps is only dependent on the applied voltage and therefore both positive and negative going ramps should trace the same curve. This can be seen to be true from the data shown in Fig. 7.1 for as the ramp rate decreases, the curves for positive and negative ramps in the 'ledge' region become essentially the same. Also under steady state, the capacitance becomes constant over a significant proportion of the C-V curve when the device is in the inversion mode. The voltage in excess of that needed to sustain the inversion region is dropped across the insulator and the trapped charge required to support this potential, $V_i$, is supplied by surface and/or bulk generation.

However, as the ramp rate increases, considering the negative going cycle first, there are more traps that are filled at a given voltage than under steady state conditions. This situation arises where the emission rate from the traps can no longer respond fully to the changing potential. Therefore under non-steady state conditions

$$\frac{dQ_t}{dt} \quad < \quad \left. \frac{dQ_t}{dt} \right|_{ss} \tag{7.2}$$

and by the principle of detailed balance and equation 7.1

$$\frac{dQ_D}{dt} \quad > \quad \left. \frac{dQ_D}{dt} \right|_{ss} \tag{7.3}$$

Subsequently under non-steady state conditions, the

100

depletion region width is greater than it was, for a given bias, under steady-state conditions. Therefore, the capacitance is reduced. And generally speaking, the faster the ramp rate, the lower the capacitance. This is shown to be the case for the least conductive of our films (Fig. 7.1a). With increasing silicon content, this effect disappears due to the increasing conductivity of the films.

Under non steady-state conditions, whether the ramp is positively or negatively going, the emission from the trap continues. Therefore, at a given bias voltage, there is less charge in the traps on the positive going than on the negative going direction. Since the system is still not in steady state, the negative going ramp displays a smaller capacitance than the positive going ramp. This effect is intuitively obvious from the data shown in Fig. 7.1a.

The analysis thus far has explained the general features of the 'ledges' that are found in the C-V data for these devices. However, a problem still exists. Figure 7.3 shows truly steady state point by point C-V curves for devices with films of the same $R_n$ values as those whose characteristics were shown in Fig. 7.1. For each point on the curve, the voltage was held for $10^3$ seconds before a value of capacitance was recorded. These curves show the same basic trends as in Figs. 7.1 and 7.2; the hysteresis decreases with increasing silicon content. However, the 'ledge' is still found to exist even for what surely must be, or very close to being, steady state conditions. It is interesting to note that the bias point at which the 'ledge' occurs, decreases with increasing

silicon content. If these voltages are compared with those from the current-field data (see Fig 6.1) it is not surprising that we find a correlation. Generally speaking, these bias points are in the high field region, where the currents are increasing exponentially. As the current increases, a large number of carriers are injected into the depletion region at the surface of the silicon. This in turn increases the amount of recombination at or near the interface reducing the minority carrier concentration at the surface. Similar effects occur whether the current is due to injection of holes from the silicon into traps or if the traps act as recombination centres. In either case the depletion region is no longer screened from further bias increases (i.e. it is no longer in the inversion mode) and the depletion region continues to grow with increasing negative bias so that the capacitance decreases as is shown in Fig. 7.3. Under these quasi-steady state conditions, it should also be noted that the hysteresis in the 'ledge' part of the curve (i.e. the difference between the positive and negative going curves). is very much reduced as expected.

As the depletion region grows. in this 'ledge' part of the C-V characteristic. more of the applied bias is dropped across the silicon depletion region as opposed to the SRN film. A comparison of Figs. 7.3 and 6.1b shows that the bias at which the devices go into this deep depletion mode corresponds almost exactly to the start of the curvature in the current-field characteristics under negative bias.

## 7.1.1 Low Frequency Dielectric Constant

From the accumulation capacitance, the low frequency dielectric constant, $\varepsilon_n$, was calculated for the films presented here. By low frequency, it is meant that the frequency of measurement was much less than optical frequencies. The actual measurements, as described in Chapter 4, were made using a Boonton capacitance meter which has an operating frequency of 1 MHz.

The results were calculated from the accumulation capacitance measured from a sample of at least 20 devices. The results are given in Table 7.1 for different $R_n$ values. For films with $R_n$ = 0.25, the currents at moderate forward bias were too large to be accommodated by the Boonton meter which was replaced by a 100 kHz phase sensitive detection, capacitance/conductance apparatus built in the Department. The errors quoted in Table 7.1 are the mean square error calculated from the devices measured. The values of excess silicon content are from the results previously shown in Chapter 5. A minimum error of +/- 0.5% is estimated.

Figure 7.4 illustrates the dependence of the dielectric constant, $\varepsilon_n$, upon the silicon content of the films. As expected, $\varepsilon_n$ increases with increasing excess silicon in the films. The trend appears to be linear over the range of excess silicon for these films. These values will later be compared with those of the calculated dynamic dielectric constant, obtained from the analysis of the I-V data in Chapter 6.

103

| $R_n$ | Excess Si (%) | $\varepsilon_n$ |
|-------|---------------|-----------------|
| 4.0   | 8.84          | $6.60 \pm 0.27$ |
| 1.0   | 11.18         | $7.16 \pm 0.41$ |
| 0.5   | 12.26         | $7.31 \pm 0.23$ |
| 0.25  | 12.75         | $7.50 \pm 0.71$ |

Table 7.1    Low frequency (1 MHz) dielectric constant as a function of gas phase ratio, $R_n$ , and excess silicon content.
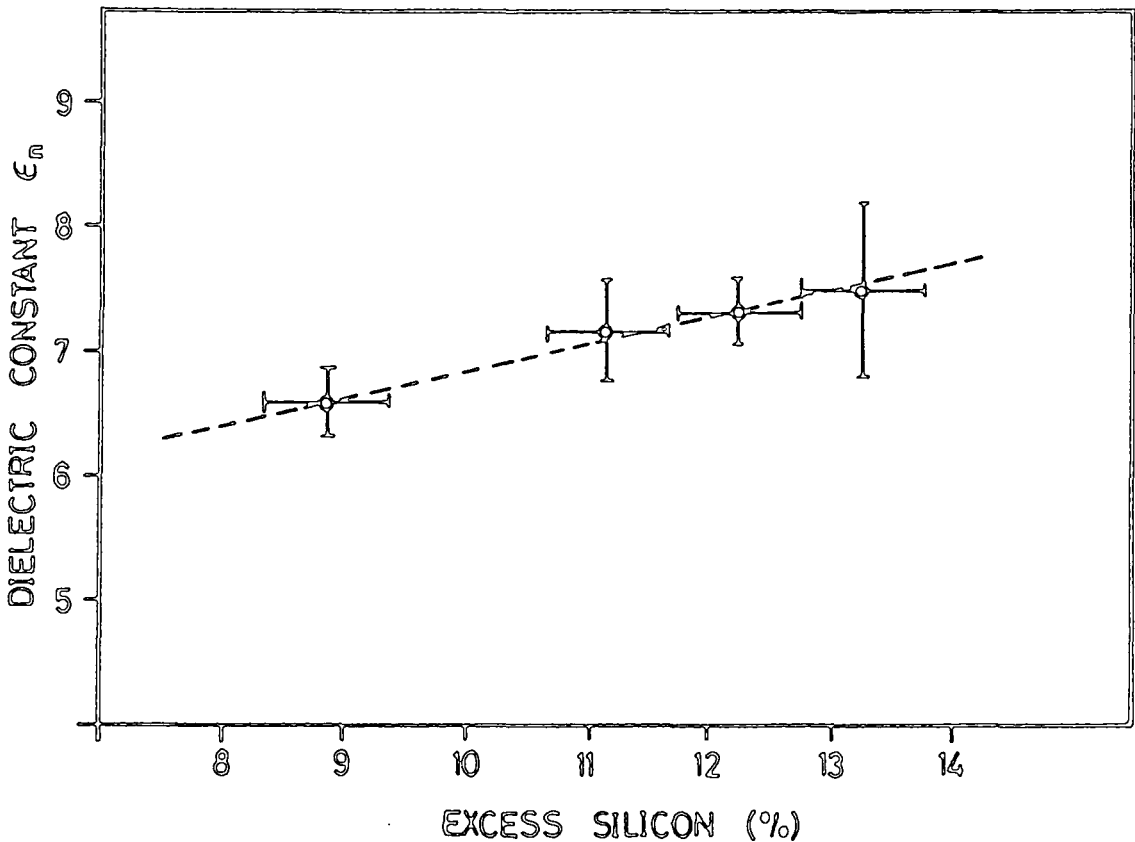


Figure 7.4    Low frequency (1 MHz) dielectric constant versus silicon content. From the data presented in Table 7.1.

## 7.2 Discussion of Transient Capacitance Results

As is evident from the data presented thus far, there is great difficulty in assessing the true nature of the conduction in these silicon-rich $Si_3N_4$ (SRN) films. This difficulty arises because of the large amount of charge that is trapped in or removed from the films under non-equilibrium or non-steady state conditions. The characteristics of the charge trapping process are unknown, but it is evident that their time constants are very long indeed. In the following sections a simplified theory is presented which accounts for most of the charge-related effects found experimentally in our films. These effects are then related back to the quasi-steady state results that were presented in the previous chapter.

In Fig. 7.5, the band diagram of an MIS, Al-SRN-Si, device is shown. The barrier heights shown are said to be known within +/- 0.1 eV [9,10] for stoichiometric nitrides. It is assumed that similar barrier heights are found with MIS devices made with SRN films. The energy levels, $E_c$ and $E_v$ represent the edge of the 'conduction' and 'valence' bands, where the 'band gap' is the mobility gap associated with amorphous materials. These energy levels represent the upper and lower limits of the so called extended states of the conduction and valence bands. The energies, $E_a$ and $E_b$, represent the edges of the band tails that arise from the amorphous nature of these films. The band tails extend well into the forbidden gap and can be thought of as closely packed discrete energy levels. The deep states or 'defect band' is situated roughly in the middle of the energy gap of the SRN film. It has been

104

Conduction band 'tail'

$E_c$

$E_a$

$\phi_{n2} = 2.1\,eV$

$\phi_{n1} = 2.05\,eV$

$E_f$

$E_c$
$E_f$

Defect 'band'

$E_v$

$\phi_{p2} = 3.0\,eV$

$\phi_{p1} = 1.95\,eV$

$E_p$

$E_v$

Valence band 'tail'

Al                      $Si_3N_4$                      Si
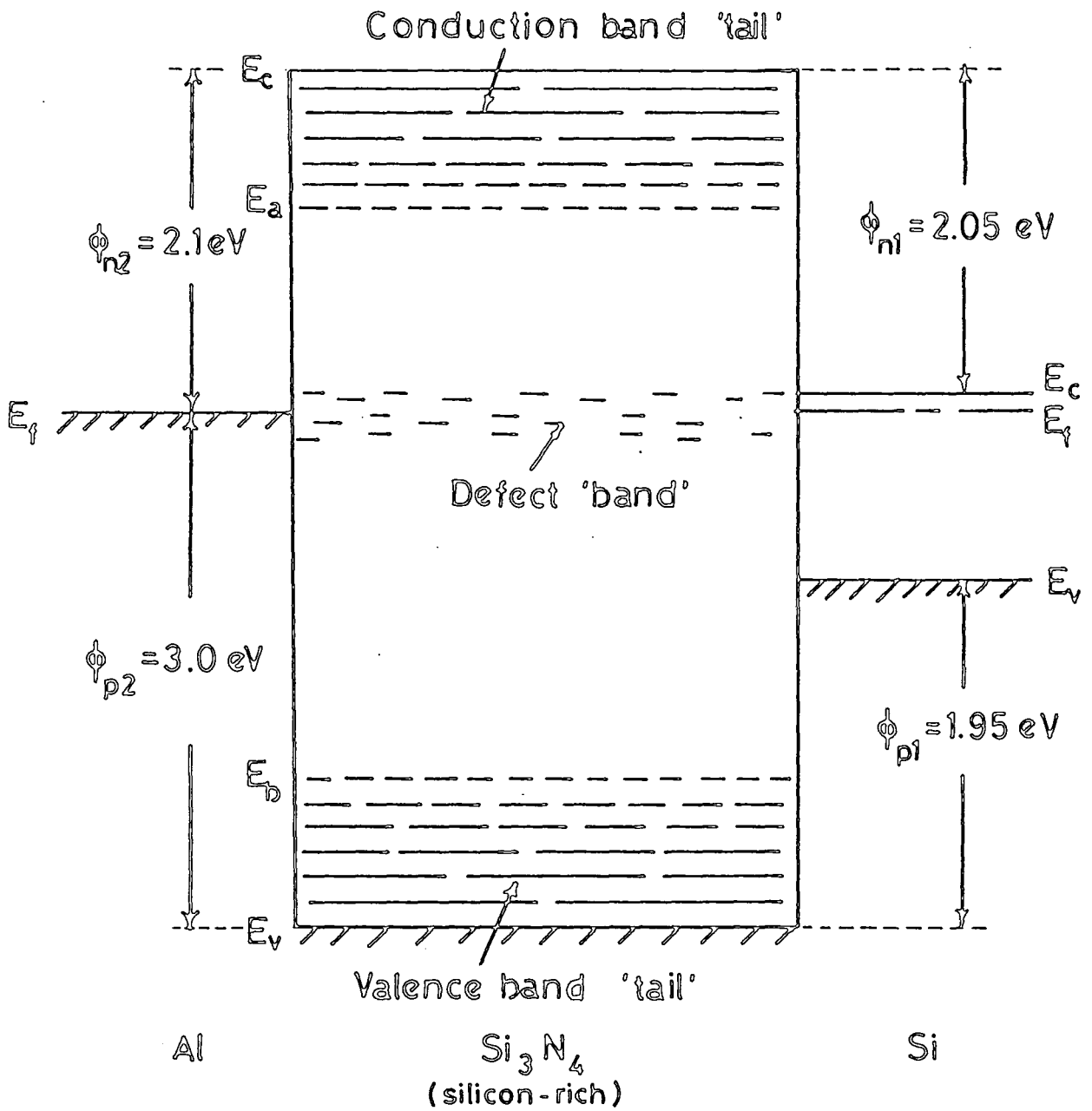                  (silicon-rich)

Figure 7.5      Energy band diagram of an Al-SRN-Si device.

suggested [11] that these states arise from the existence of dangling silicon bonds in the $SiN_x$ matrix.

Up to this point, we have assumed that the conduction in these films is due to the excitation of electrons from an isolated trap level to the conduction band. We have found that the 'effective' trap depth is about 1.1 eV. From this simplified model, and the structure shown in Fig. 7.5, one might conclude that the trap level must lie in the band tails. This. however. is unlikely. If the trapping state was within or near the edge of the band tails, for example at $E_a$, a hopping mechanism through the tails would be a much more energy efficient process than the excitation of electrons from the trap to the conduction band edge at $E_c$. The activation energy measured would then be much lower than the presently measured value. If the trap level is assumed to lie within the 'defect band' as shown in Fig. 7.5, the energy required for activation to the conduction band edge would be on the order of or greater than 2.0 eV i.e. much greater than the measured trap depth. The only plausible solution, which has been suggested before [9]. is that the conduction in these films results from Poole-Frenkel emission of trapped charge carriers from the deep level traps to the edge of the band tails at $E_a$ or $E_b$. Subsequent movement through the band tails must then be by some sort of variable range hopping [12] with a very low activation energy so as not to appreciably impede the progress of the activated carriers. Generally. these activation energies are found to be somewhat less than 0.1 eV.

The capacitance results in the previous section showed

105

that a very large amount of charge is trapped or detrapped in these films as is evident from the very large hysteresis in the C-V curves. These traps are extremely slow as large flat band shifts still occur for even the slowest ramp rates. To investigate the charge storage more thoroughly, transient capacitance and current measurements were made. This method of measuring trapped charge has been used previously [13-16] but usually for very short trapping times, $t \ll 1$ second. The charging in the present films was found to last for many seconds. and even days and weeks. Subsequently much longer transient measurements were needed.

The experimental technique was described previously in Chapter 4. However, it is pertinent here to emphasize some of its finer points. The positive case is used as the example. but the extension to negative polarities is identical.

From the measured accumulation capacitance, strong forward bias in this example, the low frequency dielectric constant was determined using equation 2.8. Given the doping concentration of the silicon. and the thickness of the SRN film, the 'ideal' flat band capacitance was calculated using equation 2.6. The potential on the device was ramped at about 5V s to a holding voltage. $V_H$. for a set length of time. (typically 120 seconds). to let the device come to a repeatable quasi-steady state with respect to the charge in the insulator. Typically. $V_H = -20$ V for positive bias voltages. $V_B$, and $V_H = +15$ V for negative bias voltages. Large voltages were used to ensure that the quasi-steady state charge condition could be reached as quickly as possible. The device voltage was then ramped to

106

a set voltage, $V_B$, for a set length of time, t. During the ramping, the capacitance of the device was monitored, and at the point where C(measured) = $C_{FB}$('ideal'), the voltage on the device, $V_{FB_O}$ was measured. After the set length of time, the applied bias was ramped back to $V_H$, during which $V_{FB}$ was measured when again C(measured) = $C_{FB}$('ideal'). The net flat band shift, $\Delta V_{FB}$, was then determined from the difference between $V_{FB}$ and $V_{FB_O}$. It should be noted that the values of $V_{FB_O}$ for positive bias and $V_{FB}$ for negative bias should remain independent of the set voltage, $V_B$, and time. It will be shown that this is indeed the case.

Figure 7.6 shows an example of transient C-V data measured manually. The characteristics illustrated here are for a film with $R_n$ = 1.0 and d $\approx$ 300 $\overset{o}{A}$. There are two sets of data shown for applied positive bias, $V_B$, of 5 and 10 volts. For these data, the holding voltage and time were $V_H$ = -20 V and $t_H$ = 120s respectively. It should be noted that the flat band shift is due to a positive shift in the right hand side of the C-V curve. The left hand side is constant with both time and applied voltage. This implies that there is an increase in negative charge stored in the films with increasing time. A similar situation occurs for negative applied bias with positive holding voltages. However, the right hand side of the curve remains constant while the left hand side shifts negatively with increasing time. This, of course, suggests an increase of net positive charge with increasing time. The example given in Fig. 7.6 shows only the shift for two values of positive bias while the graphs in Fig. 7.7 give a more
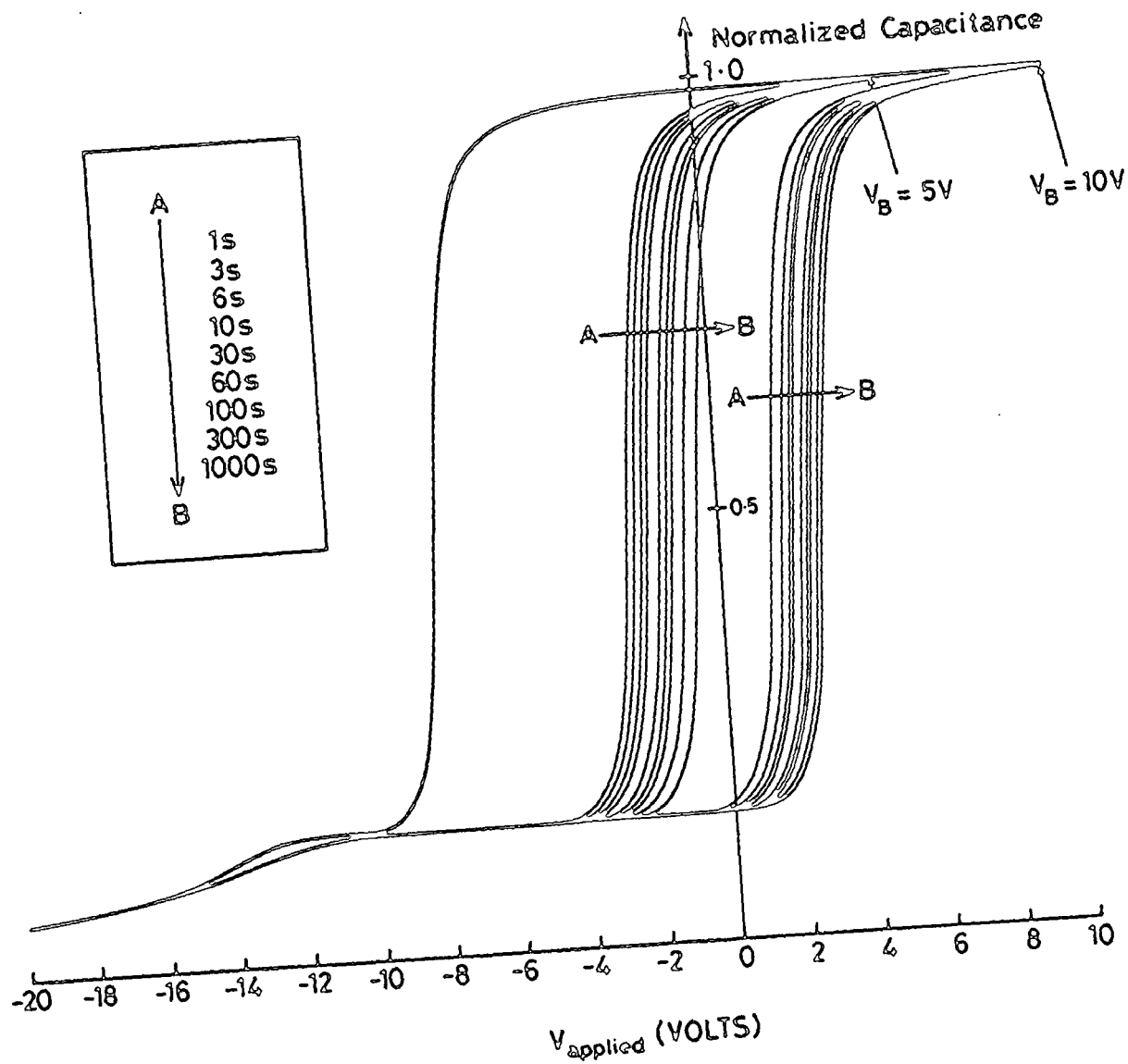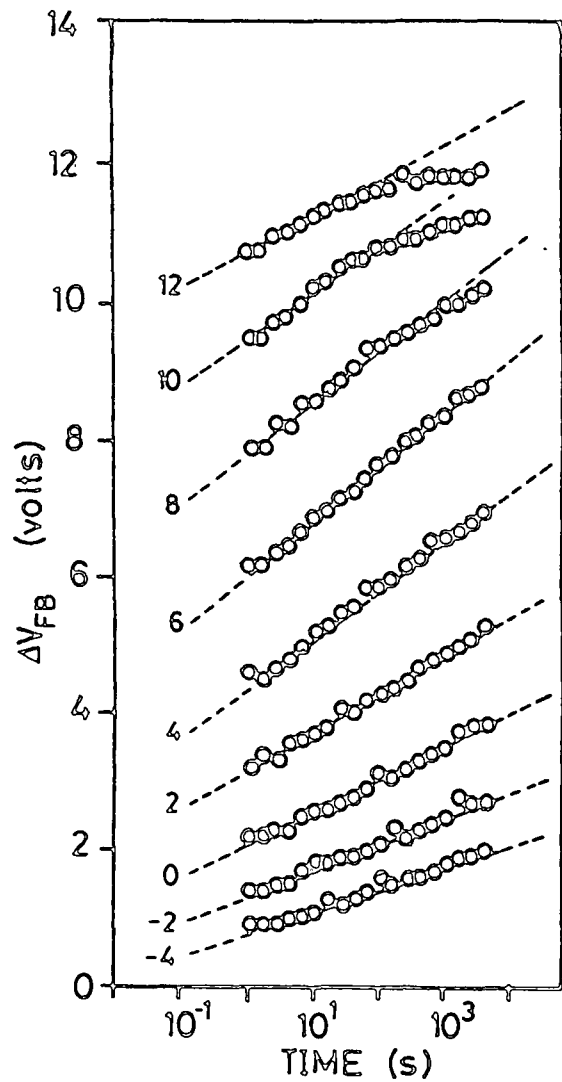
**Figure 7.6** An example of transient capacitance-voltage curves for two values of positive bias. $R_n = 1.0$, $V_H = -20$ V and $t_H = 120$ seconds.
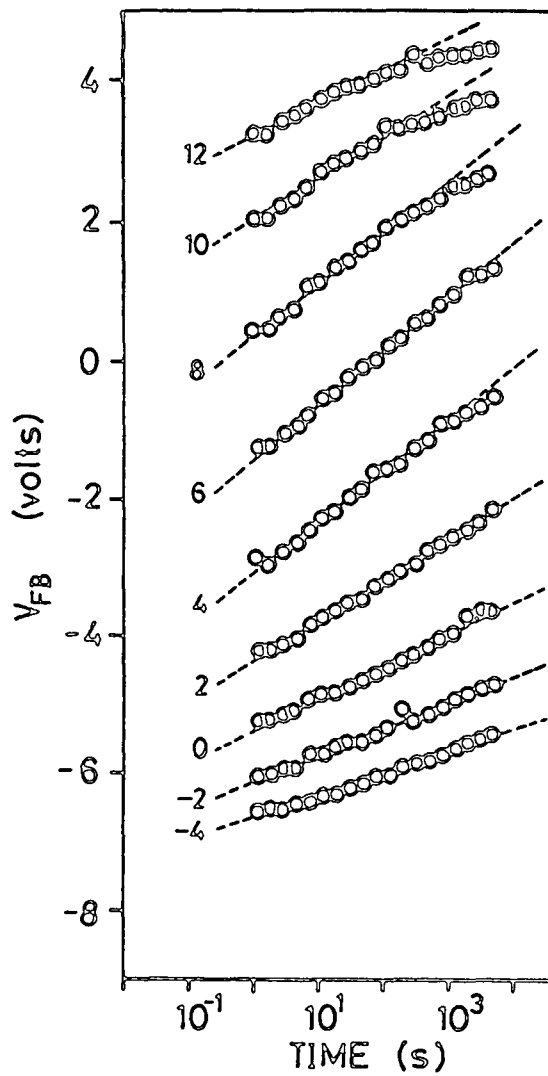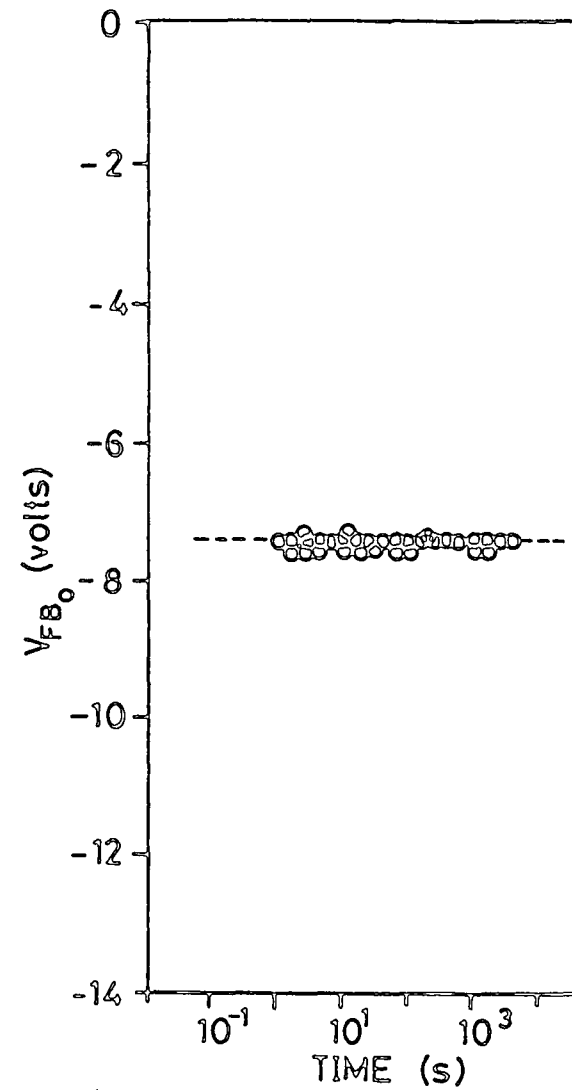
Figure 7.7    Measured flat band shift as a function of time over a range of positive bias voltages where (a) shows the net flat band shift ($\Delta V_{FB} = V_{FB} - V_{FBo}$), (b) shows the measured flat band shift (right hand side of the C-V curve) and (c) shows the reference voltage shift (left hand side of the C-V curve).

complete set of data for this device. Fig. 7.7a shows the net flat band shift, $\Delta V_{FB}$, with time. As functions of time, $V_{FB}$ (the right hand side of the C-V curve) is shown in Fig. 7.7b while $V_{FB_O}$, (the left hand side) is shown in Fig. 7.7c. Within experimental error, $V_{FB_O}$ is constant for all times and applied bias used.

Figs. 7.8 a), b), and c) show parallel results for the same device for negative applied bias. The holding voltage and time for the negative results were -15 volts and 120 seconds respectively. For the negative polarity, $V_{FB}$ is constant with time and applied voltage while $V_{FB_O}$ increases negatively with increasing time giving a net increase in the measure flat band shift, $\Delta V_{FB}$. In all cases, the flat band shift is quite clearly logarithmic in time which suggests a trapping and/or detrapping mechanism which is also logarithmic. The results also show that for all the devices net increases of negative and positive charge were found for positive and negative polarities respectively.

Figure 7.9 shows a calibration curve for the flat band shift measurements as a function of the holding voltage. For positive applied bias, ($V_B$ = +15 V). the change in $V_{FB_O}$ (normally constant) and similarly $\Delta V_{FB}$ was measured as a function of $V_H$. which was normally -20 V. For negative bias, ($V_B$ = -20 V). the shift in $V_{FB}$ and subsequently $\Delta V_{FB}$ was measured as a function of $V_H$. which was normally +15 V. The point at which the $\Delta V_{FB}$ curves cross the vertical axis was taken to be the zero shift associated with these particular holding voltages for these films. The example shown in

108
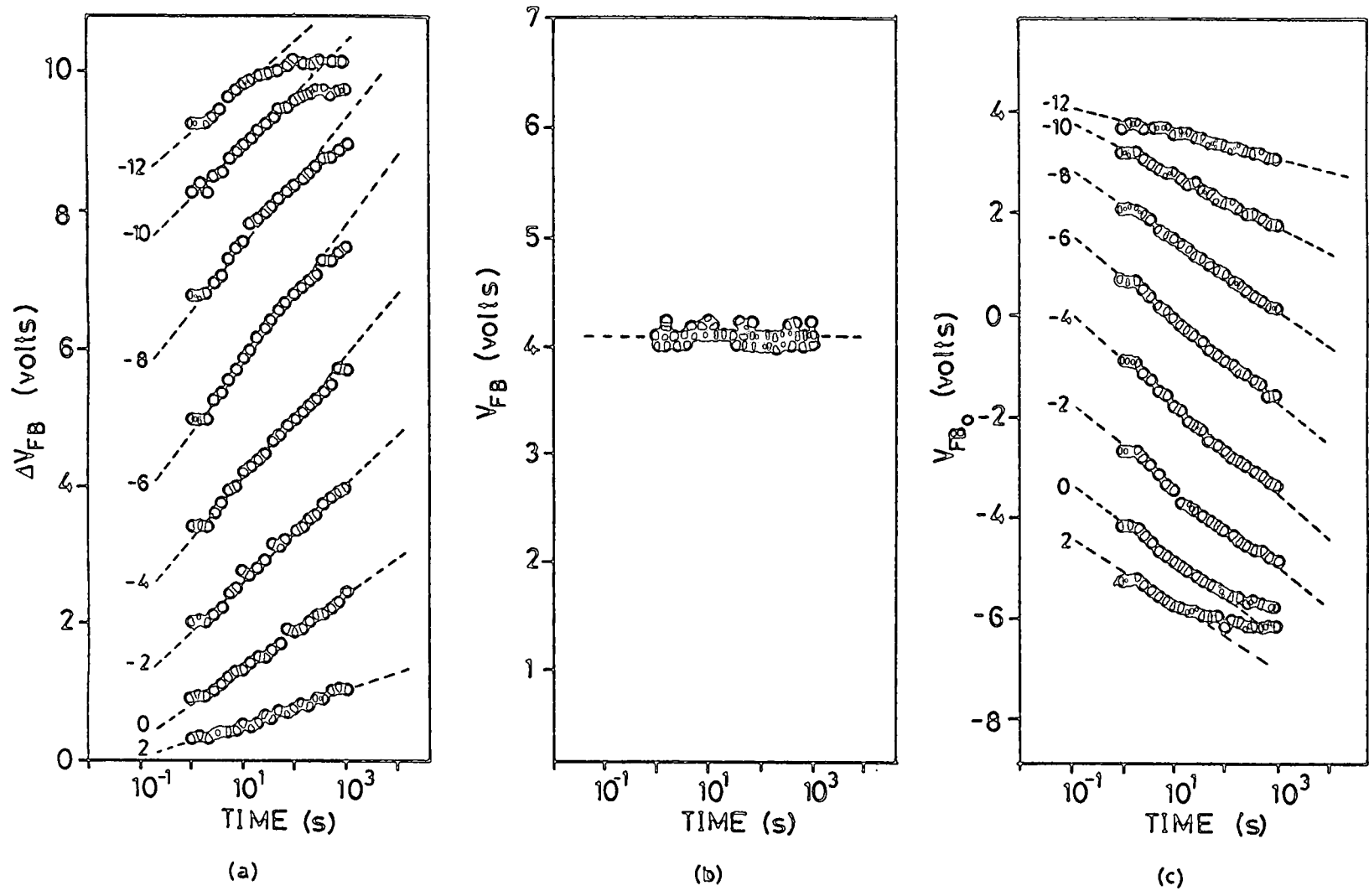
Figure 7.8    Measured flat band shift as a function of time over a range of negative bias voltages where (a) shows the net flat band shift $(\Delta V_{FB} = V_{FB} - V_{FB_0})$, (b) shows the reference voltage shift (right hand side of the C-V curve) and (c) shows the measured flat band shift (left hand side of the C-V curve).

Figure 7.9    Flat band shift calibration curves  showing  the
shift  of  the flat band reference as a function
of holding voltage.  For  positive  and  negative
bias, $V_B = +15$ V and $V_B = -20$ V respectively.

Fig. 7.9 was from a device with an SRN film of $R_n$ = 4.0. The inset shows schematically, for positive bias, the voltages that were measured to determine the flat band shift. It is interesting to no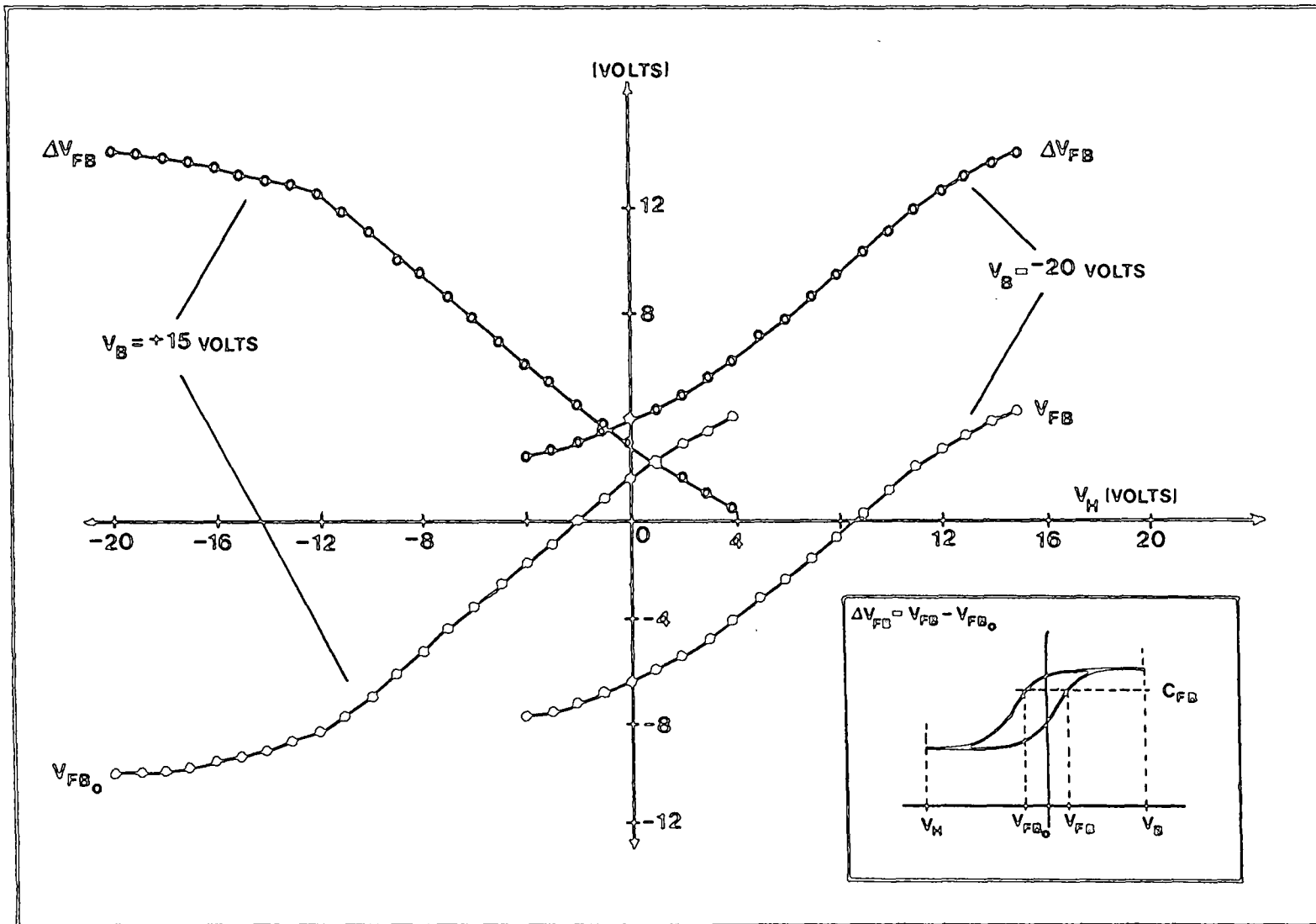te that the curves of $\Delta V_{FB}$ for positive and negative holding voltages do not intersect at $V_H$ = 0, but rather at a voltage $V_H \approx -1.0$. This is due to the different preset bias conditions for this particular measurement. The positive bias voltage (i.e. $V_B$ = +15 V) was less in magnitude than the negative bias voltage (i.e. $V_B$ = -20 V). Subsequently, for a given holding time, (100s for both positive and negative polarities), a greater amount of charge was trapped or detrapped with the larger of the two voltages. This gives a slight negative shift of the positive bias curve with respect to the negative bias curve.

From the discussion thus far, we conclude the following. Firstly, the trap level that is responsible for conduction in these films is a very deep trap and lies nearly central in the band gap. Electronic conduction results from the activation of trapped carriers into the band tails and not into the conduction band. Secondly, the trapping of a large amount of charge is evident under both positive and negative applied bias and the trapping and/or detrapping mechanism has a logarithmic time dependence. The trapped charge is positive with negative bias and negative with positive bias. Based on these two assumptions and some previously published work [17] on MNOS memory devices, the following simple model for trapping has been developed.

109

## 7.2.1 Charge Trapping Model

This model assumes a monoenergetic trap level near the interface between the silicon-rich $Si_3N_4$ (SRN) film and the silicon substrate. The traps are assumed to extend well into the SRN film and are located within the band gap of the silicon substrate. When a field is applied to the device, the bands in the insulator and the trap level are shifted in energy, and tunnelling is possible between the silicon and SRN film at a distance $x > x_o$. All charge transfer is assumed to be through direct tunnelling between the trap states in the SRN film and either the conduction or valence band of the silicon substrate. Figure 7.10 a) and b) show the energy band diagram of the device under forward and reverse bias conditions. Under forward bias it is assumed there is tunnelling of electrons from the valence band of the silicon into the trap states in the SRN film giving rise to a net increase in negative charge in the film. This is equivalent to the tunnelling of holes from the trap states to the valence band of the silicon. It is not known whether the traps in the insulator are electron, hole or electron and hole traps as their effects cannot be distinguished. However, it is assumed for simplicity that electrons are the mobile species and that the traps are essentially donor-like. (i.e. positively charged when empty). A parallel situation holds under negative bias. It is assumed that detrapping occurs under negative voltages as trapped electrons tunnel from the trap states in the SRN film into the conduction band of the silicon substrate. The details of this model will be developed for the positive polarity case
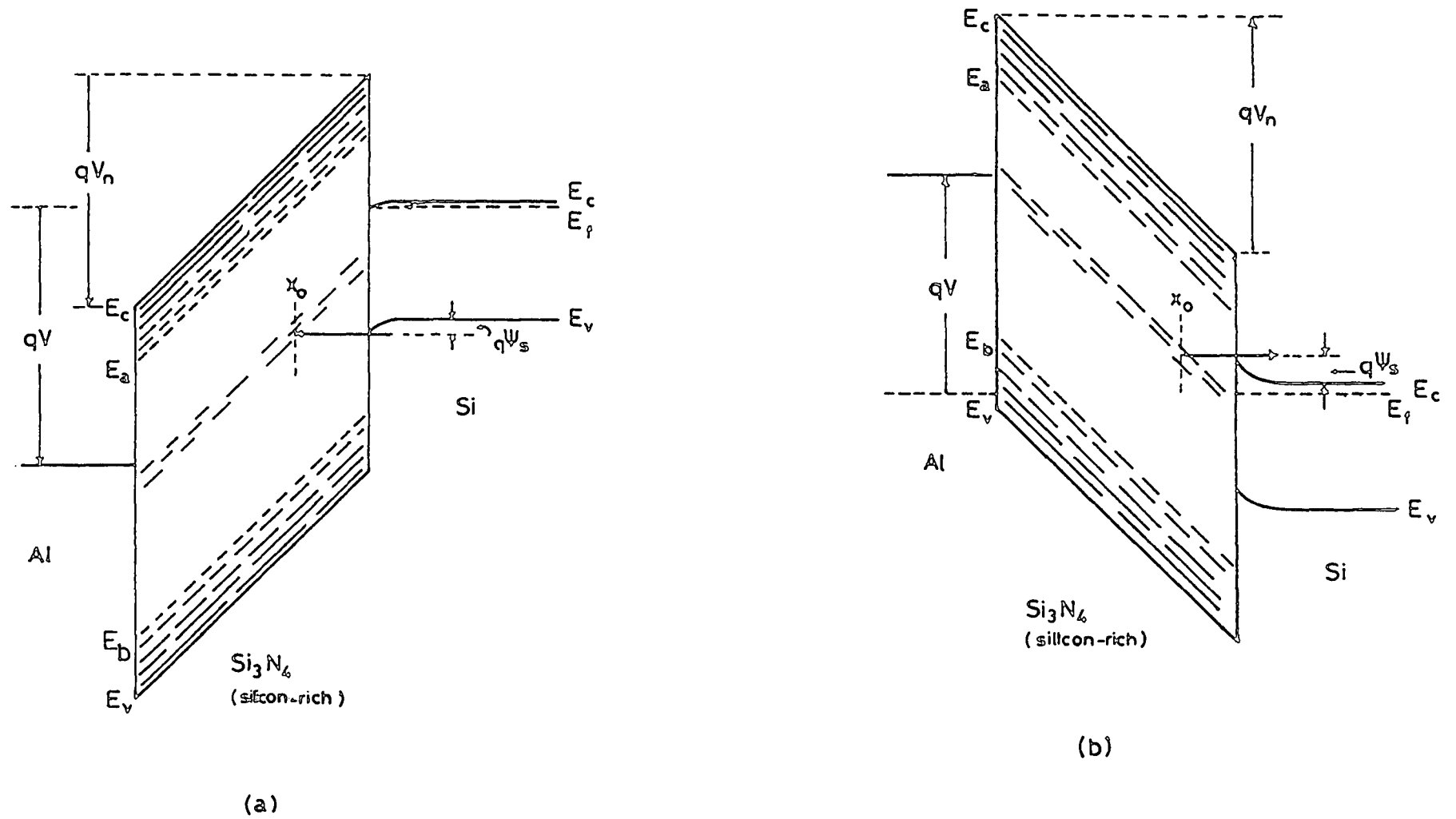
110

Figure 7.10    Energy  band  diagram  of Al-SRN-Si system under
a) positive bias and b) negative bias.

as an example. The negative polarity case yields the same result.

By definition, the rate at which charges transfer from the silicon valence band into the trap states (per unit volume, per unit time) is given by

$$T(x,t) = P(x,t) \left[ N - n_t(x,t) \right] \qquad (7.4)$$

where N is the concentration of trapping sites per unit volume. $n_t(x,t)$ is the number of filled states per unit volume and $P(x,t)$ is the tunnelling probability at a position. x. and time, t. $N - n_t(x,t)$ is simply the number of empty states at any position, x. and time. t. The transition rate is the number of empty states multiplied by the tunnelling probability. From charge conservation, the transition rate into the trapping states must be equal to the increase in the number of filled sites per unit time : i.e.

$$T(x,t) = \frac{dn_t(x,t)}{dt} \qquad (7.5)$$

Equating the right hand sides of equations 7.4 and 7.5 we obtain

$$\frac{d\, n_t(x,t)}{dt} = P(x,t) \left[ N - n_t(x,t) \right] \qquad (7.6$$

We now make the assumption that the tunnelling probability for an individual electron. tunnelling into a trap at a position x. is independent of time. Implicit in this assumption is that

111

the effective barrier height is not greatly affected by the application of an electric field. This is probably justified as the effective tunnelling barrier height is quite large (i.e. › 2.0 eV). The solution of equation 7.6, using Laplace transforms gives the following.

$$s^2 \, n_t(x,s) - n_t(t=0) + s \, P(x) + n_t(x,s) = P(x) \, N \qquad (7.7)$$

If we assume that at a time, t = 0, all of the traps are empty, (i.e. $n_t(x,t=0) = 0$), $n_t(x,t)$ is given by

$$n_t(x,t) = \int_0^t P(x) \, N \, \exp\left[ -P(x) \, t' \right] \, dt' \qquad (7.8)$$

which yields

$$n(x,t) = N \left[ 1 - \exp\left[ -P(x)t \right] \right] \qquad (7.9)$$

It is assumed that the functional form of the tunnelling probability is similar to that for tunnelling through a rectangular barrier [18]. The probability is then taken to be of the form

$$P(x) = P_o \, \exp\left( \frac{-x}{\lambda} \right) \qquad (7.10)$$

where $P_o$ is a constant and $\lambda$ is an effective constant that is dependent upon the details of the potential barrier. An

expression for $\lambda$ is given by

$$\lambda = \frac{h}{4\pi \, (2m^* \, E)^{\frac{1}{2}}} \qquad (7.11)$$

where $m^*$ is the electron effective mass in the SRN films, h is Planck's constant and E is the effective barrier height. For a rough estimate of $\lambda$, when equation 7.11 is evaluated with $m^* = m_o$ (the electron rest mass) and an effective barrier height of about 2.5 eV, $\lambda$ is of the order of 0.6 Å.

The transition rate for the entire trap distribution for a film of thickness, d, becomes

$$\pi(t) = \int_{x_o}^{d} T(x,t) \, dx \qquad (7.12)$$

By substitution of equations 7.4, 7.9 and 7.10 into 7.12, the total transition rate becomes

$$\pi(t) = \int_{x_o}^{d} NP(x) \, \exp\left[-P(x)t\right] \, dx$$

$$= NP_o \int_{x_o}^{d} \exp\left(\frac{-x}{\lambda}\right) \, \exp\left[-P_o\exp\left(\frac{-x}{\lambda}\right)t\right] \, dx \qquad (7.13)$$

Equation 7.13 can be integrated in a closed form to yield

$$\pi(t) = N\lambda \left[\frac{1 - \exp(t/t_o)}{t}\right] \qquad (7.14)$$

where the substitution

113

$$t_o = \left[ P_o \exp\left(\frac{-x_o}{\lambda}\right) \right]^{-1} \qquad (7.15)$$

has been made. The total charge transferred in a time, t, is given by

$$Q(t) = q \int_o^t \pi(t') \, dt' \qquad (7.16)$$

and with the substitution of equation 7.14 into 7.16, the exponential integral [19] gives the result

$$Q(t) = qN\lambda \left[ \ln(t/t_o) + \gamma + E_1(t/t_o) \right] \qquad (7.17)$$

where $\gamma$ is Euler's constant ($\gamma = 0.57721$) and $E_1$ is an exponential function which decays rapidly for times $t \gg t_o$ [19]. Therefore the following approximation can be made for long periods of time.

$$Q(t) = qN\lambda \left[ \ln(t/t_o) + \gamma \right] \qquad (7.18)$$

Assuming that most of the charge is trapped very close to the interface between the SRN film and the silicon substrate, the flat band shift from the C-V curves is related to the trapped charge by the expression

$$\Delta V_{FB} = \frac{Q(t)d}{\varepsilon_o \varepsilon_n} \qquad (7.19)$$

where $\varepsilon_n$ is the low frequency dielectric constant of the SRN film. Therefore for long times, $t \gg t_o$, the flat band shift is

114

given by

$$\Delta V_{FB} = \frac{qN\lambda d}{\varepsilon_o \varepsilon_n} \left[ \ln(t/t_o) + \gamma \right] \tag{7.20}$$

As is intuitively obvious, this model does predict the logarithmic time dependence of the flat band shift as has been shown to be the case experimentally.

7.2.2  Charge Trapping Model - Analysis of Flat Band Shift

From the model presented in the previous section, a plot of $\Delta V_{FB}$ versus log time yields a straight line with a gradient given by

$$\text{gradient} = \frac{qN\lambda d}{\varepsilon_o \varepsilon_n} \tag{7.21}$$

Figure 7.11 shows the flat band shift as a function of time for a range of applied voltages of both polarities for a film with $R_n = 4.0$. Similar results for films with $R_n = 1.0$ and $R_n = 0.5$ are illustrated in Figs. 7.12 and 7.13 respectively. It can been seen from these graphs that, within experimental error, the curves are essentially straight. The exception lies with the curves for the higher voltages. In the development of the model it was assumed that the only process that involved charge transfer in and out of the traps was a tunnelling process. For the lower bias voltages this appears to be valid. However, as the voltage and likewise the electric field in the SRN film is increased, there is a finite amount of Poole-Frenkel emission from the traps. As can be seen in all the high bias curves in

**Figure 7.11** Flat band shift as a function of time, for both positive and negative polarities. $R_n = 4.0$
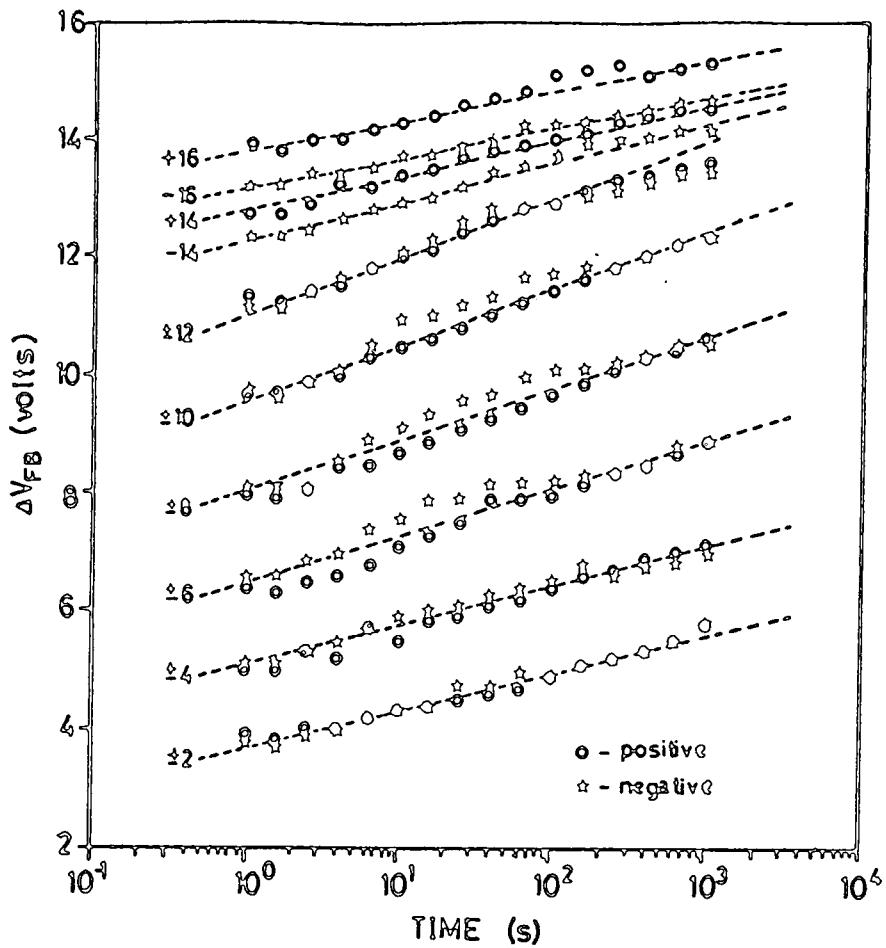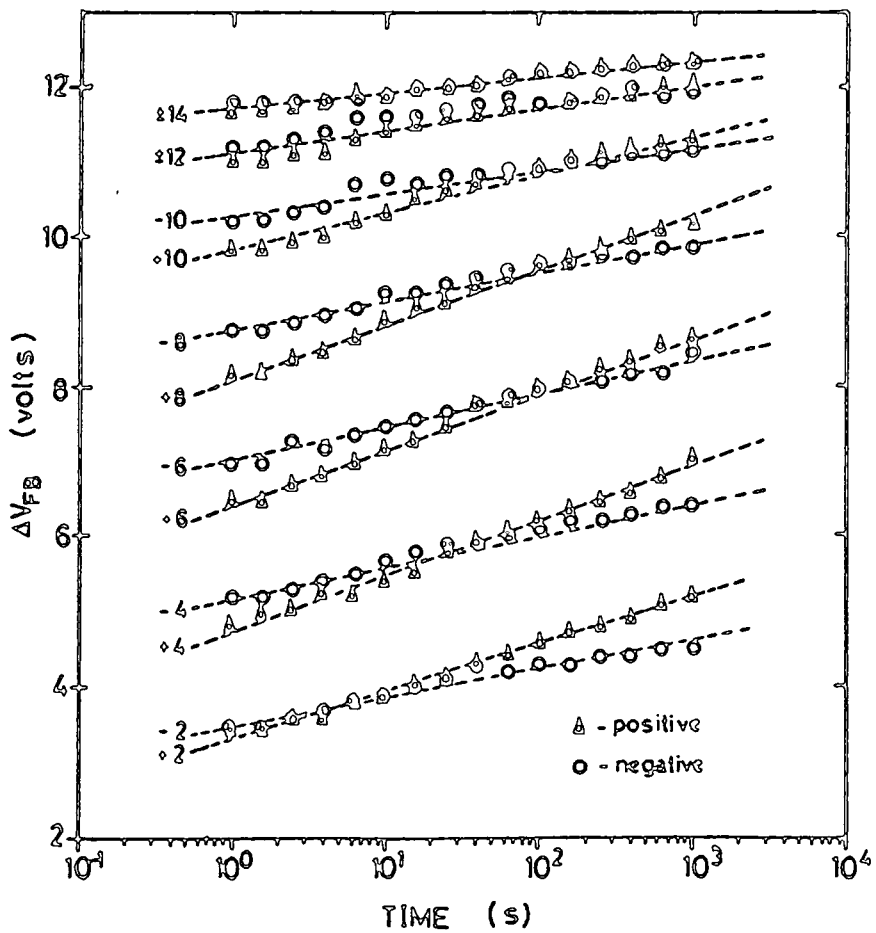


**Figure 7.12** Flat band shift as a function of time, for both positive and negative polarities. $R_n = 1.0$
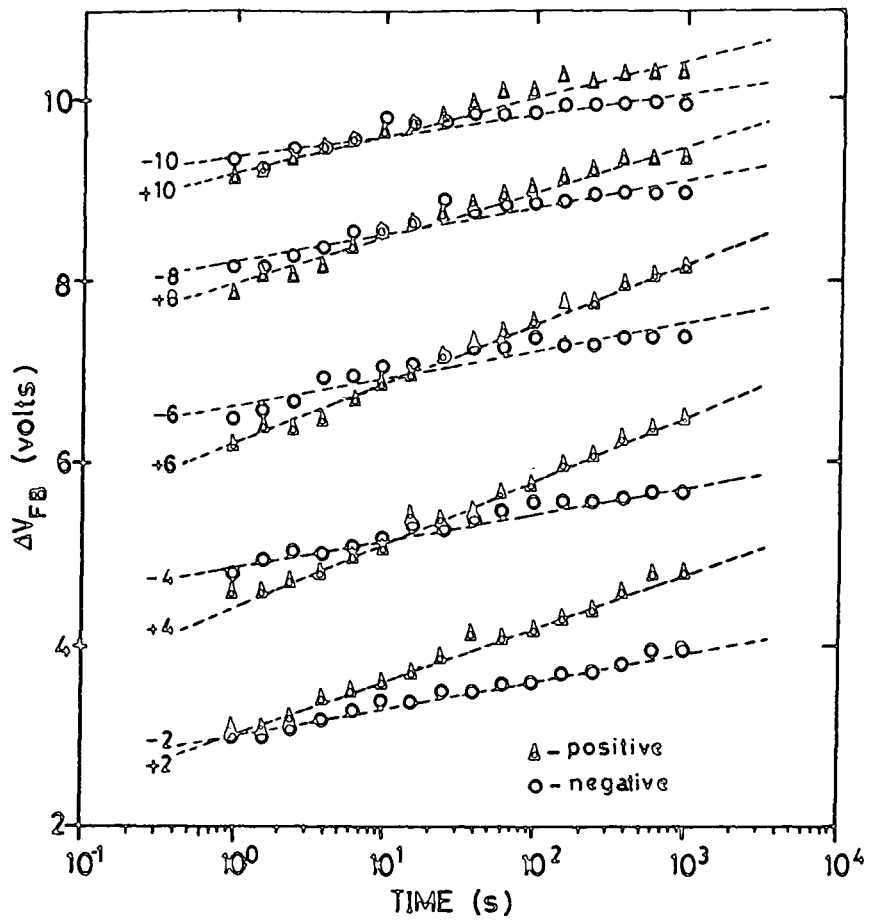
Figure 7.13    Flat band shift as a function of time, for both positive and negative polarities.   $R_n$ = 0.5
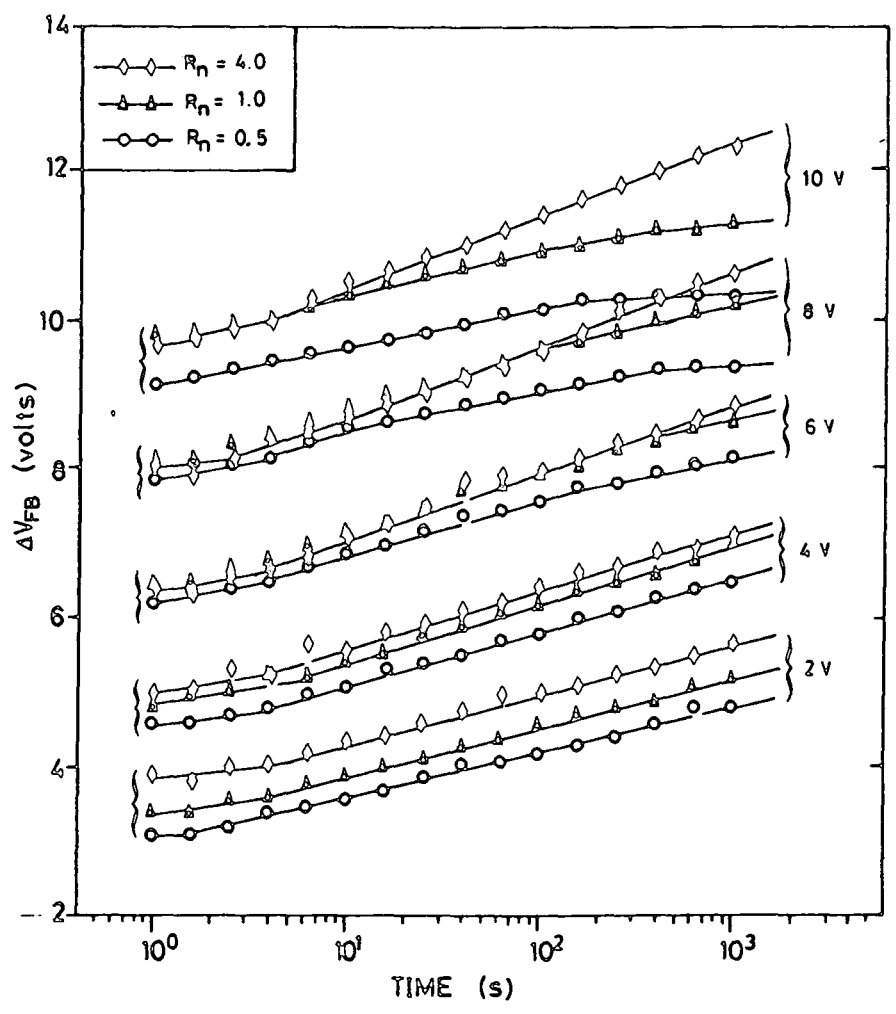


Figure 7.14    Flat  band shift as a function of time, for both positive positive bias polarity and three values of R

Figs. 7.11. 7.12. 7.13. the flat band shift tends to 'saturate' in time. It is believed that this is simply due to the error in our original assumption, with increasing electric field strength. The reduction in the shift with time could not be thought of as a complete saturation of the filled traps as the increased electric field has a tendency to empty the traps, not fill them. This would be wholly inconsistent with the present model.

For positive and negative polarity, the slopes of the transient flat band shift curves, for the low bias voltage, are essentially the same at least for the film with the lowest excess silicon content (i.e. $R_n = 4.0$, Fig. 7.11). However, for films with higher concentrations of silicon, the slope of the flat band shift is no longer independent of polarity. even at the lowest bias voltages. Within the context of our model. $\lambda$ is the only parameter that could give rise to this polarity dependence. This parameter is a function of the effective mass of the trapped carriers as well as the effective barrier height (based on a rectangular barrier: see Equation 7.11).

Assume for the moment that it is the effective mass that gives rise to the polarity dependence. If this were the case. the carriers must be essentially different in the two polarities: for example holes in one polarity and electrons in the other. The slope for the negative bias is always less than the slope for the same positive bias. This implies that the effective mass of the carriers for positive bias must be less than that for negative bias. as $\lambda$ is inversely proportional to the square root of $m^*$. In most materials, electrons have a

higher effective mass than do holes in the same material. Therefore under positive bias, the carriers would need to be holes and under negative bias, electrons. If we assume that there are both electron and hole traps in these films, from the positive bias band diagram in Fig. 7.10a the capture of an electron from the valence band of the silicon is essentially the same as emission of a hole from the trap to the valence band. Under negative bias (see Fig 7.10b), the only obvious mechanism is the emission of an electron into the conduction band of the silicon. It is interesting to note that the average ratio of the positive to negative slope is approximately constant at 1.3. There is a slight increase in the ratio for the films with $R_n$ = 0.5. A difference in carrier types is, therefore, one possible explanation of the polarity dependence of the transient flat band shift.

The only other parameter within $\lambda$ that can alter the slopes of the transient flat band curves is the effective tunnelling barrier height. The tunnelling barrier for the carriers with negative bias must be higher than under positive bias in this explanation. It is surmised, therefore, that the 'trap level' must lie closer to the conduction band than the valence band. It must also shift the 'trap level' slightly towards the conduction band edge with increasing silicon content. This would also explain the difference in the slopes of the transient flat band under different bias polarities. From the steady state analysis presented in the Chapter 6, it was conjectured that the effective trap depth did decrease slightly with increasing silicon content and as such it agrees

with this analysis.

Figure 7.14 shows the transient flat band curves for three values of $R_n$ , over a range of positive bias voltages. This figure illustrates a comparison of the curves of films of different excess silicon content. As the silicon content increases, the bias voltage at which the curves begin to 'saturate' decreases. With increasing excess silicon content in the SRN films, the conductivity increases, and not only does the trap depth decrease slightly, but the minimum voltage (or electric field) needed to initiate the Poole-Frenkel mechanism also decreases (see Fig 6.1). Once the current due to the Poole-Frenkel emission becomes greater than the transient tunnel current, the density of trapped carriers starts to decrease. The 'saturation' of the transient flat band shift curves reflect the bias at which this transition takes place.

From the slopes of the curves in Figs. 7.11, 7.12 and 7.13, the parameter $N\lambda$ was calculated and is presented in Table 7.2. The data does not show any specific trend. The variation of $N\lambda$ as a function of the excess silicon content (or $R_n$ ) is not large. This lack of any trend may be due to the uncertainty in the value of the low frequency dielectric constant, $\varepsilon_n$, especially for the films with $R_n = 0.5$. It may also be due to the errors incurred during the experimental measurement of the transient flat band shift. However, the estimated error in these values are at most $+/- 0.5$ V.

If $\lambda$ is taken to be on the order of 1 Å, the density of traps is about $3 \times 10^{19}$ $cm^{-3}$ , which is not unreasonable.

Table 7.2    The parameter $N\lambda$ extracted from the flat band shift transients for both positive and negative bias voltages.

| Bias Voltage $\div V_B$ (volts) | $R_n=4.0$, $\epsilon_n=6.60$, $d=320$ Å | | $R_n=1.0$, $\epsilon_n=7.16$, $d=300$ Å | | $R_n=0.5$, $\epsilon_n=7.31$, $d=324$ Å | |
|---|---|---|---|---|---|---|
| | $N\lambda$ (+ve) $\times10^{11}$ (cm$^{-2}$) | $N\lambda$ (-ve) | $N\lambda$ (+ve) $\times10^{11}$ (cm$^{-2}$) | $N\lambda$ (-ve) | $N\lambda$ (+ve) $\times10^{11}$ (cm$^{-2}$) | $N\lambda$ (-ve) |
| 2.0 | 3.10 | 1.78 | 3.59 | 2.06 | 3.28 | 1.68 |
| 4.0 | 3.62 | 2.12 | 4.19 | 2.45 | 3.68 | 1.55 |
| 6.0 | 3.82 | 2.34 | 4.42 | 2.70 | 3.70 | 1.53 |
| 8.0 | 3.62 | 1.99 | 4.19 | 2.31 | 2.88 | 1.58 |
| 10.0 | 2.66 | 1.55 | 3.07 | 1.79 | 2.29 | 1.24 |
| 12.0 | 1.94 | 1.23 | 2.24 | 1.44 | ---- | ---- |
| average (2-10V) | 3.36$\div$0.18 | 1.96$\div$0.07 | 3.89$\div$0.25 | 2.26$\div$0.10 | 3.17$\div$0.28 | 1.52$\div$0.02 |

7.2.3  Charge Trapping Model - Analysis of Current Transient

From the expression for the total transition rate to and from the traps, equation 7.14, the current density is given by $J = q \pi (t)$. For times $t >> t_o$, the current density becomes

$$J(t) = \frac{qN\lambda}{t} \qquad \qquad (7.22)$$

Figures 7.15, 7.16 and 7.17 illustrate the transient current over a range of positive bias voltages for $R_n = 4.0$, $R_n = 1.0$ and $R_n = 0.5$ respectively. The transient current is the current measured in conjunction with the transient flat band voltage. After the voltage had been ramped to the desired bias, and the time for that particular measurement had expired, the current was measured before the voltage was ramped back to the holding voltage.

From equation 7.22, the slopes of the curves in Figs. 7.15 - 7.17, should be equal to (-) unity if the the assumption is made that the only mechanism contributing to the current is the transfer of charge in and out of the traps by direct tunnelling. The intercept should yield the value of $N\lambda$. Table 7.3 presents the calculated results of the gradients and $N\lambda$ as a function of $R_n$ using a least squares fit. For the characteristics at low bias voltages, the magnitude of the gradients are close to unity. The $N\lambda$ values are of the same order as those extracted from the flat band shift characteristics. However, as the magnitude of the bias is increased, the curves deviate from our model. The increase
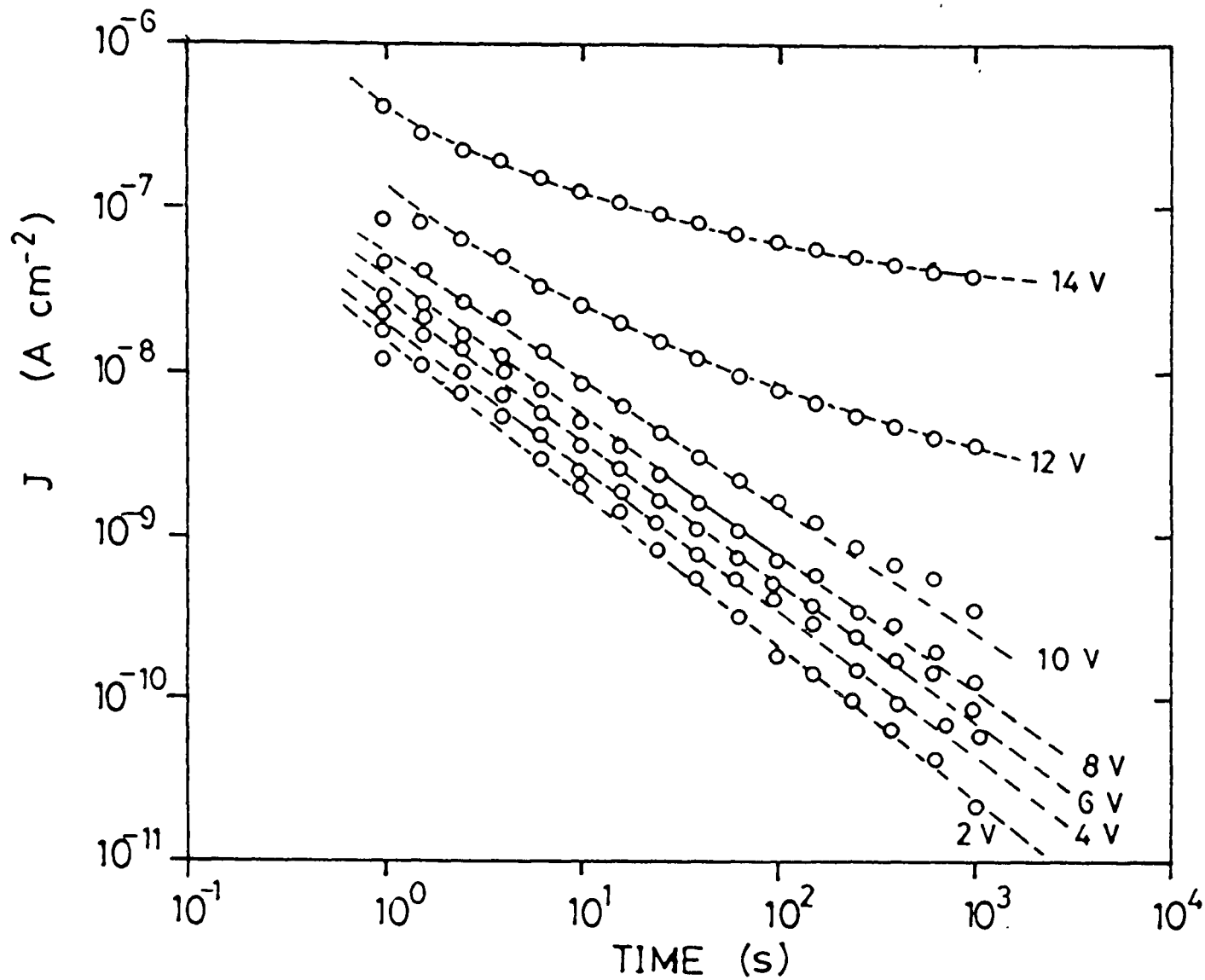
119

Figure 7.15    Current   transient   (J vs t),   for   a   range   of
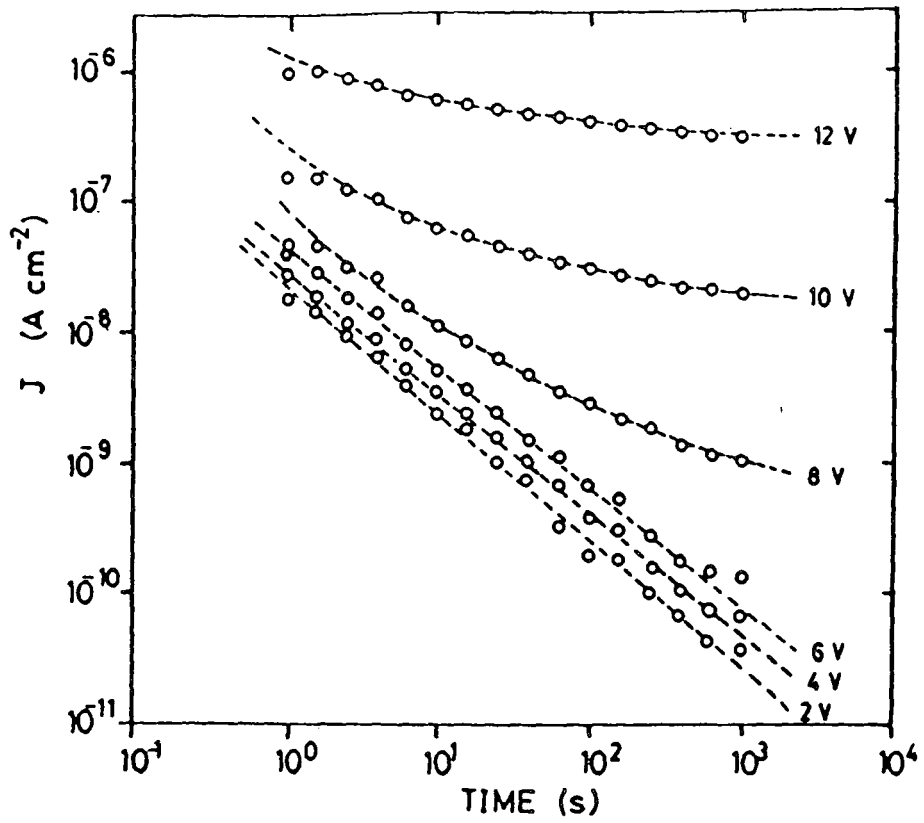positive bias voltages for films with $R_n$ = 4.0.

Figure 7.16    Current  transient  (J vs t),  for  a  range  of
positive bias voltages for films with $R_n$ = 1.0.
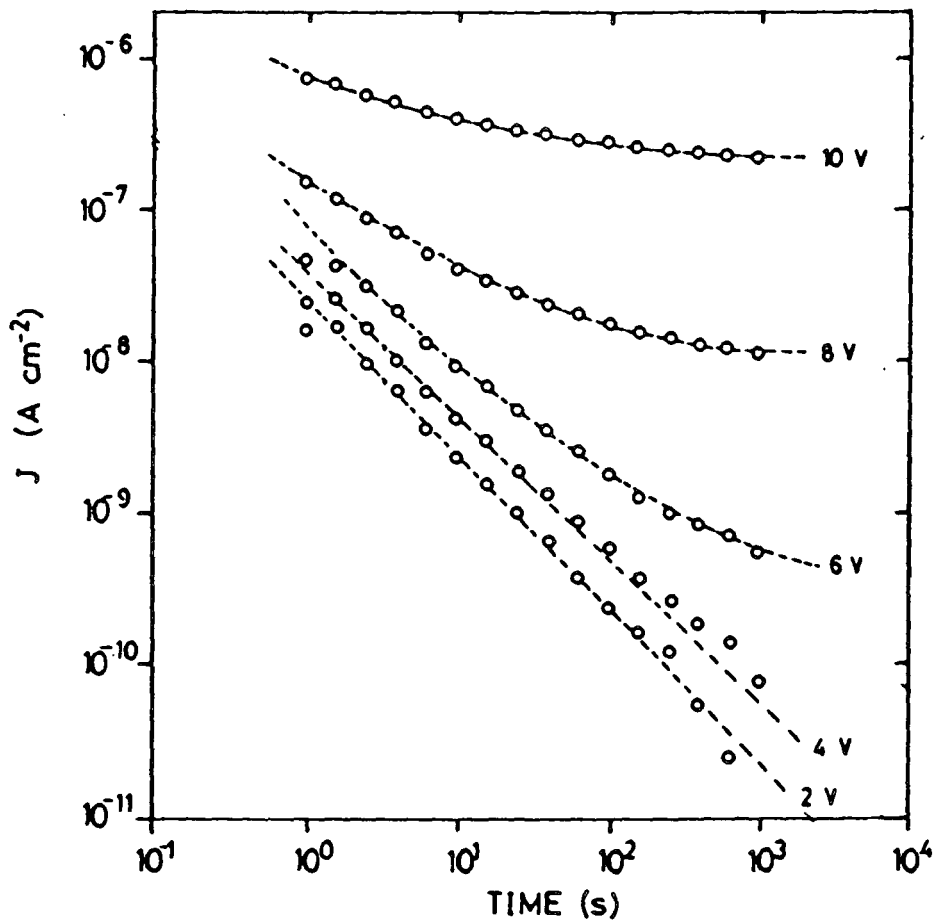


Figure 7.17    Current  transient  (J vs t),  for  a  range  of
positive bias voltages for films with $R_n$ = 0.5.

Table 7.3    The gradient and the parameter $N\lambda$ extracted from the positive bias current transients for three $R_n$ values.

| Bias Voltage $+V_B$ (volts) | $R_n = 4.0$ | | $R_n = 1.0$ | | $R_n = 0.5$ | |
|---|---|---|---|---|---|---|
| | gradient | $N\lambda$ $\times 10^{11}$ (cm$^{-2}$) | gradient | $N\lambda$ $\times 10^{11}$ (cm$^{-2}$) | gradient | $N\lambda$ $\times 10^{11}$ (cm$^{-2}$) |
| 2.0 | -0.802 | 0.78 | -0.970 | 1.42 | -1.00 | 1.42 |
| 4.0 | -0.809 | 1.16 | -0.852 | 1.42 | -0.844 | 1.91 |
| 6.0 | -0.977 | 2.12 | -0.839 | 2.34 | -0.686 | 3.16 |
| 8.0 | -0.836 | 2.12 | -0.606 | 3.16 | --- | --- |
| 10.0 | -0.726 | 2.86 | --- | --- | --- | --- |

in current, at any given time, must be due to the onset of Poole-Frenkel emission from the traps. The bias point at which the current transients deviate from the model is about the same as that at which the flat band characteristics 'saturate'. At this bias voltage, the current due to Poole-Frenkel emission from the traps is greater in magnitude than the tunnel current.

The relaxation of the Poole-Frenkel current, at high electric fields, is most likely to be due to a balancing of the emission from the traps and the effect that the trapped space charge has on the local electric field and therefore on further emission. A dynamic equilibrium is reached when the rate of Poole-Frenkel emission from the traps is equal to the rate of carriers tunnelling into the traps.

Figures 7.18, 7.19 and 7.20 illustrate the current density-electric field characteristic for delay times of 1, 10 100 and 1000 seconds for films with $R_n$ = 4.0, $R_n$ = 1.0 and $R_n$ = 0.5 respectively. The inset in each figure shows the calculated dynamic dielectric constant calculated from the gradient of the high field section of each curve. Firstly, it can be seen from these graphs, that there is a remarkable difference in the current field characteristics as a function of bias time. This reflects the effect of the trapped charge on the local electric field within the SRN field.

It should be remembered that these measurements were taken in parallel with the flat band shift curves. The ramp rate used for these measurements was about 5 V.s and the holding voltage was -20 V. With this in mind, one cannot expect a one second reading to be of great accuracy. For example, to ramp

Figure 7.18    Schottky plots (J vs F$^{\frac{1}{2}}$ ), for positive bias, for delay times of 1s, 10s, 100s, and 1000s for a film with R$_n$ = 4.0.    Inset gives the calculated dynamic dielectric constant, (calculated from the slope), as a function of time.

The inset table contained within the figure:

| Time | $\varepsilon_d$ |
|------|------|
| 1 s | 5.09 |
| 10 s | 4.31 |
| 100 s | 3.71 |
| 1000 s | 3.44 |

Figure 7.19    Schottky plots (J vs $F^{\frac{1}{2}}$), for positive bias, for delay times of 1s, 10s, 100s, and 1000s for a film with $R_n = 1.0$. Inset gives the calculated dynamic dielectric constant, (calculated from the slope), as a function of time.

| Time | $\varepsilon_d$ |
|------|------|
| 1 s | 5.26 |
| 10 s | 4.49 |
| 100 s | 4.04 |
| 1000 s | 3.67 |

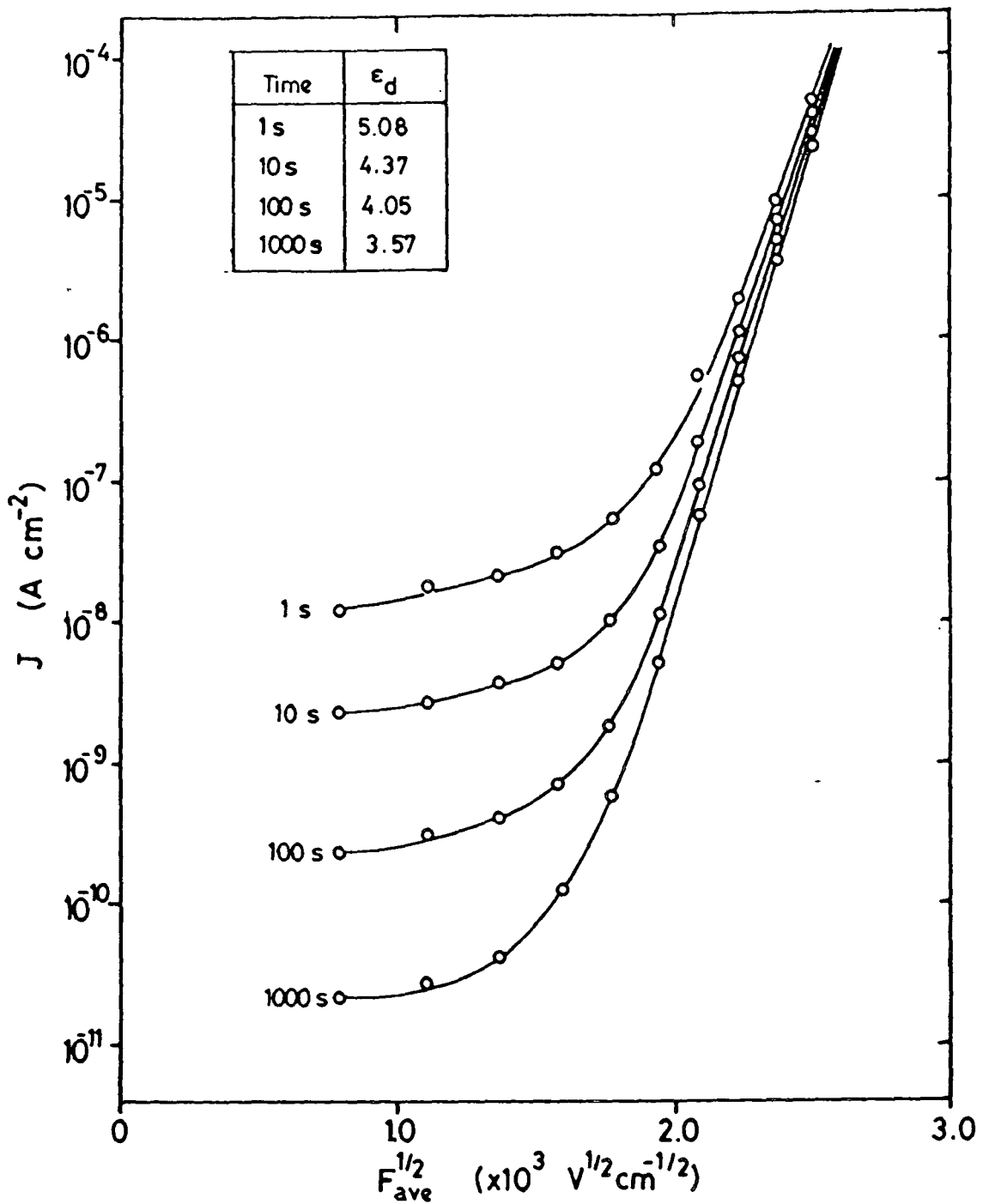**Figure 7.20** Schottky plots ($J$ vs $F^{1/2}$), for positive bias, for delay times of 1s, 10s, 100s, and 1000s for a film with $R_n = 0.5$ Inset gives the calculated dynamic dielectric constant, (calculated from the slope), as a function of time.
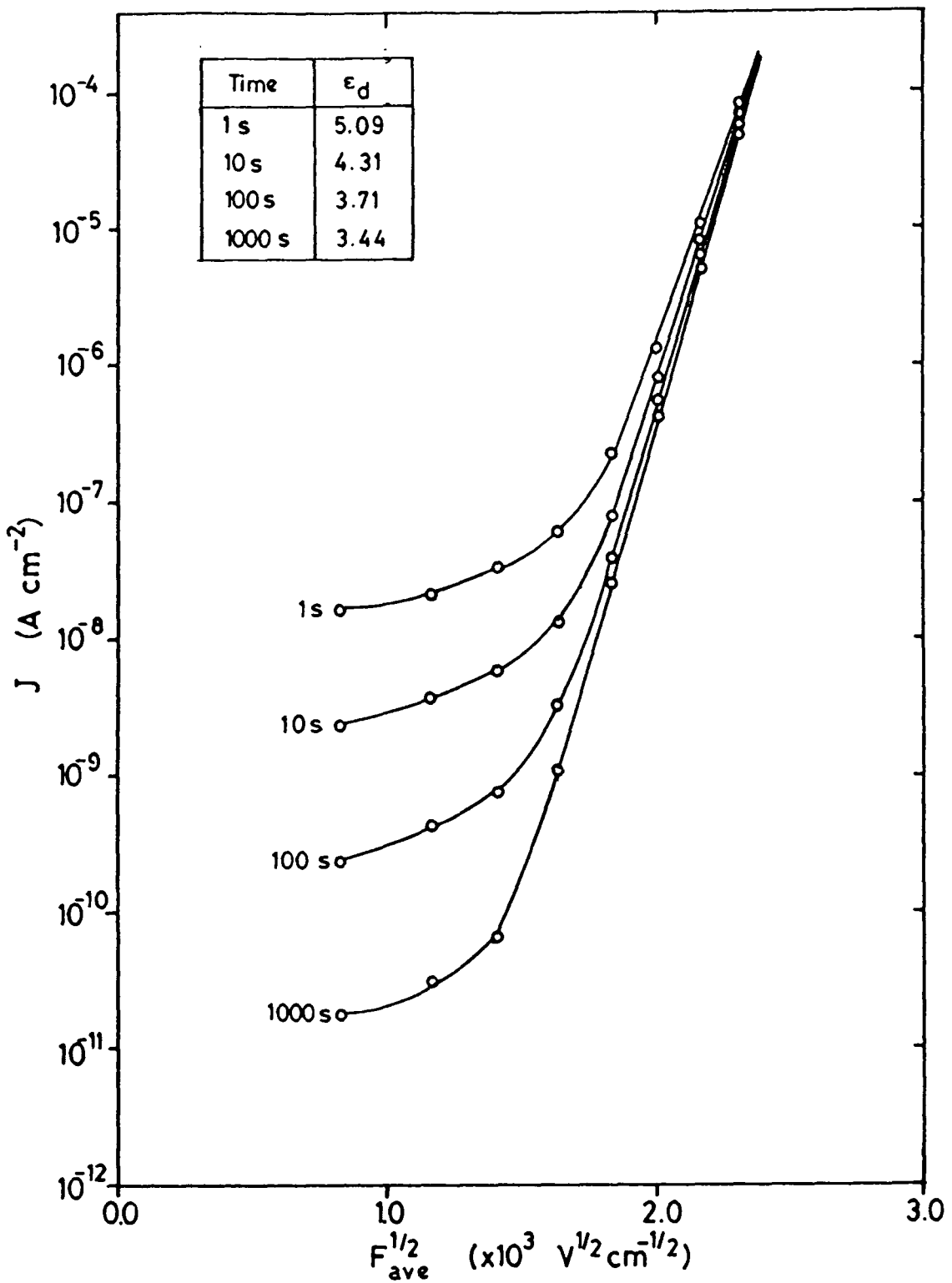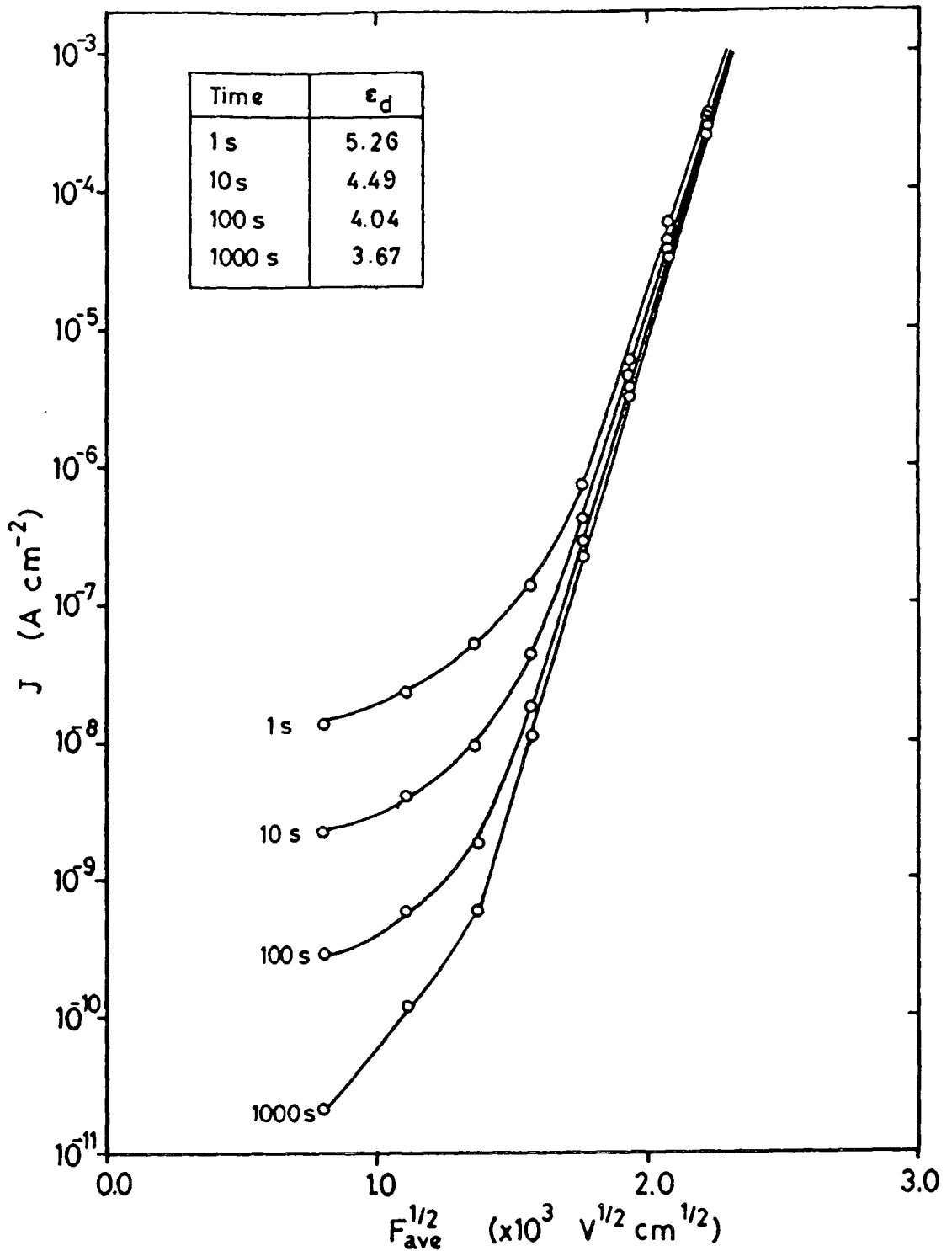
from -20 V to, say +10 V, would take about 6 seconds and during all this time the traps are being filled and/or emptied. For times less than about 10 seconds the analysis of these curves should therefore be treated with care.

As was expected from the previous analysis in Chapter 6, the effect of the trapped charge is very significant. The calculated dynamic dielectric constant appears to decrease dramatically as a function of the delay time for all the films measured. The experimental errors in the calculated dynamic dielectric constant were not calculated for these results as the number of samples was very low. For the shortest time periods, the errors are estimated to be rather large and of the order of +. - 0.5, while for the longest time they are of the order of + - 0.2. These estimates are obtained from the total mean square error in the gradients and then calculated through to the dielectric constant. Taking into account these rather poor estimates of the error, there still seems to be an increase in the calculated dynamic dielectric constant with increasing excess silicon content. However, the most dramatic effect for all films, is the decrease in the calculated dynamic dielectric constant with time. For short bias times, the values are much more reasonable than those extracted from the steady state results. For stoichiometric values of silicon nitride, the optical dielectric constant is about 4 and the low frequency dielectric constant is about 7. The values obtained for the short bias times are all between these limits for all values of excess silicon content.

## 7.3 Summary

A model has been presented that explains the charge storage in the SRN films as reflected by the shift in the flat band voltage with time. Under positive bias the charge storage is due to either the injection of electrons from the silicon valence band into the traps or to the emission of holes from the traps into the valence band. The latter appears to be the most likely and it accounts for the positive shift in the flat band voltage corresponding to an increasing stored negative charge with increasing bias time. For negative bias voltages, the emission of electrons from the traps into the silicon conduction band, leaving behind ionized donors, is responsible for the negative shift in the flat band voltage with time, and thus for the increase in positive charge in the films. The above charge transfer mechanisms are by direct tunnelling.

For high electric fields, the Poole-Frenkel mechanism dominates over the emission or capture of carriers through tunnelling. As the electric field increases, the emission of carriers into the band tails reduces the total number of trapped carriers and tends to 'saturate' the transient flat band.

The current transients for low bias voltages are also due to the tunnelling of charge carriers into and out of these trapping levels. Again at high electric fields, the emission of carriers out of the traps into the band tails causes the current to deviate from the presented model. The balancing of the rate of capture of tunnelling carriers and the rate of Poole-Frenkel emission leads to the eventual relaxation of the high field characteristic.

The values of the dynamic dielectric constant calculated from the gradients of the Schottky plots are also found to be a function of the trapped charge. To obtain realistic values, very short delay times must be used. The calculated dielectric constant is between 5.0 and 5.3 for the present SRN films. The use of steady state analysis for the extraction of the dynamic dielectric constant leads to erroneous results unless the effects of the trapped charge are taken into account.

## References for Chapter 7

[1]  See for example E.H. Nicollian and J.R. Brews, MOS (Metal Oxide Semiconductor) Physics and Technology, John Wiley and Sons, New York, Chapters 5, 7 and 11, (1982).

[2]  D.M. Brown and P.V.Gray, J. Electrochem. Soc., 115, 760 (1968).

[3]  A. Goetzberger and J.G. Irvin, IEEE Trans. Electron. Dev., ED-15, 1009 (1968).

[4]  B.E. Deal, E.L. Machenna and P.L. Castro, J. Electrochem Soc., 116, 997 (1969).

[5]  F.H. Hielscher and H.M. Preier, Solid State Electron., 12, 527 (1969).

[6]  J.G. Simmons and L.S. Wei, Solid State Electron., 16, 43 (1973).

[7]  J.G. Simmons and L.S. Wei, Solid State Electron., 16, 53 (1973).

[8]  L.S. Wei and J.G. Simmons, Solid State Electron., 17, 1021 (1974).

[9]  L. Sullivan and H.C. Card, J. Phys. D : Appl. Phys., 7, 1531 (1974).

[10] A.M. Goodman, Appl. Phys. Lett., 13, 275 (1968).

[11] J. Robertson and M.J. Powell, Appl. Phys. Lett., 44, 415 (1984).

[12] see for example N.F. Mott and E.A. Davis, Electronic Processes in Non-Crystalline Materials, Oxford University Press, London (1971).

[13] R.H. Walden, J. Appl. Phys., 43, 1178 (1972).

[14] B.H. Yun, Appl. Phys. Lett., 27, 256 (1975).

[15] L.I. Popova, B.Z. Antov and P.K. Vitanov, Thin Solid Films, 36, 157 (1976).

[16] P.C. Arnett and D.J. DiMaria, J. Appl. Phys., 47, 2092 (1976).

[17] E.C. Ross and J.T. Wallmark, RCA Review, 30, 366 (1969).

[18] see for example E. Merzbacher, Quantum Mechanics John Wiley and Sons, New York, 93 (1961).

[19] M. Abramowietz and I.A. Stegun, Editors, <u>Handbook</u> <u>of</u> <u>Mathematical</u> <u>Functions</u>, 9th Edition, Dover Publications, New York, 228 (1972).

# Chapter 8

## Growth and Characterization of
## Silicon-Rich Oxide (SRO) Thin Films

### 8.1 Growth of Silicon-Rich Oxide (SRO) Thin Films

The system used to grow the films of silicon-rich oxide (SRO) in Durham was an atmospheric pressure chemical vapour deposition (CVD) reactor. The structure of an atmospheric CVD reactor is very similar to the low pressure CVD system that was used to grow the silicon rich $Si_3N_4$ thin films as shown in Fig. 4.1. All of the SRO films studied here were grown at temperatures between 600 and 700 $^o$C. Nitrogen was used as the carrier gas while the reactants were silane ($SiH_4$) and nitrous oxide ($N_2O$). The flow of the carrier was maintained at either 15 or 35 litres/minute. The reactant flow rates were varied between 5 and 50 ml/minute depending on the desired film composition.

The composition of the films was controlled by varying the gas phase ratio of the reactant gases. The gas phase ratio, $R_O$ is given by

$$R_O = \frac{\text{flow rate of } [ \; N_2O \; ]}{\text{flow rate of } [ \; SiH_4 \; ]} \qquad (8.1)$$

Therefore an increase in the value of $R_O$ would give a decrease in the silicon content of the grown film.

For CVD grown silicon dioxide films used industrially as passivating or insulating layers, the gas phase ratio is

126

typically $R_O > 100$ [1] but this value is very dependent on the growth conditions and the choice of the reactants. However, it has been found that to produce a noticeable change in the conductivity of the films, a value of $R_O < 10$ is needed [1]. As quite highly conducting films were of interest, they were grown in the range $R_O < 2.0$ .

All films were grown on an n-type silicon substrate. Aluminium top contacts of various sizes were evaporated onto all films through a contact mask and gold was deposited to form back contacts. The thickness and refractive index of all films were measured using standard ellipsometry techniques.

In the first instance a great many SRO films were grown. This was done to establish not only the range of excess silicon content that could be obtained, but also to produce films that were of uniform composition and thickness. These films, a great many of which were used for analysis presented in this chapter, were used to calibrate our CVD reactor.

## 8.2  Structural Analysis of Silicon-Rich Oxide (SRO) Films

A number of different experimental techniques were used to assess the structural and elemental composition fo the SRO films.  These included reflection high energy electron diffraction (RHEED). Auger electron spectroscopy (AES) and Rutherford backscattering spectrometry (RBS).  A discussion of these techniques and the experimental results for the SRO films is included in the following sections.

8.2.1  Rutherford Backscattering Spectrometry (RBS)

The details of the Rutherford backscattering technique have been presented in Section 5.2. Two sets of samples were examined for the author by Dr. C. Jeynes of Surrey University using this technique to determine the elemental composition of our thin films as a function of the silicon-rich oxide (SRO) gas phase ratio, $R_O$.

With the use of backscattering spectrometry, the elemental composition of the films can be determined. This technique gives an absolute measure of the silicon concentration. The deposition parameter, $R_O$, is very dependent upon the particular system used for film growth and it is not transferable between films grown using different systems.

Figure 8.1 illustrates an example of the measured spectrum for a film grown at $650\,^\circ C$ for a deposition time of 5 minutes with $R_O = 1.0$. The x-axis in this figure is the energy axis for the spectrum where each channel corresponds to a calibrated energy. The y-axis is the scattering yield with units of counts or counts per channel. As can be seen, there are two distinct peaks in the spectrum as expected. The peak at the lower end of the energy axis corresponds to the oxygen yield and depth, while the higher energy peak corresponds to the silicon yield and depth. The actual calculation of the total amount of silicon and oxygen in the films is performed by a computer integration of the peaks shown in Fig. 8.1.

The results are tabulated in Table 8.1 for films grown at T=650 $^\circ C$ and T=625 $^\circ C$. The actual silicon and oxygen surface concentrations are given along with their relative percentage
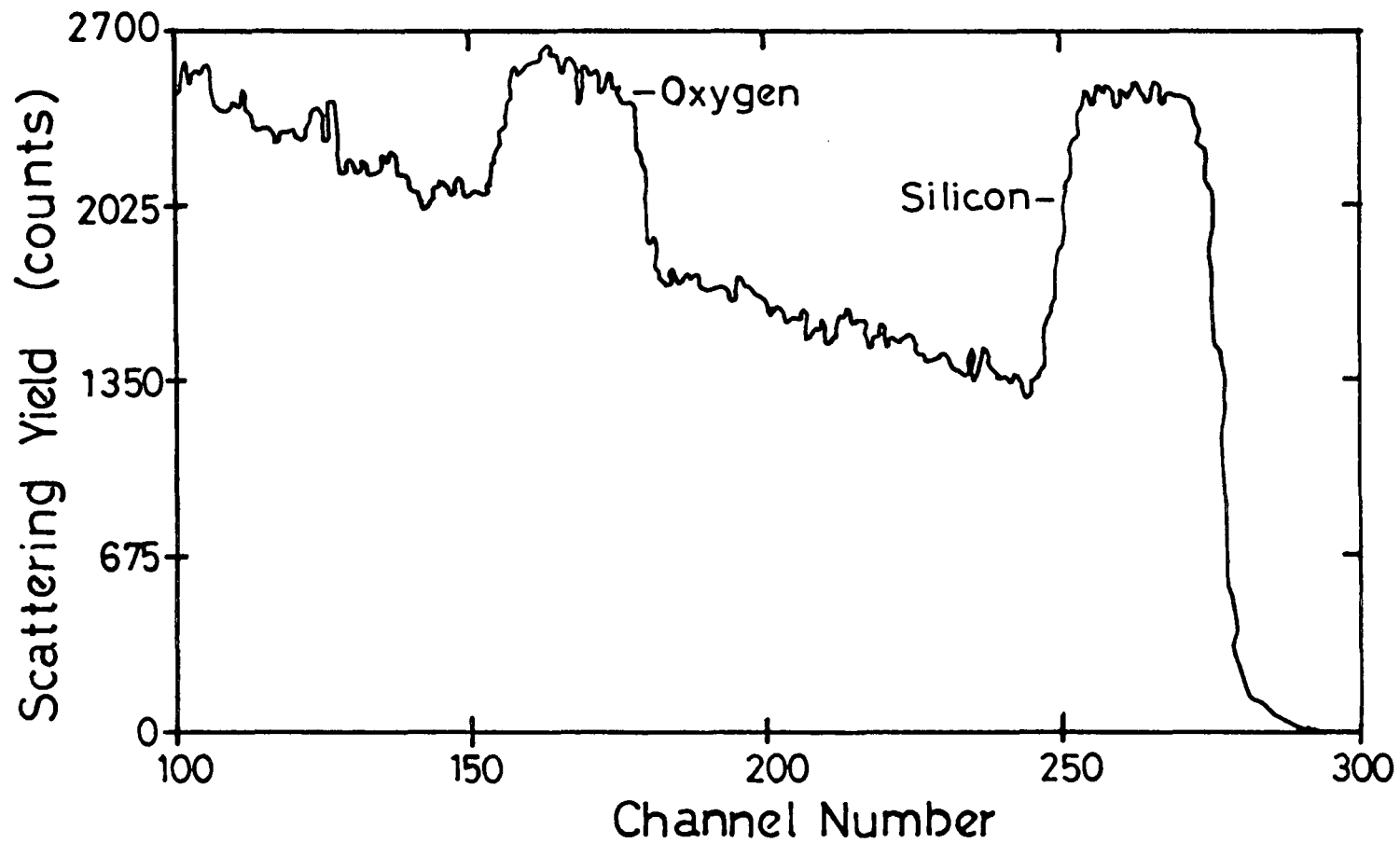
Figure 8.1     Rutherford backscattering spectrum of an SRO film with $R_O = 1.0$, $T = 650$ °C and a deposition time of 5 minutes.

| | $R_o$ | Run time (min.) | Si concentration $\times 10^{17}$ ($cm^{-2}$) | O concentration $\times 10^{17}$ ($cm^{-2}$) | Silicon (%) | Oxygen (%) | Excess Silicon (%) | Average Excess Silicon (%) |
|---|---|---|---|---|---|---|---|---|
| | 1.0 | 5 | 4.55 | 3.15 | 59.1 | 40.9 | 25.8 | 27.5 ± 2.7 |
| | | 10 | 9.80 | 5.90 | 62.4 | 37.6 | 29.1 | |
| $T = 625\ ^oC$ | 0.5 | 5 | 7.10 | 2.90 | 71.0 | 29.0 | 37.7 | 38.2 ± 0.3 |
| | | 10 | 14.0 | 5.54 | 71.6 | 28.4 | 38.3 | |
| | 0.25 | 5 | 8.39 | 2.37 | 78.0 | 22.0 | 44.6 | 44.1 ± 0.4 |
| | | 10 | 18.5 | 5.60 | 76.8 | 23.2 | 43.5 | |
| | 1.0 | 5 | 4.89 | 3.43 | 58.8 | 41.2 | 25.4 | 23.7 ± 2.9 |
| | | 10 | 11.3 | 9.14 | 53.3 | 44.7 | 22.0 | |
| $T = 650\ ^oC$ | 0.5 | 5 | 8.81 | 5.42 | 61.9 | 38.1 | 28.6 | 28.1 ± 0.3 |
| | | 10 | 18.9 | 12.2 | 60.8 | 39.2 | 27.4 | |
| | 0.25 | 5 | 10.7 | 4.54 | 70.2 | 29.8 | 36.9 | 35.7 ± 1.4 |
| | | 10 | 19.5 | 9.25 | 67.2 | 32.2 | 34.5 | |

Table 8.1    Data from Rutherford backscattering giving an elemental analysis of the SRO films as a function of deposition temperature and time and gas phase ratio.

contributions. The excess silicon content, quoted in Table 8.1, is the excess amount of silicon in the films relative to stoichiometric silicon dioxide (33.33% silicon). These results illustrate that with decreasing gas phase ratio the excess silicon in the films increases. However, there is quite a spread of results even for films grown at the same temperature but for different lengths of time. The averaged results are presented in the last column in Table 8.1. The errors quoted for the averages are the mean square errors.

The relationship between the gas phase ratio and excess silicon is not linear and it appears to be more logarithmic as shown in Fig. 8.2. These results not only tell us about the silicon 'richness' of the films but also give a calibration for further growth of similar films using this particular system. It is shown from this data that a wide range of excess silicon content in the SRO films may be obtained with the suitable adjustment of the deposition conditions.


## 8.2.2 Auger Electron Spectroscopy (AES)

Electron spectroscopy techniques measure the kinetic energy of electrons that are emitted from matter as a consequence of bombarding it with ionizing radiation or high energy particles. Various processes take place when atoms are exposed to ionizing radiation. The simplest is direct ionization of an electron from the valence or inner shell. The energy of the emitted electron is the difference between the ionizing radiation energy and the binding energy or ionization energy of the electron. For a given atom, a range of emitted energies
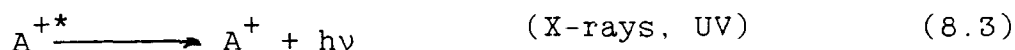
129
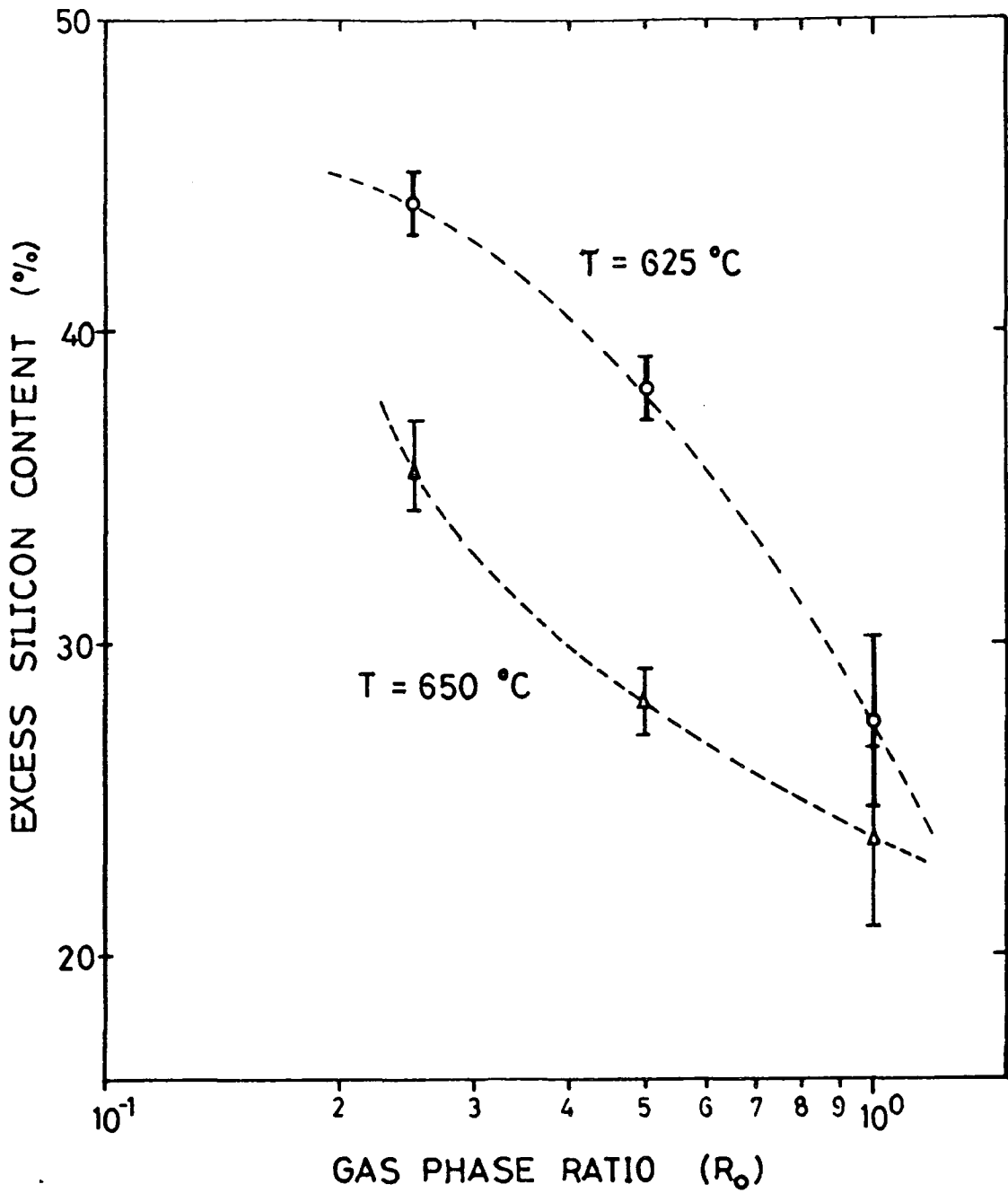
**Figure 8.2**   Excess   silicon   content   (over   stoichiometric
silicon dioxide) as  a  function  of  gas  phase
ratio, $R_O$ ,  for deposition temperatures of 625
and 650 $^\circ$C.

is obtained corresponding to the ionization energy of electrons from different inner and outer valence shells. The measurement of these energies provides a means in which to identify atoms and to determine their relative concentrations in an alloy or material. This process is known as electron spectroscopy for chemical analysis (ESCA).

Consider an atom being excited by ionizing radiation as in the ESCA technique. The process may be given by [2]

$$\text{Atom A} \xrightarrow{\text{radiation}} A^{+*} + e^- \qquad (8.2)$$
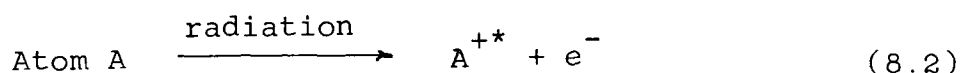
where $A^{+*}$ refers to the ionized atom which is in an excited state. This excited state arises either if an electron is ejected from an inner shell, leaving a vacancy, or if other electrons in the atom have been promoted to higher, normally empty levels during radiation. The excited atom decays when electrons drop into vacancies in lower energy levels. Energy is consequently released by one of two methods:

$$A^{+*} \longrightarrow A^+ + h\nu \qquad \text{(X-rays, UV)} \qquad (8.3)$$

or

$$A^{+*} \longrightarrow A^{++} + e^- \qquad \text{(Auger electrons)} \qquad (8.4)$$

The energy may be emitted as electromagnetic radiation, which is the normal method for producing X-rays, but for lighter atoms UV photons are usually produced. Alternatively, the

130

energy may be transferred to another (outer shell) electron in the same atom. This electron is then ejected from the atom. Such secondary ionized electrons are known as Auger electrons and it is the detection of these electrons as a function of energy that leads directly to the identification of materials.

Figure 8.3 shows a schematic diagram of the system that was used to perform the Auger analysis. This work was carried out for the author by Dr. D.J. Thomson at Stanford University. The system consists of an electron gun, a sputter ion gun, a magnetic shield and a detection unit. The electron gun is the source for the supply of electrons used to ionize the material held by the target holder. The energy of electrons for the present samples was 5 keV. The electrons ejected from the sample are then focused on to the detector, by the magnetic shield. The energy of the electrons detected can be swept through a range to determine the Auger spectrum of the material. Quite often the detection of Auger processes is difficult due to background emissions. Most Auger systems use the the first derivative of the measured Auger signal. The ion sputter gun supplies a beam of ions that can be used to etch away the surface of the sample in situ. The Auger technique is a surface sensitive technique and to obtain a profile of composites of the sample, the surface must be etched away while the measurement of the Auger signal takes place. Xenon was used as the active species for the sputtering of the samples.

An example of the Auger signal as a function of energy is shown in Fig. 8.4. The plotted signal is the first derivative of the actual detected signal. This technique is used to
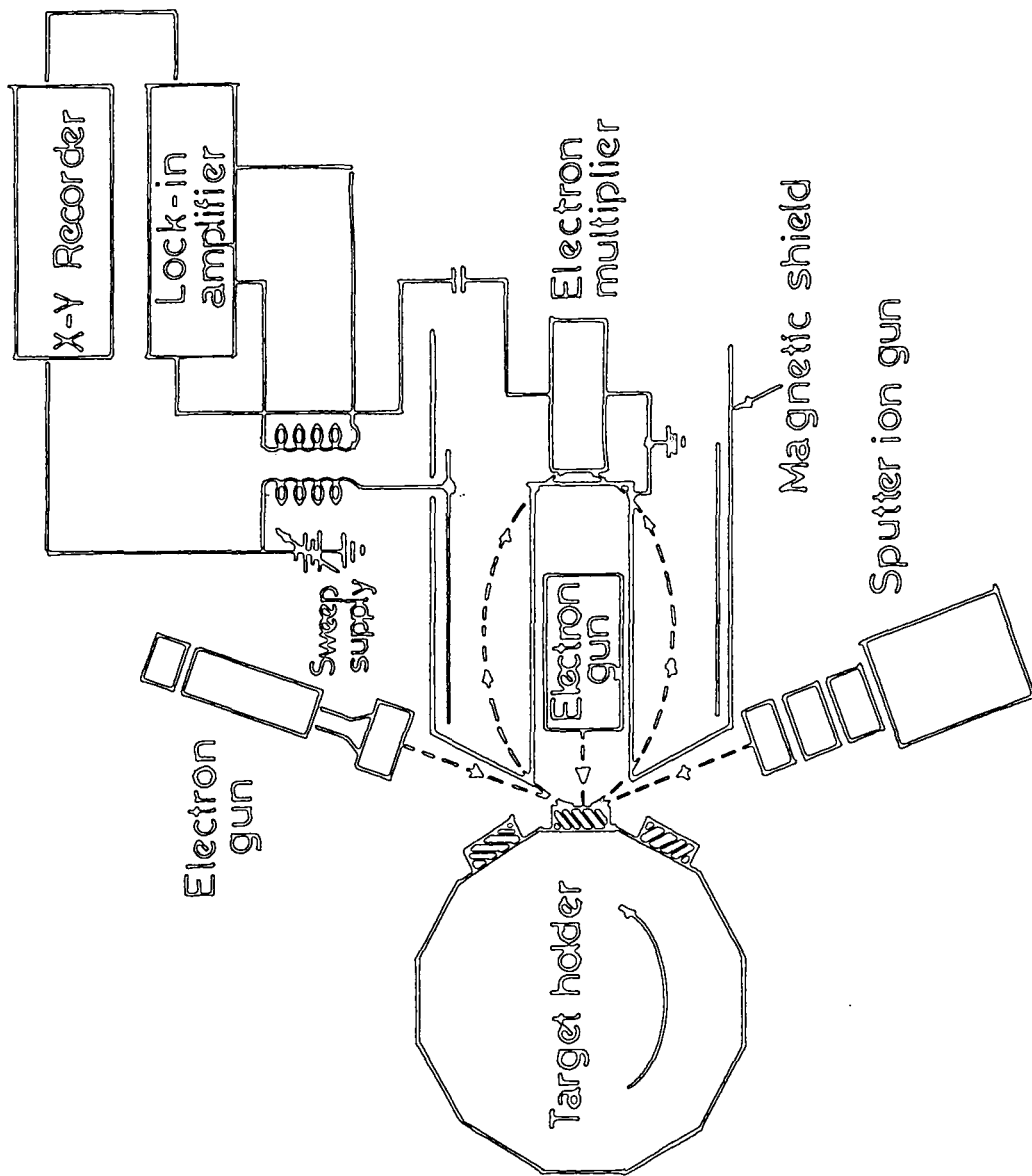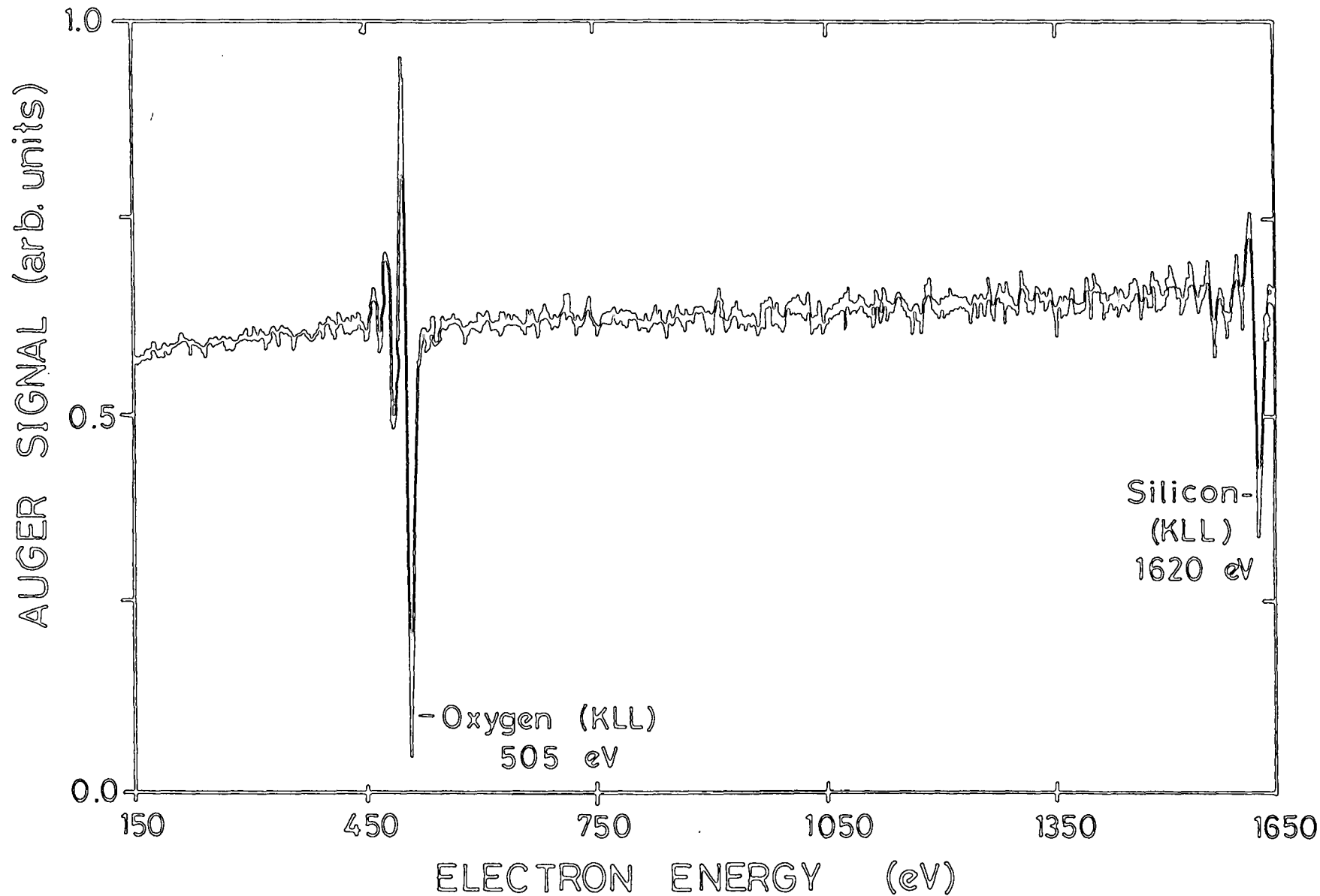
Figure 8.3   Schematic   diagram   of   Auger   spectroscopy
apparatus.

Figure 8.4    A typical Auger spectra for the SRO films.    The
spectra shown is the first    derivative    of    the
actual measured signal.

enhance the resolution of the signal. There are two prominent peaks shown. The lower energy peak corresponds to a well known Auger transition in oxygen at 505 eV, involving K and L inner shells. A similar transition is noted from the silicon at 1620 eV which corresponds to a KLL transition. There is also the possibility of using a lower energy silicon transition (LVV) at 92 eV but this has been found to be very sensitive to the particular bonding arrangement of the silicon [3] in amorphous films making compositional analysis very difficult. Once a calibration has been established. from the measure of the peak to peak (P-P) signal, (i.e.the first derivative). for each particular transition of interest. the elemental composition can be determined. To obtain a profile of the elemental composition, each of the transitions is monitored as the sample is etched away with an ion beam. The system was calibrated using a thermally grown silicon oxide where the compositions were found to be 33% and 67% for silicon and oxygen respectively.

Figure 8.5 shows an example of a measured profile. The solid line at the top is the silicon 1620 eV transition and the dotted line is the 505 eV oxygen transition. The solid line at the bottom was a measured carbon signal. This may be an artifact of this particular system arising from the fact that the samples were grown on top of a graphite susceptor. Although they might be expected to contain some trace amounts of carbon. such a large percentage as that shown in Fig. 8.5 is unlikely, so that the source is unidentified although it may be due to hydrocarbons in the Auger apparatus itself [3].
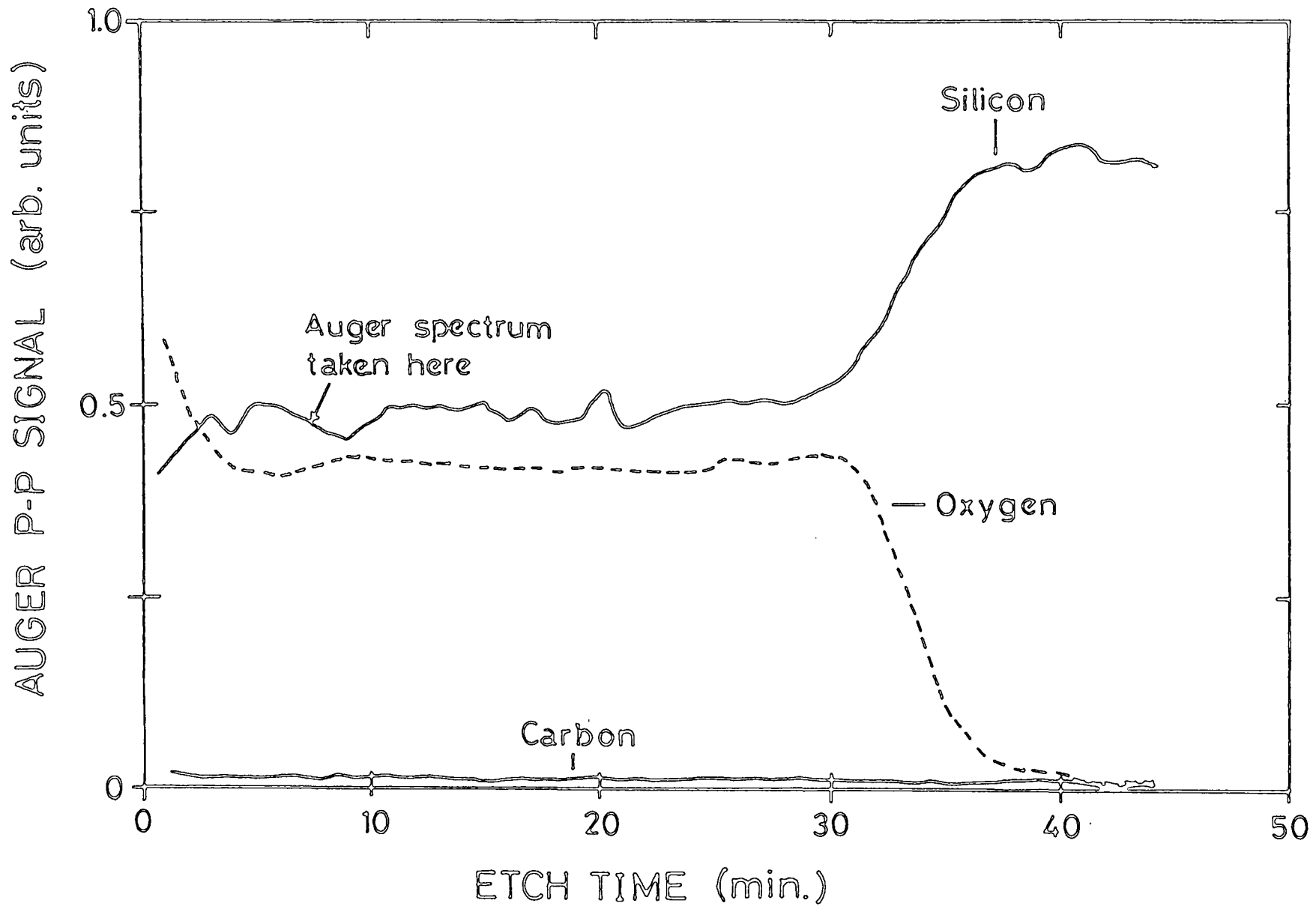
Figure 8.5    Profile of silicon and oxygen content in an SRO
              from using the Auger technique, showing the
              position at which the spectrum of Fig. 8.4 was
              taken.

The y-axis of Fig. 8.5 is the peak to peak differentiated Auger signal while the x-axis is the etching time of the film. Assuming that the etch rate is constant throughout the film, the x-axis can be translated directly into a film thickness. Through the majority of the film , the concentration of the silicon and oxygen is essentially constant. At the surface (i.e. where the etch time is zero) there is a slight increase in the oxygen concentration and a corresponding decrease in silicon concentration. This is quite reasonable as these films contain excess amounts of silicon when compared to silicon dioxide. Therefore, they contain free silicon which may be oxidized when exposed to the atmosphere, thus decreasing the ratio of the silicon to oxygen concentration at the surface. At the other end of the profile. the silicon concentration increases while the oxygen concentration decreases as would be expected. However. the transition is gradual implying that there is an almost linearly graded transition region of a substantial thickness near the SRO-silicon interface.

The results from the Auger measurements are given in Table 8.2. For these films the reactant temperature and carrier gas flow were 650 $^{o}$C and 15 litres minute respectively. These results are not directly comparable with those of the RBS analysis as the growth conditions. particularly the main $N_2$ flow rate, were not the same. The error in the calculated concentrations of silicon, oxygen and carbon was estimated to be about 4%. Within the experimental error. these films have essentially identical compositions. The concentration of the carbon in these films is assumed to be an artifact of the

| $R_o$ | $SiH_4$ flow rate (ml/min) | $N_2O$ flow rate (ml/min) | Thickness ($\overset{o}{A}$) | Thickness (from Auger) ($\overset{o}{A}$) | Silicon concentration (%) | Oxygen concentration (%) | Carbon concentration (%) | Excess silicon concentration (%) |
|---|---|---|---|---|---|---|---|---|
| 1.0 | 44.0 | 44.0 | 334 | 300 ± 50 | 47.2 | 48.5 | 4.23 | 13.9 |
| 0.5 | 19.5 | 9.75 | 191 | 150 ± 30 | 45.9 | 50.2 | 3.80 | 12.6 |
| 0.5 | 19.5 | 9.75 | 488 | 430 ± 50 | 46.4 | 50.0 | 3.54 | 13.1 |

Table 8.2      Data from Auger spectrscopy giving an  elemental analysis of the SRO films.

measurement apparatus and not an accurate compositional element. From this limited set of data, it appears for low main $N_2$ flow rates, the excess silicon content is relatively independent of the gas phase ratio, $R_O$ . This was not the case for the films grown for the RBS analysis.

## 8.2.3  Reflection High Energy Diffraction (RHEED)

The RHEED technique, as described in section 5.1 was used to examine the SRO films in the same way as for the SRN films. As mentioned previously, this technique gives only structural and not compositional information.

Films of gas phase ratio ranging from $R_O$ = 1.0 to $R_O$ = 0.25 were grown to be examined using the RHEED technique. All of these films were deposited on n-type silicon substrates and they had a thickness of approximately 2500 Å

Almost all the RHEED patterns, at first glance showed very diffuse rings suggesting that the films were particularly amorphous with very small grain sizes, much less than 100 Å. An example of the RHEED pattern from such a film is shown in Plate 8.6. It is evident that this film is made up of amorphous $SiO_x$ with very little structure.

It is known that hydrogen fluoride (HF) and particularly buffered HF etch are selective etches that can be used to remove silicon dioxide from silicon surfaces. Samples were etched in 10% HF and in buffered HF for very short periods of time (< 30 s) to enhance any pattern that might arise from the free silicon in the films. The diffraction patterns were found to be essentially the same as that illustrated in Plate 8.6.
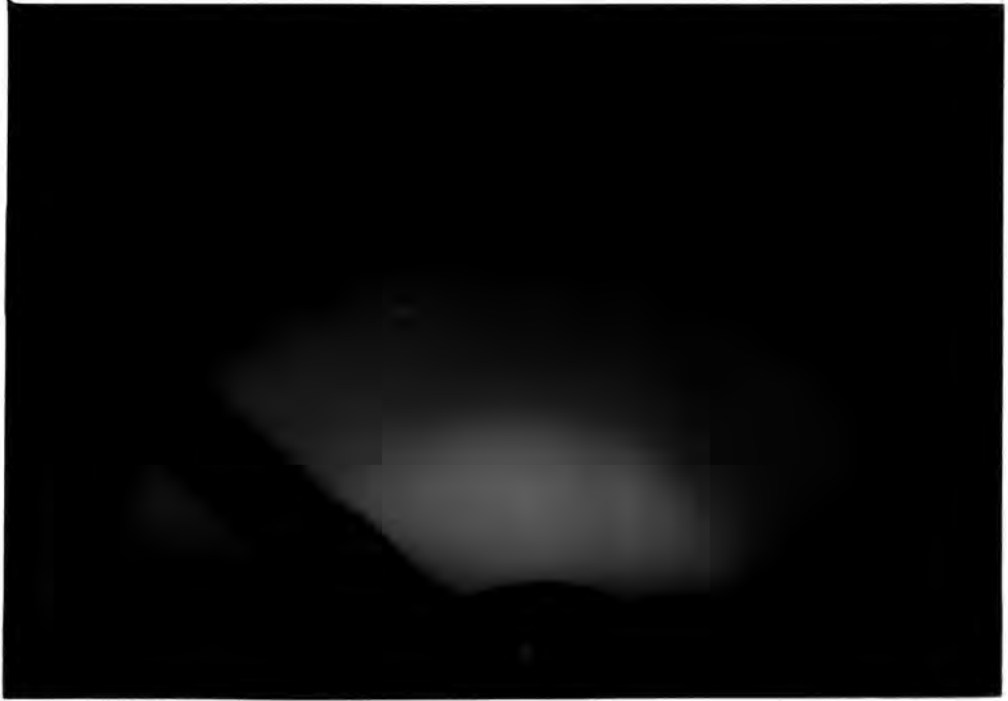
Plate 8.6    A RHEED diffraction pattern of an as  grown,  HF
            dipped, SRO film with $R_O$ = 1.0.



Plate 8.7    A RHEED diffraction pattern of an HF dipped, SRO
            film with $R_O$ = 1.0, after annealing in  nitrogen
            for one hour at 1000 °C.

However, after annealing in nitrogen for an hour at 1000 $^{o}$C, and etching in 10% HF for about 30 s, the diffraction patterns showed much more structure. Plate 8.7 shows the pattern of an SRO film with $R_O = 1.0$ that was annealed and etched. Table 8.3 shows a comparison on the resultant d-spacings of this film and those of silicon. This strong correlation suggests that after annealing, the crystallites of free silicon in the SRO film grow appreciably although overall the films are still amorphous since the rings are still very diffuse.

## 8.2.4 Wet-Etch Characteristics of SRO films

A number of simple wet etch experiments were performed by Miss. E. Geake under the direction of the author in an attempt to determine the profile of the silicon and oxygen concentrations from the refractive index measured using ellipsometry. Figure 8.8 shows the etch rate of SRO films with $R_O = 1.0$. for both buffered and 10% HF. The process used was as follows. SRO films of thicknesses about 5000 Å were grown using a value of $R_O = 1.0$. The thickness and refractive index of the as-grown (unannealed) films were measured using standard ellipsometric techniques. The samples were then etched for a set period of time after which the index of refraction and thickness were again measured. This process was repeated until the film was completely etched away.

As expected the buffered HF etch rate was much faster than that of the 10% HF, since buffered HF etches silicon dioxide more rapidly than dilute HF. It is interesting to note, however, that for two different measurements, the etch rate

| $R_O = 1.0$ | | Silicon X-ray Data | |
|---|---|---|---|
| d($\text{Å}$) | I | d($\text{Å}$) | $I/I_O$ |
| 3.15 | vs | 3.14 | 100 |
| 1.95 | s | 1.92 | 60 |
| 1.68 | m | 1.64 | 35 |
| 1.38 | m | 1.36 | 18 |
| 1.26 | w | 1.25 | 13 |
| 1.13 | w | 1.11 | 17 |
| 1.06 | vw | 1.05 | 9 |

Table 8.3    Plane spacing, d, corresponding to the diffraction
rings of Plate 8.7 for an annealed, HF dipped,
SRO film with $R_O$=1.0. The spacings for silicon,
obtained from ASTM X-ray data are given for
comparison.

I = Relative intensity of electron diffraction
ring in order from very strong (vs) to very
weak (vw). m=medium.

$I/I_O$ = Intensity of X-ray diffraction ring relative
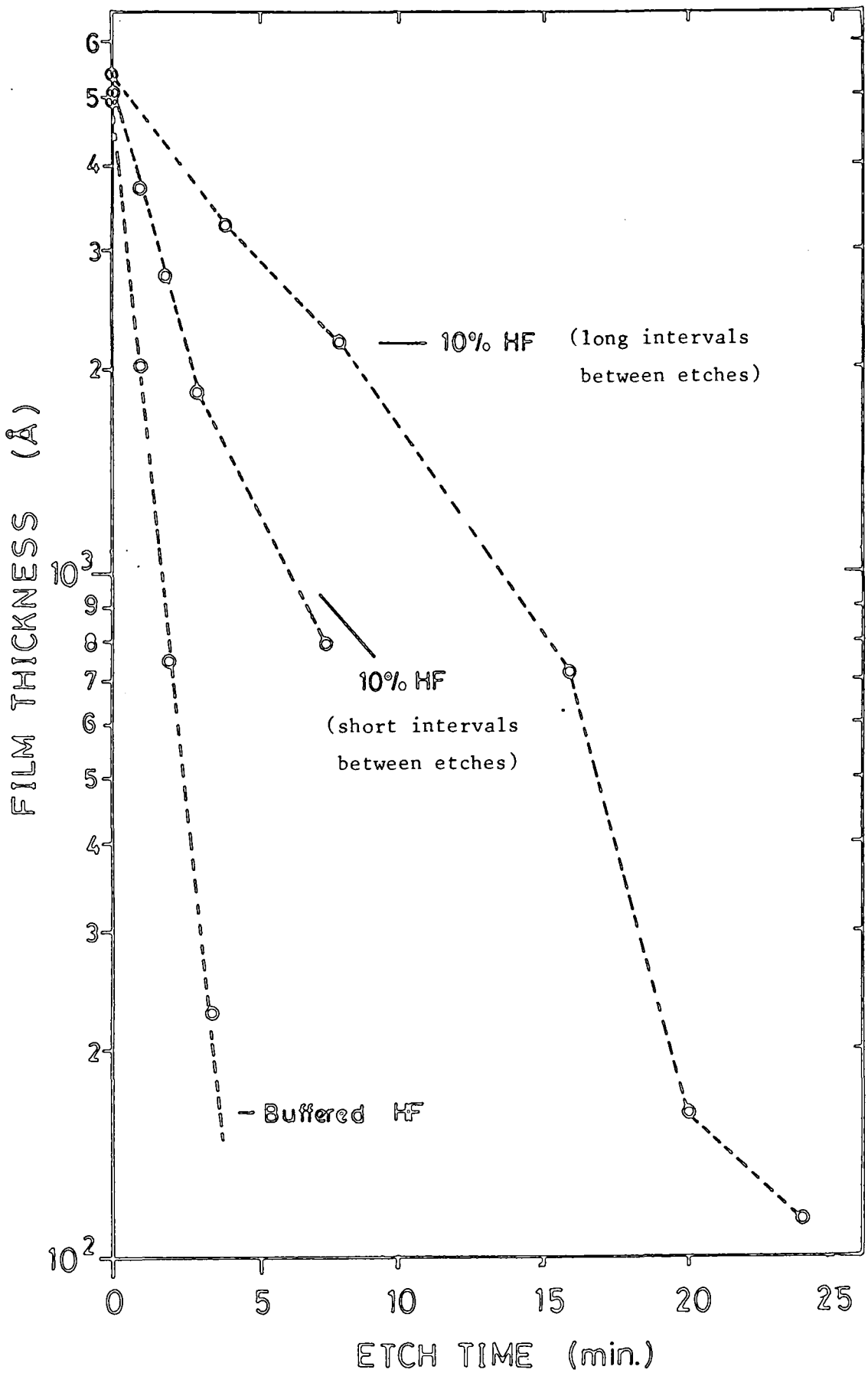to the strongest (%).

**Figure 8.8**     Wet Etch characteristics of SRO films in 10% and buffered HF.

depended on the precise procedure. The only difference between the two 10% HF curves in Fig. 8.8 is in the time intervals at which the etch was stopped and the thickness measured. For the shorter time intervals the etch rate is much faster. It is assumed that when the sample is removed from the etch, a certain amount of the excess silicon near the bare surface is oxidized. The 10% HF is a selective etch and can remove silicon dioxide at a rate 100 times that for silicon. For this reason, as the time intervals become shorter, the surface is oxidized that many more times and subsequently removed all the faster.

Figure 8.9 shows the measured refractive index as a function of the thickness of the samples. These results are the parallel to those in Fig. 8.8. For all etches, there is a decrease in the refractive index as a function of the thickness. However, from the Auger results it was found that the concentration of silicon was essentially constant throughout the film but with an increase towards the substrate end of the film. The decrease in refractive index implies just the opposite. However each time the films is removed from the etch, the surface is re-oxidized as the film. The ellipsometry technique is not a surface sensitive technique but it gives some average values for the total composition over the thickness of the film. As the film becomes thinner, a larger percentage is oxidized after each etching step. Therefore as the film is etched away, the measured refractive index decreases and approaches the value of $SiO_2$ .
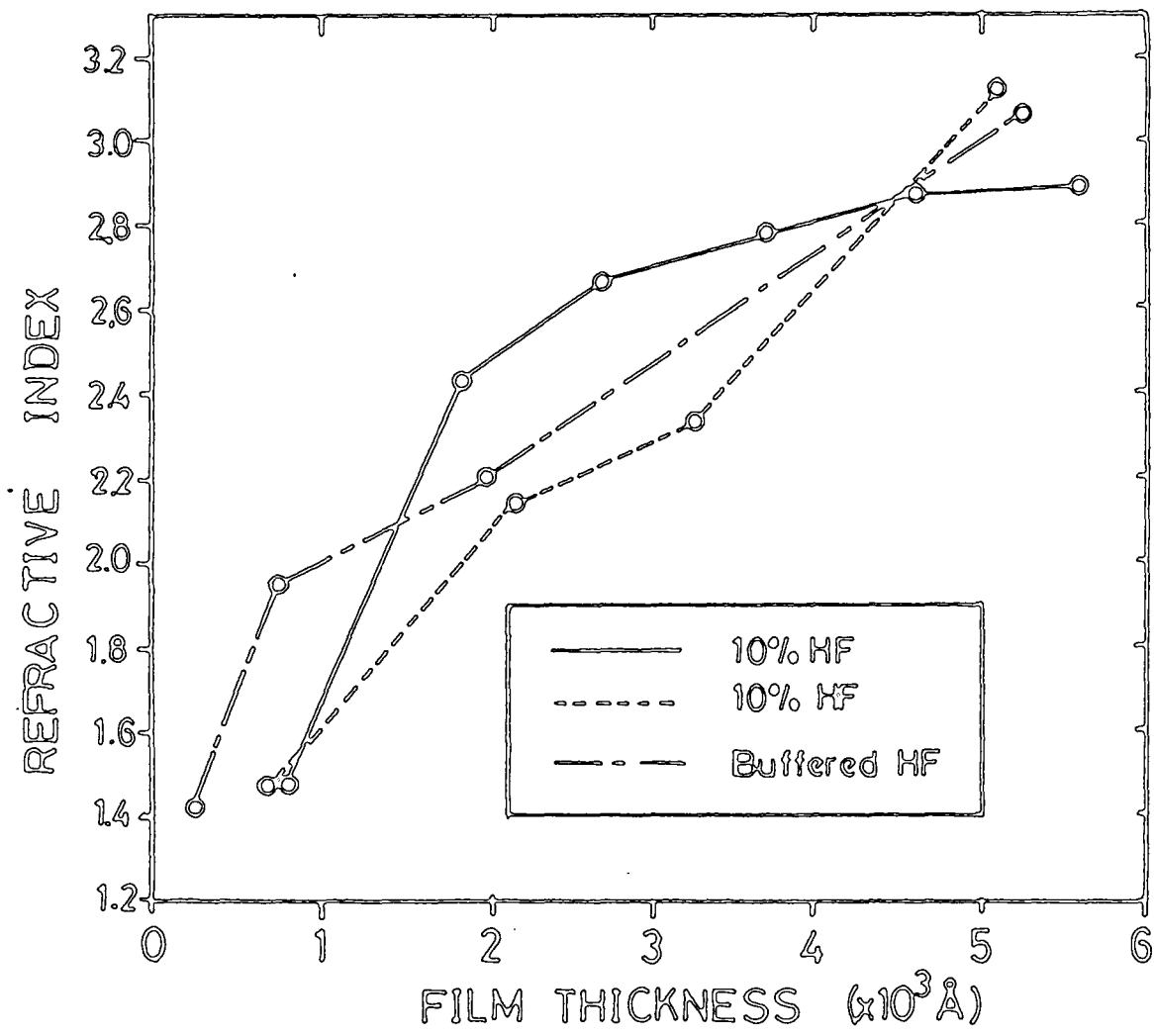
Figure 8.9    Refractive index of an SRO film with $R_O = 1.0$, as function of thickness. Sample was progressively wet etched using 10% and buffered HF.

## 8.3  Conduction in Silicon-Rich Oxide (SRO) Films

Since the first reports of silicon-rich silicon dioxide or as it is sometimes called, semi-insulating polycrystalline silicon (SIPOS) in 1975, the interest in this material has grown considerably [1,4-20]. However, even though its main uses in passivation and injecting structures appear to be fairly well established, there is still some controversy about the mechanism responsible for conduction. Up to the present, the conduction in SRO has been attributed to three very distinct physical phenomena. Some researchers [8,9] have taken a more macroscopic approach and assumed that a symmetrical Schottky barrier is formed at the boundary between the crystallites and the surrounding matrix. This case can only be true, however, if the size of the crystallites is much larger than their separation and it yields results similar to those for polycrystalline silicon where the grain sizes are extremely large. Probably the most convincing argument thus far [19], attributes the conduction in SRO to a Fowler-Nordheim like tunnelling of electrons between potential wells associated with silicon crystallites in an $SiO_2$ matrix. The third conduction mechanism that has been put forward is that of Poole- Frenkel emission from relatively deep traps associated with the silicon crystallites, to the conduction band or band, tails of the surrounding matrix.

Figures 8.10 a) and b) show typical current voltage characteristics for SRO films grown on an n-type silicon substrate with aluminium and gold top and back contacts respectively. The lower curve in each figure illustrates the
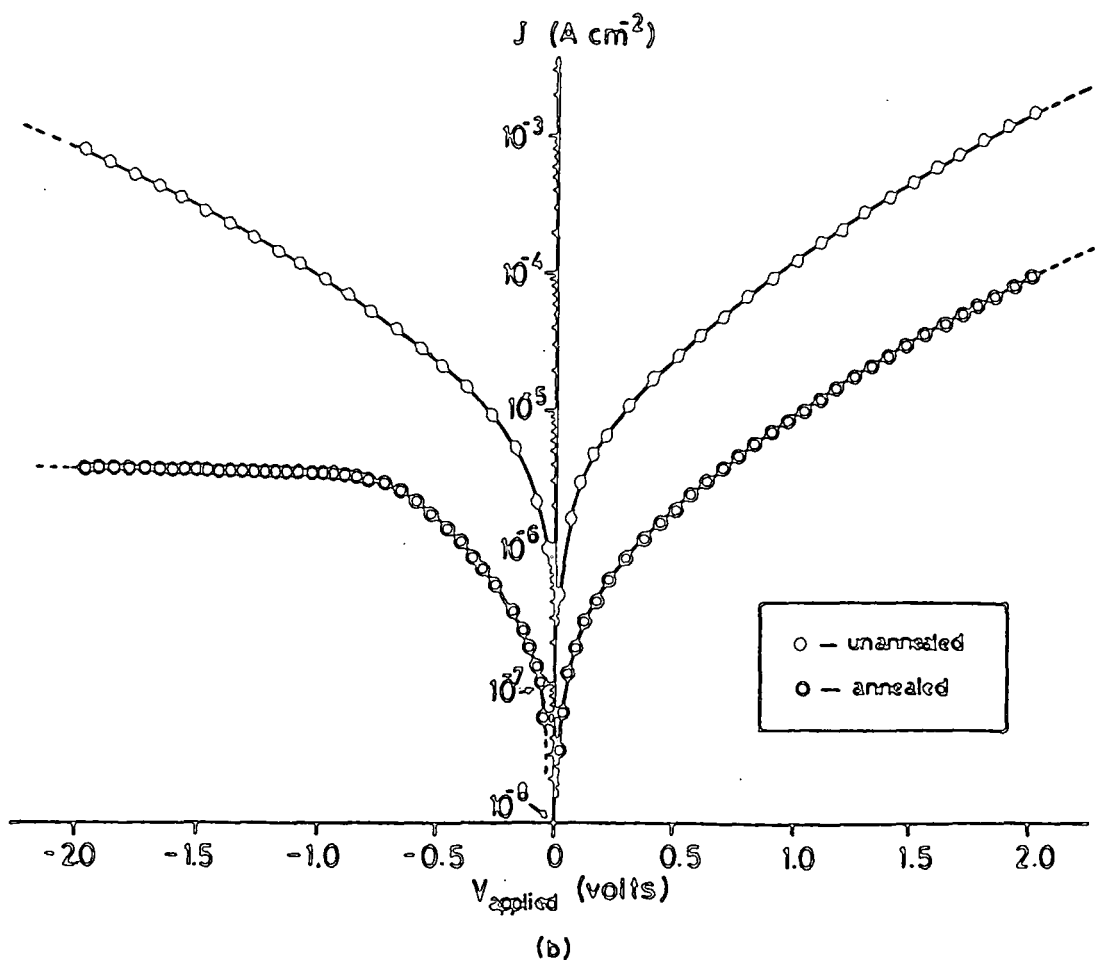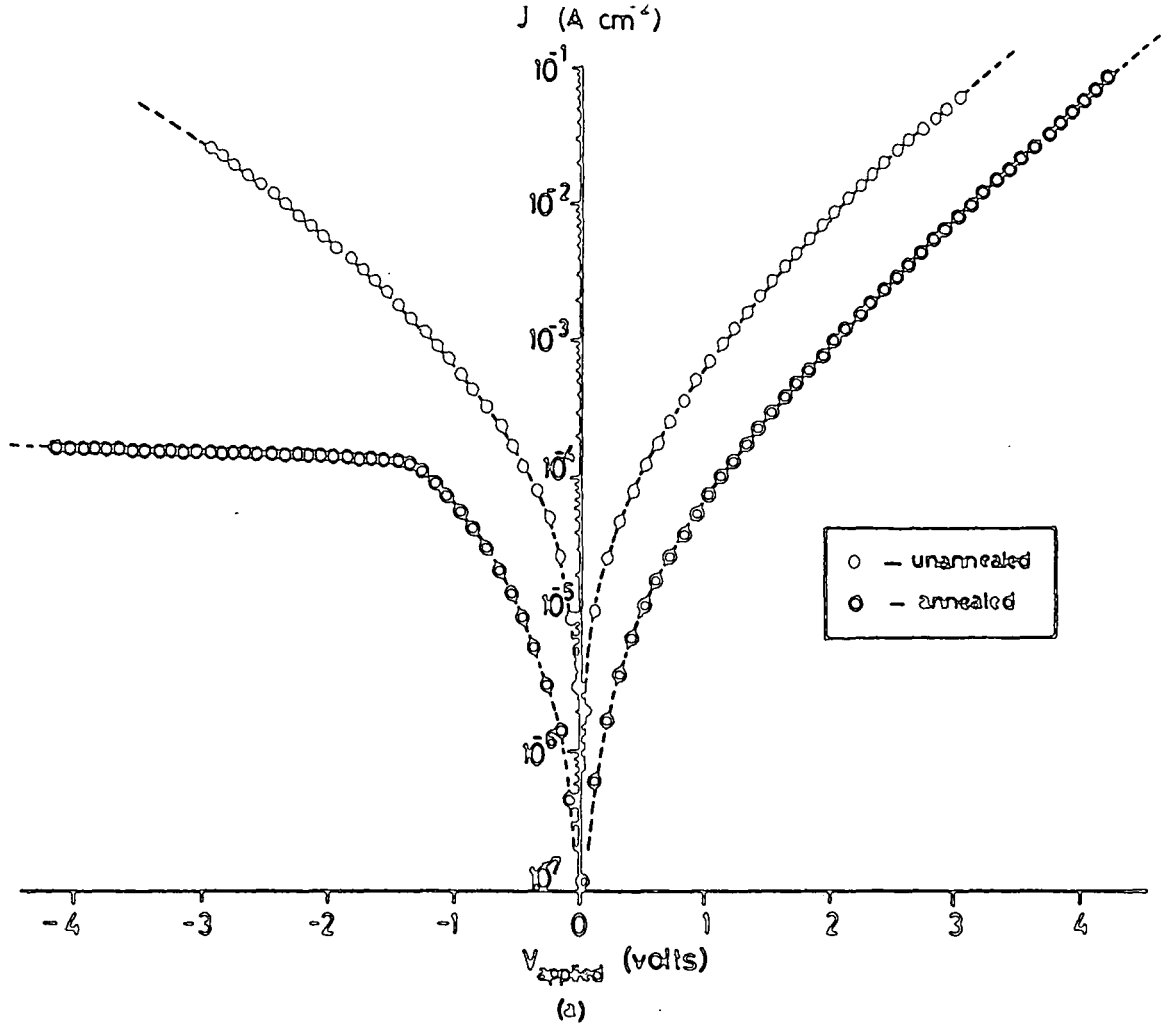
Figure 8.10    Current-voltage characterisitc of an Al-SRO-Si
device with an SRO film thickness of a) 378 Å
and    b) 634 Å.    (see  Table  8.4  for  growth
conditions)

characteristic for films that were annealed in nitrogen for an hour at 1000 $^\circ$C. The unannealed films show a very symmetrical characteristic. The annealed films, however, show a saturation in reverse bias which may be explained by the conditions below the metal. It is believed that during the annealing process, the top portion of the SRO films becomes oxidized producing a thin, insulating film on top of the SRO film. In all cases the current of an annealed film, at any given voltage, was less than that for the as-grown film. This implies that the oxide is most likely to be of a thickness greater than tunnelling dimensions (i.e. ～ 50 Å). Since the SRO film is much more conductive than the top oxide layer, the device behaves similar to that of an MIS diode where the current saturates in reverse bias. The symmetrical nature of the I-V characteristics of the unannealed films, however, suggests that whatever the mechanism for conduction in these films it is most likely to be bulk limited at least for the unannealed films. In the following sections each of the aforementioned electronic processes is reviewed in the light of these measurements. In Table 8.4 a summary of the parameters extracted for each of the different conduction mechanisms is given along with the growth conditions for each of the SRO films.

## 8.3.1 Symmetrical Schottky Barrier Model(SSB)

The symmetrical Schottky barrier model was first proposed by Tarng [8] in 1978 and further experimental evidence [9] has given support to the theory. We consider the films to contain silicon crystallites separated by a small gap of surrounding

| Growth Conditions | $n = 2.41$, $d = 378$ Å<br><br>$N_2 = 35$ 1/min.<br><br>$N_2O = 50$ ml/min.<br><br>$SiH_4 = 50$ ml/min. | | $n = 2.46$, $d = 634$ Å<br><br>$N_2 = 10$ 1/min.<br><br>$N_2O = 55$ ml/min.<br><br>$SiH_4 = 55$ ml/min. | |
|---|---|---|---|---|
| | unannealed | annealed | unannealed | annealed |
| Symetrical Schottky Barrier | $d = 48$ Å   (+ve)<br>$\phi_b = 0.68$ eV<br><br>$d = 44$ Å   (-ve)<br>$\phi_b = 0.58$ eV | $d = 44$ Å   (+ve)<br>$\phi_b = 0.72$ eV | $d = 91$ Å   (+ve)<br>$\phi_b = 0.73$ eV<br><br>$d = 79$ Å<br>$\phi_b = 0.72$ eV | $d = 90$ Å   (+ve)<br>$\phi_b = 0.80$ eV |
| Poole-Frenkel | $\varepsilon_d = 6.06$ (+ve)<br>$\varepsilon_d = 8.59$ (-ve) | $\varepsilon_d = 5.49$ (+ve) | $\varepsilon_d = 4.14$ (+ve)<br>$\varepsilon_d = 5.16$ (-ve) | $\varepsilon_d = 4.44$ (-ve) |
| Fowler-Nordheim | $\phi_{eff} = 0.13$ eV (+ve)<br><br>$\phi_{eff} = 0.13$ eV (-ve) | $\phi_{eff} = 0.21$ eV (+ve) | $\phi_{eff} = 0.06$ eV (+ve)<br><br>$\phi_{eff} = 0.06$ eV (-ve) | $\phi_{eff} = 0.06$ eV (+ve) |

Table 8.4    Parameters extracted from the analysis of the current-voltage characteristics of the SRO films.

SiO$_x$ matrix as shown in Fig 8.11 (a), where the silicon grains contain both donor and acceptor states that can arise from the existence of impurities such as oxygen. It has been found [9] that silicon can contribute donor and acceptor states at 0.16 and 0.38 eV, respectively, below the conduction band edge. As the SiO$_x$ matrix surrounding the silicon crystallites is assumed to be much smaller that the crystallites themselves, it is assumed that the material may be thought of as similar to polysilicon with grain boundaries and give rise to a Schottky-type barrier on both sides of the gap. The net density of ionized acceptors and donors, (i.e. $N_g = N_d - N_a$ ) and the total charge density is shown schematically in Fig. 8.11 (b). In equilibrium, the Fermi levels in the grain and the grain boundary or surrounding matrix must line up, causing a redistribution of charge and resulting in the space charge region. The electric field arises from the space charge and it supports the band bending around the grain boundaries as shown in Fig 8.11 (d).

In general the current-voltage relationship of a (non-symmetrical) Schottky barrier is given by

$$J = J_s \left[ \exp\left(\frac{qV}{kT}\right) - 1 \right]$$  (8.5)

where k is the Boltzmann constant, T is the absolute temperature and $J_s$ is the saturation current. For our case, if we assume that all the grain sizes are the same, the total voltage, V, is dropped evenly across each of the grains in series. Therefore, the relationship between the total voltage,

139
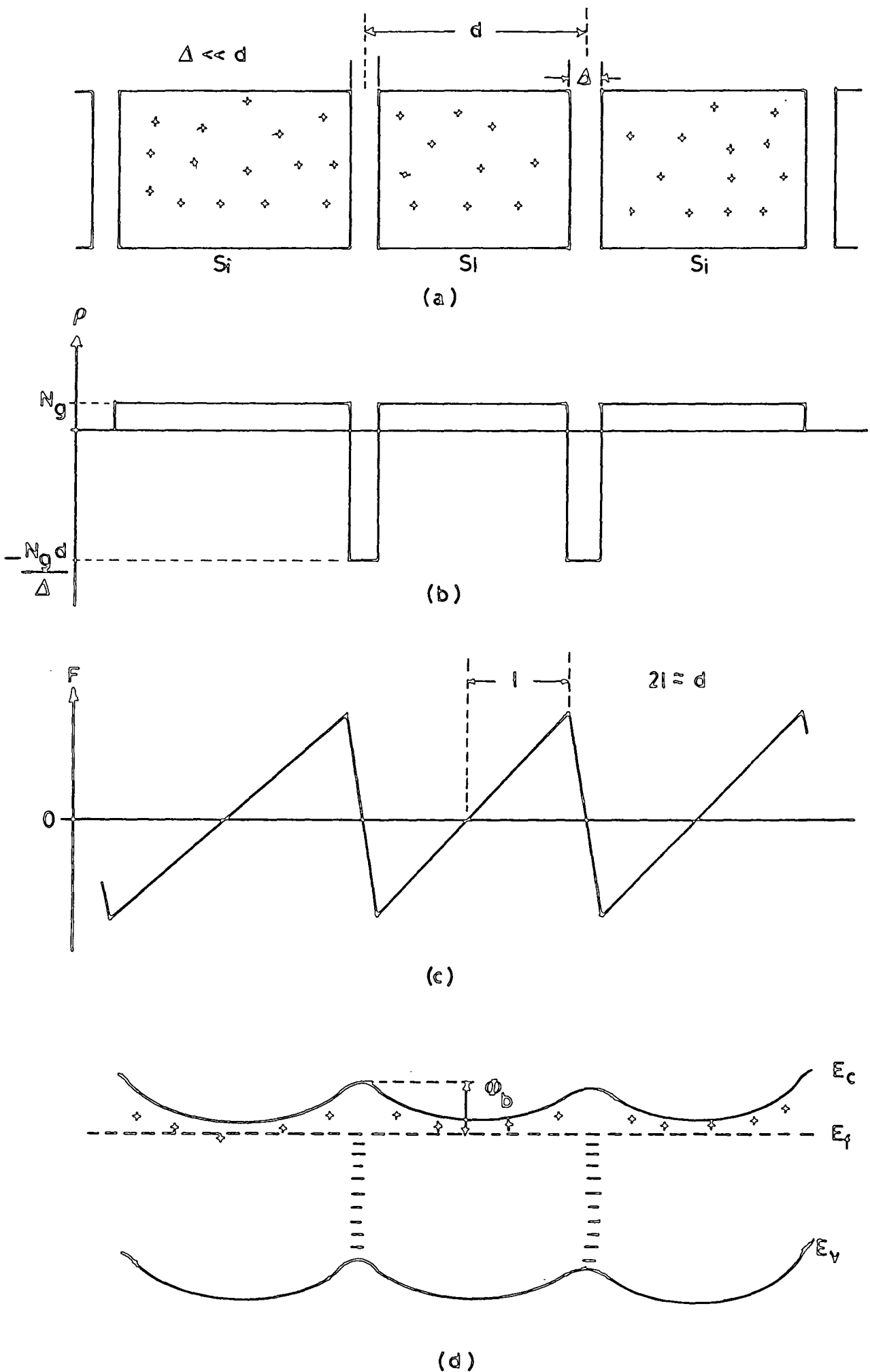
Figure 8.11 Schematic diagram of the symmetrical Schottky barrier (SSB) formed by grain boundaries showing a) physical structure, b) charge distribution, c) electric field, and d) energy band structure.

V, and the voltage dropped across each grain is given by

$$V_i = V/2g \qquad (8.6)$$

where $g$ is the number of grains is series. The factor of 2 in the denominator arises because only half the voltage drop per grain occurs between the centre of the grain and the corresponding boundary. If we now consider that there exists a symmetrical Schottky barrier the total current density is given by [9]

$$J = J_s \left[ \exp\left(\frac{qV}{2gkT}\right) - \exp\left(\frac{-qV}{2gkT}\right) \right] \qquad (8.7)$$

or

$$J = 2J_s \sinh\left(\frac{qV}{2gkT}\right) \qquad (8.8)$$

where

$$J_s = A^{**}T^2 \exp\left(\frac{-\phi_b}{kT}\right) \qquad (8.9)$$

and $A^{**}$ is the modified Richardson constant, and $\phi_b$ is the effective barrier height at the grain boundary.

Figures 8.12 a) and b) show the current characteristics given previously in Fig. 8.10. The unannealed negative bias curve is not shown as it does not reflect the nature of the SRO film itself. The solid lines in each of the curves represents a best line (least squares) fit from the SSB model. The effective trap depth and the average grain size were deduced from the best line fit and from the known thickness of the films.

Firstly it should be noted that the best line fit although generally correct is not as good a fit as has been found [9].
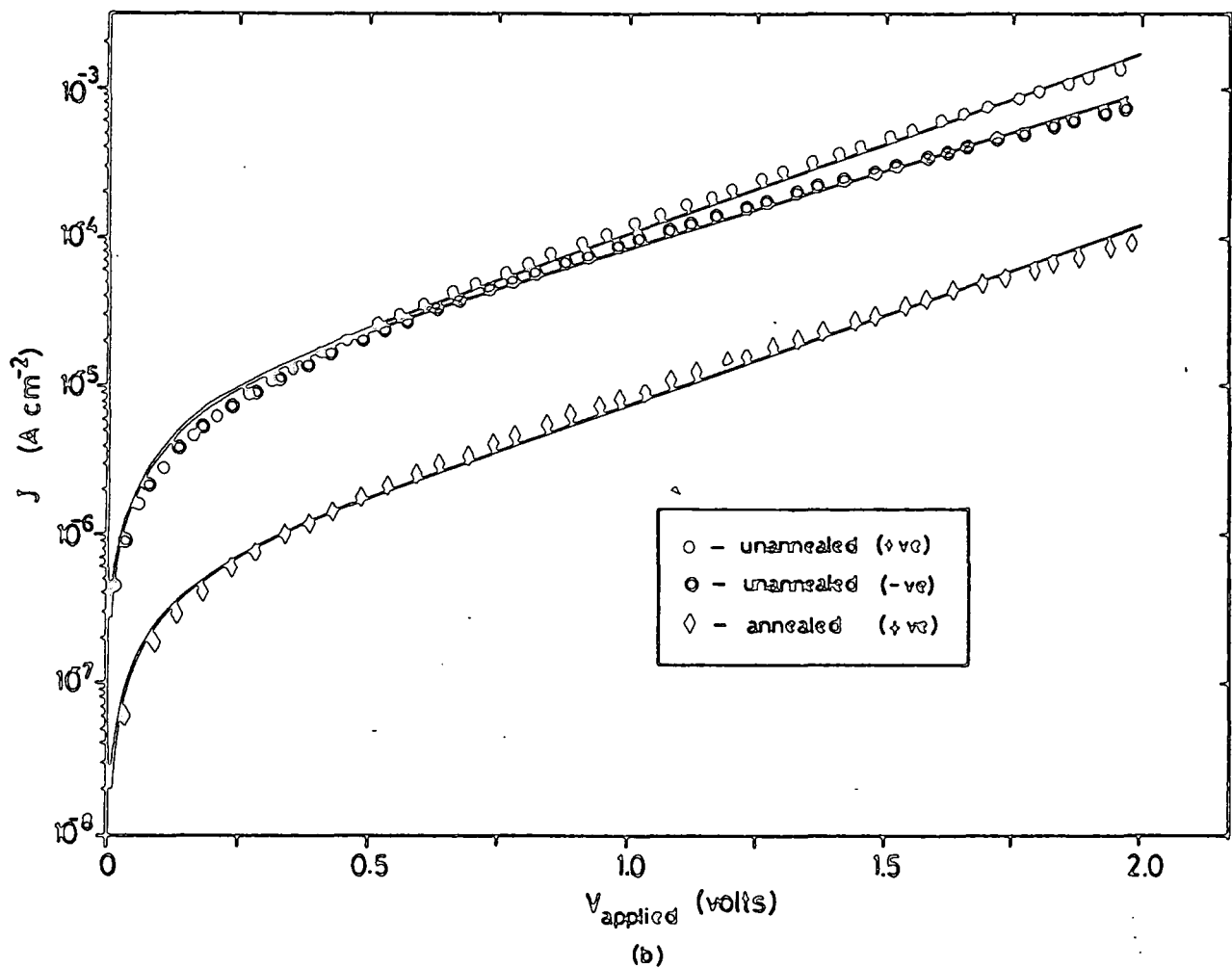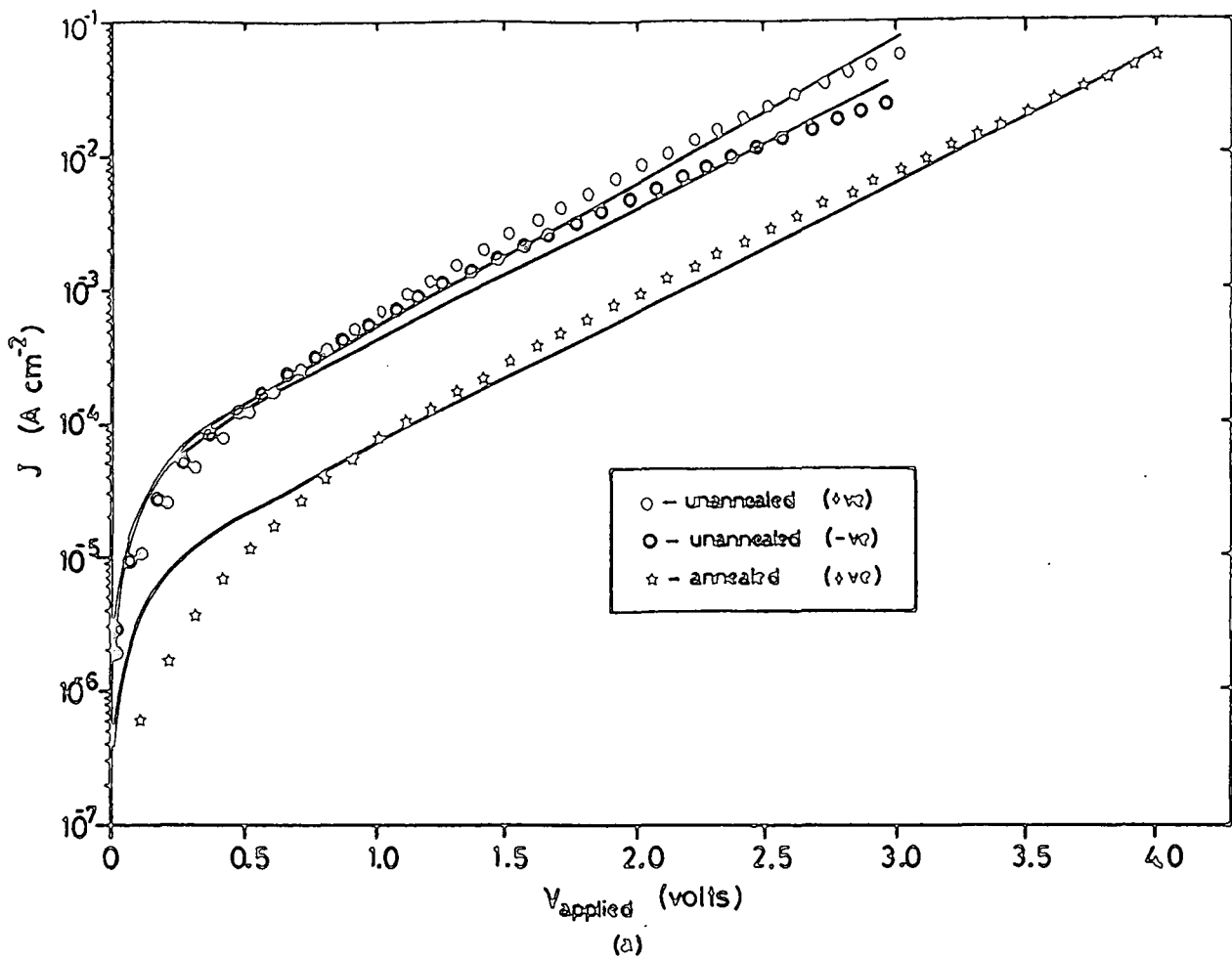
140

Figure 8.12 Data of Figs. 8.10a and 8.10b replotted, respectively in a) and b), where the solid line represents the least squares fit to equation 8.8 of the SSB model.

The model does predict the general trends of these characteristics. From the values of the saturation current (equation 8.9), the value of the effective barrier height was determined. For simplicity the effective mass was assumed to be equal to the rest mass of an electron and hence the Richardson constant used was 120 A cm$^{-2}$ K$^{-2}$. The effective barrier heights for these films are given in Table 8.4. For the unannealed films, the barrier height is found to be approximately constant at about 0.7 eV, the exception being the negative bias case of one of the annealed films. Tarng [8] and Zommer [9] used this model but derived values from an Arrhenius plot (J vs 1/T) which yields a more correct result. They both found a very good fit to their data and barrier heights of the order of 0.45 eV and 0.6 eV respectively. This disagreement could result from a difference in the elemental composition of the particular films used. Zommer [9] reported that his films contained 24 atomic percent oxygen which gives about 42% excess silicon (over stoichiometric SiO$_2$). Tarng [8] did not report a value for his films, but both these values are higher than for the present films although one would expect the effective barrier height to be greater for our films. It is also curious that the value reported for polysilicon is of the order of 0.45 eV [8] which is quite a lot lower than that of the present films and thus gives rise to some doubt of the accuracy of this model.

For the thinner of the two samples, the average grain size, d, was found to be about 46 Å. For the thicker film, this value is about double. These values are of the order one

141

would expect from the RHEED analysis, but it is impossible to verify without an in-depth transmission electron microscopic (TEM) study. Others [6] have found that the grain size of as-grown SRO films is on the order of 100 Å or less but that the size is extremely dependent upon deposition and post-deposition conditions. The most surprising result is that there is no evidence from this model of an increase in the grain size with annealing, which is known to occur [6]. For these reasons a substantial amount of doubt exists about the validity of the symmetrical Schottky barrier (SSB) model.

## 8.3.2  Fowler-Nordheim Tunnelling Model

Figure 8.13 shows an energy band diagram of the silicon-SRO interface. The films are thought to be made up of silicon crystallites surrounded by an amorphous $SiO_x$ matrix. The bottom of the 'conduction band' in the insulator is assumed to be similar in energy to that of $SiO_2$. Assuming that the main contributor to the conduction are electrons, for simplicity, there are a number of different mechanisms that could account for the movement of charge through the SRO films. The dashed line in Fig. 8.13, number 1, illustrates direct tunnelling from the conduction band of the silicon into the 'conduction band' of the SRO film. The dotted line, number 2, shows the path an electron would take assuming it were to tunnel from crystallite to silicon crystallite. The third mechanism shows tunnelling from deep traps in the $SiO_x$ matrix into the silicon crystallites. Emission from the silicon crystallites into the 'conduction band' of the $SiO_x$ matrix
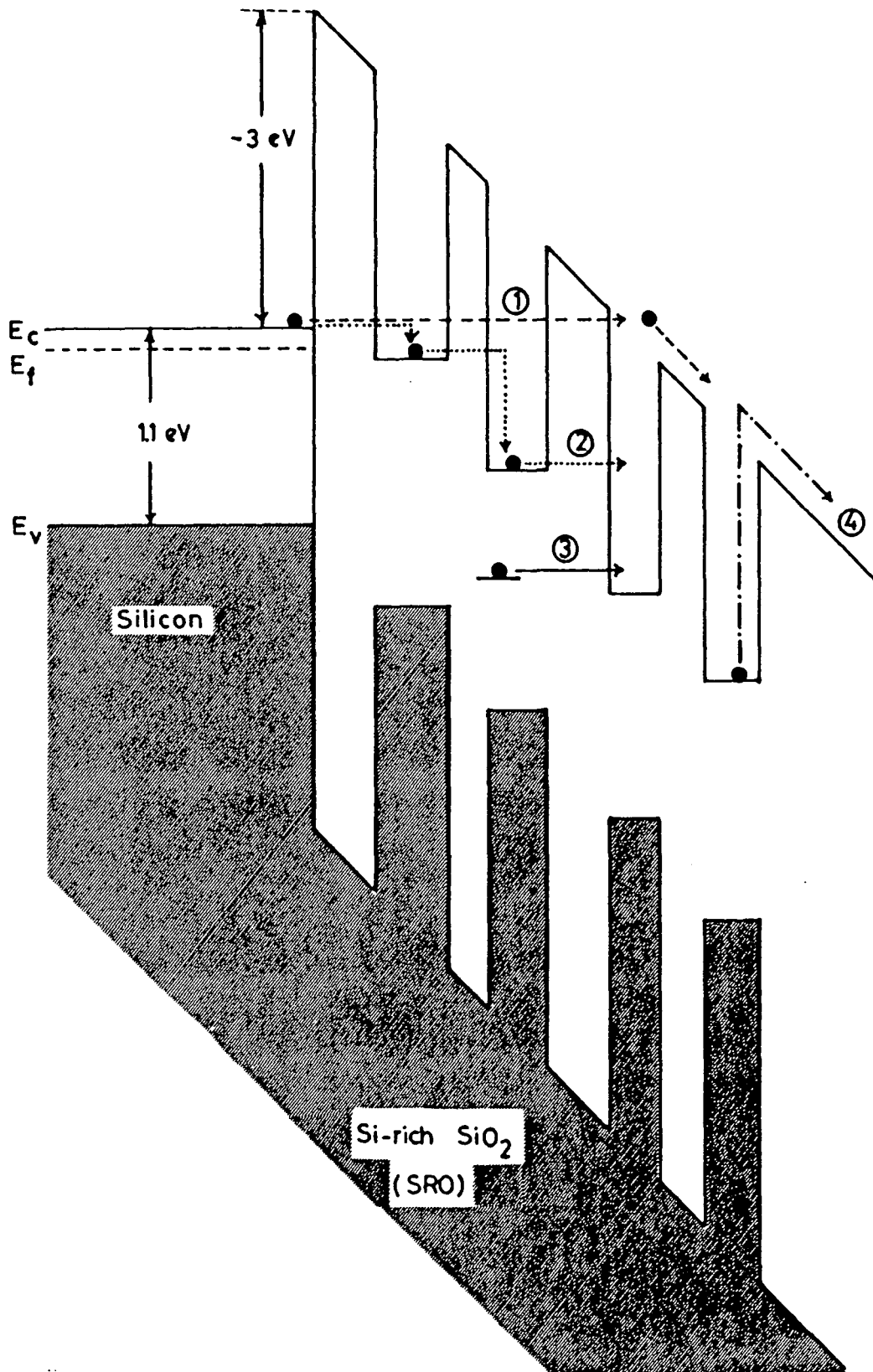
Figure 8.13    Energy band diagram of the interface between the
silicon substrate and the SRO film showing
direct tunnelling from silicon to SRO conduction
band (dashed line 1), tunnelling from
crystallite to crystallite (dotted line 2),
tunnelling from deep level centres into the
silicon crystallites (solid line 3) and
Poole-Frenkel emission from the silicon
crystallites to the SRO conduction band
(dot-dashed line 4).

could also occur due to the Poole-Frenkel mechanism as shown by the dash-dot line, number 4.

From an energy point of view, the direct tunnelling of electrons from the silicon into the 'conduction band' of the matrix would seem to be the least probable, as there is a 3 eV barrier to overcome. This would also imply a contact limited conduction which does not seem to be the case as the I-V characteristics are symmetric with respect to the polarity of the applied bias. Direct tunnelling into the crystallites from deep traps ι within the $SiO_x$ matrix would also have a large effective barrier to surmount. The last mechanism, Poole-Frenkel emission, might also seem to be unlikely due to the relatively high initial barrier to overcome which, even with very substantial electric field, could not be reduced significantly. This is based on the assumption that the electrons must be emitted into the 'conduction band' of the surrounding matrix. However, if band tails were to extend significantly into the energy gap or if there was a large transition region of excess silicon between the crystallites and the matrix, emission could occur as was found to be the case with the SRN films. The discussion of the Poole-Frenkel results is given in the following section.

Ron and DiMaria [19] have developed the model based on the tunnelling of carriers from silicon crystallite to crystallite. They assumed a very simple energy band system where the silicon crystallite was represented by a potential well within a silicon dioxide matrix as shown in Fig. 8.14. The crystallites are assumed to be spherical with a radius, a, and the energies
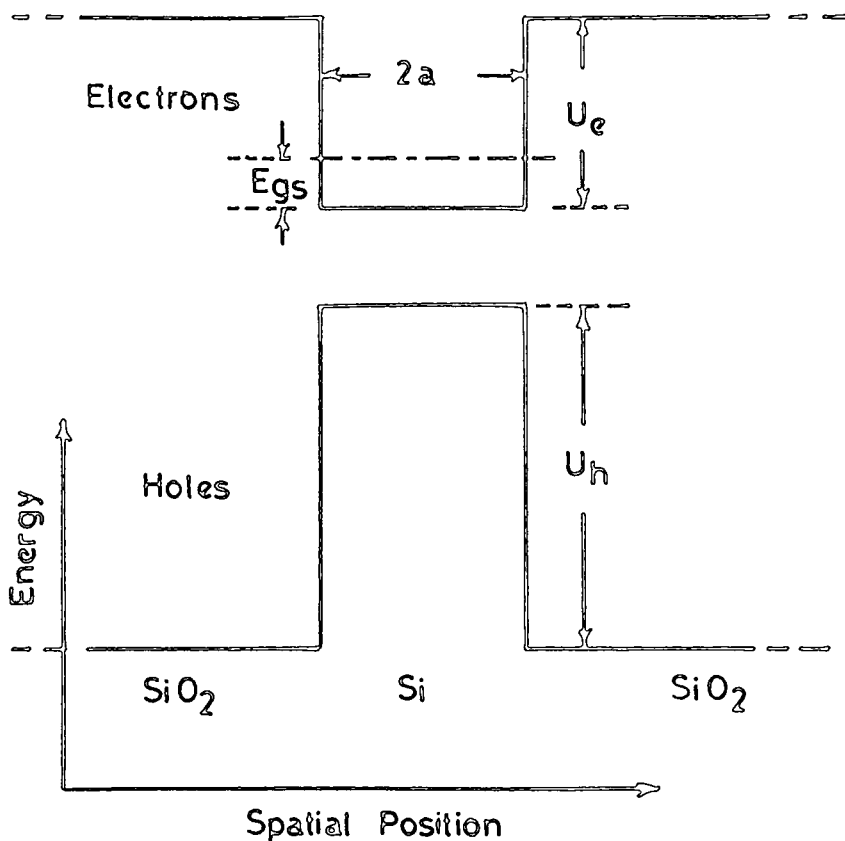
143

Figure 8.14    Schematic  diagram  of the potential of a 'well'
              associated with a silicon 'island' in an SiO$_2$
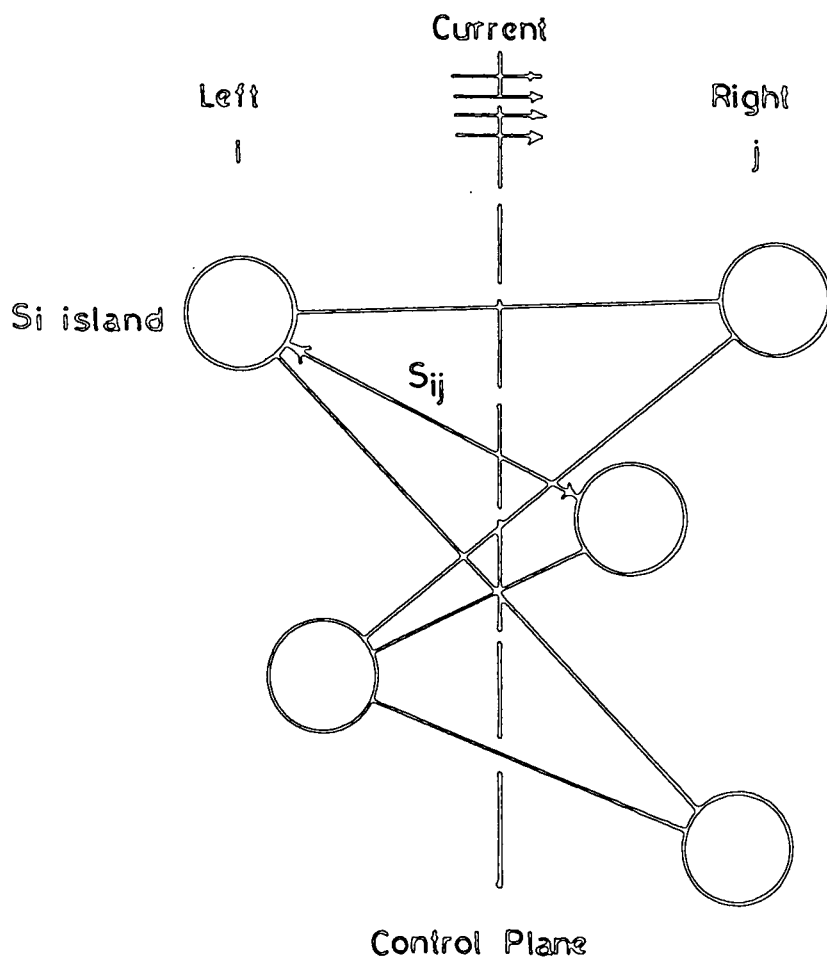              matrix.



Figure 8.15    Schematic    representation    of    the    silicon
              'islands' and currents.

$U_e$ and $U_h$ are the differences between the silicon and silicon dioxide conduction and valence bands respectively. Electrons and holes can be bound to these potential wells. The 'local' conduction band is the effective potential for electrons as is the 'local' valence band for holes. The value, $E_{gs}$, is the energy ground state for an electron in the potential well.

It was assumed that the crystallites were all of approximately the same size. A percolation treatment was used (see Fig. 8.15) to add the tunnelling probabilities and determine a final current expression. Consider that inside the sample there is an imaginary plane of unit area perpendicular to the electric field. The current density is equal to the sum of the electronic charges crossing the plane per unit time, i.e.

$$J = q \sum_i \sum_j T_{ij}$$

(8.10)

where $T_{ij}$ is the tunnelling probability and i is summed over all the potential wells on the left hand side of the unit plane and j over the wells on the right hand side provided the line $S_{ij}$ that connects the two wells crossed the plane. Assuming a random distribution of crystallites. the current density was found to be

$$J = q \ N_w \ 1 \ \frac{E_{gs}}{\hbar} \exp \ (-\xi)$$

(8.11)

where $N_w$ is the average number of wells per unit volume, 1 is the typical path length, $\xi$ is a function derived from the tunnelling probabilities and the j summation is now over the proper right hand side neighbours of the ith island on the left hand side as shown in Fig. 8.15. Due to the exponential nature

144

of the expression of the current linking two islands. the individual terms in the summation vary over many orders of magnitude depending on the relative position and energies of the particular pair of wells. Therefore the 'weak links' in the system, i.e. small current connections, are unimportant in the summation, and can be neglected. Effectively only current links with an 'effective strength' or magnitude above some critical value need be considered. Based on these assumptions the current density was found to be of the form [19]

$$J = C \, q \, N_w \, s_c \, \frac{E_{gs}}{\hbar} \, \exp(-\bar{F}/F) \tag{8.12}$$

where C is a numerical factor on the order of one, $s_c$ is the critical length needed for contribution to the current, F is the electric field strength and

$$\bar{F} = F_o \left[ 1 - \left[ 1 - \frac{q s_c F}{U_e - E_{gs}} \right]^{3/2} \right] \tag{8.13}$$

where

$$F_o = \frac{4}{3} \left[ \frac{2 m_e^*}{q^2 \hbar^2} \right]^{\frac{1}{2}} (U_e - E_{gs})^{3/2} \tag{8.14}$$

At high electric fields. $\bar{F}$ depends weakly on F and the current displays a Fowler-Nordheim type of dependence on the electric field.

Figure 8.16 a) and b) shows plots of the current density as a function of the inverse of the electric field for the SRO films (see Table 8.4 for growth conditions). From the high field regions the values of the effective barrier height,
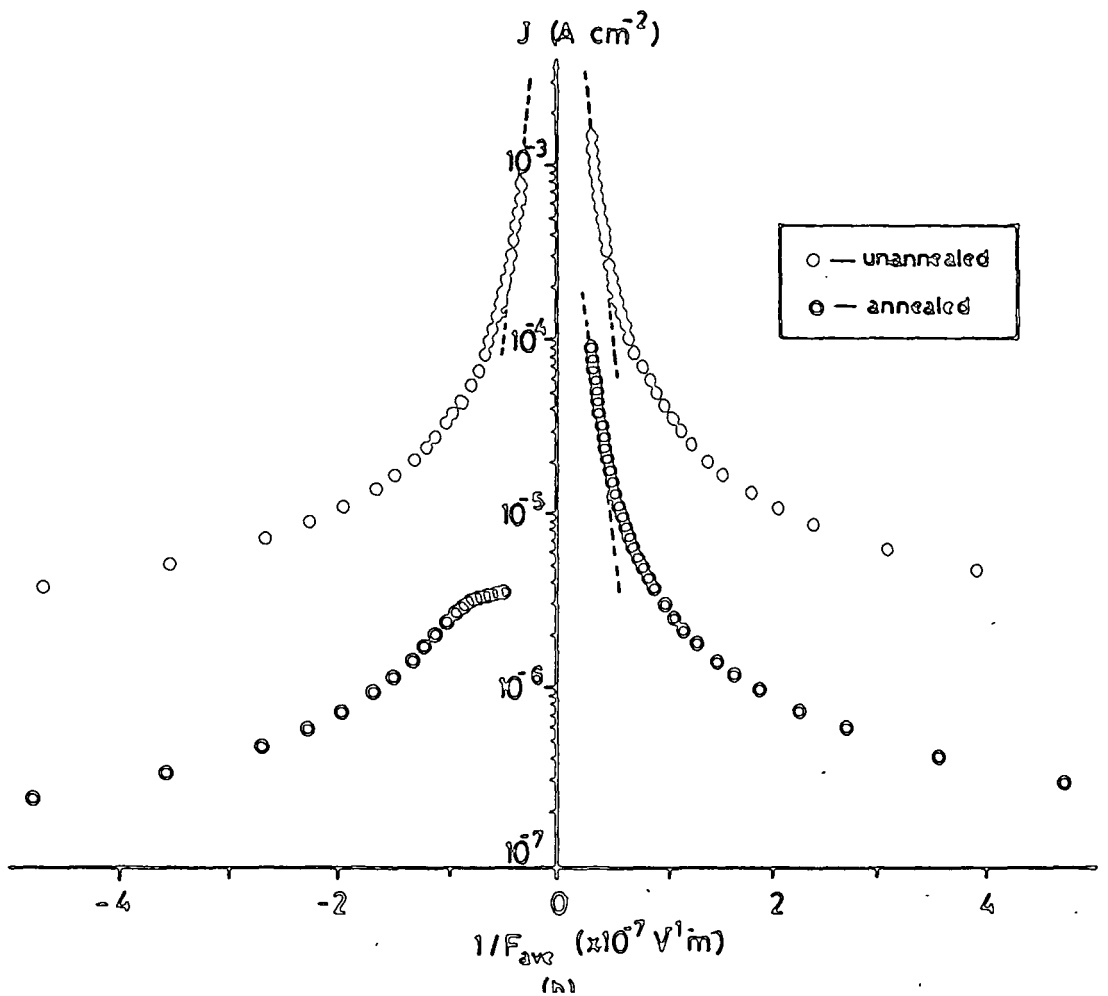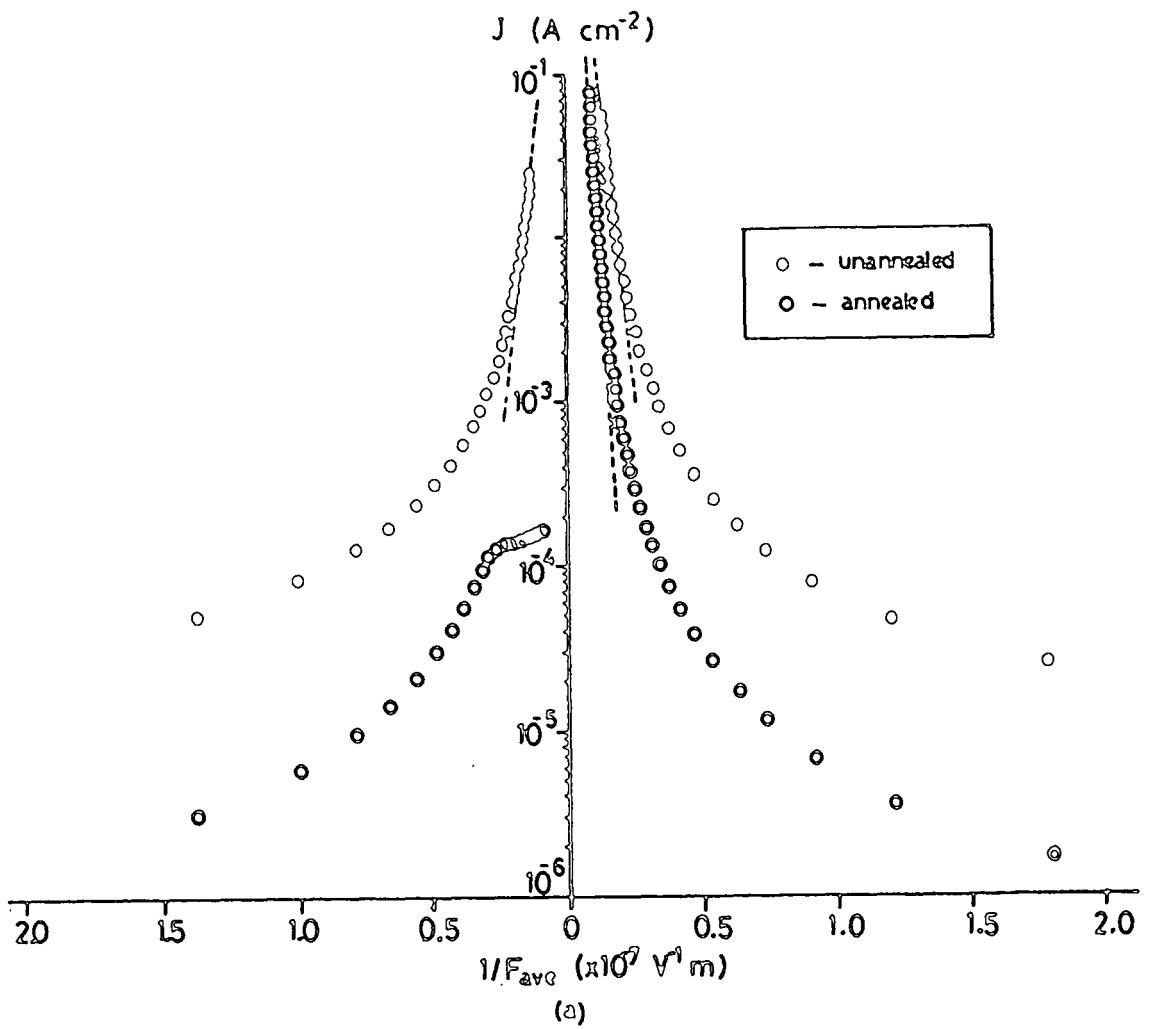
145

Figure 8.16    Data of Figs. 8.10a    and    8.10b    replotted, respectively in a) and b). on a Fowler-Nordheim plot.

$\phi_{eff}= U_e - E_{gs}$ in equation 8.12, was determined. These results are not convincing as the barrier heights show a polarity dependence for the thinner of the two films. For the thicker film the effective barrier height is extremely low and substantially different from that of the thinner film. There is also little difference in the barrier heights of the annealed and unannealed films. It is known that the size of the crystallites increases with annealing and as such, the barrier height should be substantially changed which it is not. Finally, even if the curves shown in Fig. 8.16 are expanded in an attempt to show the 'linear' portion of the curve, the 'linearity' is still somewhat doubtful. It therefore seems unlikely, that Fowler-Nordheim tunnelling between the crystallites is responsible for the conduction in these films.

### 8.3.3 Poole-Frenkel Emission Model

The final possibility that we are to consider for the conduction mechanism in these films is Poole-Frenkel emission. It is assumed firstly that due to the very large initial barrier height (i.e. about 3 eV, see Fig. 8.13) emission must take place from the crystallites into the band tails of the surrounding amorphous matrix. The details of Poole-Frenkel emission have been dealt with in detail in Chapter 3 and will not be repeated here.

The current density from Poole-Frenkel emission is proportional to the square root of the electric field. Figure 8.17 shows the current density as a function of the square root of the average electric field for the devices as shown
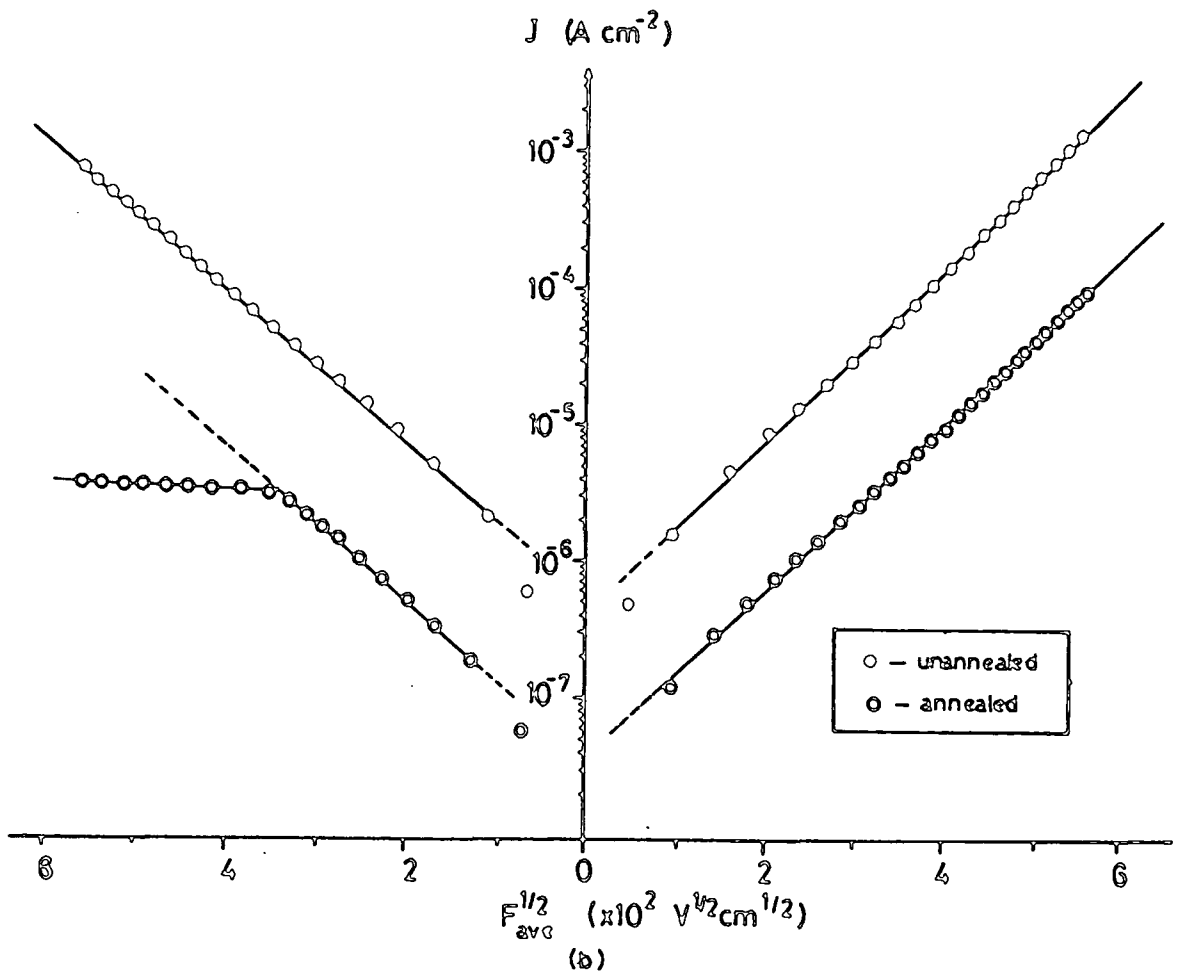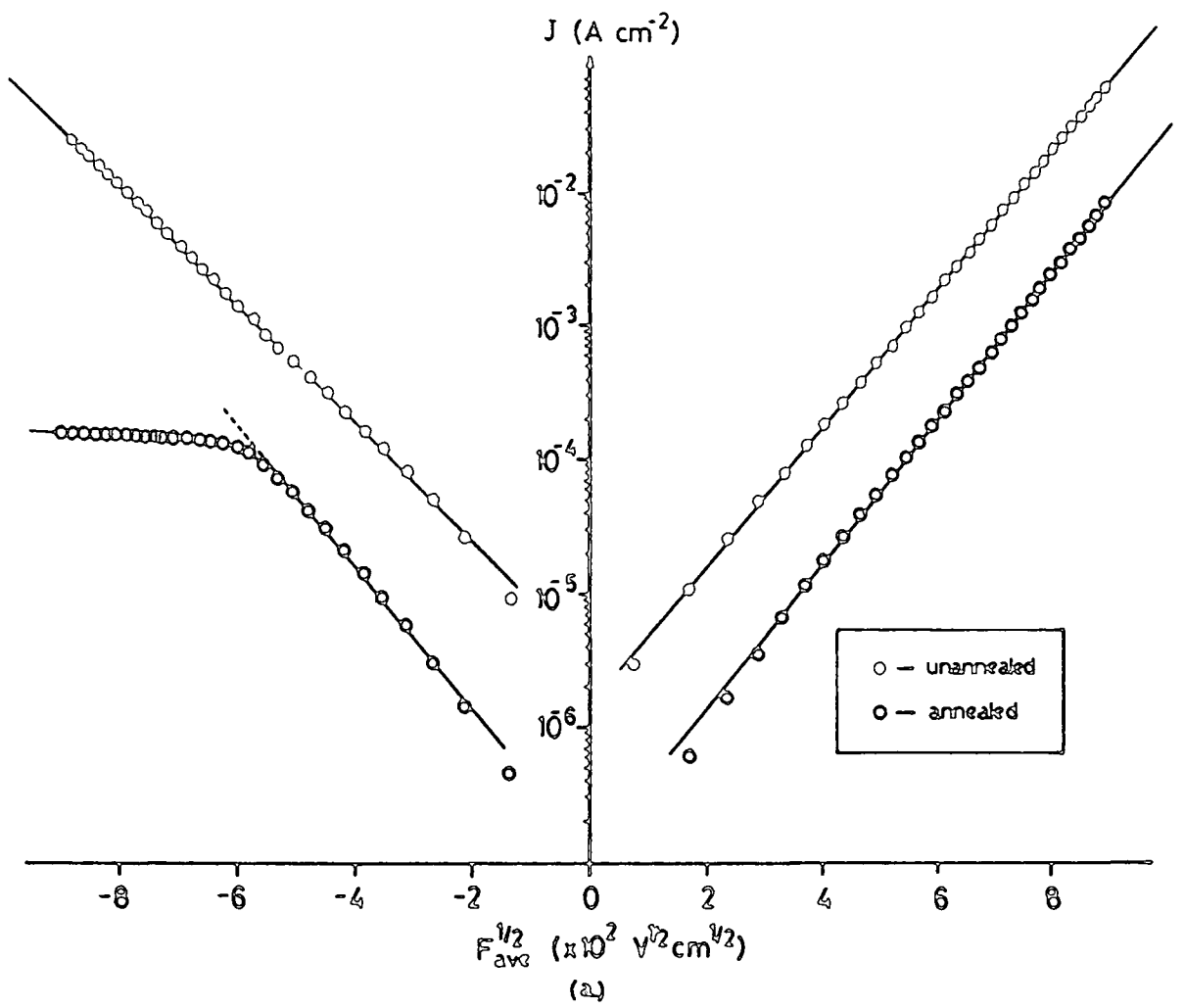
146

.

<u>Figure 8.17</u>   Data of Figs. 8.10a and 8.10b replotted, respectively in a) and b), on a Schottky plot.

previously. These curves are very linear response on these plots. From the gradient the calculated dynamic dielectric constant was determined giving the values in Table 8.4 The index of refraction of these films measured from ellipsometry was found to be of the order of 2.4 so that the optical dielectric constant is about 5.9 and the calculated dynamic dielectric constant should be approximately the same [21]. Table 8.4 shows a fairly large variation in the values obtained but they are within reasonable limits considering the that these films. although grown under the same deposition conditions, may not be compositionally alike. The optical dielectric constant for silicon dioxide is about 2.1 and the SRO films should have a value somewhat greater. The effect of the surface potential was not taken into account and it could be responsible for the apparent difference in the dynamic dielectric constant as a function of bias polarity. It has been found that the silicon content of films with lower $N_2$ carrier gas flows tends to have a lower excess silicon content. It is therefore possible that the excess silicon content in the thicker of the two films shown is less than that of the thinner film. This could account for the calculated dynamic dielectric constant being lower for the thicker of these films.

8.3.4 Summary

From this very limited study it is extremely difficult to ascertain the true nature of conduction in the silicon-rich oxide (SRO) films. The evidence seems to point towards the

147

Poole-Frenkel mechanism being responsible although it would be wrong to dismiss entirely any of these models as this is a very limited study and the conclusions should be treated accordingly The SRO films produced have been assumed to be compositionally the same material. It is well known, however, that such films are very dependent upon the conditions of growth. It is possible that the present films are not compositionally alike hence there may be reasonable cause to expect the conduction should different. The RES analysis showed that even films grown with the same deposition parameters but of different thickness did not contain identical concentrations of excess silicon.

## References for Chapter 8

[1]     D. Dong, E.A. Irene and D.R. Young, J. Electrochem. Soc., 125, 819 (1978).

[2]     A.R. West, Solid State Chemistry and its Applications, John Wiley and Sons, New York, Section 3.2.2, (1984).

[3]     D. Thomson, Stanford University, private communication.

[4]     T. Matsushita, T. Aoki, T. Ohtsu, H. Yamamoto, H. Hayashi, M. Okayama, and Y. Kawanaw, supplement to Jap. J. Appl. Phys., 15, 35 (1976).

[5]     T. Matsushita, T. Aoki, T. Ohtsu, H. Yamamoto, H. Hayashi, M. Okayama, and Y. Kawanaw, IEEE Trans. on Electron. Dev., ED-23, 826 (1976).

[6]     M. Hamasaki, T. Adachi, S. Wakayama and M. Kikuchi, J. Appl. Phys., 49, 3987 (1978).

[7]     M. Hamasaki, T. Adachi, S. Wakayama and M. Kikuchi, Solid State Comm., 4. 591 (1977).

[8]     M.L. Tarng, J. Appl. Phys., 49, 4069 (1978).

[9]     N. Zommer, IEEE Trans. on Electron. Dev., ED-27, 2056 (1980).

[10]    J.F. Verway, W. Ruis, and I. Sens, Rev. Phys. Appl., 13, 821 (1978).

[11]    D.J. DiMaria, K.M. DeMeyer, C.M. Serrano and D.W. Dong, J. Appl. Phys., 52, 4825 (1981).

[12]    N.T. Theis, J.R. Kirtley, D.J. DiMaria, and D.W. Dong, INFOS '83 Conf., Errlangan, The Netherlands, North-Holland Publishers. 134 (1983).

[13]    D.J. DiMaria, D.W. Dong, C. Falcony, T.N. Theis, J.R. Kirtley, J.C. Tsang, D.R. Young and F.L.Pesavento. J. Appl. Phys., 54, 5801 (1983).

[14]    D.J.Robbins. D.J. DiMaria, C. Falcony and D.W. Dong. J. Appl. Phys., 54, 4553 (1983).

[15]    S. Yokayama, D.W. Dong, D.J. DiMaria and S.K. Lai. J. Appl. Phys., 54, 7058 (1983).

[16]    S.K.C. Lai, D.J. DiMaria and F.F. Fong, IEEE Trans. on Electron. Dev., ED-30, 894 (1983).

[17]    D.J. DiMaria, D.W. Dong, F.L. Pesavento, C. Lam and S.D. Brorson, J. Appl. Phys., 55, 3000 (1984).

[18] D.J. DiMaria, J.R. Kirtley, E.J. Pakulis, D.W. Dong, T.S. Kuan, E.L. Pesavento, N. Theis, J.A. Cutro and S.D. Brorson, J. Appl. Phys., 56, 401 (1984).

[19] A. Ron and D.J.DiMaria, Phys. Rev. B, 30, 807 (1984).

[20] D.W. Tong, J.L. Benjamin and W.R. Van Dell, IEEE Trans. on Electron. Dev., ED-33, 779 (1986).

[21] S.M. Sze, J. Appl. Phys., 38, 2951 (1967).

# Chapter 9

## Conclusions and Suggestions for Further Work

### 9.1 Conclusions

Silicon-rich silicon nitride (SRN) films were grown with excess silicon concentrations varying from 8.8% to 12.8% by varying the reactant gas phase ratio from $R_n = 4.0$ to $R_n = 0.25$. All films were found to be predominantly $\alpha\text{-Si}_3\text{N}_4$ with free silicon crystallites being found in the films with the greatest silicon content. The conduction mechanism at high temperatures and electric fields is shown to be due to Poole-Frenkel emission of trapped electrons (holes) from relatively deep defect levels to the conduction (valence) band or band tails. From a steady-state analysis the effective trap depth, $\phi_t$ was found to be approximately 1.1 eV and it decreased slightly with increasing silicon content of the films. The value of the calculated dynamic dielectric constant was used to indicate how well the experimental results fitted to the steady-state Poole-Frenkel conduction theory. It was found to vary from 3.6 to 4.0 with changes in excess silicon content from 8.8% to 12.3%. These low values were attributed to the build up of space charge near the injecting contact. The pre-exponential factor C. which is related to the density of defect states was found to increase with increasing silicon content. Based on these results it was concluded that for thin films ($< 1000$ Å) steady state analysis cannot be considered accurate unless the effects of trapped space charge are taken

into account. A build-up of space charge results in a calculated dynamic dielectric constant substantially lower than would normally be acceptable. Polarity and thickness dependencies of the I-V characteristics are also due to the trapped charge in these thin films.

To account quantitatively for the trapped charge in the SRN films, transient flat band and current measurements were performed. For positive (negative) applied bias voltages, the flat band shift was in a positive (negative) direction, thus implying a net increase in negative (positive) charge within the film. A logarithmic time dependence was found for the transient flat band shift while for long periods of time (i.e. t › 1s) the current transient was inversely proportional to time. A model used for charge trapping in MNOS structures was adapted to the metal-SRN-silicon structure and was found to predict such a logarithmic charge trapping mechanism. The model was based on the assumption that charge carriers, holes for negative bias and electrons for positive bias, tunnelled from the silicon valence and conduction bands or their associated band tails into the SRN film. Very good agreement was found between the data and the model predictions for low electric fields. At high electric fields, the situation becomes complicated by Poole-Frenkel 're-emission' from the traps which leads to a saturation of the flat band shift with time. At high electric fields, the current transient also becomes dominated by Poole-Frenkel emission of trapped carriers. The current relaxation at high electric fields is therefore due to a balancing between two interrelated

phenomena. A steady-state is reached when the rate of Poole-Frenkel emission from the traps is equal to the rate at which carriers are tunnelling into the traps.

It was also found from the current transients that the calculated dynamic dielectric constant decreases with increasing time. That is to say that as the time increases, the amount of space charge increases which in turn decreases the calculated dielectric constant. From the Schottky curves for times of one second, $\varepsilon_d$ was found to vary from 5.09 to 5.26 for excess silicon contents of 8.8% to 12.3%. It was therefore concluded that to obtain an accurate value of the dynamic dielectric constant, measurements must be performed for very short times before the build-up of a significant density of trapped charge. For these SRN films the density of trapping centres near the SRN-silicon interface was found to be of the order of $3 \times 10^{19}$ cm$^{-3}$.

A preliminary investigation of the properties of silicon-rich oxide on silicon was carried out. RHEED, RBS and AES analysis techniques showed that the SRO films were amorphous with very small crystallites. Annealing at high temperatures produced a substantial growth of the crystallites. The films were found to be of basically uniform composition throughout their thickness. A slight increase in oxygen content was found at the surface of the films and was attributed to oxidation of the excess silicon in the film prior to the metal deposition. A large transitional region was also found near the silicon-SRO interface where there was a gradual increase of silicon and a gradual decrease of oxygen as the

interface was approached.

The conduction in silicon-rich oxide (SRO) was investigated using standard I-V techniques. These films did not show the long current transients characteristic of the silicon-rich silicon nitride, indicating fewer space charge effects. Three models of steady-state conduction were investigated. These were a symmetrical Schottky barrier model similar to that used for polycrystalline silicon, a model based on Fowler-Nordheim tunnelling between silicon crystallites in the SRO film and a model based on Poole-Frenkel emission from the silicon crystallites into the conduction band or band tails of the film. From this very limited study it was extremely difficult to assess the true nature of the conduction in the silicon-rich oxide (SRO) films, but the evidence seemed to point towards the Poole-Frenkel mechanism being responsible for conduction. However, it would be wrong to dismiss entirely either of the other two models as this was a very limited study and the conclusions should be treated accordingly.

These results showed that the conductivity of silicon-rich silicon nitride (SRN) and silicon-rich silicon dioxide (SRO) can be varied over orders of magnitude with the adjustment of the deposition parameters. For devices, such as the MISS switch, where a semi-insulating layer is needed, control of the conductivity is paramount to be able to tailor the devices to specific applications. The SRN films, however, would be of limited value for such devices, as the charge storage, which has been shown to be extremely slow, would be a detriment to high speed operations. On the other hand, the SRO films would

154

most likely be applicable to these devices, as they showed no charge storage as the SRN films did.

## 9.2 Suggestions for Further Work

For the silicon-rich silicon nitride (SRN) a number of extensions to the present work could be undertaken for future investigations. An extension to the charge trapping model could be developed to include the loss of charge carriers at high electric fields due to Poole-Frenkel emission. Also the effect of the trapped space charge on the local electric field near the injecting contact should be included in the local field calculation within this model. On the measurement side, much faster flat band transient measurements are needed to obtain information about the effect of the Poole-Frenkel emission at high electric fields on the tunnelling of charge into the traps.

A greater range of excess silicon content of both the SRN and SRO films would show the transition in the conduction mechanisms from silicon-rich nitride or oxide to polysilicon films.

As the study of the conduction mechanisms for the SRO films was limited much more analysis need be undertaken. The connection between the growth technique and the electronic conduction needs to be investigated in detail. It is not clear at the present time how the electronic conduction changes with changes in the silicon content of the films. For this type of a study, in depth structural analysis, including RBS, AES, SIMS, RHEED, TEM, X-ray diffraction, infrared spectroscopy,

etc., would give the necessary link between the conduction mechanisms and the growth technique. If the conduction is truly Poole-Frenkel, as we have concluded, and therefore based on the trapping and detrapping of injected charge, transient C-V and I-V measurements will give more insight into the actual trapping mechanisms in the SRO films. Film thickness variation and I-V and C-V measurements over a large range of temperatures would also reveal much information.

The nature of the charge storage in the SRN films may preclude its use from high speed devices but applications in memory devices are possible. The SRO films do not seem to have such charge storage problems. This work has shown that the conductivity of silicon-rich films can be varied over a very large range. Both SRN and SRO films could therefore be used for devices where such variations in conductivity are needed.